



HAL
open science

Short and long term analysis of upper plate deformation in northern Chile subduction zone with GPS and tiltmeter data

Gianina Meneses-Provoste

► **To cite this version:**

Gianina Meneses-Provoste. Short and long term analysis of upper plate deformation in northern Chile subduction zone with GPS and tiltmeter data. Earth Sciences. Université Paris sciences et lettres, 2018. English. NNT: 2018PSLEE022 . tel-02088340

HAL Id: tel-02088340

<https://theses.hal.science/tel-02088340>

Submitted on 2 Apr 2019

HAL is a multi-disciplinary open access archive for the deposit and dissemination of scientific research documents, whether they are published or not. The documents may come from teaching and research institutions in France or abroad, or from public or private research centers.

L'archive ouverte pluridisciplinaire **HAL**, est destinée au dépôt et à la diffusion de documents scientifiques de niveau recherche, publiés ou non, émanant des établissements d'enseignement et de recherche français ou étrangers, des laboratoires publics ou privés.

THÈSE DE DOCTORAT

de l'Université de recherche Paris Sciences et Lettres
PSL Research University

Préparée à l'École Normale Supérieure

Analyse à court et long terme de la déformation de la plaque supérieure dans la zone de subduction du nord du Chili avec des données GPS et d'inclinométrie

Short and long term analysis of upper plate deformation in northern Chile subduction zone with GPS and tiltmeter data

Ecole doctorale n°560

Ecole Doctorale des Sciences de la Terre

Spécialité : Sciences de la Terre et de l'Environnement

Soutenue par :

Gianina

MENESES-PROVOSTE

le 06 Décembre 2018

Dirigée par :

Christophe VIGNY

Laboratoire de Géologie de l'ENS

COMPOSITION DU JURY :

M. VIGNY Christophe – **Directeur de thèse**
Laboratoire de Géologie, ENS-Paris

Mme LASSERRE Cécile – **Rapporteur**
Laboratoire de Géologie, ENS-Lyon

Mme ROLANDONE Frédérique – **Rapporteur**
ISTeP, Sorbonne Université

M. BERNARD Pascal – **Examineur**
Sismologie - IPGP

M. MAZZOTTI Stéphane – **Président du jury**
Géosciences - Risques, Université de Montpellier

M. NOCQUET Jean-Matthieu – **Examineur**
Tectonique, IPGP/Geoazur-Nice



Laboratoire de Géologie, École Normale Supérieure
Ecole Doctorale des Sciences de la Terre et
de l'Environnement et Physique de l'Univers

Thèse présentée pour obtenir le titre de
DOCTEUR EN SCIENCES DE LA TERRE
Spécialité: Géophysique

Gianina MENESES-PROVOSTE

**Short and long term analysis of upper plate
deformation in Northern Chile subduction zone
with GPS and tiltmeter data**

Soutenue le 06 Décembre 2018 devant le jury composé de

Christophe VIGNY	Directeur de thèse	ENS-Paris
Cécile LASSERRE	Rapporteur	ENS-Lyon
Frédérique ROLANDONE	Rapporteur	ISTeP, Sorbonne Université
Pascal BERNARD	Examineur	IPGP
Stéphane MAZZOTTI	Président du jury	Université de Montpellier
Jean-Matthieu NOCQUET	Examineur	IPGP/Geoazur-Nice

Contents

Contents	i
List of Tables	iv
List of Figures	v
Acknowledgments	ix
Préface	1
Preface	4
1 Introduction	7
1.1 Different phases of the subduction seismic cycle	7
1.2 The concept of coupling on the seismogenic zone	9
1.3 Transient deformation during the seismic cycle	10
1.3.1 Transient aseismic slip	11
1.3.2 Viscoelastic relaxation of the mantle	12
1.4 The North Chile subduction zone	14
2 Searching for short-term transient events in North Chile subduction zone	19
2.1 GPS time series	20
2.2 The problem	25
2.3 Common mode noise and local mapping approach	25
2.4 Methodology	27
2.5 Complementary data: Long base tiltmeter measurements	30
2.6 Results	31

2.6.1	Summary : A catalog of small transient events found in North Chile . . .	35
2.6.2	Transient displacements detected in north Chile subduction zone	35
2.6.3	Conclusion	67
3	A long term change on the deformation accumulation	68
3.1	Introduction	68
3.2	Improving precision on GPS time series of 15 years duration	72
3.2.1	The Mass distribution effect	72
3.2.2	Seasonal variations observed in Northern Chile	74
3.2.3	Hydrological correction for northern Chile GPS time series	74
3.2.4	GPS time series correction	78
3.2.5	Velocity error estimation and the concepts of white and colored noise .	81
3.3	Results: Long term velocity change detected by geodetic instruments	82
3.4	Possible phenomena explaining the velocity change observed	86
3.5	Two-dimensional viscoelastic finite-element model of an intermediate-depth earth- quake	89
3.5.1	Description of the model	89
3.5.2	Viscoelastic mantle rheology	92
3.6	Results: 2D-model sensitivity to geometrical and rheological parameters	94
3.7	Three-dimensional viscoelastic finite element model of Tarapaca 2005 earthquake	98
3.7.1	Abstract	98
3.7.2	Introduction	99
3.7.3	Tarapaca 2005 earthquake and GPS observations	101
3.7.4	Velocity decrease after Tarapaca earthquake	103
3.7.5	Finite element modeling	106
3.7.6	Coseismic displacement from Tarapaca earthquake	108
3.7.7	Results: viscoelastic deformation after Tarapaca Earthquake	111
3.7.8	Discussion	117
3.7.9	Conclusion	119
4	Instrumental gap between Central and North Chile is filled: new results regarding coupling complexities and the Andean sliver motion	120
4.1	Brief review of the principal results of the study	152

4.1.1	Anomalies of the interseismic velocity pattern	152
4.1.2	The new local sliver hypothesis and the coupling distribution founded for Taltal	154
4.1.3	Interseismic velocity calculation	156
4.1.4	Do Taltal velocities represent the interseismic period?	157
Conclusions		159
Bibliography		162
A Appendix A (chapter 2)		172
B Appendix B (chapter 3)		174

List of Tables

2.1	Results obtained after 15 years analysis of GPS data with Pyacs.	34
2.2	Summary of transient events founded between 2008 and 2011 in North Chile. .	36
3.1	Availability of northern Chile GPS stations from 2000 to 2015.	76
3.2	Elastic parameters increasing with depth.	91
3.3	Parameters of different rheologies used in this study.	111
A.1	RMS information for stations corrected between September 2008 and February 2009.	172
A.2	RMS information for stations corrected between May and October 2010.	173
B.1	Tarapaca 2005 postseismic velocity values.	176
B.2	Tarapaca 2005 observed coseismic displacements	176

List of Figures

1.1	Stages of the seismic cycle and deformation patterns associated.	8
1.2	Friction regimes from Scholz [1998].	10
1.3	Episodic tremor and slip phenomena in Cascadia.	11
1.4	Slow slip in different subduction zones.	12
1.5	3 different snapshots of different periods during the seismic cycle on different subduction zones.	13
1.6	Seismic context of Chilean margin (1976-2010).	15
1.7	Interseismic velocities and coupling in northern Chile.	16
1.8	Seismic context of Chilean margin (1976-2015).	17
1.9	Seismic crisis associated to Iquique earthquake 2014.	18
2.1	Four local-regional networks of GPS.	24
2.2	Time span configuration for 15 years GPS data analysis	27
2.3	2 examples of Pyacs performance.	29
2.4	2 seismograms showing an intermediate depth earthquake in 2005.	30
2.5	Tiltmeter instrument.	32
2.6	2 examples of time series corrected with Pyacs contrasting in the number of reference stations.	33
2.7	Reference and Pyacs corrected stations for the period between October 2013 and March 2014. Seismic crisis before Iquique 2014 is included.	37
2.8	Filtered horizontal components of time series for coastal stations recording seismic crisis in 2014.	39
2.9	Filtered horizontal components of time series for inland stations recording seismic crisis in 2014.	40

2.10	Filtered vertical components of time series for coastal and inland stations recording seismic crisis in 2014.	41
2.11	Difference between coseismic and observed displacements corresponding to the foreshock activity from Iquique 2014 earthquake (figure from F. Boudin (Per. Comm.)).	43
2.12	Tiltmeter register recording foreshock activity to Iquique earthquake during 2014 (figure from F. Boudin (Per. Comm.)).	44
2.13	4 slow seismic slip events founded in 2014.	45
2.14	Slow seismic events preceding Iquique earthquake (Socquet <i>et al.</i> [2017]). . .	47
2.15	Ground deformation for several sites in northern Chile before Iquique 2014 (Socquet <i>et al.</i> [2017]).	48
2.16	Time series showing 40 days of transient displacement during 2008-2009. . . .	50
2.17	Plain view of stations and transient horizontal displacements observed during 2008-2009.	51
2.18	Example of environmental changes triggering a transient displacement.	53
2.19	Small transient event detected at IQQE, UAPE and PICA cGPS sites in 2010. . .	56
2.20	North and vertical components of the station IQQE.	56
2.21	Horizontal transient displacements detected by 3 sites in 2010.	57
2.22	Very small or non-existent displacements founded for the east component on coastal and eastern stations.	58
2.23	Earthquake M_w 6.0 in 2009 detected by 2 coastal GPS stations.	59
2.24	GPS stations configuration and seismic events during 2009.	61
2.25	Transient event detected by the sites HMBS and PB01 during 2009.	62
2.26	Recordings from IQQE and CRSC during 2009.	63
2.27	Total transient displacements detected in 2009.	64
2.28	3 recordings detecting a small transient displacement during 2011.	65
2.29	GPS station setting and transient displacements founded in 2011.	66
3.1	Examples of viscoelastic models for one shallow and one subduction earthquake.	70
3.2	Characteristics of Tarapaca 2005 earthquake.	71
3.3	Fourier series and GRACE modeled curves representing annual hydrological variations.	73
3.4	Seasonal signals for Northern Chile GPS stations	75

3.5	Comparison between velocities calculated with and without hydrological correction.	77
3.6	Instrumental changes affecting 4 of 5 stations records.	78
3.7	Seasonal corrected time series sampled every 10 days.	80
3.8	Velocities before and after Tarapaca 2005.	82
3.9	Observed postseismic signal for combined and other stations.	84
3.10	Comparison between observed coseismic and postseismic displacements.	88
3.11	Scheme of the grid of a 2D viscoelastic finite element model.	90
3.12	Scheme of different rheologies.	92
3.13	Modeled postseismic deformation for 3 different viscoelastic rheologies of the asthenosphere.	95
3.14	Postseismic deformation including a low viscosity channel of different longitudes.	97
3.15	Characteristics of Tarapaca 2005.	102
3.16	Velocities before and after Tarapaca 2005.	104
3.17	Postseismic deformation associated with Tarapaca 2005 earthquake recorded by 5 cGPS stations.	105
3.18	Afterslip and slow slip possible patterns contrasted with observed postseismic displacements.	106
3.19	Three-dimensional grid for Tarapaca 2005 earthquake occurring in Chile.	107
3.20	Description of a simple Burgers rheology.	108
3.21	Horizontal and vertical coseismic displacements from Tarapaca 2005 (model and observations).	110
3.22	4 site time series contrasted with 4 viscoelastic models.	112
3.23	RMS curve for 11 models with Burgers rheology.	115
3.24	Observed and preferred model postseismic velocities.	116
3.25	Best model fitting the 4 available stations.	117
4.1	Interseismic velocity field and coupling distribution from Métois <i>et al.</i> [2016]	121
4.2	Evolution of sGPS network between 2010 and today (2016).	123
4.3	GPS network of regions of Atacama and south Antofagasta.	124
4.4	New velocity field for Atacama region in northern Chile.	153
4.5	Coupling model for the region of Atacama from Métois <i>et al.</i> [2016].	154
4.6	Preferred model of coupling for Atacama region.	155

4.7	Global reference frame used in velocity field calculation for Taltal.	156
4.8	Amplitude of postseismic deformation in the zone of Taltal.	157
4.9	Horizontal time series in the Atacama region.	158
B.1	Horizontal velocity decrease for 5 GPS stations recording before 2005.	175
B.2	7 years of horizontal deformation predicted by preferred model.	176

Acknowledgments

We all improve our thinking and creative skills guided by our interests and empowered by our own resolution, but so many times in our life we are pushed on by external forces, either to remind us of our strengths in low moments, or to push us forward to get levels we did not know were possible. The thesis process made me more than aware of all these external forces and now I want to thank you all.

I want to start thanking Philippe Agard and all the people involved in the ZIP project without which these pages disappear. Many thanks to all the members of the jury who kindly accept to attend and contribute to my work. I want to thank of course my supervisor, Christophe Vigny for all he taught me, but specially for always trust on me. Thanks Luce Fleitout for your dedication to my project, your knowledge is immense and I was lucky to have you guiding part of my work. Thanks Sergio Ruiz for putting in my mind the right words in our sporadic but honest conversations the first years here. Thanks Raul Madariaga for being an inspiration for so many and for always trusting on my work, you will have always my admiration. I want to thank Marcos Moreno for including me in his research team during my short stay at GFZ and pushing me to go further. Many thanks to J.M. Nocquet and J. -D Garaud for shearing your methods and knowledge with me. Finally, I want to thank Frederick Boudin for all those interesting scientific discussions we had, and Emilie Klein for always being available to help me.

New friends I met here were essential in so many ways. Thanks Marija, Sarah (chicas) for your friendship and so many great talks. Slaven, Michele, Casper and Jonas for making me laugh so much and for being just so good people. Zippies thank you all for the fun and memorable moments. People from the lab: Evangelia, Tim, Kristel, H el ene, Emilie, Audrey, Damien D., Damien W., C edric B., thanks for all those conversations, moral support and specially Montagne time. Li, Lavinia, Paoline, Claire and Eva we met at the end of this adventure, but not enough late to get the best impression of you.

Gracias familia por la paciencia y el apoyo, por entender y aceptar mis decisiones siempre de la mejor manera. Gracias mamá, Claudia, Magda y Cristóbal por dejarme ir, por resistir con fuerza los terremotos emocionales y por recibirme una y otra vez. Gracias a toda la gran familia que tengo (presentes y los que tristemente han partido), por mantener la comunicación, por la preocupación y las palabras de apoyo siempre tan oportunas. Gracias a todos los amigos por mantenerse siempre cerca en estos años intensos. La separación intensificó la confianza de muchas relaciones fraternales preexistentes, hizo otras evolucionar a cosas diferentes y potentes, e hizo también posible afortunados reencuentros de los que me encuentro en constante sorpresa y admiración. Gracias especialmente a Paz, Efraín, Andrés, Alma, Chuck y Pequeña, sin ustedes era imposible. Gracias Isabel por las excelentes conversaciones científicas que me entregaste y especialmente por tus palabras y compañía. Thanks my love for your incredible support, wise words, love and care. Meeting you during this period has been intense, but fundamental to keep me courageous.

Finalmente quiero dar gracias a mi padre, quien me inculcó la curiosidad, la lectura y sin saberlo, el seguir caminos fuera de la norma. Si bien no alcanzaste a ver este final, supongo que estarías orgulloso de todo lo que he aprendido y de la persona en que me he convertido.

Préface

Le moteur de la tectonique des plaques sur notre planète est la subduction. Les zones de subduction, où les plaques convergent, impliquent le recyclage de la lithosphère océanique dans le manteau convectif pour former une croûte continentale par migration vers le haut de la partie fondue de la plaque. Dans ce processus d'enfoncement à long terme, la plaque supérieure accumule des contraintes qui sont instantanément libérées sous forme de séismes, se répétant sur un processus cyclique : le cycle sismique de la subduction (SEC). Néanmoins, le glissement rapide sur les failles n'est pas le seul processus contribuant à la déformation pendant la SEC. L'augmentation du nombre d'instruments sismiques et géodésiques permanents surveillant ces régions au cours des dernières décennies a été fondamentale pour mieux comprendre les autres phénomènes qui se produisent dans les zones de subduction. L'un d'eux est le glissement aisé-sismique, un processus à basse fréquence observé sous différentes formes, y compris le steady creeping des failles ou le glissement lent transitoire. Exemples de signaux transitoires sont l'afterslip qui se produit autour de la zone qui a glissé lors d'un séisme et les séismes à glissement lent (SSE) dont la durée est beaucoup plus longue que les séismes "normaux". De la même importance est l'effet du stress induit par un tremblement de terre dans le manteau. Parce qu'il se comporte comme un corps viscoélastique, le manteau détend ce stress au cours d'un processus de déformation lent, durable (plusieurs années ou décennies) et à grande échelle (centaines à milliers de km). Par conséquent, tous ces phénomènes ont un impact sur la déformation de la plaque supérieure et doivent être pris en compte dans l'analyse du budget de glissement sur la SEC. Ensuite, le couplage entre les plaques - ou le verrouillage sur l'interface de subduction - pendant la période d'accumulation intersismique peut être correctement déduit. Il en résulte une meilleure estimation de l'aléa sismique d'une région. Sur la base de cette prémisse, la principale motivation de ce travail est de contribuer à la détermination de l'état actuel de verrouillage de l'espace sismique nord de la zone de subduction chilienne.

Afin d'aider les lecteurs à suivre facilement ce manuscrit, **Chapitre 1** résume les concepts les plus pertinents pour ce travail. Les sections suivantes traitent de trois sujets différents liés à la question d'intérêt : 1. l'acquisition des données, 2. l'analyse des données et 3. la modélisation. Les deux dernières constituent la partie principale de cette étude, qui a été menée dans deux directions : l'analyse et l'interprétation des déformations transitoires à court terme (jours, semaines) et à long terme (plusieurs années) détectées par les stations GPS permanentes déployées dans le nord du Chili. **Chapitre 2**, décrit la recherche exhaustive des signaux transitoires à court terme (jours à semaines) dans les séries temporelles géodésiques à partir de stations continues enregistrant depuis plus de 15 ans. Ce travail vise à contribuer au débat actuel sur la question de savoir si des glissements lents se produisent ou non dans la zone de subduction chilienne. Jusqu'à présent, un seul cas de glissement lent associé à la phase de nucléation d'Iquique 2014 (M_w 8.1) a été rapporté. Nos résultats, obtenus après filtrage et analyse approfondie des séries temporelles consacrées à la réduction de leur bruit inhérent, indiquent l'existence de seulement 3 événements susceptibles de correspondre à de petits épisodes de glissement sismique se produisant entre 2009 et 2011, avec des durées de quelques semaines et des amplitudes qui ne dépassent pas 4 mm. De plus, l'occurrence de l'épisode de glissement sismique plus important simultané à l'activité du séisme d'Iquique 2014 est confirmée, et l'analyse est poussée plus loin à l'aide d'enregistrements par inclinomètres à longue base. Grâce à cette analyse affinée et à la sensibilité de cet instrument, il est possible d'identifier 4 événements de glissement lent distincts dans la plus grande région de glissement lent révélée par les données GPS, survenus au cours des 3 mois précédant le choc principal avec des magnitudes comprises entre M_w 5.8 et 6.2. **Chapitre 3** décrit l'analyse à long terme de la série temporelle du cGPS, réalisée afin d'identifier les changements mineurs mais significatifs des tendances sur de longues périodes (\sim ans). Les données disponibles indiquent une diminution à long terme de la déformation de la plaque supérieure après le séisme de profondeur intermédiaire de Tarapaca 2005 (M_w 7.7). La recherche d'une explication à cette baisse de vitesse nous a conduit à tester l'effet viscoélastique de l'asthénosphère sur la déformation de surface déclenchée par une rupture profonde (\sim 100 km de profondeur). Nous construisons un modèle 3D viscoélastique réaliste d'éléments finis viscoélastiques et avons essayé les rhéologies viscoélastiques de Maxwell et Burgers. Nous trouvons une très bonne correspondance entre le signal postsismique observé associé à cet événement et la déformation postsismique modélisée à l'aide d'une rhéologie de Burgers avec une viscosité à long terme de $1.9e+18$ Pa s, contestant l'hypothèse d'une diminution du couplage

intersismique menant éventuellement à le megathrust d'Iquique. Enfin, comme nous l'avons mentionné précédemment, l'acquisition de nouvelles données géodésiques a constitué une part importante de ce travail. Au cours de cette thèse, 2 campagnes GPS ont été réalisées, concernant des instruments GPS non permanents (sGPS) déployés dans le désert d'Atacama (nord du Chili). Ces données de campagne n'ont pas été incluses dans l'analyse des séries temporelles, mais elles étaient très nécessaires pour combler une lacune instrumentale entre 24° et 28° , ce qui était essentiel pour la réalisation d'études récentes (Métois *et al.* [2016]; Klein *et al.* [2018]) contribuant à l'évaluation des risques sismiques dans la région en améliorant les informations existantes sur sa distribution du couplage. Le chapitre final 4 montre le travail de Klein *et al.* [2018], et comprend un bref aperçu discussion de la principale problématique qui y est exposée : nous trouvons une nouvelle Zone de Couplage Faible (LCZ) à la latitude de la ville de Taltal (25°), coupant une longue portion de la subduction du nord du Chili en deux segments couplés distincts, aux caractéristiques géométriques différentes. Cette découverte conduit à la réestimation de l'extension plausible de la future rupture et donc du risque sismique dans la région.

Preface

The engine of plate tectonics on our planet is subduction. Subduction zones, where plate converge, involve the recycling of oceanic lithosphere in the convective mantle to form continental crust by upward migration of the melted part of the slab. In this long-term sinking process, the upper plate accumulate stresses that are instantaneously released in the form of earthquakes, repeating over a cyclic process: the so-called seismic earthquake cycle (SEC). Nevertheless, fast slip on faults is not the only process contributing to the deformation during the SEC. The increase of permanent seismic and geodetic instruments monitoring these regions during the last decades has been fundamental to gain insight into other phenomena taking place in subduction zones. One of them is aseismic slip, a low-frequency process observed in different forms including steady fault creeping or transient slow slip. Examples of the latest are the afterslip that occurs around the area that has slipped during an earthquake, and slow slip earthquakes (SSEs) with much longer durations than “normal” earthquakes. Of the same importance is the effect of stress induced by an earthquake in the mantle. Because it behaves like a viscoelastic body, the mantle will relax this stress during a slow, long-lasting (several years to decades) and large-scale (hundreds to thousands of km) deformation process. Consequently, all these phenomena impact the upper plate deformation and have to be considered in slip budget analysis over the SEC. Then, coupling between the plates - or locking on the subduction interface - during the inter-seismic accumulation period can be correctly inferred. This in turns leads to a better estimation of the seismic hazard of a region. Following this premise, the principal motivation of this work is to contribute to the determination of the actual locking state of the north seismic gap of the Chilean subduction zone.

In order to help the readers to easily follow this manuscript, **Chapter 1** summarizes the most relevant concepts pertinent to this work. The following sections address three different topics related to the question of interest: 1. data acquisition, 2. data analysis and 3. modelization. The

latest two comprise what is the main part of this study, which was conducted along two directions: analyzing and interpreting both short-term (days, weeks) and long-term (several years) transient deformations detected by permanent GPS stations deployed in north Chile. **Chapter 2**, describes the exhaustive search for short term transient signals (days to weeks) in geodetic time series from continuous stations recording for more than 15 years. This work aims at contributing to the current debate of whether slow slip events do occur in the Chilean subduction zone or not. Up to now, only a single and debated case of slow slip associated to the nucleation phase of Iquique 2014 (M_w 8.1) has been reported. Our results, obtained after thorough filtering and analysis of the times series devoted to reduce their inherent noise, indicate the existence of only 3 events that are likely to correspond to small episodes of aseismic slip occurring between 2009 and 2011, with durations of few weeks and amplitudes that do not exceed 4 mm. Furthermore, the occurrence of the larger aseismic slip episode simultaneous to the foreshock activity of Iquique 2014 earthquake is confirmed, and the analysis is pushed further with the help of long-base tiltmeter records. Thanks to this refined analysis and to the sensitivity of this instrument, 4 distinct slow slip events can be identified in the larger region of slow slip revealed by GPS data, occurring during the 3 months previous to the mainshock with magnitudes ranging between M_w 5.8 and 6.2. **Chapter 3** describes the long-term analysis of the cGPS time series, conducted in order to identify small but significant changes of trends over long durations (several years). Available data indicate a long-term decrease of the upper plate deformation after the intermediate depth earthquake of Tarapaca 2005 (M_w 7.7). Searching for an explanation for this velocity decrease lead us to test the viscoelastic effect of the asthenosphere on surface deformation triggered by deep failure (~ 100 km depth). We build a realistic 3D viscoelastic finite element model and tried Maxwell and Burgers viscoelastic rheologies. We find a very good correspondence between the observed postseismic signal associated to this event and the modeled postseismic deformation using a Burgers rheology with a long-term viscosity of $1.9e+18$ Pa.s, challenging the hypothesis of a decrease of interseismic coupling eventually leading to the megathrust failure of Iquique. Finally, as mentioned earlier, acquisition of new geodetic data has been an important part of this work. During this thesis 2 GPS surveys were performed, concerning non-permanent GPS instruments (sGPS) deployed in the Atacama desert (northern Chile). These campaign data were not included in the time series analysis but were much needed to fill an instrumental gap between 24° and 28° , which was essential for the realization of recent studies (Métois *et al.* [2016]; Klein *et al.* [2018]) contributing to the seismic hazard assessment

of the region by refining existent information about its coupling distribution. Final **Chapter 4** shows the work of Klein *et al.* [2018], and includes a brief discussion of the main problematic exposed in it: we find a new Low Coupling Zone (LCZ) at the latitude of the city of Taltal (25°), cutting a long portion of the northern Chile subduction into two distinct coupled segments, with different geometrical characteristics. This finding leads to the re-estimation of the plausible extension of the future rupture and thus, the seismic hazard in the region.

Chapter 1

Introduction

1.1 Different phases of the subduction seismic cycle

The subduction seismic cycle is a concept which enclose different phases of deformation related with the convergence between plates and the consequent strain accumulation and stress release in the form of megathrusts earthquakes. Its simplest form was derived from the elastic rebound theory (Reid [1910]), originally based on surface observations from San Francisco 1906 earthquake occurred in San Andreas transform fault. It proposes that the nature of the deformation slowly accumulated before an earthquake is elastic; thus, the sudden release of this strain during an earthquake produces a response of opposite sign and equal magnitude, canceling each other. More than 50 years after the formulation of this theory, Fedotov *et al.* [1977] is the first to adapt this concept to subduction zones. Despite the fact that certain studies at the time already include the viscoelasticity of the mantle in their models, in those years the subduction cycle was commonly described as composed by 2 stages: an **interseismic phase** characterized by long-term elastic strain accumulation (several decades or centuries) determined by the convergence between plates and the locking of their contact interface, followed by a **coseismic phase** that occurs when the friction in this interface is suddenly overcome, producing fault slip (earthquake) and deformation for several seconds or even minutes. Geodetic and geological measurements at the coast of subduction zones confirm the transition from interseismic to coseismic characterized by the rebound of this zone: coastal subsidence and uplift before and after a seismic event is a process that repeats through seismic cycles (see figure 1.1, A-B). This simplified model inspired several other studies proposing periodicity in the occurrence of earthquakes (Shimazaki &

Nakata [1980]), opening the possibility for earthquake prediction. This stream was interrupted by the development of geodetic techniques during the nineties, which allowed the detection of transient deformation contaminating the interseismic period. These transient signals were the manifestation of non-linear phenomena taking place in subduction zones: aseismic slip and viscoelastic relaxation of the mantle excited by an earthquake. Among them, the ones triggered by stress changes produced during the coseismic phase define what is the **postseismic phase** (see figure 1.1, C), today a recognized stage of the seismic cycle with durations from years to decades. The existence of these non-linear processes and evidence of accumulation of permanent (non-elastic) deformation, significant at geological timescales, revealed the complexity of the seismic cycle of mega-earthquakes.

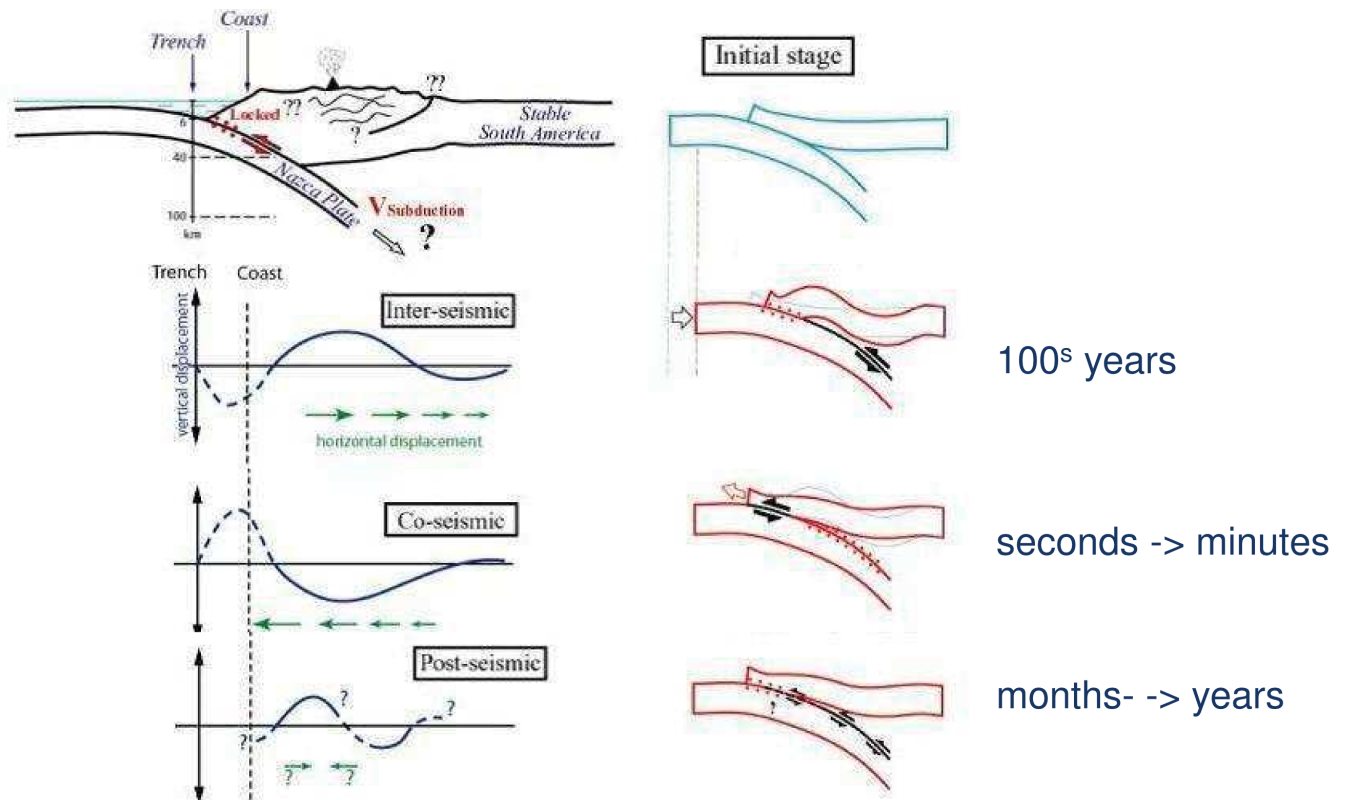


Figure 1.1: Figure from Chlieh [2003] describing patterns of deformation observed for each stage of the seismic cycle.

1.2 The concept of coupling on the seismogenic zone

The main reason to improve our understanding in all processes involved in the seismic cycle lies principally in achieving the assessment of the seismic hazard in subduction zones. Nevertheless, despite of all the current progress on comprehending subduction earthquakes, is still not completely clear how to determine the magnitude and extension of an expected event in advance. Both characteristics seem to be closely related with the actual state of coupling between plates, founded to be an heterogeneous distribution of locked and low coupled zones. For instance, several large ruptures have been found to be correlated with highly coupled patches identified during the interseismic period (Ruegg *et al.* [2009]; Moreno *et al.* [2010]; Métois *et al.* [2013a]), and decoupled regions proposed to be possible barriers for rupture extension (Perfettini *et al.* [2010]; Kaneko *et al.* [2010]). Nevertheless, coupling is a complex concept that involves several characteristics describing the mechanical interaction between 2 sides of a fault. For example, in a purely kinematic approach, a coupling factor is inferred by the inversion of geodetic deformation measurements. This factor commonly varies between free sliding of the 2 sides of a fault (or coupling ratio of 0), when the convergence and dislocation velocities are the same, and a completely locked fault (or coupling ratio of 1), when there is not relative displacement between the plates. The concept of coupling can as well give insight about interacting forces and fault properties, but this has to be always separated from the merely kinematic description mentioned above (Wang & Dixon [2004]).

The coupling pattern in the subduction plane seems to be related with the frictional regime governed by the laboratory-derived constitutive laws of slip rate and state (Dieterich [1979]; Ruina [1983]). Slipping of locked regions of the interface, subjected to the force exerted by the convergence between plates, depends strictly on whether the static coefficient of friction (μ_s) is overcome. The type of resultant displacement will strictly depend on the dynamic coefficient (μ_d) of friction which in turn varies with the slip velocity and material properties. If μ_d increase during the sliding creating more resistance, the resulting continuous displacement is under the regime of “velocity-strengthening”, a behavior that allows to explain aseismic slip episodes. In the opposite case that μ_d decrease as the fault slides, what it is obtained is a “velocity-weakening” unstable (and conditionally stable) behavior of irregular slip, the appropriated environment to explain fast earthquakes ruptures, which are nucleated in unstable areas to then propagate to conditionally stable regions (see figure 1.2).

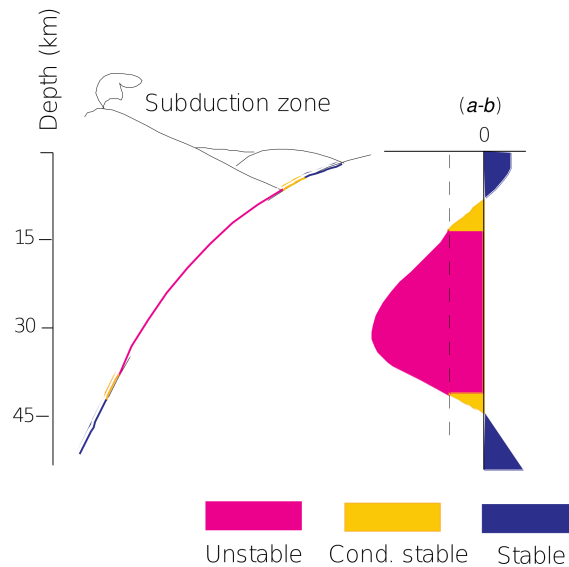


Figure 1.2: Modified from Scholz [1998]. Different frictional regimes in function of depth for a subduction zone. Parameter $(a-b)$ corresponds to the velocity dependence of steady-state friction.

1.3 Transient deformation during the seismic cycle

The seismic cycle is determined by the repetition of characteristic earthquakes. This type of events are high frequency seismic slip processes with typical durations of seconds or minutes. They correspond to rock fracture after the strain accumulation process during the interseismic period, fracture that is fast enough to release elastic waves. This period between earthquakes is contaminated by several other slip phenomena, triggered or not by coseismic slip. For instance, quasi-static (or **aseismic**) slip has been observed in different regions, which in contrast with regular earthquakes is a slower process that can last from days to months. This term refers both to steady slip (creep) and transient movements, like slow slip earthquakes or the afterslip phenomena (Peng & Gomberg [2010]; Avouac [2015]). Furthermore, large earthquakes trigger the **viscoelastic response of the mantle**, another transient phenomenon producing measurable surface deformation. These different processes are described in more detail in the following sections.

1.3.1 Transient aseismic slip

Contrary to seismic slip, **slow slip events** (SSE) are a low-frequency process, commonly accompanied by the release of high frequency seismic energy in the form of low amplitude and low frequency seismic waves or non-volcanic tremor (see figure 1.3). The associated phenomena of slow slip and tremor has been identified in several subduction zones, and is named by Rogers & Dragert [2003] as episodic tremor and slip (ETS). In contrast with regular failure, slow slip events have longer seismic source times, with a duration of days, weeks or even months, producing surface displacements of several tens of centimeters (Peng & Gomberg [2010]).

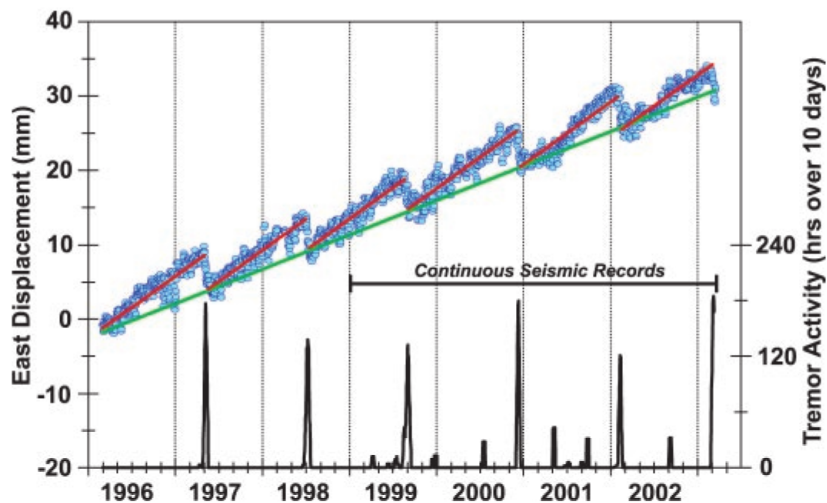


Figure 1.3: Figure from Rogers & Dragert [2003] showing east deformation (blue circles) recorded during 7 years by a continuous GPS site in Cascadia, characterized by episodic seismic tremor (picks shown in the bottom graph) occurring simultaneously with slow slip reverse displacements. Green line represents the interseismic trend, while red lines show higher trends between slip events. The episodic recurrence is a particular characteristic of this zone.

Mostly all studies detecting slow slip in different subduction zones (see figure 1.4) as Japan (Hirose & Obara [2005]; Ito *et al.* [2007]), Cascadia (Rogers & Dragert [2003]; Schmidt & Gao [2010]), Mexico (Radiguet *et al.* [2011]), among others, locate its source on the plate interface, recurrently on the downdip extension of the thrust fault, although modeled solutions are commonly non-unique. Aseismic slip occurring here increase the stress on the shallower parts of thrust faults, possibly preparing the conditions for a mega-thrust rupture (Dragert *et al.* [2004]; Ito *et al.* [2007]; Peng & Gomberg [2010]); however, clear evidence of slow slip triggering megathrusts earthquakes is still on debate.

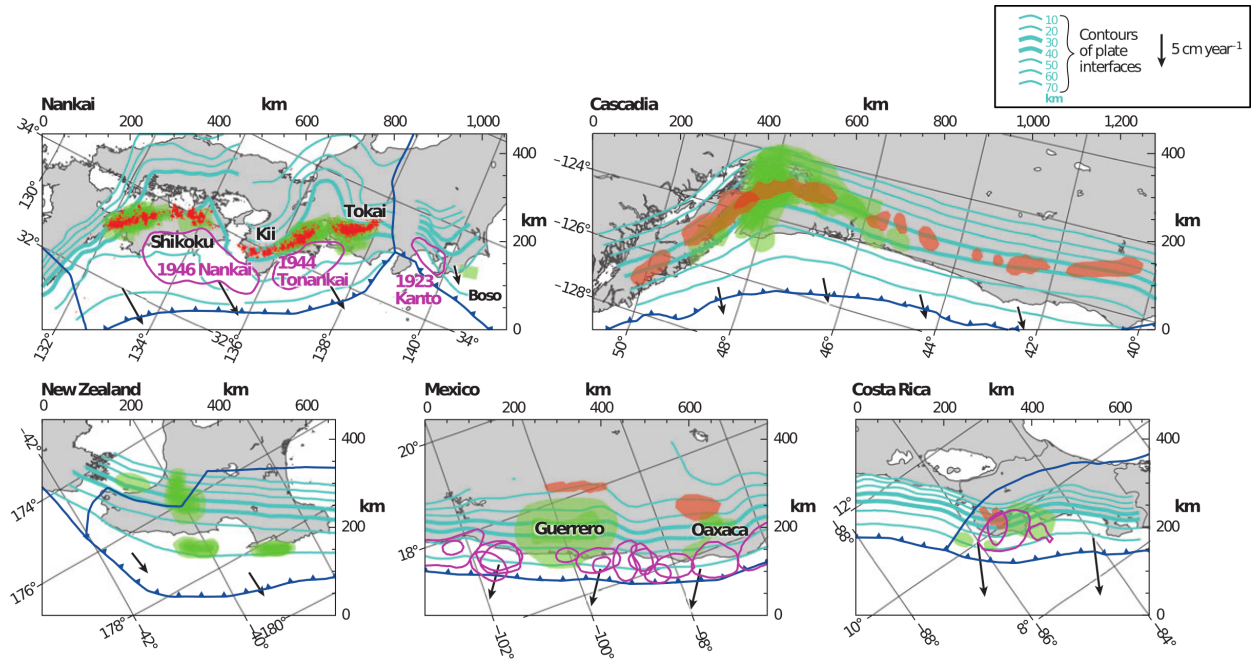


Figure 1.4: Modified from Beroza & Ide [2011]. A sample of different slow slip episodes occurring in subduction zones worldwide. Slow slip and tremor are represented by green and red areas respectively. Contours of plate interfaces correspond to light blue lines. Megathrust rupture areas for some subduction zones are drawn in purple. Black arrows represent velocities. ETS correspond with subduction zones with young plates ($< 50Ma$).

1.3.2 Viscoelastic relaxation of the mantle

In the last decades, the increase on the number of geodetic instruments monitoring subduction zones and the improvement on their accuracy (nowadays reaching millimeters), have allowed to study in more detail crustal deformation following mega earthquakes. Cortical displacement measurements during the interseismic period have revealed the existence of time-dependent deformation not only measurable locally near the rupture, but rather to global distances, and lasting for several decades after mega-earthquakes (Hu *et al.* [2004]; Trubienko *et al.* [2013]; Klein *et al.* [2016]). These far-field geodetic observations confirm that processes occurring in the surroundings of the thrust fault can not be directly responsible for this large-scale deformation. What explains this far-field deformation relates with the viscoelasticity of the mantle. Once a coseismic rupture occurs, the stress field is modified triggering the response of inner viscoelastic layers of the Earth; the asthenosphere initially resists the coseismic movement, to later relax the stresses slowly, producing deformation towards the trench with durations ranging from months to several decades depending on the magnitude of the event. The rheology of

the mantle is responsible for its dual behavior: a viscoelastic material will be considered elastic in short-time scales, while properties of a fluid-viscous material will govern at larger time-scales ranging between 10^{11} and 10^{17} seconds (Turcotte & Schubert [2002]). Thus, deformation during the first years after an earthquake is controlled not only by instantaneous and time-dependent displacements occurring on the fault (seaward movement on the surface), but also by the transitory phase of the viscoelastic relaxation of the mantle (landward movement on the surface). In the following years, what predominates is the long-term mantle relaxation and re-locking of the fault, both producing deformation of opposite signs. In this way, crust velocities far from the rupture are mostly due to the long-term viscoelastic relaxation effect. For this reason, decades after a mega-earthquake, the interseismic velocity pattern often shows far-field vectors still moving seaward, while the re-locking of the subduction interface dominates the near-field producing inland deformation (see figure 1.5-b). Considering viscoelasticity in models of the seismic cycle is thus fundamental in order to differentiate time-dependent deformation due to viscoelastic relaxation from what may be wrongly interpreted as time dependent slip on the fault.

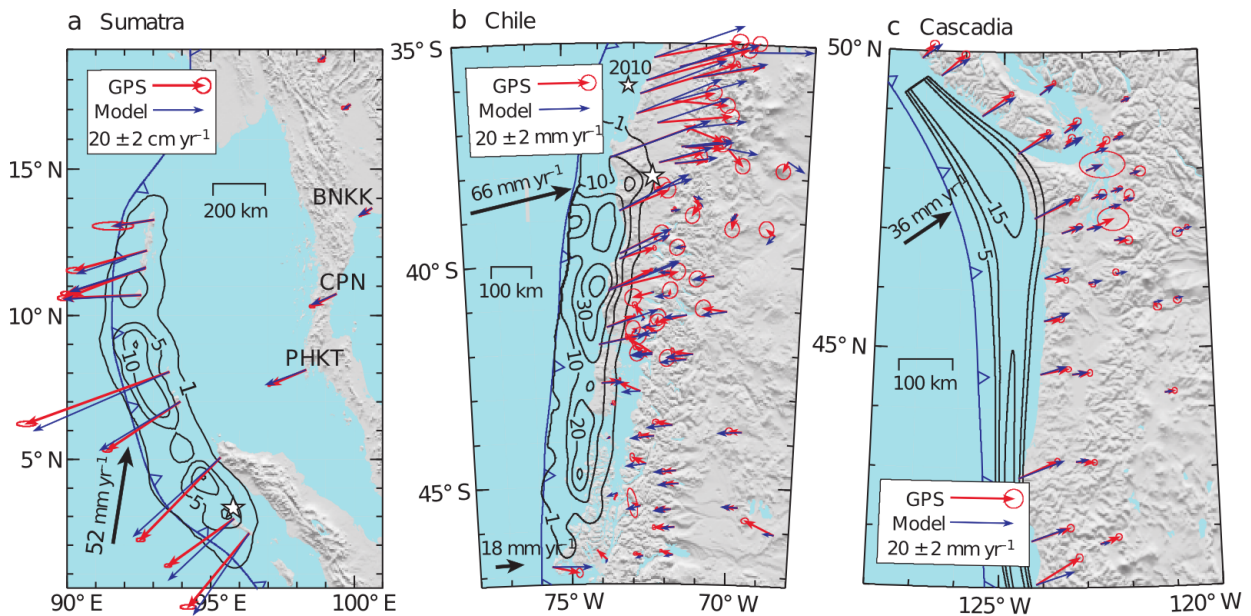


Figure 1.5: Figure from Wang *et al.* [2012]. Horizontal velocity field observed (red) and obtained using a viscoelastic model (blue) during 3 different periods of the seismic cycle. Each period corresponds to a different convergent margin. A: 1 year after the M_w 9.2 Sumatra of 2001. B: 4 decades after M_w 9.5 Valdivia earthquake in 1960. C: 3 centuries after Cascadia earthquake magnitude $M_w \sim 9.0$ of 1700.

1.4 The North Chile subduction zone

Chile is a long and narrow territory that extends for more than 4000 km from north to south, along a very seismically active subduction zone. In this region, on average affected by a mega earthquake ($M_w > 8.0$) every 10 years, took place the megathrust earthquake of Valdivia 1960 M_w 9.5, the largest event recorded so far. Seismicity information of the most active area of the Chilean subduction zone (up to 40° S) is shown in figure 1.6. This compiling image, modified from Métois [2012], provide temporal and spatial characteristics of historical and instrumental earthquakes up to 2010. These seismic activity, aside from confirming the recurrence of mega ruptures, make evident the imbalance between seismic activity of the northern part and the rest of the margin (M_w 8.8 Maule 2010 already filled the southern seismic gap). Taking into account the lack of mega earthquakes produced in this region since 1877 and the relatively fast convergence velocity between the plates of 6-7 cm/yr (Angermann *et al.* [1999]; Vigny *et al.* [2009]), the northern part of Chile subduction zone has been recognized as an important seismic gap. For this reason, this region has been permanently monitored during the last decades by geodetic and seismic instruments in order to obtain information about the evolution of the seismicity and deformation in a region that is prone to break. Métois *et al.* [2013b] use elastic inversion of northern Chile interseismic velocities, collected in several geodetic campaigns performed between 2000 and 2012 (figure 1.7-A) and free from co- and post-seismic signals, to obtain the interseismic coupling between the plates. From this study is inferred 2 main segments of high coupling separated by a low coupling zone at the latitude of Iquique (see figure 1.7-B). This known seismic gap remained silent since the megathrust earthquake of 1877 to April 2014, when the interseismic earthquake of Iquique M_w 8.1 breaks 150 km of its northern part. From figure 1.8 (edited from Klein [2015]), that includes seismicity until 2015, is clear the current state of the gap and the particular changes produced by this event on the curves representing the seismicity of the margin.

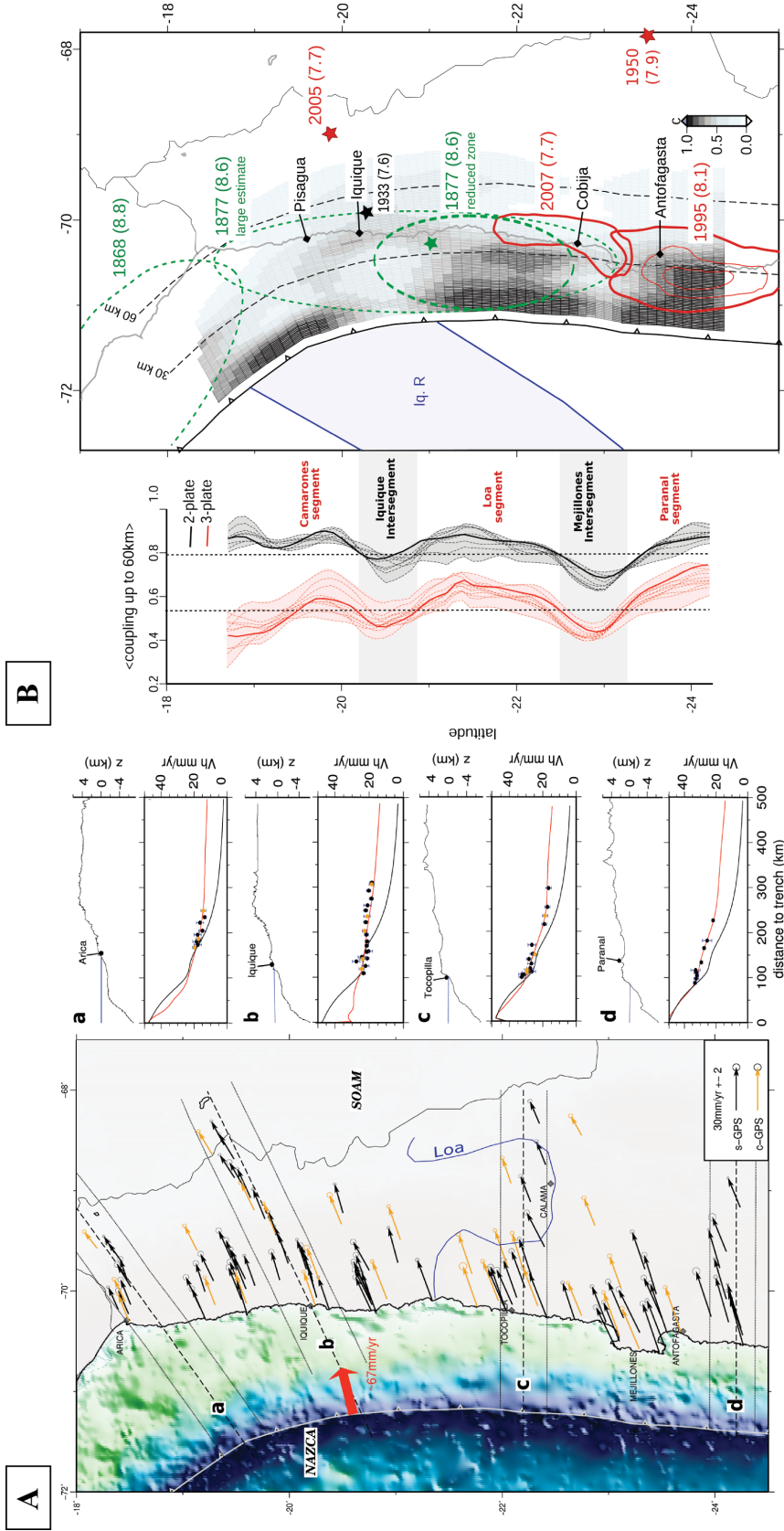


Figure 1.7: Figure modified from Métois *et al.* [2013b]. A: Interseismic velocity field calculated from campaign and continuous deformation data obtained during the period 2000–2012. Velocity vectors are calculated respect to the South American plate. On the right, 4 profiles (a,b,c & d) of 30 km width show vertical velocities. A simple first order model (Chlieh *et al.* [2004]) and the preferred model of this study are represented by the black and red curves. B: Seismic interseismic coupling distribution obtained from their preferred 3-plates model including the rigid motion of an Andean sliver. Northern part consists on 2 high coupled segments separated by the low coupling segment of Iquique.

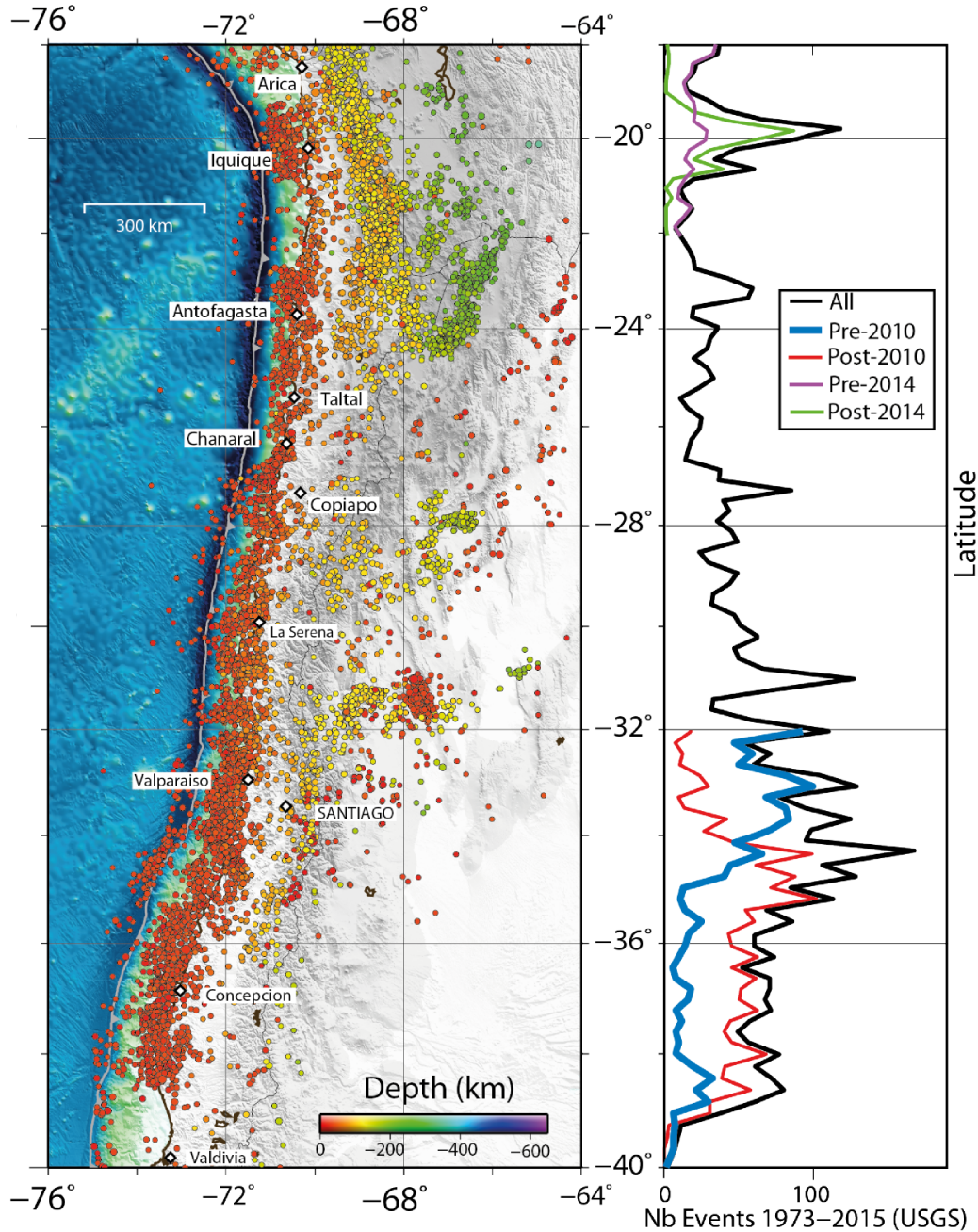


Figure 1.8: Figure modified from Klein [2015]. Seismicity distribution along Chile subduction zone from 1976 to 2015. Number of events for this period is represented by the black curve on the right. Colored curves represent number of events pre- and post- seismic crises of both Iquique 2014 (north) and Maule 2010 (south).

The seismic crisis related to Iquique earthquake (01/04/2014) is particular because is preceded by numerous foreshock events, striking the zone more intensely from January 2014. This precursory activity was distributed in 2 main swarms, the northern one demarcating what would correspond to the area of the main rupture, and the second southern cluster preparing the area of

the largest aftershock. Figure 1.9 depicts the difference of seismicity rate for the periods 2010-2013 and 2013-2016, and gives more detail about the temporal evolution of the events.

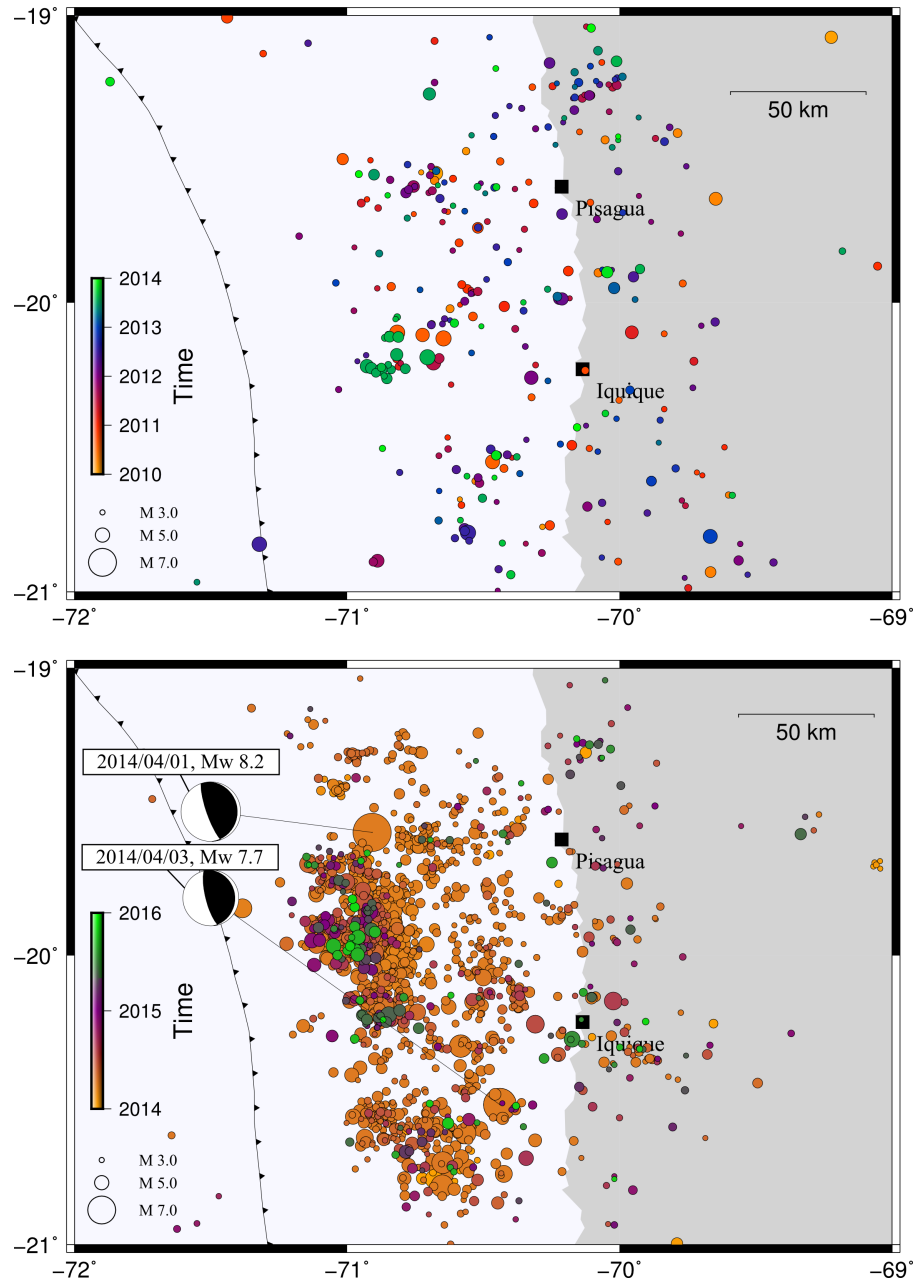


Figure 1.9: Seismicity distribution (Chile Seismological Center locations) corresponding to the period between 2010 to 2016, divided in pre- and post- 2014 periods (top and bottom maps respectively). Date and focal mechanism of the main shock and the largest aftershock are indicated in the figure. Seismic activity associated to Iquique earthquake is characterized for being divided in 2 important clusters, separated approximately at the latitude of Iquique (bottom figure).

Chapter 2

Searching for short-term transient events in North Chile subduction zone

In contrast with other subduction zones like Japan or Sumatra among others, in Chile there is no clear evidence of transient slip associated to slow slip events. The first observation in North Chile of this type, coincides with the foreshock activity corresponding to Iquique earthquake M_w 8.1 which struck the zone on 1 April 2014 (Ruiz *et al.* [2014]; Schurr *et al.* [2014]; Bedford *et al.* [2015]; Socquet *et al.* [2017]). However, whether the episode can be qualified as aseismic slip is still debated. Schurr *et al.* [2014] argue that the transient signal registered for cGPS instruments is entirely explained by the cumulative co-seismic displacement associated to the clustered seismic activity previous to the mainshock. Similarly, Bedford *et al.* [2015] can explain the majority of cGPS positions as seismic slip considering sensible ranges of source errors, except for the seismic activity of March 2014 which exceed uncertainties range and it is proposed as aseismic slip associated to foreshock afterslip. On the contrary, Ruiz *et al.* [2014] determine that only a 20% of the cumulative displacement can be attributed to the largest foreshock (16 March, M_w 6.7) of the seismic crisis, and that the remaining seismic activity does not give account for the observed transient displacement. They suggest aseismic slip taking place in the low coupling zone in front of Iquique starting at least from March 2014, event that seems to trigger the numerous seismic swarms occurring in the zone. Socquet *et al.* [2017] on the other hand, set the starting date of a similar aseismic slip event as early as June 2013. A relevant point to consider here is that a good part of the differences between all these studies, comes from the sensitivity of predicted displacements to slight variations of the moment tensor param-

eters corresponding to the largest event of the foreshock sequence (M_w 6.7). For instance, only a small rotation of the slip vector of this seismic event lead to large differences on the observed displacements at coastal stations, this because their locations are in the vicinity of a nodal plane. The transient associated to the seismic sequence of 2014 is the largest registered in this region, but only amounts to less than 20 mm in 3 weeks, i.e. less than 1 mm/day. The difficulty on identifying such small transient signals lies in the comparable magnitude between these displacements and their uncertainties; thus, the possibility that smaller events exist hidden in the noise of GPS time series is high.

In this chapter we will explore systematically 15 years of noise-filtered cGPS signals from North Chile with the purpose of detecting all possible transients signals, whether they are seismic or a-seismic. Beyond detection, we aim at quantifying their size, duration and “shape” (i.e. moment time function), all quantities being of first importance in the hope of analyzing and understanding the physical mechanism of their sources.

2.1 GPS time series

Time series product of Global Positioning System (GPS) show the variation with time of the position of a point located on the Earth surface. Due to the direct relation between crustal displacements and stress field affecting the Earth, monitoring the evolution of this positions is a powerful tool to infer characteristics of Earth internal processes taking place during the seismic cycle.

Determining a position by using GPS techniques requires to measure distances (geometric ranges) between a GPS station and 4 or more satellites at the same time. Satellites are orbiting at around 20.000 km away from the Earth and the minimum of 4 is necessary to determine the 4 unknown parameters (3 coordinates of the position and time). Geometric range is obtained in terms of carrier phases; that is to say, measuring the phase of the wave sent from the satellite to the receiver. Thus, the total distance will be the phase difference between this signal and the one the receiver replicates, together with the integer number of wavelengths completed in this trajectory. This last quantity is called integer ambiguity, which resolution is a complex and difficult process, not implemented in all positioning techniques and softwares.

There are many other complexities in this process that have to be solved, like obtaining accurate

orbits of satellites, signal delay from the atmosphere, clock errors, receiver noise and multipath effect related to signal reflection on objects near the receiver antenna. Overall, there are two methods to solve these range biases and thus calculate site positions: Precise Point Positioning (PPP) and differencing techniques. The PPP approach gives the absolute coordinates of a site (still relative to a pre-existing network), processing sites one at a time. The satellite clock errors are handled using clock corrections calculated otherwise and published by JPL. Ambiguities can be, but are usually not resolved, in a PPP process. Differencing techniques, particularly the double difference used in this work and performed by the software GAMIT/GLOBK (King & Bock [1999]) explicitly form the double-differences that allow to eliminate both receiver and satellite clock errors. They usually give more precise daily positions than the PPP method because they also usually include the ambiguity resolution. This relative point positioning solution provides the position of one site with respect to another: the baseline. Differencing techniques are more time consuming than PPP and limited by computer memory size since the actual number of observables grows with n^2 (rather than n for PPP), n being the number of stations including in the process.

The more relevant steps followed to obtain relative coordinates by using GAMIT are:

1. Homogenization of the raw data transforming different receiver observation files (daily files per station) on a common ASCII format: RINEX (**TEQC** software).
2. Module **MAKEX** transforms RINEX format into specific GAMIT format and separates RINEX files in phase files and clock files (X and K files respectively).
3. Module **MODEL** calculates the theoretical phase and the covariance matrix representing the sensitivity of the model to the parameters (station and satellites coordinates (L y T files), earth movements, propagation model, etc.)
4. Module **AUTCLN** is an essential step in which observed phases (C files) are cleaned, meaning large differences between predicted and observed phases, that allow to identify erroneous measurements, are flagged so that they are not used in the station position determination. Cycle leaps are also flagged and corrected. This program can be run several times during the processing.

5. Finally, module **SOLVE** estimates the parameters in a least squares approach (minimizing residuals between predicted and observed phases by adjusting the parameters of the model, among them station positions) including ambiguity resolutions. It produces loosely constrained solutions (H files) including the estimated parameters and the full covariance matrix.

The whole process can be iterated as many times as necessary to achieve convergence to the set of model parameters yielding the best fit (the smaller residuals).

At the end of this process we obtain daily H-files containing daily free solutions for all the stations included in the calculation, giving relative site positions (baselines) with a typical precision of 1-2 mm for the horizontal components and 3-5 mm for the vertical component. Baselines are precise but always ambiguous: one never knows which end is moving. Then, apart from simple geometries, baselines rates of change are difficult to plot and analyze. Therefore, and because we want to determine deformation with respect to the South American Plate, it is necessary to first enlarge the scale of our network to the whole continent and second, map these baselines into a reference frame. For this purpose, during the processing we first need to include stations from regional networks in South America. We merge our Chilean data set with 25 RAMSAC (Argentina) stations, 20 RBMC (Brasil) stations, 2 Bolivian stations and a dozen of stations located in South America from the International GNSS Service (IGS), allowing to obtain daily H-files including baselines with all these sites to all our sites. Due to the considerable calculation time, product of the large number of stations, this process is divided in 2 or 3 sub-networks depending on the period (see figure 2.1), with several sites in common in order to link the solutions at a later stage. As a result, some baselines are explicitly processed and computed in double-differences, when others are determined only through the combination.

The way of defining the sub-networks is made by following the “rule of thumb” which consists on to keep the number of stations in a given sub-network below 100. The smaller the number, the faster the double-difference process. However, processed baselines usually have a better precision than not-processed baselines (because of ambiguity resolution); consequently the larger the sub-net, the better the precision.

It is standard procedure with GAMIT (SOPAC processing of IGS global network) to build sub-networks of an arbitrary equal number of stations (generally 60, depending on computer capacities) randomly picked every day so that sub-networks are always different but statistically “equivalent” and “homogeneous”, with on average a comparable and stable number of short, medium and long baselines. For our process, we choose not to follow this procedure but rather fix the sub-networks once and for all, so that a given baseline is processed in the same way everyday.

Then, the mapping into a global reference frame is achieved by combining our regional continental scale processing (2 or 3 sets of daily H-files) with the SOPAC processing of the IGS network (8 sets of daily H-files including approximately 400 stations globally distributed).

The last stage consists on mapping all relative coordinates into the stable International Terrestrial Reference Frame (ITRF) (Altamimi *et al.* [2011]). We use a subset of 40-50 stations with well known coordinates and perform a daily Helmert transformation to adjust our coordinates to the ones of ITRF. In this work, we use the 2008 realization of the ITRF, so-called ITRF08. Finally, by repeating the process for each day we obtain time series of absolute coordinates with respect to the ITRF. We produce both daily time series and weekly time series (time series in which H-files are combined over the successive GPS weeks rather than day-by-day). Weekly time series have less high-frequency noise because orbits are better constrained over a week than over a day. Therefore, they are perfectly suited for establishing long trends with the best precision but they do not allow to analyze short term transients occurring over days (see details about the use of daily time series, and thus the short term approach, in the next sections).

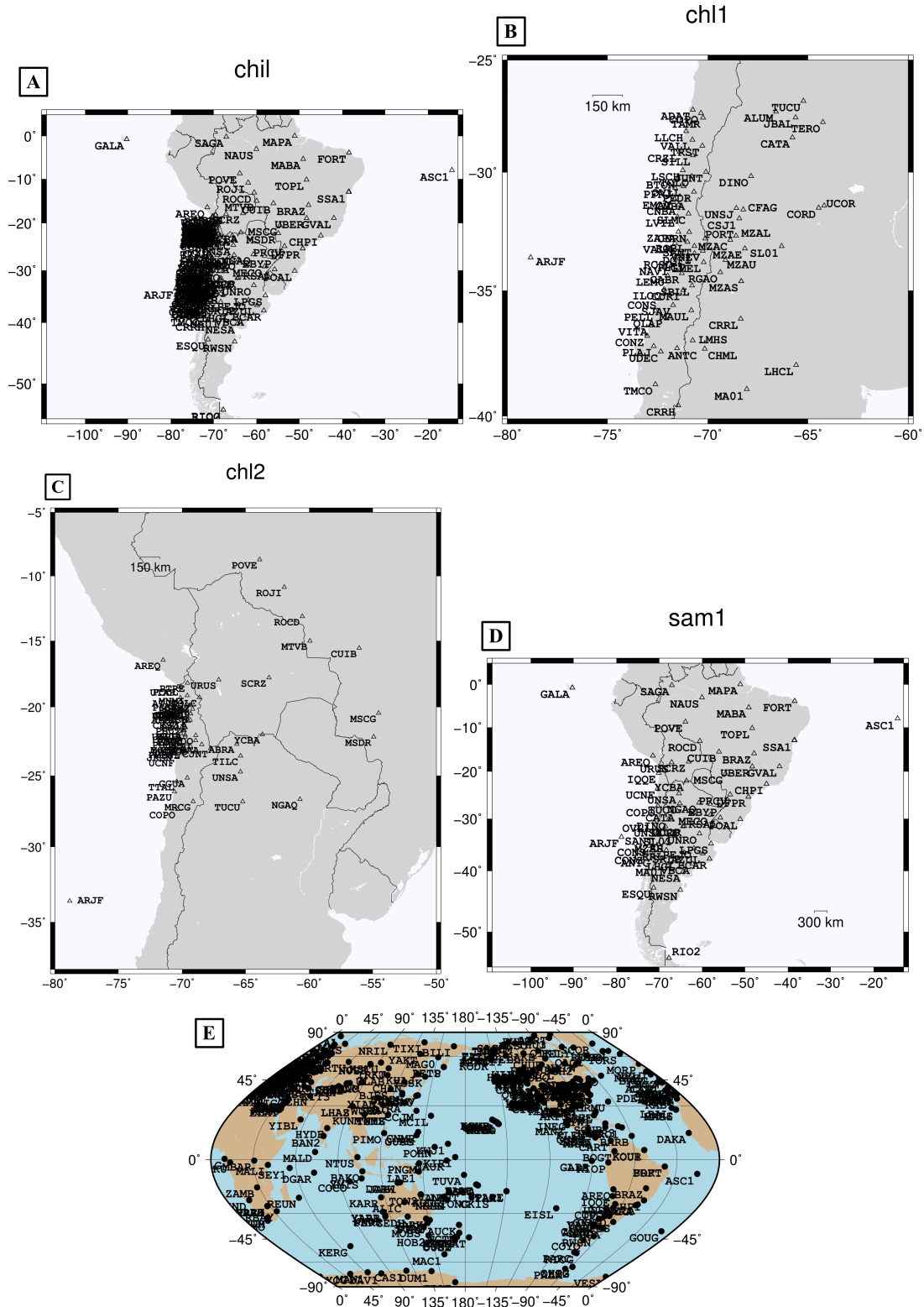


Figure 2.1: A to D: 4 GPS sub-networks used in GAMIT calculation to obtain absolute positions for Chilean stations. The sub-network “chil” is used throughout the period 2000-2008, before the number of stations started to grow rapidly. Beginning of 2009, subnet “CHIL” is split into two subnetworks “CHL1” for central Chile and “CHL2” for North Chile. E) Depict the IGS global network.

2.2 The problem

The major difficulty in detecting transient signals in raw GPS time series is the daily position noise. The GPS noise spectrum is not white, but rather correlated, and its complexity lies in the multiple and diverse phenomena involved in its origin. For example, over a time scale of seconds to days there are multipath effects, ionospheric and tropospheric errors. Over longer time scales, loading phenomena (hydrology, meteorology) as well as instrumental instabilities (monuments) affect daily positions. Typical time series obtained with standard methods have a noise level of ± 3 mm per day for the horizontal components and much higher values for the vertical component. Therefore, some important slow slip episodes of low amplitude (some millimeters) and short duration might be hidden under this high frequency noise. For instance, the largest transient event detected in the Chilean subduction zone (some weeks before Iquique earthquake) shows 10–15 mm of displacement during 3 weeks, meaning less than 1 mm per day. Thus, even after a transient signal is detected, the challenge remains to quantify it with precision. In particular, if we are interested in understanding the physics behind these signals, we need to correlate them with the seismicity. For this matter we need to determine the exact time of the beginning and the end of the event, along with any important feature of the transient deformation, possibly with a better resolution than a day.

Therefore, in order to differentiate between seismic and aseismic events leaving aside effects caused by non-tectonic influence, or in other words, to detect and quantify tectonic displacements accurately, we first need to reduce the noise of the raw time series.

2.3 Common mode noise and local mapping approach

Raw GPS time series are affected by several sources of noise that might be confused with tectonic signals. An important error affecting the time series is the common mode error (CME). Similarly as a transient signal from tectonic origin is recorded in a time series, the CME is observed as a deviation from a linear trend seen at several stations in a given area. It is mostly caused by errors in the reference frame and orbit mismodeling. There are several techniques to remove the CME. Most standard methods estimate the CME by stacking time series from sites considered stable in the area of interest, and then removing this average signal from the sites of

interest (Schurr *et al.* [2014]; Socquet *et al.* [2017]). One of the main drawbacks of these techniques, is that important part of the actual signal might be eliminated together with the noise, considering their sensitivity to the choice of the sites included or excluded from the calculation of the averaged signal. Because fluctuations are still present in time series after the removal of CME, several authors apply sliding window filtering in order to smooth the signal. While this is efficient, it renders the interpretation difficult specially because sliding window filtering is not a causal filter; it is very likely that it smears out signal both before and after the time of the event we are interested.

We have chosen the multi-purpose program PYACS (Yet Another Combination Software) (Per. Comm. J.M. Nocquet) to decrease the noise of raw time series. Pyacs methodology does not apply any mathematical filter to the data to eliminate common mode signals. Its approach is based on the idea that there is some similar spatially correlated noise at the local scale. Consequently, mapping a solution in a local and stable reference frame, somehow forcing a linear motion with time for all the reference sites, yields CME-free time series. Although re-estimated positions are no longer mapped in a global reference system but a local one, deviations from a linear trend are only due to local tectonic transient deformation. Another important factor influencing the improvement of solutions quality is the shortening of the baselines (those implying the reference stations) compared to the raw solution. To be effective, this new local reference frame has to be composed by a minimum of 4 stable stations with a good geometric coverage of the area of interest. The choice of stations to build the local reference frame of course is important, and we show how we reach a good stable reference frame through trial and error and rejection of unsuitable stations.

Pyacs uses unconstrained H-files (relative positions) as input data, obtained in this case by a combination of the different sub-networks and IGS network as described in 2.1. The transformation of this free solution to absolute positions (before performed by fitting ITRF global stations coordinates with module GLORG), is now made by Pyacs which will calculate the best possible time series expressed in the ITRF by using the reference file available and its associated file of discontinuities, both obtained from the most recent IGS updated solution. Pyacs works with a lighter version of the Solution Independent Exchange (SINEX) format: the sub-SINEX format (sSN); the transformation of H-files to sSN format largely reduces the calculation time. Pyacs method to determine raw time series is characterized by performing a Dikin estimation (outliers identification) based on the norm L1 as previous stage to the calculation of the Helmert

transformation. Thus, this approach automatically identifies the stations that contaminate the solution (position residue higher than three times the median of position residues) before performing the mapping.

2.4 Methodology

We analyze 16 years of GPS data starting from 2000. As mentioned in the previous section, Pyacs uses a group of stable reference stations to eliminate the CME. Consequently, due to the variability of the number of stations with time during this large period, we developed a strategy to find stable reference frames for shorter periods of time. We divided the whole period in a succession of 6-month windows, each overlapped with the previous one by 2 months (figure 2.2).

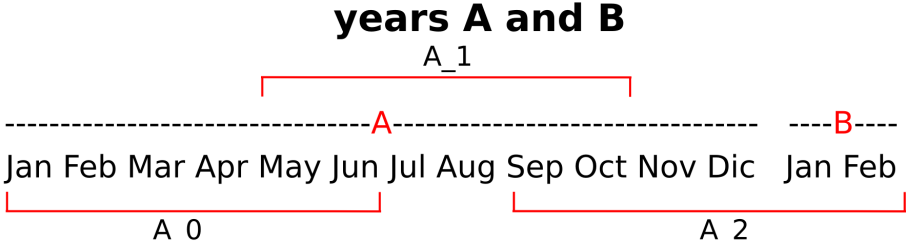


Figure 2.2: Time window configuration used to analyze 15 years of GPS data with Pyacs. For 2 consecutive years (A, B), 3 time spans are shown as: A_0 (January - June, year A), A_1 (May - October, year A) and A_2 (September - December, year A; January - February, year B). Each time span is overlapped by 2 months.

Working with 6 months windows is optimal because it allows to choose a suitable number of stable reference stations; shorter periods are not efficient to detect transient displacements with a duration of months, and stability in the number of reference stations over longer time spans becomes difficult to obtain. This is specially relevant for a variable network as the one we are working with. For instance, the median number of available stations before 2003 in the zone of interest is 8, and increases to 24 for the period between 2004 and 2015; however, still during this period stations suitable to serve as reference suffer data gaps here and there, and have to be rejected.

Once we chose the reference stations after checking RMS values, data gaps and possible outlier values in the time series obtained with Pyacs ITRF first solution, we re-calculate a Helmert transformation, now in this new local reference frame. This process can be iterated several times until reaching the smallest displacement and velocity deviation at each reference station. Generally, convergence is achieved after between 2 and 4 iterations.

Two examples of the comparison between raw (Globk or Pyacs) and Pyacs filtered GPS time series can be seen in the figure 2.3. The top figure shows a typical result obtained for a period with no earthquakes nor transient signals at station ATJN. For this period in particular, with a pick on the number of available stations, the reference system consists of 13 sites (see right figure). The RMS is reduced by 26 % for the north component, 41 % for the east component and 57 % for the vertical component, with respect to the Pyacs raw solution (ITRF reference frame). The filtering removes oscillations and apparent transitory signals which probably corresponded only to common mode noise. The figure in the bottom shows the particular case of FBAQ time series during 2005 affected by a step-like displacement that is difficult to detect and quantify in the raw time series, but is obvious in the Pyacs-filtered time series. A jump of $6.9 \text{ mm} \pm 1 \text{ mm}$ is detected in the north component on 3 February, 2005. This offset coincides with an earthquake cataloged as intermediate depth event for both: CSN (Chilean seismological center) and USGS (United States Geological Survey) agencies, with hypocenter located at $\sim 110 \text{ km}$ depth and a rather small magnitude of $M_w 4.7$. Despite this, its detection at a GPS station remains unlikely, even if the station is only 40 km away from its epicenter, according to the more accurate localization from CSN (both epicenters are indicated in the figure). Only 2 seismological stations (LPAZ and LVC), more than 200 km to the south and north of the event respectively, recorded this event. These seismograms (figure 2.4) do not reveal any anomaly or a shallower secondary event taking place at the same time, leaving unclear the interpretation of this displacement. However, detecting (and removing) these type of jumps in the time series (whether we understand their origin or not) is of great importance for the estimation of coseismic and postseismic displacements associated to the large intermediate earthquake of Tarapaca 2005 ($M_w 7.9$) which occurred only 4 months afterwards.

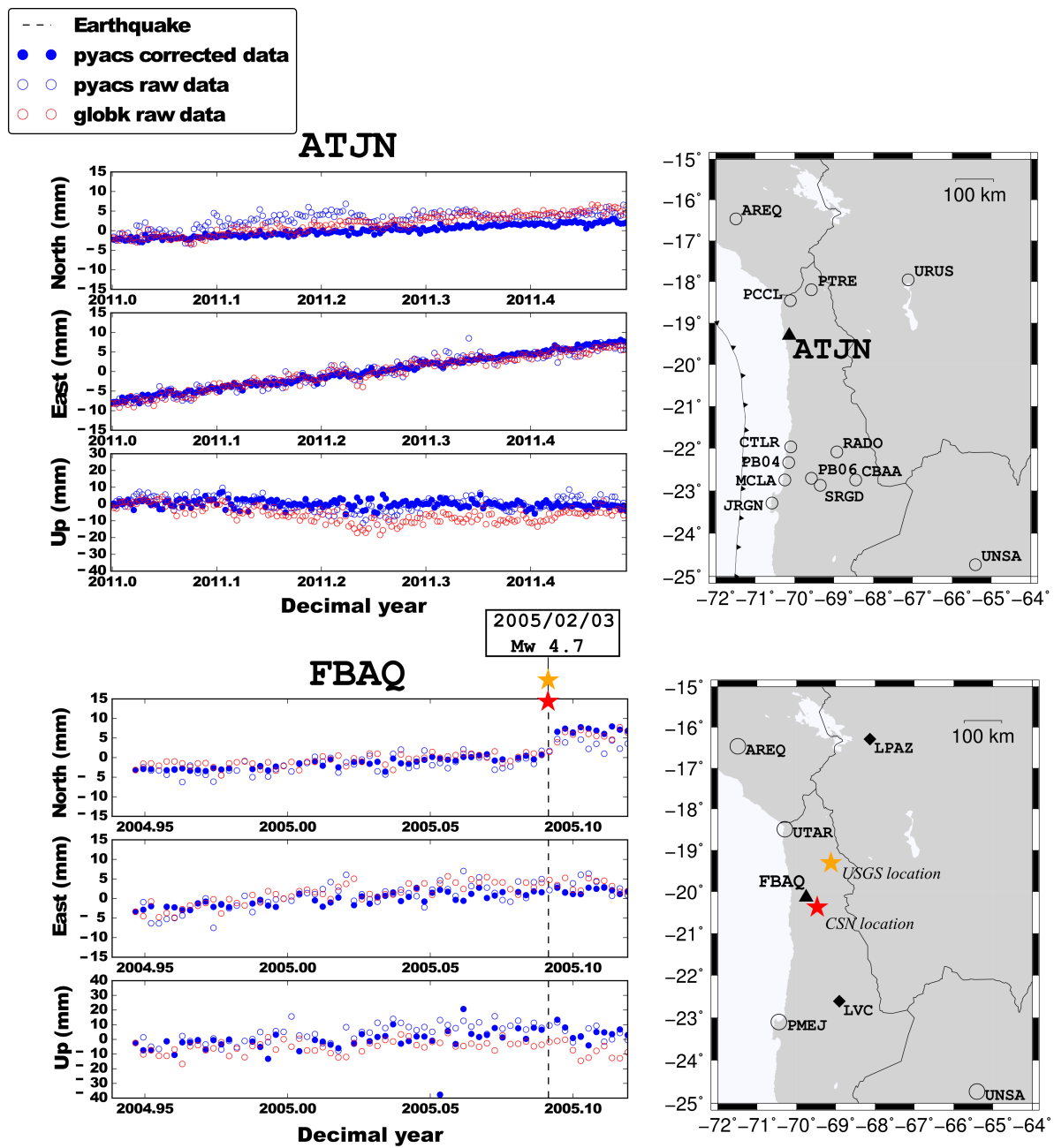


Figure 2.3: Two examples showing raw GPS time series from the process performed by Globk (red open circles), Pyacs (blue open circles), and Pyacs filtered time series (blue filled circles). Top: raw and Pyacs-filtered time series for the station ATJN with a duration of 6 months. Site location and reference stations used for Pyacs filtering are indicated in the map. Bottom: All data available for the station FBAQ between May and October 2004. An intermediate earthquake of M_w 4.7 (dashed line) occurred not far from the site, coinciding with a 3.5 mm offset easily detected on the north component after Pyacs filtering. Earthquake location from 2 different agencies is indicated in the adjacent map with red (CSN) and orange (USGS) stars, together with reference and filtered stations. The only 2 available seismic stations are represented with black diamonds.

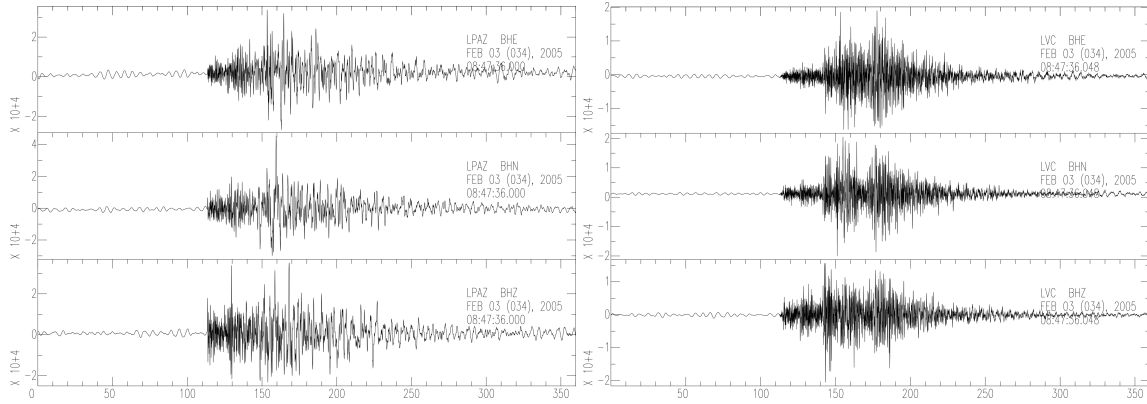


Figure 2.4: 2 available seismograms recording an intermediate depth earthquake occurred in 2005/2/3, M_w 4.7. Location of LVC and LPAZ seismic stations is shown in the figure 2.3.

2.5 Complementary data: Long base tiltmeter measurements

A tiltmeter is a highly sensitive strain detector instrument even capable of recording the free oscillations of the Earth caused by largest earthquakes. It is often used in combination with geodetic and gravimetric networks. The long base tiltmeter is based on a very simple concept: 2 pots filled with liquid (distilled water works fine) are connected by a long tube of tens to hundreds of meters. Any ground motion or deformation results in ground surface inclination (a tilt), which produces a difference in the water level in either pots. This difference in level is measured in each pot mechanically (displacement of a floating device) or optically (laser reflection and/or refraction on the surface). These instruments are very sensitive and the measurements are contaminated by ambient noise (vibrations) and thermal variations. Because of this, they are usually located underground, sometimes even at hundreds of meters depth, in abandoned mine tunnels where temperature and hygrometry are extremely stable and surface noises and vibrations are considerably attenuated. The characteristic arid climate and the existence of abandoned mines in the Atacama desert (northern part of Chile) makes this zone an ideal environment for placing these instruments. In 2012, a long-base tiltmeter (30-50 m long) of two components was installed 150 m below surface in the Santa Rosa abandoned mine, 15 km east from Iquique (see figure 2.5). With this type of instrument, the differences in water level are measured by linear variable displacement transducer (LVDT) sensors which detect displacements of silica floaters placed in the pots (Boudin *et al.* [2008]). Noise level and tilt drift of these LVDT sensors, and thus of the instrument, are approximately $0.01 \mu\text{m}$ and 10^{-7} rad/year (Per. Comm. F. Boudin).

The tiltmeter is extremely sensitive (5×10^{-9} rad) which corresponds to a vertical displacement of 0.5 mm over a 100 km long baseline (or 0.05 mm over a 10 km long baseline), when the sensitivity of the GPS is rather flat around 1-2 mm at all distances. The difference of performance between GPS and long-base tiltmeter instruments varies depending on the distance to the source producing the deformation. For distances smaller than 100 km, long-base tiltmeters have better resolution and precision than GPS; the contrary is true for larger distances, making these instruments really complementary. Also, contrary to the tiltmeter, the GPS does not drift, so that a GPS determined motion is always “true” or “exact” if not accurate. Therefore, the tiltmeter is better suited to detect transients over a rather short period of time, when the GPS is more efficient at quantifying the total motion over a possibly long duration. Another aspect of this complementarity lies in the correlation with seismicity. Because it samples the deformation at one point per second, a signal in the tiltmeter can be immediately correlated with the occurrence of an earthquake. On the contrary, the precise position of the GPS relies on the accumulation of measurements over a considerable time (at least one hour, very commonly a full day). With daily positions, if several displacements occur the same day (earthquakes or a-seismic episodes of slip), it is impossible to decipher between them. Even worse: it is expected that we observe the GPS station motion the day after it actually occurred, but it could be the same day if the displacement occurs early enough in the day that the average daily position is post-event. So, in all cases, it is impossible to determine the timing of an event within 1-2 days using daily cGPS.).

2.6 Results

We have analyzed 35 sub-periods (see figure 2.2) for 15 years of GPS data. Due to the small number of reference stations available before 2006, the precision of the vertical component is significantly improved by Pyacs filtering only after this date. The median RMS value for this component decrease from 8.2 mm before 2006 to 2.4 mm after this date. In contrast, Pyacs filtering is efficient on the horizontal components over the entire period; median RMS value, on north and east components of Pyacs corrected time series for the complete analysis period, is 0.5 mm and 0.7 mm respectively. These sub-millimetric values lead us to think that millimetric jumps and transients can be detected after the Pyacs filter has been applied, and without any of the biases that come with standard CME removal methods commonly used.

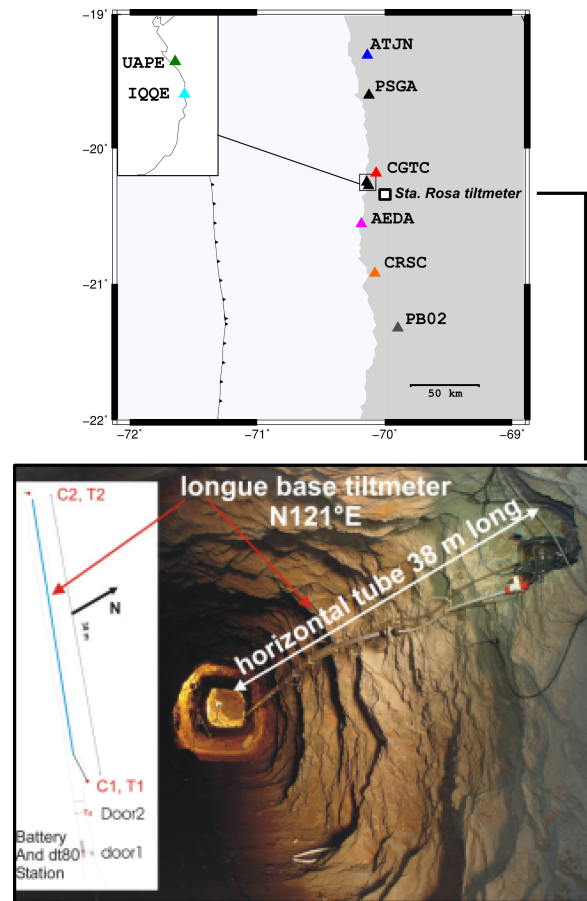


Figure 2.5: Up: GPS coastal stations (triangles) and tiltmeter (square) locations. Down: Long-base tiltmeter instrument located 150 m under surface in Santa Rosa mine.

Figure 2.6 illustrates the differences between corrections performed before and after 2006, indicating respective RMS values. We can see a large decrease of 70% on the RMS for the vertical component. Similar value for horizontal components, lower than 1 mm, are reached in both cases: low or high number of reference stations involved in noise filtering.

After applying Pyacs filtering in our 6-month long time series, we found different perturbations of the expected linear trend: defined offsets produced by earthquakes, slope changes and transient events with demarcated boundaries. All these events, detected by one or more stations, are summarized in table 2.1 for each of the 35 analyzed windows. Here it is important to recall that period subscripts 0, 1 and 2 refer to time windows between the months January-June, May-October and September-February, the latest spanning 2 consecutive years (see figure 2.2). Because our analysis is associated to a particular time window, trend changes have no precise meaning in this case and we do not interpret them.

The most significant cases of transient displacements, i.e. detected by more than one station, are summarized in the following section.

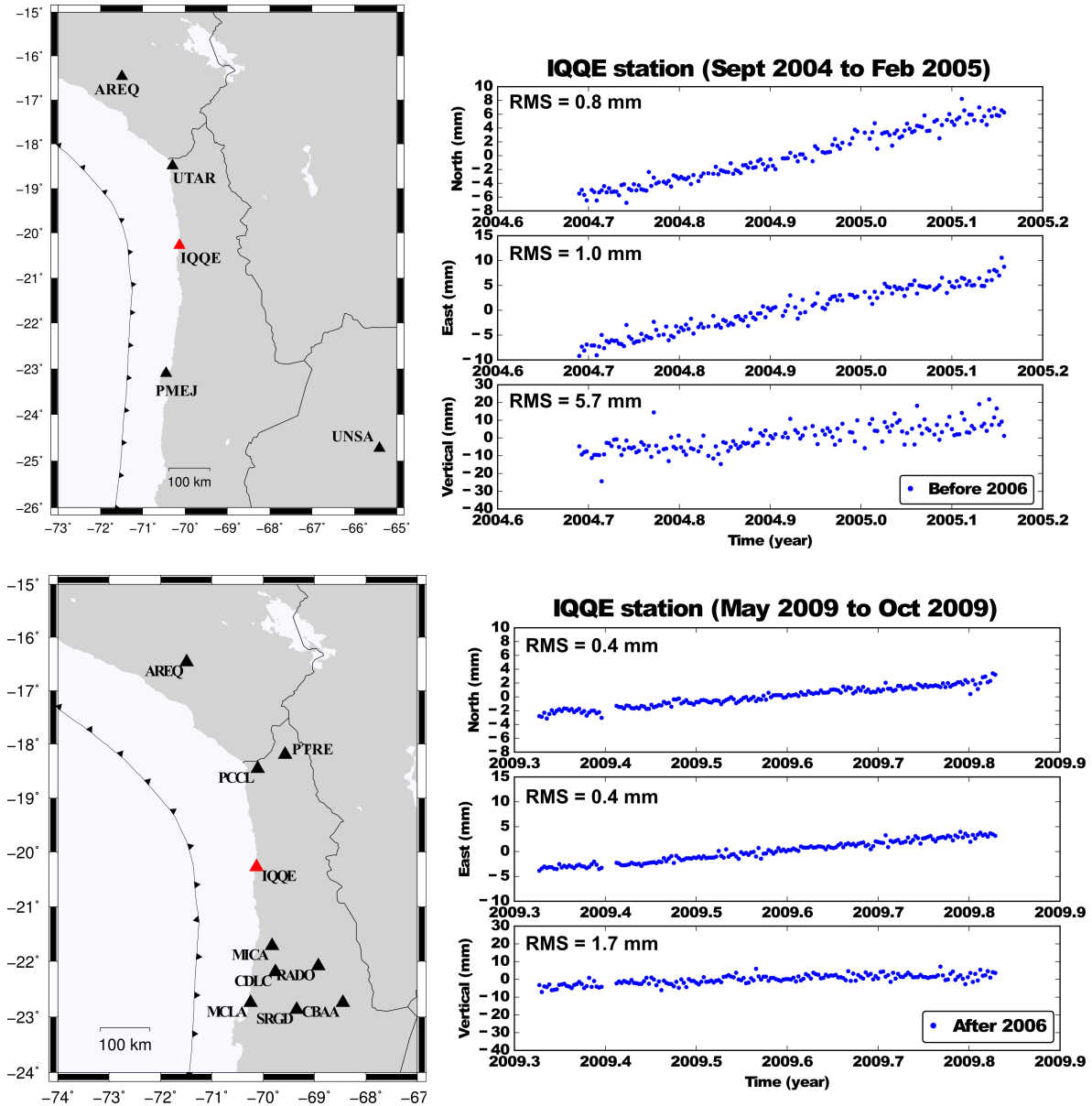


Figure 2.6: Two time series for the station IQQE filtered with Pyacs for periods pre- (top) and post-2006 (bottom). From this date the number of available stations starts increasing. Maps displayed on the left side show the arrays of available reference stations involved in the correction (black triangles). Exact time spans for the 6-months windows are specified for each case.

Reference stations information				Corrected stations information										Perturbation of a linear trend				
Average RMS [mm]				Before correction					After correction					Earthquake			Slope change	
Period	N°	North	East	Vertical	N°	North	East	Vertical	North	East	Vertical	North	East	Vertical	Earthquake	Transient event	Slope change	
2002.0	4	3.70	6.65	8.60	2	3.80	7.10	9.50	3.10	3.00	21.90							
2002.1	5	3.62	4.96	7.54	3	3.37	6.20	8.77	1.33	2.37	10.40						X	
2002.2	5	3.30	4.74	7.20	3	3.13	5.97	8.43	1.13	3.97	6.93							
2003.0	5	2.42	3.92	6.82	3	2.15	4.60	6.45	1.15	2.95	6.20							
2003.1	5	2.34	3.00	5.74	4	2.15	3.00	5.10	1.05	1.55	5.00							
2004.0	5	2.18	2.86	5.28	5	2.13	3.33	5.40	0.80	1.40	6.80						X	
2004.1	4	2.27	2.47	5.70	5	2.08	2.22	6.16	0.70	1.08	5.82							
2004.2	4	2.30	2.90	5.88	5	2.33	3.10	10.73	1.17	1.90	11.07			X				
2005.0	4	2.12	2.78	4.92	5										X			
2005.1	4	2.28	2.25	4.12	7										X			
2005.2	6	1.60	2.60	4.57	8	1.55	2.54	4.69	0.78	1.10	16.70						X	
2006.0	7	2.09	3.14	4.56	8	2.10	3.21	4.87	0.59	0.87	7.69							
2006.1	7	2.40	2.23	5.09	7	2.44	2.29	5.24	0.39	0.57	3.03				X			
2006.2	8	1.89	2.36	4.69	7	1.90	2.28	4.75	0.62	0.73	3.35				X			
2007.2	8	2.76	2.34	4.36	14	2.16	2.14	4.30	0.87	1.29	4.24			X	X			
2008.0	11	3.05	3.35	4.99	14	1.74	2.58	4.45	0.60	0.85	2.73			X	X			
2008.1	9	1.88	2.90	4.21	13	1.72	2.67	3.36	0.35	0.51	1.78				X			
2008.2	11	3.98	4.52	4.50	14	1.68	3.00	3.96	0.48	0.67	2.75			X	X			
2009.0	12	3.21	4.47	3.58	11	1.74	2.26	3.59	0.55	0.78	2.65			X	X			
2009.1	9	1.87	2.30	3.34	12	1.25	1.53	3.27	0.40	0.55	2.24				X			
2009.2	14	4.36	3.88	4.96	15	1.70	2.50	5.90	0.60	1.10	4.20			X	X			
2010.0	10	2.46	3.65	3.96	15	1.84	1.84	3.78	0.54	0.78	2.73							
2010.1	12	2.48	2.54	3.77	14	1.71	2.31	3.71	0.42	0.63	2.10				X			
2010.2	14	4.64	4.62	3.48	15	1.48	1.76	3.30	0.44	0.61	2.48				X			
2011.0	13	2.08	4.14	4.09	13	1.55	1.33	3.94	0.46	0.65	2.55				X			
2011.1	13	2.13	1.89	3.52	11	1.29	1.32	3.37	0.41	0.56	2.05			X	X			
2011.2	13	4.81	3.62	3.86	14	1.41	2.13	3.70	0.53	0.73	2.78				X			
2012.0	12	1.66	3.68	4.53	14	1.51	1.56	4.53	0.54	0.78	2.85							
2012.1	12	1.82	1.86	3.67	15	1.08	1.04	3.37	0.35	0.53	1.82				X			
2012.2	12	4.80	3.88	4.27	17	1.51	2.11	4.06	0.49	1.01	2.54				X			
2013.0	14	2.04	3.89	3.78	18	1.53	1.84	3.90	0.51	0.97	2.57						X	
2013.2	10	4.12	3.57	5.02	16	0.99	1.47	4.20	0.50	0.77	2.43						X	
2014.0	6	2.18	3.17	5.67	18										X			
2014.1	12	1.61	3.43	3.22	16	1.05	2.57	2.76	0.49	1.97	2.05				X			
2014.2	9	3.27	3.16	4.32	18	1.29	1.35	3.09	0.52	0.77	2.47						X	

Table 2.1: Perturbations of the linear trend of time series founded after Pyaes filtering. These events are marked with an X for each analyzed period. Subscripts 0, 1 and 2 on period nomenclature refer to windows delimited between the months January-June, May-October and September-February respectively as it is described in figure 2.2. Average RMS values for reference and corrected stations are indicated, excepting for the periods where a large earthquake affected all the corrected time series.

2.6.1 Summary : A catalog of small transient events found in North Chile

With displacements being detected by at least 3 cGPS stations, we identified 5 cases of transient deformation occurring in the region. 4 of these events, occurring in 2008, 2009, 2010 and 2011, have defined limits with a maximum duration of 36 days and total displacements of several millimeters. The total displacement produced by these events together with information about their duration is given in table (2.2).

Nevertheless, the first case analyzed here corresponds to transient displacements associated with the precursory seismic activity of Iquique 2014 earthquake. Because this event occurs simultaneously to a seismic crisis striking the zone previous to the main event, its analysis is more complex than the rest of events founded. During this period, the non-seismic total displacement found at 5 cGPS time series filtered with Pyacs was modeled by F. Boudin (manuscript in preparation), resulting in the characterization of 4 slow seismic events. This special event, and the rest of detected transient displacements mentioned above, will be described in detail in the following section.

2.6.2 Transient displacements detected in north Chile subduction zone

Case 1: Transient displacement several months before the large Iquique earthquake of 2014

The six-month window time series between September 2013 to February 2014 (block 2013_2) reveal an abrupt trend change on stations located in front of the foreshock seismic activity preceding the large M_w 8.1 Iquique earthquake occurring on 01 April 2014. To better capture this signal we shift this 6-month windows analysis one month forward in order to include positions until one day before the mainshock. The array of GPS stations available for this period of persistent precursory seismic activity to the main shock (between January and March), is displayed in figure 2.7 (top). We selected a group of stations which qualifies as reference stations (black dots) for being stable in time and surrounding the seismic crisis area without being affected by it.

	Stations	Displacements			Duration			Comments
		north (mm)	east (mm)	vertical (mm)	starting (date)	end (date)	total time (days)	
Case 2	MNMI	-0.5	-1.6	16.8	2008/11/25	2009/01/04	40	Displacements product of artifacts of unknown origin
	HMBS	-1.7	-2.5	17.5	2008/11/25	2009/01/04	40	
	PSGA	-0.4	-2.8	5.0	2008/11/25	2009/01/04	40	
Case 3	UAPE	-0.2	-1.9	-	2010/07/31	2010/08/15	14	Real a-seismic shallow slip in front of Iquique
	IQQE	-0.01	-0.8	-	2010/07/31	2010/08/15	14	
	PICA	-0.02	-0.9	-	2010/07/31	2010/08/15	14	
Case 4	HMBS	1.6	-3.1	-	2009/04/17	2009/05/23	36	Possible a-seismic deep slip between Pisagua and Iquique simultaneous to a seismic cluster in front of Pisagua
	PB01	0.9	-1.7	-	2009/04/17	2009/05/23	36	
	IQQE	-0.4	-1.0	-	2009/04/17	2009/05/23	36	
Case 5	PSGA	-	-2.1	-	2011/07/28	2011/09/02	36	Real a-seismic shallow slip in front of Pisagua
	PCHA	-	-0.8	-	2011/07/28	2011/09/02	36	
	CHMZ	-	-1.8	-	2011/07/28	2011/09/02	36	

Table 2.2: Summary of transient events founded between 2008 and 2011 in North Chile.

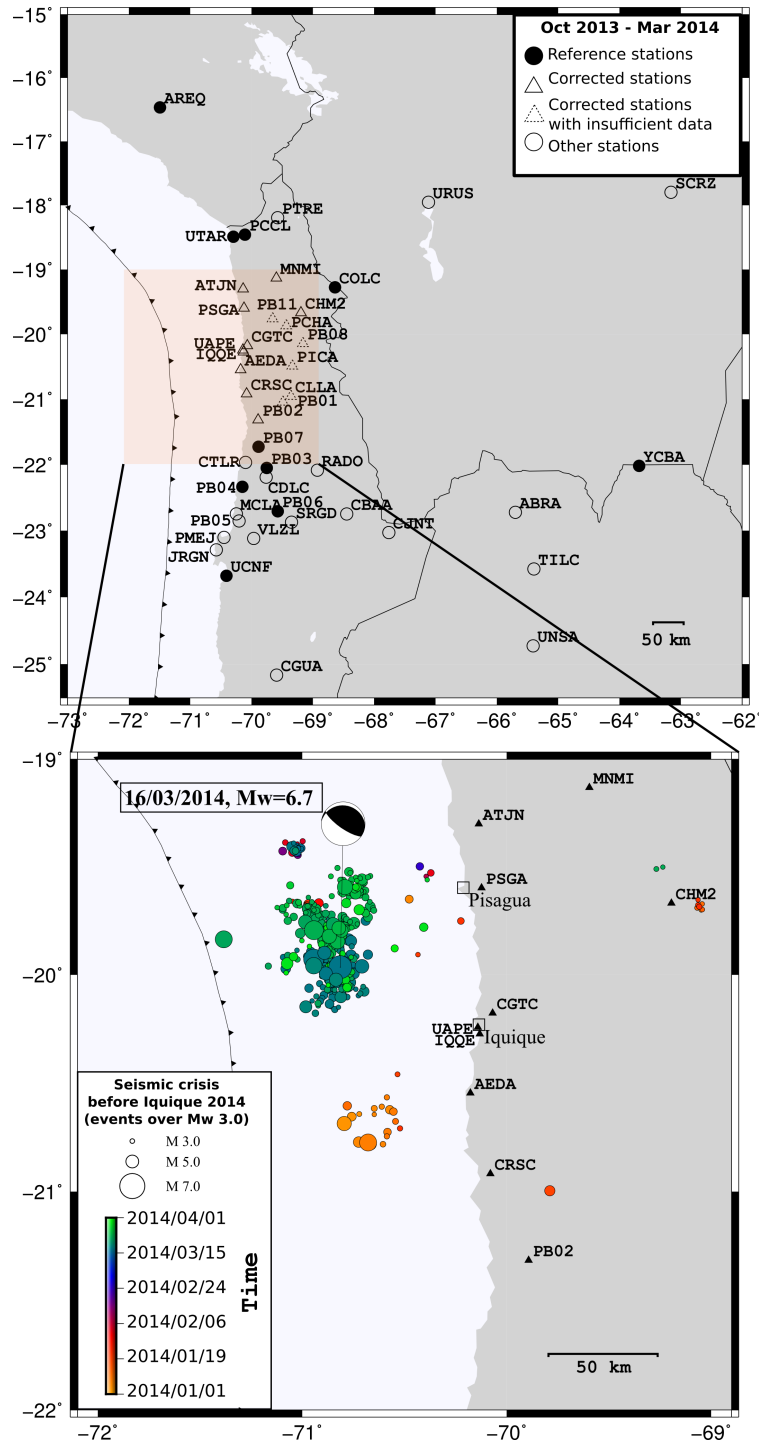


Figure 2.7: Top: reference and corrected sites for the period between October 2013 and March 2014. Sites referred as other stations did not qualify to be used as reference stations. Bottom: a zoom of the area highlighted in orange shows foreshock activity during 2014 preceding the M_w 8.1 earthquake in April 2014. The seismic crisis is represented by circles differentiated in time (color) and magnitude (size). The largest foreshock is highlighted, indicating focal mechanism (USGS), magnitude and date of occurrence. The figure includes only seismic events over M_w 3.0 with depths up to 50 km, obtained from the Chilean Seismological Center catalog.

Figure 2.7 (bottom) shows the mentioned seismic activity corresponding to this period. It is evident from it the sharp increase of seismicity after the occurrence of the M_w 6.7 event of March 16 (events marked in shades of green), almost in front of the site PSGA. The particular reverse focal mechanism of this event (included in the figure) indicates a rupture perpendicular to the trench, different from typical focal mechanisms of thrust earthquakes in subduction zones, aligned to the trench direction. It is important to take into consideration the uncertainty of this solution in the prediction of coseismic displacements at stations like UAPE and IQQE, which are located very close to one of the nodal planes. Before this large foreshock, around 100 km to the south, a less intense swarm of subduction events takes place. Nevertheless, the marked transient signal detected on several coastal stations starts 10 weeks before the large seismic cluster of March 2014, at the beginning of January 2014. Figure 2.8 shows horizontal components of time series from coastal stations recording before and after the seismic crisis, sorted by latitude and detrended for the period prior 2014. Because no data is recorded for the station UAPE before 2014, it is not possible to detect the precise initiation of a transient displacement; although, time series of this site have been detrended by the pre-2014 velocity found for its neighboring station IQQE, and are included in the figure. Mostly all time series from stations located in the coast, specially the southern sites, are affected by a large transient signal during January 2014, with a total transient displacement around AEDA, comparable with the coseismic deformation associated to the northern seismic cluster led by the large M_w 6.7 event. In the case of the 2 inland stations (MNMI and CHMZ) recording for the periods mentioned here (figure 2.9), horizontal components of the southern site seem to detect transient deformation around the same date. Finally, transient deformation found on vertical components of all stations (see figure 2.10) is not clearly visible due to the higher noise level, with the exception of the inland site of MNMI, which apparently is subsiding around 1 cm before the foreshock on March 16.

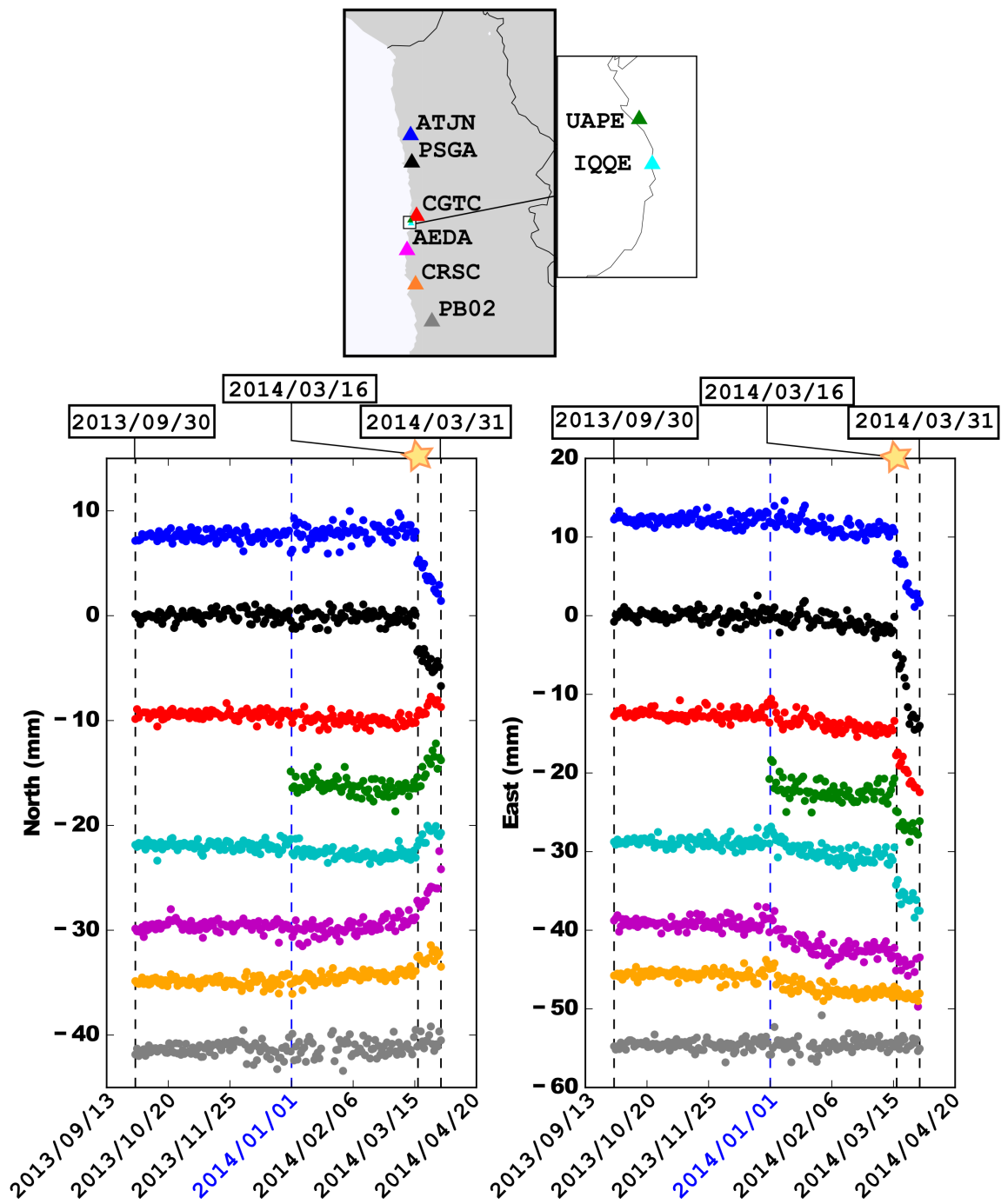


Figure 2.8: Detrended (for the period previous to 2014) horizontal components of Pyacs filtered time series at coastal sites (color code in map on the top). Due to the data gap in UAPE time series and taking advantage of their proximity, the pre-2014 trend of IQQE is subtracted from both sites. The start of a transient signal is clear from early 2014 (blue dashed line) in the southern sites (from CGTC to CRSC), stations located in front of the small seismic swarm of January 2014. Start and end dates of the records and larger event of the foreshock crisis (yellow star) are indicated with dashed lines in the figure.

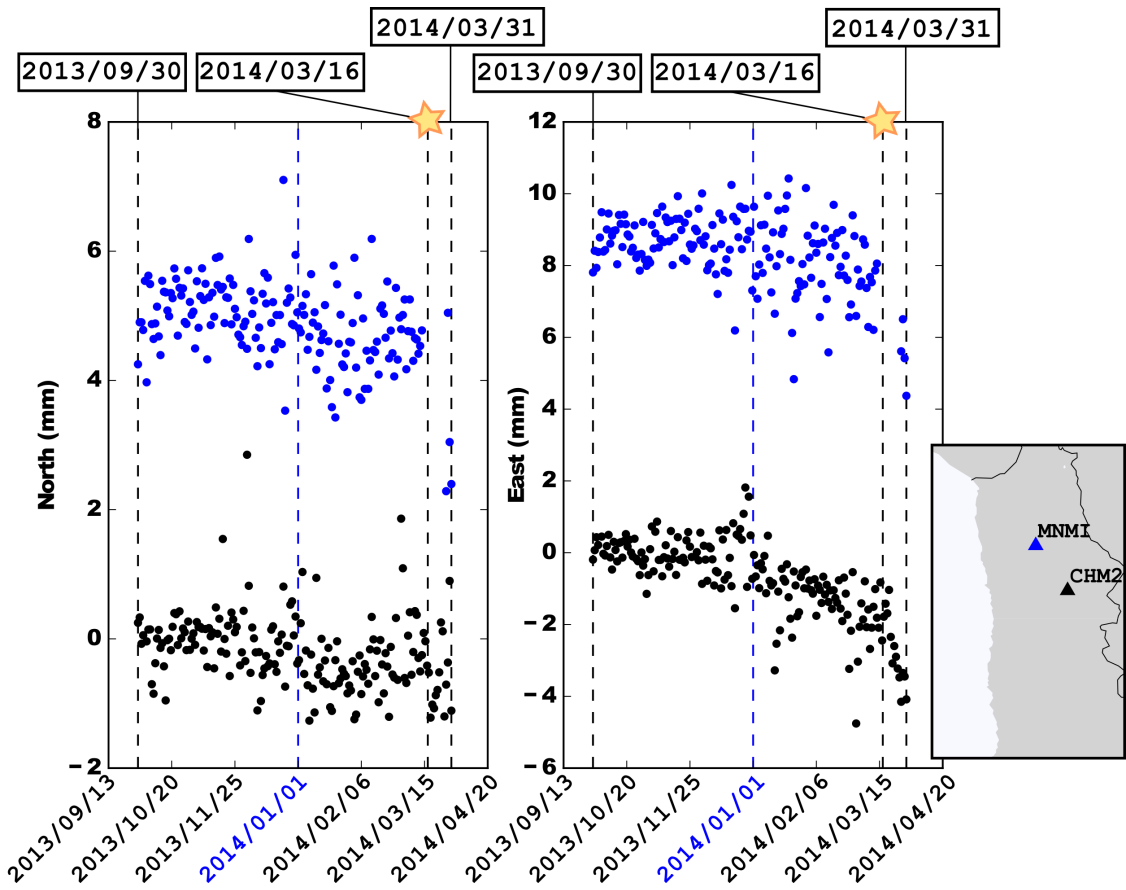


Figure 2.9: Detrended (for the period previous to 2014) horizontal components of Pyacs filtered available time series at inland sites (only 2 stations recorded the complete period). Time span of the records correspond to displacements between October 2013 and end of March 2014. Large foreshock on March 16 is indicated as a yellow star. Transient starting date is indicated as a blue dashed line.

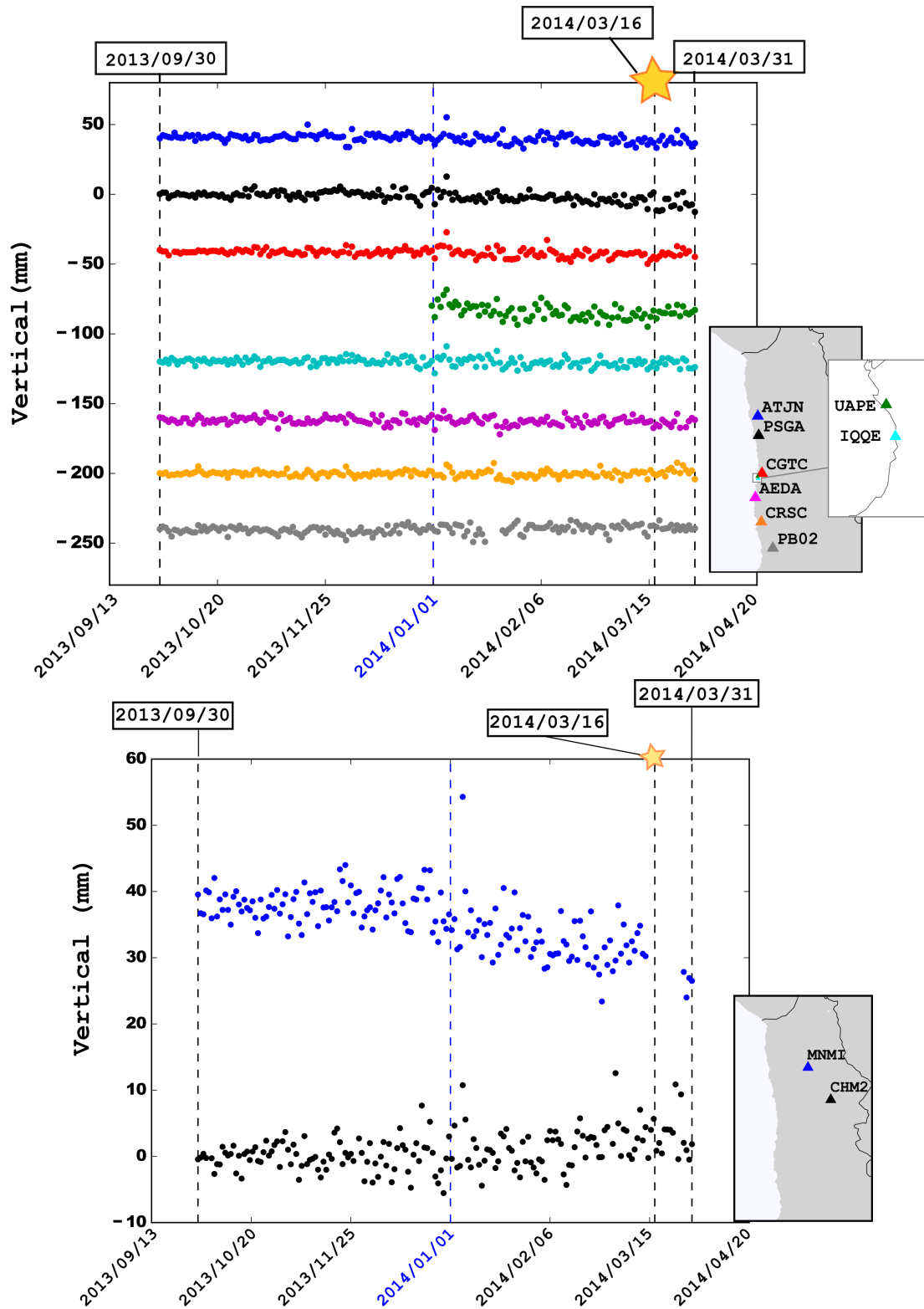


Figure 2.10: Detrended (for the period previous to 2014) vertical components of Pyacs filtered time series at coastal (top) and inland (bottom) GPS sites. Time series are color-coded following the inset with the stations location.

F. Boudin (manuscript in preparation) use these time series together with records from the long-base tiltmeter of Santa Rosa (see section (2.5)) to evaluate the possibility of slow slip occurring simultaneously to, or before, the foreshock activity of Iquique 2014. This study finds that the displacements observed at coastal stations are only partially explained by the co-seismic deformation associated with the moment magnitude of the precursory events to Iquique earthquake, specially for 2 stations (IQQE and AEDA – both near the city of Iquique) located south of the region where the mainshock was nucleated. A significant part of the displacements observed during January to March, a seismically calm period previous to the seismic activity triggered by the large foreshock of March 16th (see figure 2.7), is attributed to slow slip. For the second period, starting at the beginning of March until the mainshock of 01 April, geodetic data show displacements that remain on the edge of the coseismic probability distribution (figure 2.11), indicating a higher probability (with respect to the first period) that the observed displacements are explained by co-seismic contribution only. However, tiltmeter data reinforce the hypothesis of aseismic slip occurring during this period as well.

During both periods, the correlation between the tiltmeter data and the cGPS data in its vicinity is remarkable. But the tiltmeter data brings something essential: its sensitivity and resolution allow to identify 4 distinct episodes of transient deformation, originated in 4 distinct regions between January and March (see figures 2.12 and 2.13). Following the work of F. Boudin, is possible to identify 2 aseismic slow-slip events occurred during each period. During the first months, 2 aseismic events were located at the east edge of the asperity associated to the principal aftershock (see rupture contours on figure 2.13), with aseismic moments of 1.7×10^{18} (M_w 6.1) and 1.3×10^{18} (M_w 6.0). Other 2 aseismic slip episodes, with aseismic moments of 6.3×10^{17} (M_w 5.8) and 2.2×10^{18} (M_w 6.2), were located southern and northern part of the same asperity.

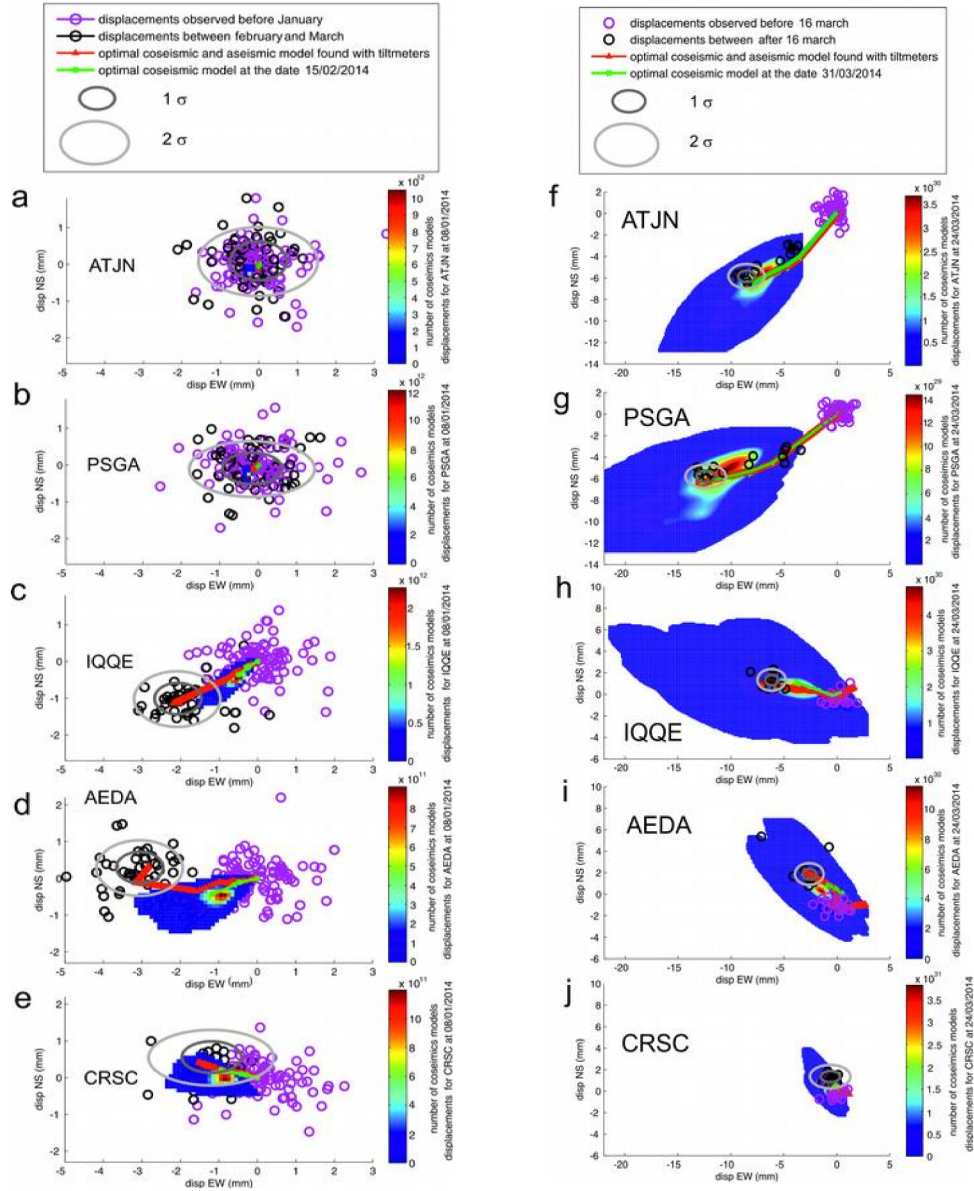


Figure 2.11: Figure from F. Boudin (Per. Comm.) showing at 5 permanent GPS stations the probability density functions of coseismic displacement (blue to red distribution) and observed displacements (black circles) corresponding to the precursory activity to Iquique 2014 earthquake (January - March 2014). This period is divided in 2: from January to 16 March (a-e) and from 16 March to the mainshock (f-j). Purple circles correspond to reference positions.

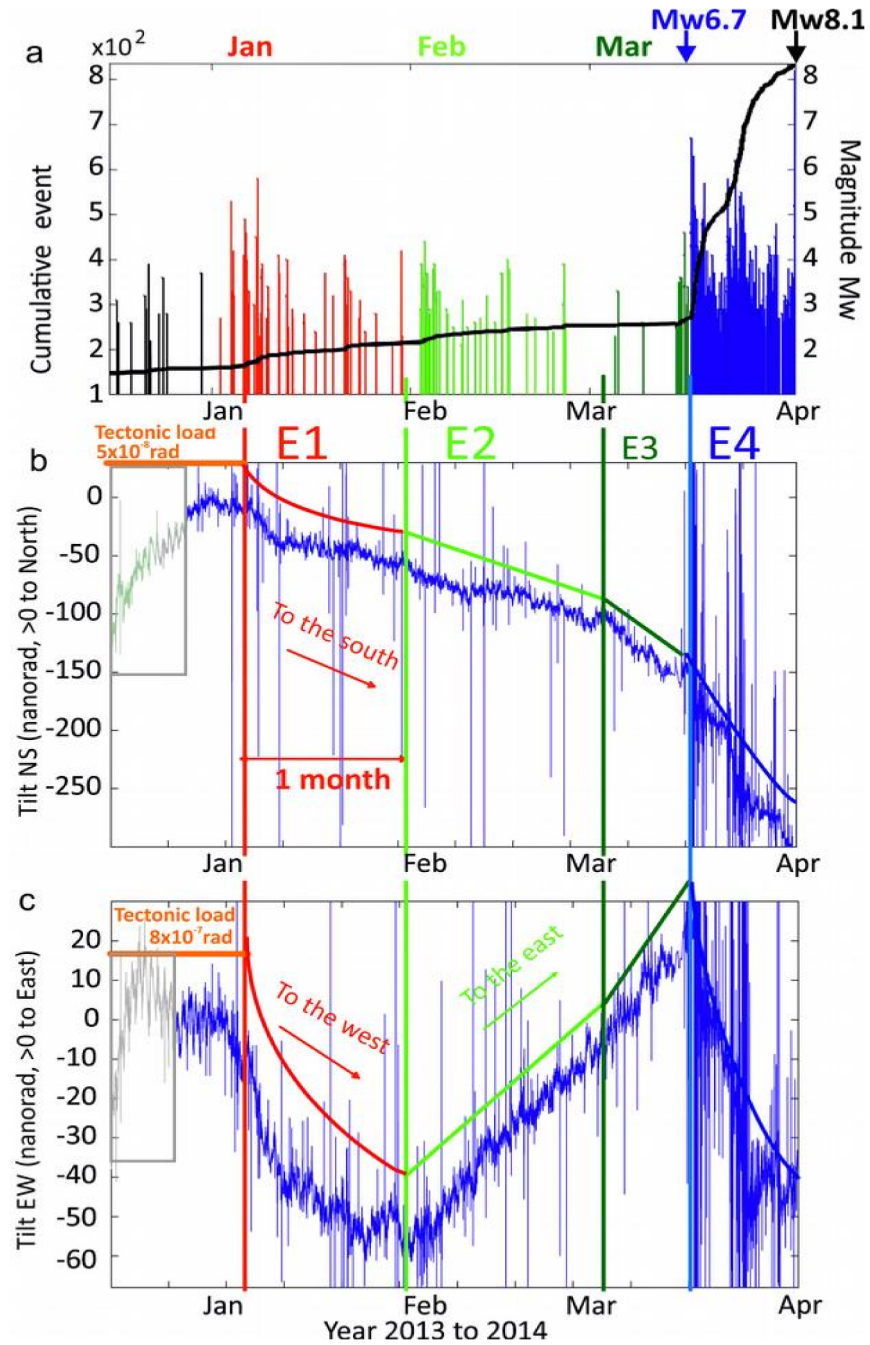


Figure 2.12: Figure from F. Boudin (Per. Comm.) showing (a) statistical information about foreshock activity from Iquique earthquake during 2014, (b) & (c) north and east components from the tiltmeter instrument located near Iquique. Occurrence periods for the 4 modeled aseismic slip episodes are differentiated by color.

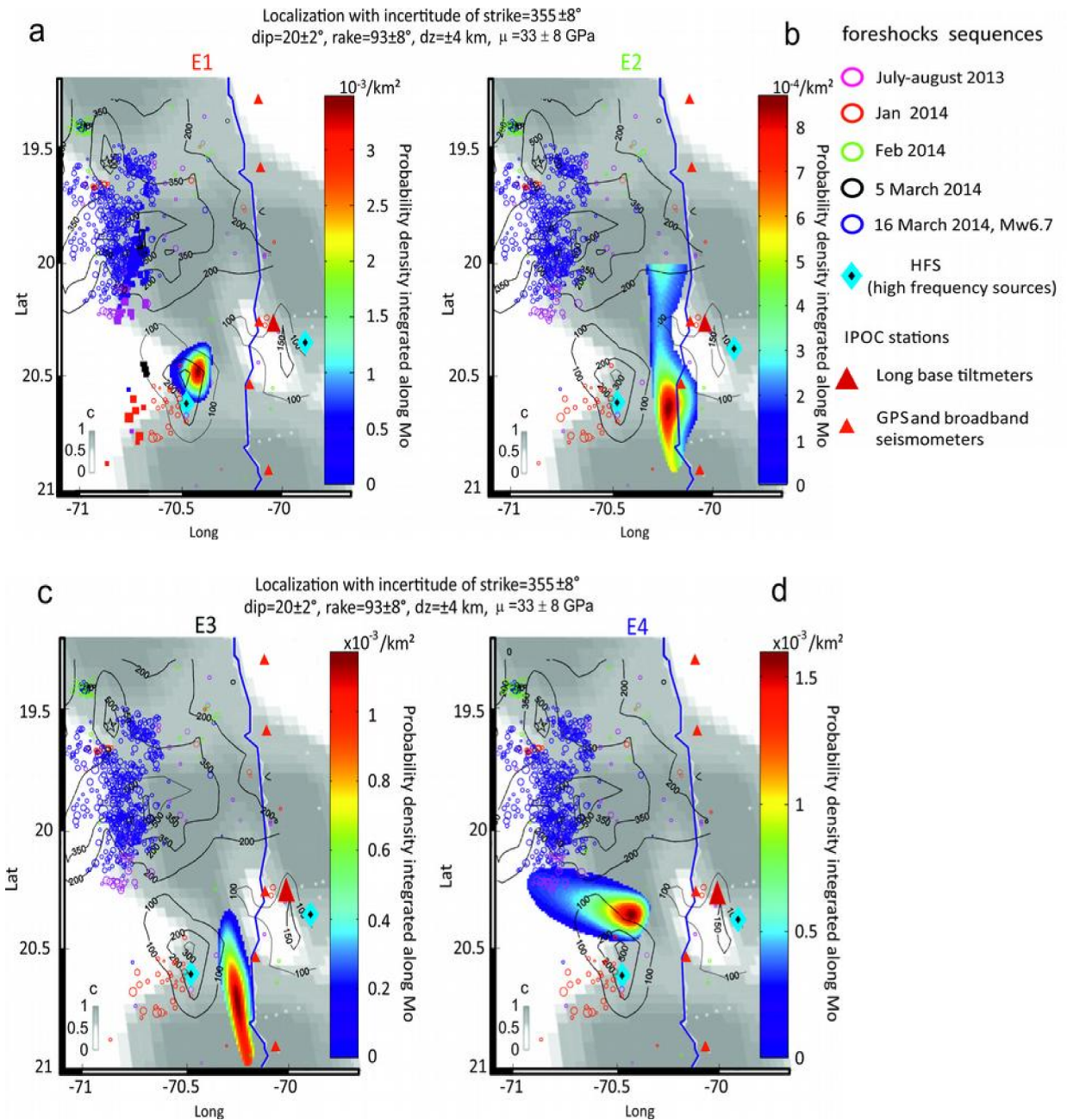


Figure 2.13: Figure from F. Boudin (Per. Comm.). The PDF functions of the four SSE locations are color-coded according to the fit to all corrected tilt and GPS aseismic components. For each location, an elementary thrust dislocation is considered on the interplate, with an area of 10 km x 10 km. Foreshock seismicity is plotted following color codes indicated in the legend. Ruptures corresponding to the main event (north) and principal aftershock (south) are shown as black contours. The gray background is the interseismic coupling (darker is stronger) calculated by Métois *et al.* [2016].

It is important to emphasize that unlike the combination tiltmeter/geodetic instruments, using only GPS data to analyze transient deformation produce a “blurry view” that do not allow to see anything more detailed than one general motion originated from a larger area. The use of these instruments simultaneously reveals a more realistic situation, where several episodes of slow slip are distributed in smaller areas, with durations that fit the scaling law for slow earthquakes (Ide *et al.* [2007]). Thus, the scenario where several slip episodes precede a large rupture, brings an important distinction from a seismological point of view: it is not one very large “velocity strengthening” area that is aseismically slipping around a locked asperity, it is rather several much smaller “velocity strengthening” areas that are dispatched in between locked asperities and that are slipping when given the opportunity.

Several authors have analyzed the foreshock activity preceding 2014 Iquique earthquake M_w 8.1 (Ruiz *et al.* [2014]; Schurr *et al.* [2014]; Kato & Nakagawa [2014]; Bedford *et al.* [2015]; Socquet *et al.* [2017]). For instance, using seismological and geodetic data, Socquet *et al.* [2017] predict one long-term large slow slip event of magnitude M_w 6.5 surrounding the main shock patch (blue contours, figure 2.14) and corresponding to displacements occurring between July 2013 and the largest foreshock M_w 6.7 (8-months time-span). They identify as well a second aseismic slip event of magnitude M_w 7.0, occurring simultaneously to the 2-weeks largest precursory seismic cluster which started with this foreshock on March 16th (purple contour on figure 2.14).

We think that the differences between our results and what has been found by other studies analyzing this precursory activity, lie in the different pre-processing methods used in each work. For instance, to reduce time series noise, it is common to apply all sorts of filters to the data. Seasonal signals can be removed by fitting a pair of sinusoidal terms (together with a linear trend) to each time series (eg. Socquet *et al.* [2017]). Then, both high and low frequency noise are reduced by applying common mode filtering (CME): an average signal is computed by stacking time series from a subset of selected “stable” stations, and subtracted from all other “moving” stations time series (eg. Schurr *et al.* [2014]; Socquet *et al.* [2017]). Finally, the residual high frequency noise can be even more reduced by applying a temporal sliding window (Schurr *et al.* [2014] and Bedford *et al.* [2015] use an 8-days sliding window).

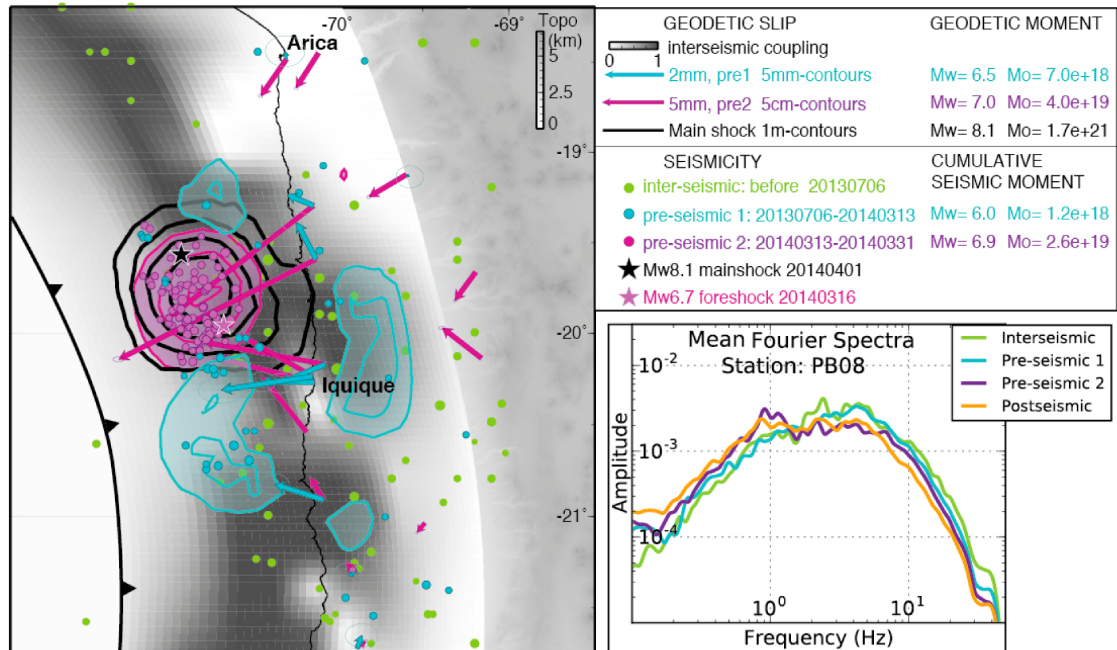


Figure 2.14: Figure from Socquet *et al.* [2017]. Left: Long- and short-term slip events (in blue and purple respectively), preceding the Mw8.1 mainshock, superimposed on the interseismic coupling distribution Métois *et al.* [2016] in gray, and the co-seismic slip 1m contours in black. Foreshock seismic activity for the same periods is also shown (in blue, purple and green, $M_w > 4$). Epicenters of the main shock and the Mw6.7 foreshock are shown as black and pink stars. Right Inset: Mean Fourier spectra computed for interface earthquakes ($5.1 < M_w < 5.2$) grouped into 4 different time periods: interseismic in green, pre-seismic 1 in cyan, pre-seismic 2 in purple, and post-seismic in orange. Station PB08 being located at an even distance of the earthquakes studied, the computed variations in Fourier spectra shapes should be unaffected by variations in attenuation but instead characterize earthquake's source.

Although powerful, these methods have their drawbacks. Seasonal signals for example do not have constant amplitude cycles, and are sometimes shifted in time (either because the meteorology itself is shifted or because of delays in the earth response to a changing seasonal load). Thus, the fit by a pair of sinusoidal terms of constant phase and amplitude is not perfect and leaves a significant misfit. Worse, it can introduce a bias (through aliasing) on the long term trend determination. The case of the station PB02 (21.5°S, far south of Iquique) is also worth noting: it is included in the CME determination of Schurr *et al.* [2014] and Bedford *et al.* [2015] on the claim that it is “stable”, but Socquet *et al.* [2017] do not use it and on the contrary shows a large transient at this station, as large as the one they find at station PSGA at 19.5°S, at the latitude of the seismic crisis (see figure 2.15). Finally, applying a sliding window to average the signal (Schurr *et al.* [2014]; Bedford *et al.* [2015]) is certainly efficient to smooth the data, but it also smears out the daily signal over a longer period (both before and after the events) and renders the daily correlation with the seismicity impossible.

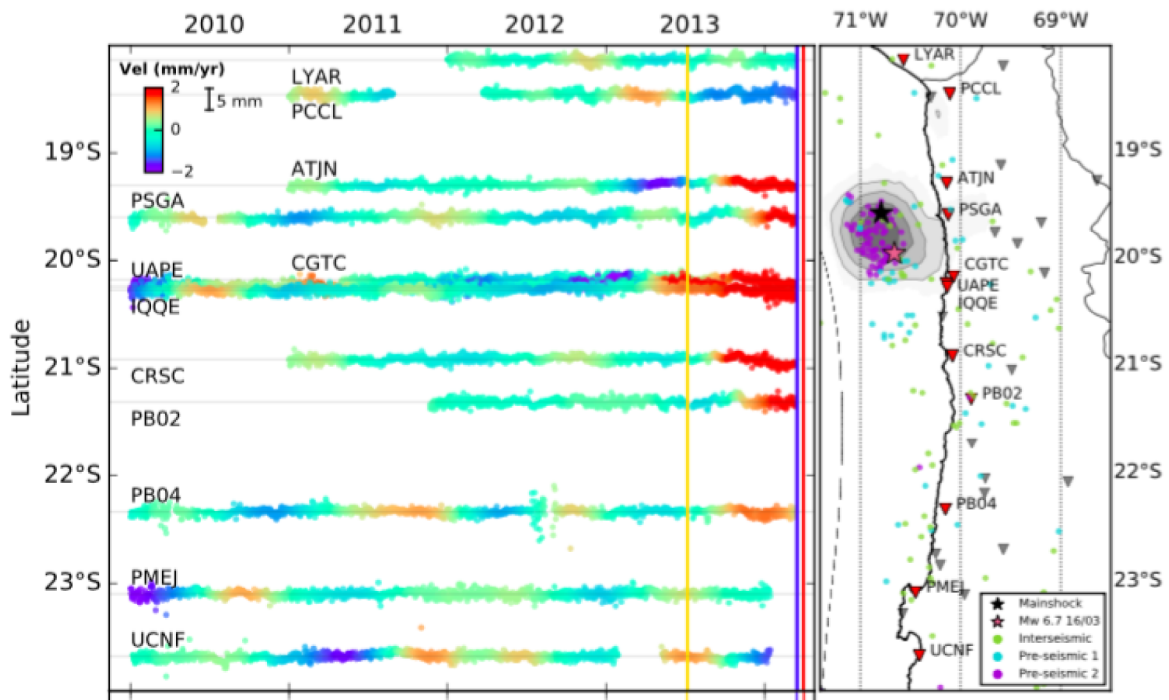


Figure 2.15: Part of the figure from Socquet *et al.* [2017]. Pre-seismic ground deformation over a four-year period, before the April 1st 2014 megathrust in North Chile. Left: Trench perpendicular, detrended time series of coastal cGPS, sorted by latitude. Colors show the variation of average GPS velocities computed in 6-month sliding windows. Right: Map of seismicity: foreshock activity color-coded by periods, epicenters of Mw8.1 mainshock and Mw6.7 foreshock are indicated by black and pink stars, Mw8.1 slip distribution with 1-meter contours. Triangles indicate the location of GPS stations, the red ones being stations whose time series are shown to the left.

In conclusion, this study contributes to the debate with two important findings:

- Following Ruiz *et al.* [2014] and contrary to Schurr *et al.* [2014], we conclude that aseismic slow slip occurred during the foreshock activity to Iquique earthquake, striking intensely the region during January and March 2014.
- Following Socquet *et al.* [2017] we conclude that this slow slip started months before the intense precursory seismic activity triggered by the event of March 16th (M_w 6.7). On the other hand, we do not observe the same starting date than Socquet *et al.* [2017], which argue a duration of 8-months. We think that this early starting date is product different filtering methods used.
- It is not one large but rather several smaller episodes of slow slip that are identified thanks to the sensitivity of the tiltmeter. They occurred around the large 2nd earthquake of Mw

7.8 which occurred April 3rd just south of the city of Iquique, possibly contributing to its triggering.

Case 2: An apparent transient signal north of Iquique, November-December 2008

Between September 2008 and February 2009, 3 out of 10 available stations (HMBS, MNMI, PSGA) recorded a transient signal starting around November 29. For this period there is a significant number of reference stations and the RMS obtained for the corrected signals is less than 1 mm for horizontal components (see table A.1 in appendix A). This means that displacements of several millimeters are detectable and will be recognized as a tectonic transient signal if they exhibit some level of spatial and temporal coherence. The figure 2.16 shows corrected time series for these 3 stations. The trend corresponding to the period prior to the event was subtracted in order to enhance the transient and allow a better quantification of its duration and amplitude. The signal detected corresponds to a slow drift with a duration of 40 days for both horizontal components, stronger on the east. In contrast, the vertical component exhibits a jump from one day (29/11/2008) to the next. Measured vertical offsets are 17.5 mm, 16.8 mm and 5.0 mm downward for HMBS, MNMI and PSGA respectively. This abrupt offset is neither related to an earthquake (see figures 2.16 and 2.17 for temporal and spatial earthquake locations) nor to a registered antenna change. For 2 of these stations (HMBS and PSGA), the date where the vertical offset is detected coincides with a maintenance visit which do not document any instrumental manipulation or change. On the other hand, the vertical jump observed at MNMI occurs one day before (28/11/2008) compared with the other 2 stations, and there is no record of a visit around this date. Even if the information given in these reports is reliable, and the processing of data is commonly based on this information, it is still very likely that a human factor is the cause of this transient displacement. Thus, we find it unlikely that a strange jump detected at 3 stations would not be related to a visit made at those 3 sites the same day or the day before. Additionally, the fact that no anomalous signal is detected at stations ATJN (near PSGA) nor at IQQE and UAPE, 2 coastal stations near HMBS, makes the hypothesis of a transient signal of tectonic origin very unlikely.

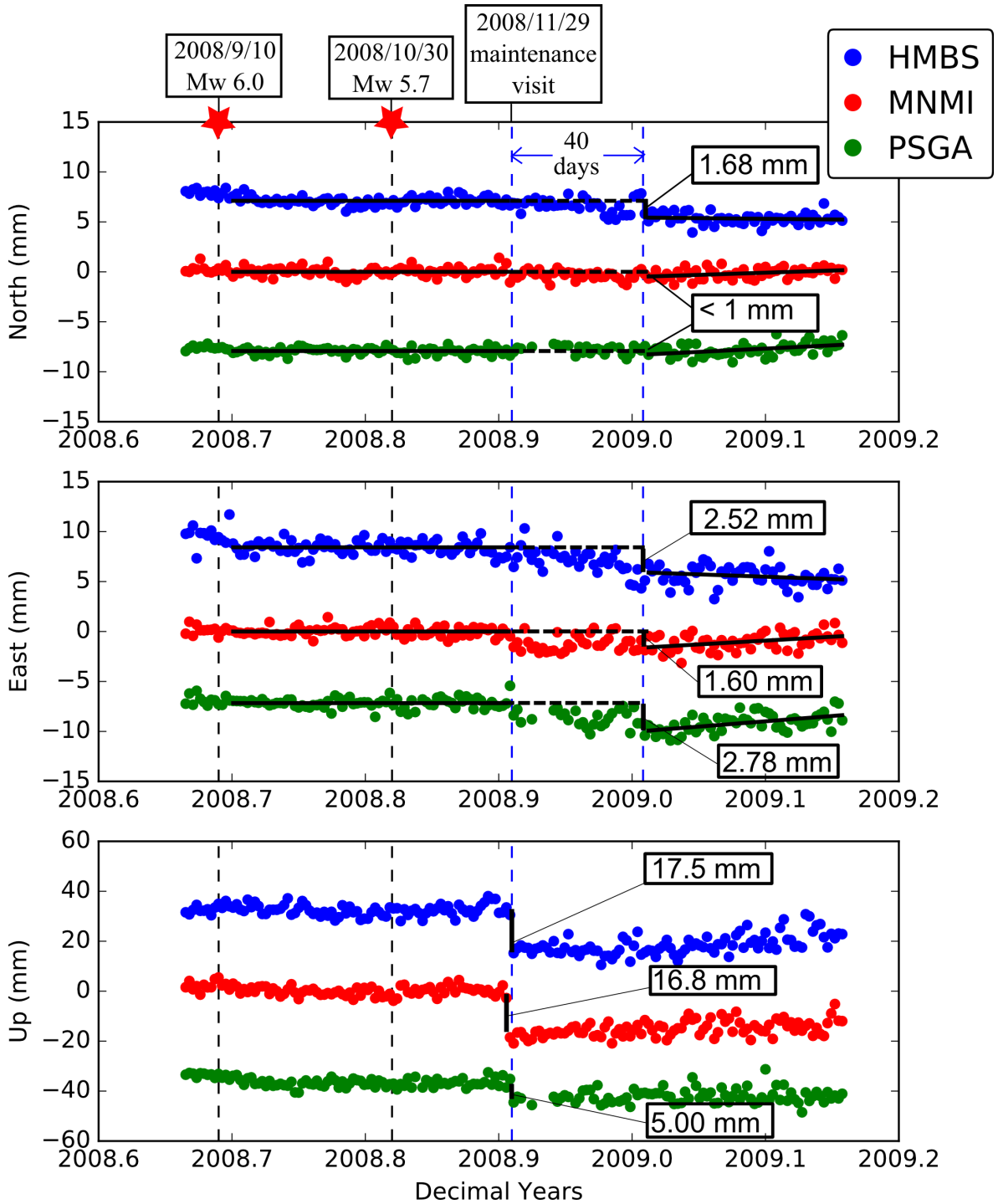


Figure 2.16: Pyacs filtered time series for 3 stations showing 40 days of an horizontal transient signal (blue dashed lines), which starts with a vertical offset not related to earthquakes (red stars). Time series are detrended for the period preceding a routine visit to the station (first blue dashed line) which marks the beginning of the transient. Small black vertical lines represent the estimation of the offset for the vertical component and the total transient displacement experienced by the horizontal components. Horizontal black lines are the result of a linear least squares fitting.

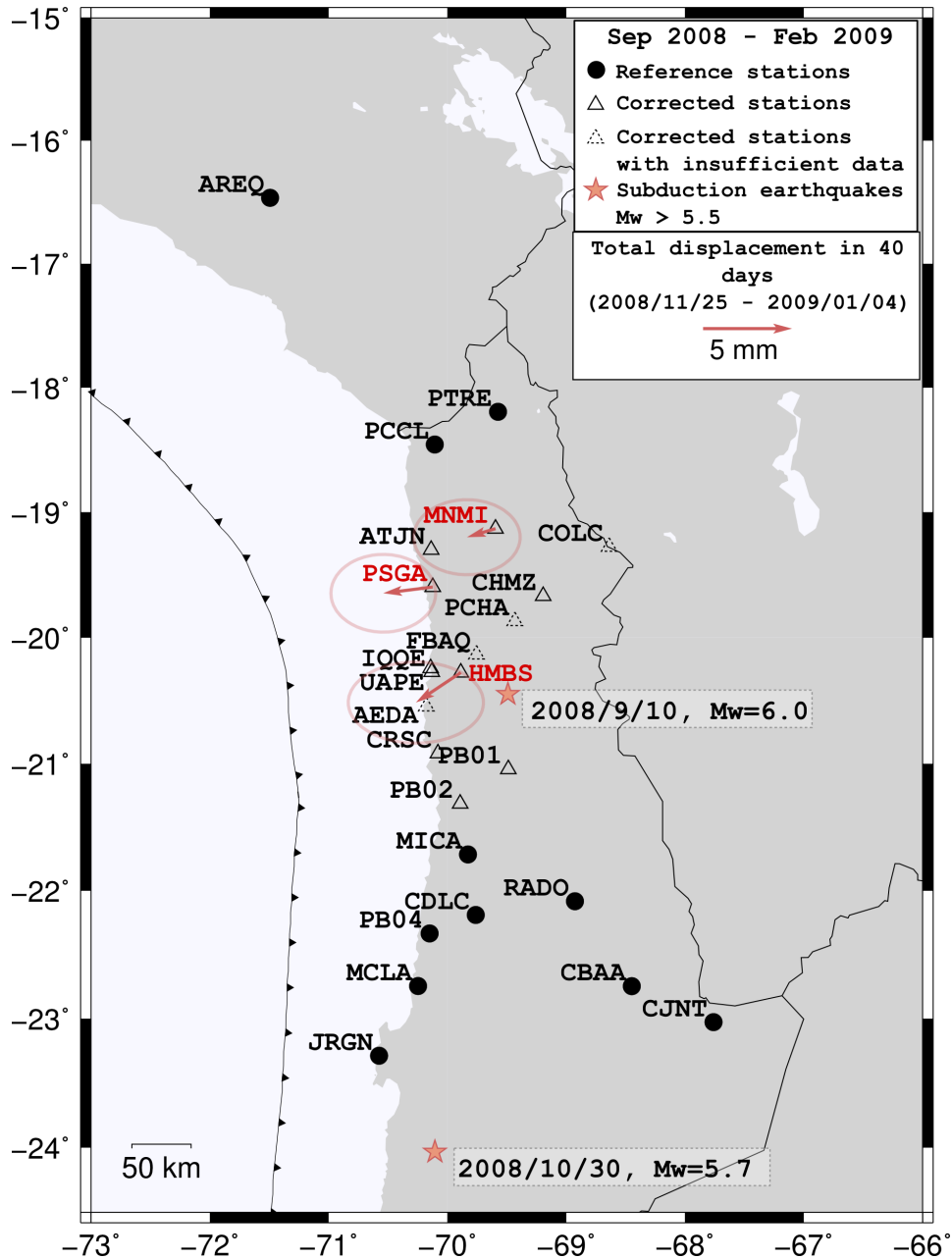


Figure 2.17: Pyacs settings: reference stations (full dots – 11 stations) and filtered stations (open triangles). Total transient displacements found at 3 corrected stations (in red) are depicted by arrows with their respective error ellipses. The transient signal had an approximate duration of 40 days. 2 earthquakes taking place in the region during this period are marked as red stars.

There are many different ways to contaminate cGPS records with careless practices or unwanted and unexpected natural phenomena that will mostly show up as a vertical offset. They are mentioned and briefly discussed in the following.

Change of antenna or receiver, including subtle modifications

Certainly, changes in the equipment produce alterations on the continuity of the positions record. Antenna changes will mostly affect the vertical component because of the modification of the phase center height. Even a simple upgrade of the receiver firmware can have important and unexpected consequences, for example if different parameters are set to different default values. Among these parameters, the cutoff angle is of primary importance since it is well known that addition or exclusion of low elevation angle data is likely to change the height estimation. Also, if the antenna phase center is not exactly at the rotation center of the antenna, any misalignment of the antenna with the North (either magnetic or geographic) or any change in this alignment, will result in a small but significant horizontal displacement. Therefore dismounting the antenna for cleaning for example is very hazardous since the realigning to the north is made with a different compass. Therefore, recording and keeping track of all instrument modifications or antenna changes is extremely important for a correct processing of the data. A non-documented instrument change has important consequences on the positioning due to a possibly wrongly determined antenna phase center height or horizontal position.

Environmental changes

Environmental changes can affect the determination of the position. That can be the case of vegetation alterations in the surroundings, the trimming or fall of a tree or the accumulation of snow, dust or animal dirt over the antenna. There is a very good example of this phenomenon affecting a station located in Indonesia during the spring of 2003. An apparent transient signal showed up at the station at the beginning of the year. During an inspection visit mid 2003, an ant nest was discovered inside the radome of the antenna, mostly between and inside the choke rings but also covering part of the LNA (the active antenna). After the cleaning of the antenna by the removal of all organic matter, the radome was properly reinstalled. Next day of positioning showed the return to the exact normal trend. A kinematic solution was run over a period of time including the cleaning and the nest removal: it showed a short period of 1 hour with a decrease of the number of satellites (exactly during the cleaning) and a vertical offset of 8-10 centimeters once the cleaning is done. The transient signal in fact recorded the growing of the nest and is consistent with different phases of the occupation of the radome by the ants in differ-

ent directions (first to the north, then to the west), and its final removal (see figure 2.18). Thus, the continuous growing of the nest was inducing an increasing mask of dust and eggs delaying the signal and obscuring the antenna for low angle elevation data at a particular azimuth.

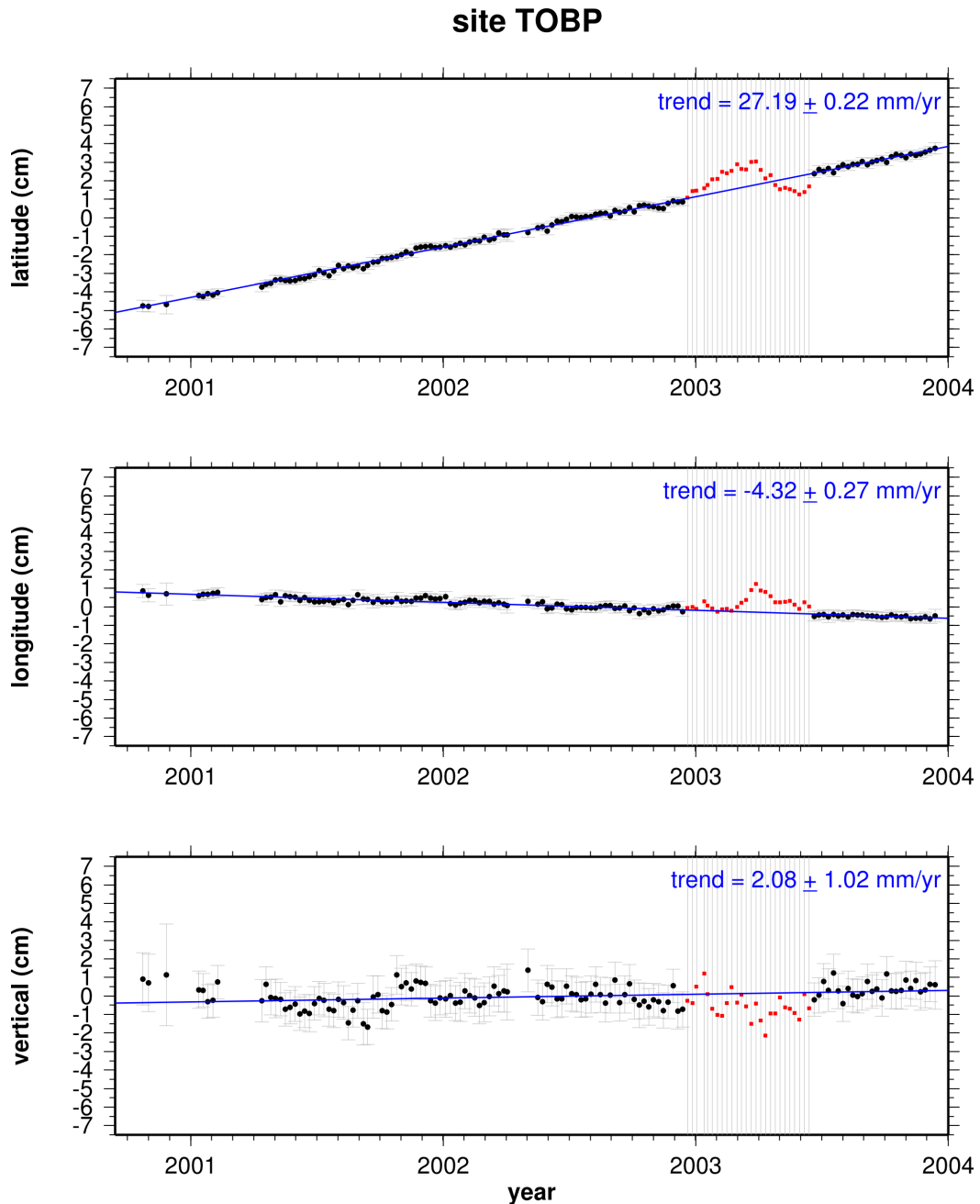


Figure 2.18: Site Toboli, Central Sulawesi (Indonesia), showing a transient displacement (red dots) related to the evolution of an ant nest inside the antenna radome during the spring of 2003. Time series show immediate return to normal trends once the nest is removed. Courtesy of Wim Simons, TU-Delft.

Screwing of the antenna

The stability of the monument in time is an important factor for continuous GPS measurements. Wind, temperature and humidity changes can make the antenna unscrew itself. Human intervention is another factor to consider, either from a member of the survey team or external. In order to maintain the convention of antenna alignment to either magnetic or true North, the antenna might be reset occasionally.

Changes in the analysis

Different models (atmosphere, etc.), algorithms or analysis strategies can induce a change in the recorded positions. We try to avoid this as much as possible by always reprocessing the entire data set with the same setting/models as soon as a new scheme is applied.

In conclusion, there are many reasons why a jump (and even a transient motion) could be an artifact. In the case of our data set, which comes from stations located in the desert, the dry climate together with the absence of external agents (animals and people) and the low number of incidents affecting the stations despite the frequent maintenance visits, supports the authenticity of the signal as tectonic. Nevertheless, this argument is more robust for the observation concerning the east component (several millimeters during more than a month) than for the vertical component jump coincident with a maintenance visit which definitely casts a doubt.

Case 3: A small transient displacement in 2010 near Iquique

During the time lapse between May and October 2010, the numerous available stations together with significant seismic events only occurring at the beginning and end of this period, allow to obtain time series with low dispersion. We achieved an average standard deviation of 0.5 mm and 0.4 mm for east and north components of Pyacs corrected stations (see table A.2 in appendix A).

A transient of only few millimeters can be seen clearly despite its small size on the east component of 2 stations located very close one each other: IQQE and UAPE. This transient has a duration of 14 days and apparently it is detected as well in PICA, a station located landward at ~ 90 km from IQQE, for which the trend preceding the transient is not completely recovered after it, making its exact identification less accurate (see figure 2.19). North components do not register transient displacement during this period. Similarly, with a standard deviation over 2 mm, the vertical component of our time series do not seem to detect any anomalous signal (see figure 2.20 with the north and vertical component of the station IQQE as an example). The figure 2.21 shows transient displacements in a plain view for these 3 stations, detected mostly in the east and occurring in a 14-days span corresponding to the period between 2010/07/31 and 2010/08/15. The figure shows as well corrected and reference stations used for Pyacs, and the epicenters of 2 earthquakes over magnitude M_w 5.0 striking the zone at the start and end of the studied period: a subduction event on May (2010/05/06, M_w 6.5) and an intermediate depth event in October (2010/10/27, M_w 5.8), none of them affecting reference stations. Transient displacements during this 14-days period were calculated for the rest of the corrected stations and shown in figure 2.22, separating between coastal and inland sites. In general, coastal stations show what it seems to be a consistent but very small westward transient as well as the recovery of the trend after the period of 14 days. In contrast, for inland stations, apart from showing a smaller displacement than the average dispersion on time series, the trend preceding the event is not longer recovered, especially in the case of the station MNMI which presents a larger seaward transient signal starting at the same time than the transient event but with no clear end, in coincidence with the signal observed in the inland site PICA after this date (see figure 2.19).

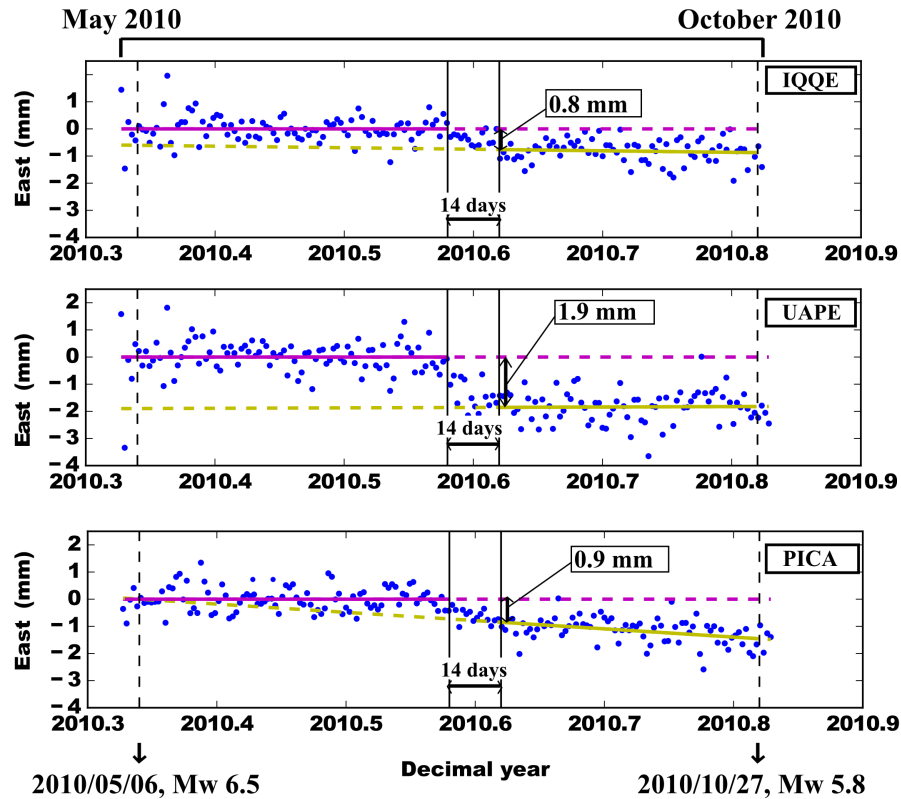


Figure 2.19: East components of times series corresponding to IQQE, UAPE and PICA stations (see map in 2.21 for their location). These 3 stations record a small but consistent transient displacement in a time span of 14 days (indicated in the figure). All sites record less than 2 mm offset but slopes before and after the event are practically the same for 2 of 3 stations. 2 earthquakes occurring before and after this period are shown in time series as 2 vertical dashed lines. Lines represent the best fit to displacements before (purple) and after (yellow) the event.

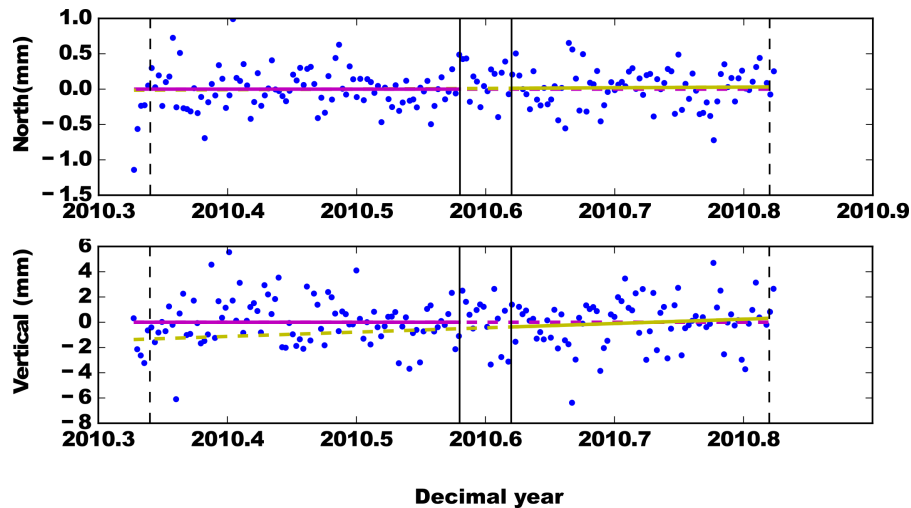


Figure 2.20: North and vertical components of station IQQE recording a non-existent or imperceptible transient displacement in these directions. Conversely, a 14-days westward signal is detected at this station and the sites UAPE and PICA.

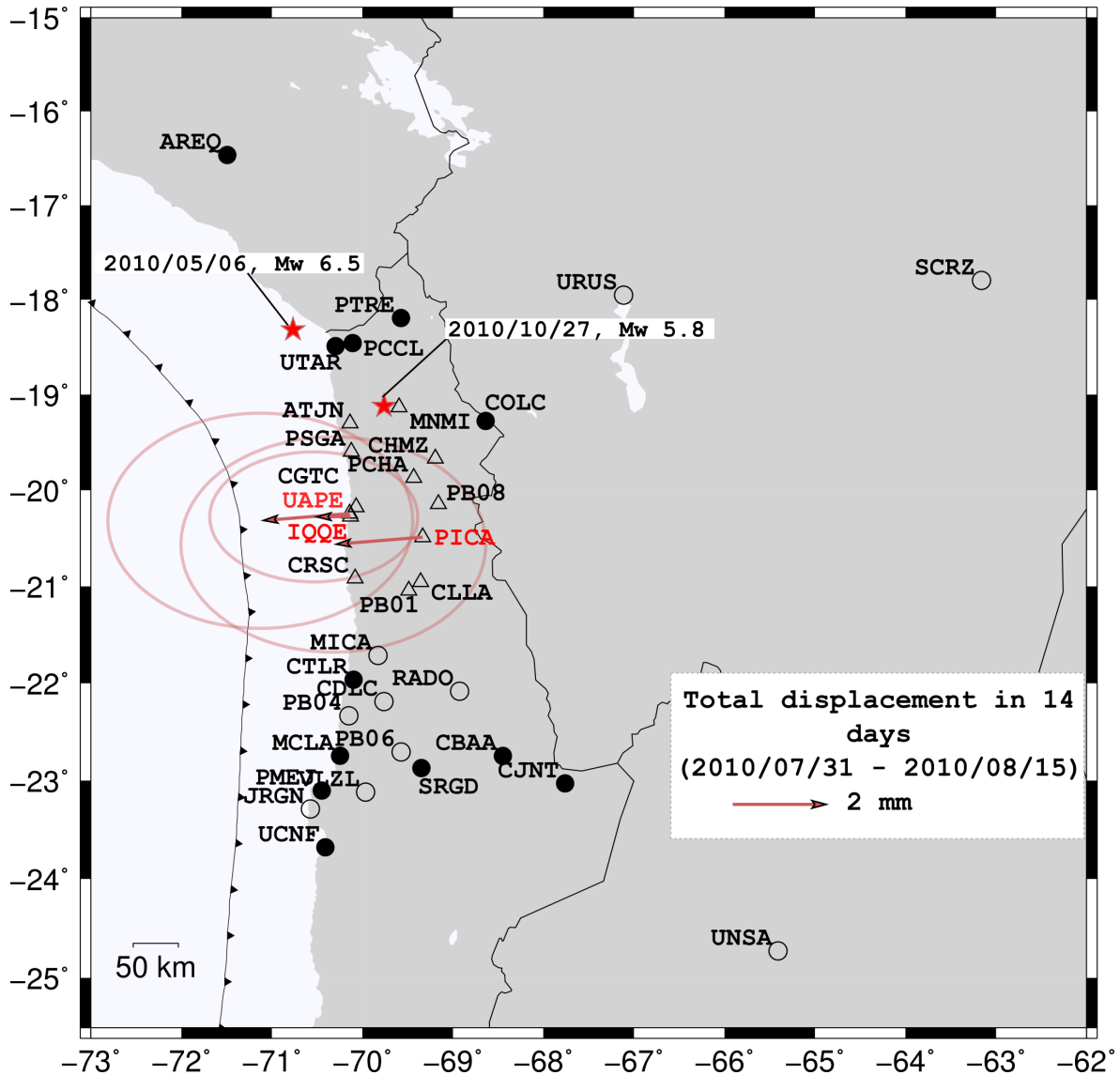


Figure 2.21: Reference sites (black circles), corrected sites (triangles) and available stations but not suitable to be used as reference sites (unfilled circles) in Pyacs calculation. Transient displacements recorded mostly in the east component of time series of 3 stations (highlighted in red) are shown as arrows together with the 95% confidence ellipse errors. 2 earthquakes occurring at the beginning and end of the 6-months time series period are represented as red stars.

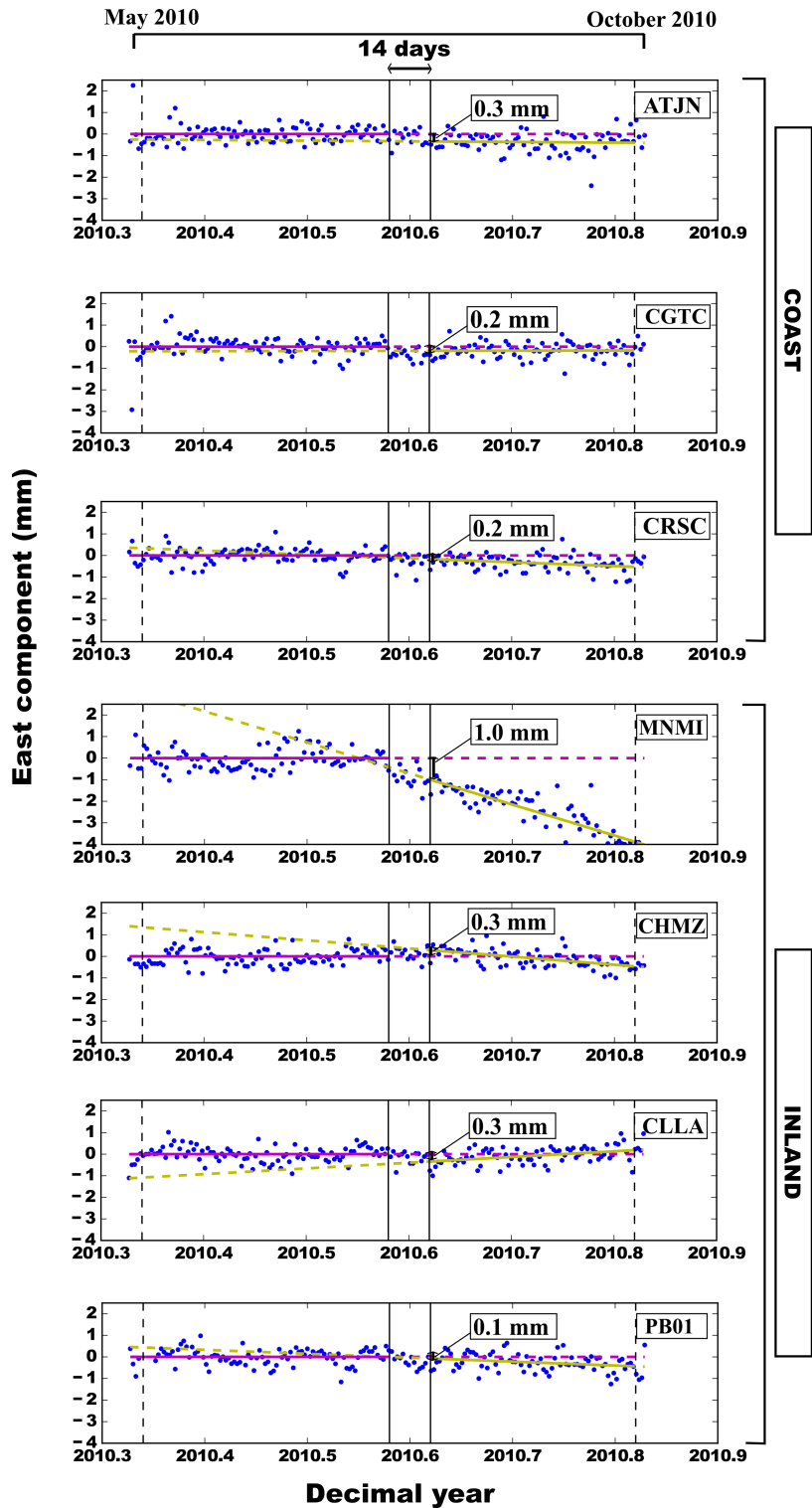


Figure 2.22: East component times series of coastal and inland stations showing a very small or null displacement during the first 2 weeks of August 2010 (limits indicated as black vertical lines). Calculated displacements for this period are under the noise level and thus is not possible to consider these signals as supporting information validating the signal founded in the east component of several stations.

Case 4: Another transient event in front of Iquique-Pisagua in 2009

Between January and June 2009, time series of 2 coastal station (ATJN and PSGA) detect the coseismic jump produced by a subduction earthquake magnitude M_w 6.0 with epicenter ~ 60 km in front of PSGA (Chilean seismological service location). The horizontal coseismic offset produced by this event occurred on April 17th can be easily determined in these Pyacs filtered time series (see figure 2.23), corresponding to the closest stations.

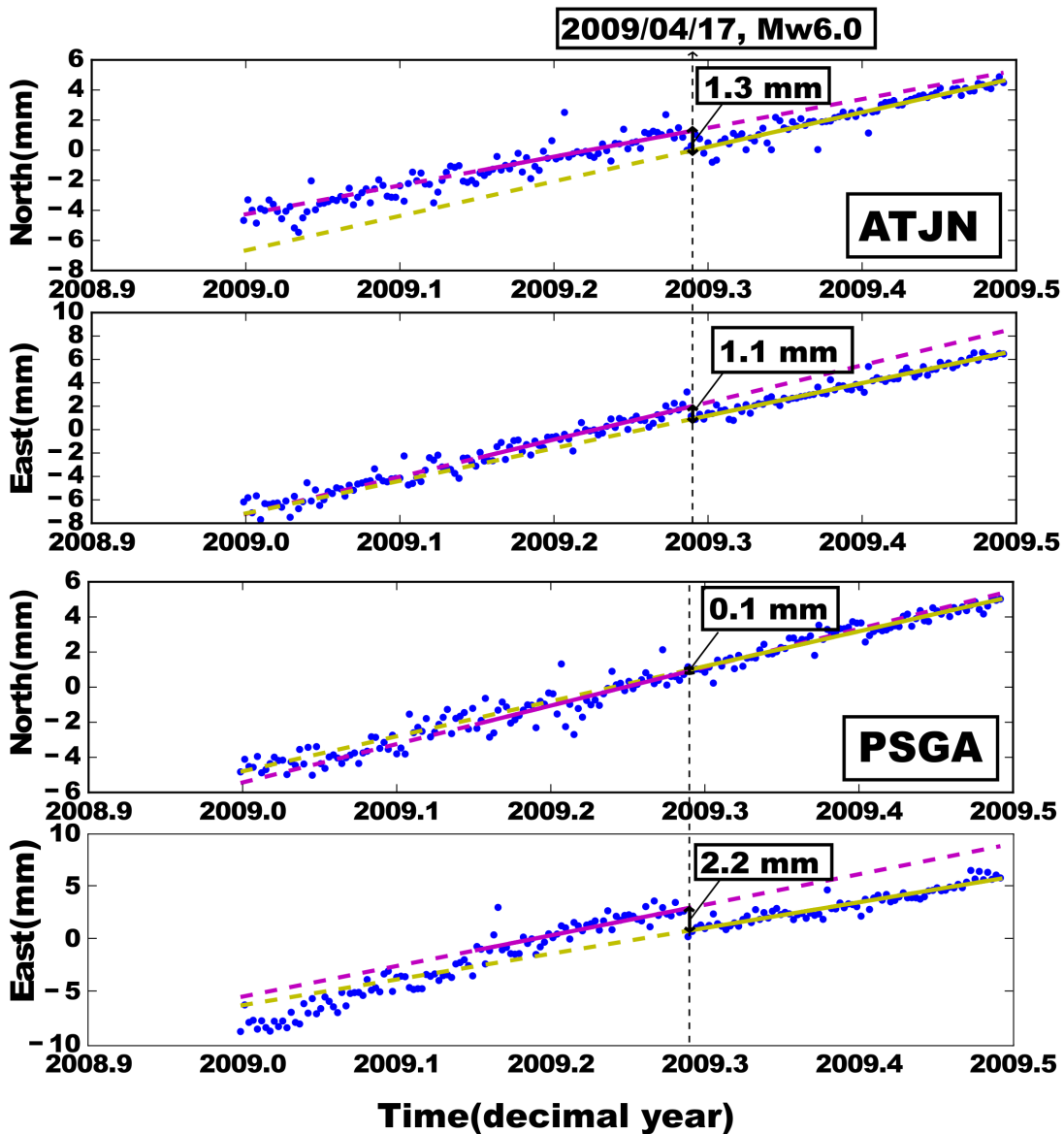


Figure 2.23: Coseismic offset produced by a subduction earthquake of magnitude M_w 6.0, detected in 2 sites: ATJN and PSGA. The figure shows Pyacs filtered time series recording between January and June in 2009. The offset associated to the event is indicated for each component.

Seismic events with magnitudes higher than M_w 3.0 (and up to 80 km depth) occurring during the complete year 2009, together with the setting of available GPS stations (reference and corrected) during the 6-months analysis window (January-June 2009) are shown in figure (2.24). Circles varying from orange to purple represent seismic events occurred during the first half of 2009 (the 6-months analysis period), with 2 earthquakes over magnitude M_w 5.5 (indicated in the figure) occurring during this time span. Seismicity distribution of the complete year 2009 reminds the foreshock activity of Iquique earthquake in 2014 (see figure 2.6.2), with one large seismic cluster in front of the station PSGA. Similarly to the seismic crisis of 2014, apparent transient slip is detected at stations located ~ 100 km south of the main cluster. In this case, simultaneously to the M_w 6.0 subduction earthquake, 2 southern GPS stations (HMBS and PB01) record a transient displacement of more than 1 cm in both north and east components (figure (2.25)). Contrary to the situation in 2014, the stations recording a transient movement correspond to 2 inland stations.

In contrast, at southern coastal stations as CRSC, UAPE and IQQE, this transient signal is undetectable (figure 2.26). In the case of IQQE, and for the same period when the transient is detected at inland stations, is possible to measure a very small component (~ 1 mm) of a westward transient signal, but with an error comparable to the one of HMBS associated to a much smaller displacement. CRSC and UAPE on the other hand, show a difference in the RMS starting on the same date, but either the signal of the event here is too small to be detected or is not detected at all.

Figure 2.24: GPS stations setting (corrected and reference sites) for the period between January and June in 2009. Seismicity occurring during 2009 is represented by circles differentiated by magnitude (size) and time (color). Major events from the 6-months studied period are indicated with white labels.

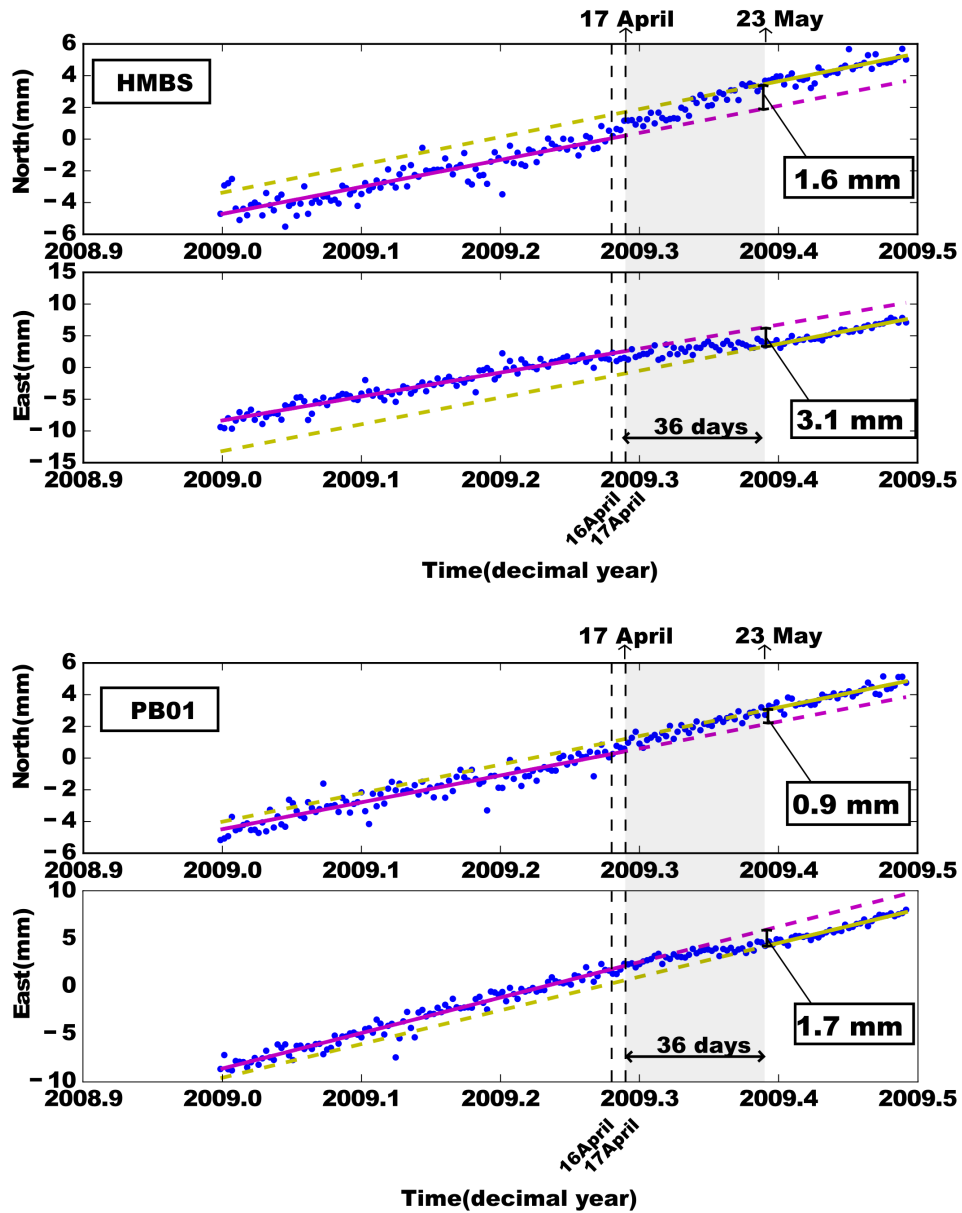


Figure 2.25: Time series from the sites HMBS and PB01 recording a transient signal during 36 days represented by a shadowed rectangle. Horizontal displacements are showed for each component and station and 2 earthquakes with magnitude over M_w 5.5 preceding the transient signal are indicated with vertical dashed lines.

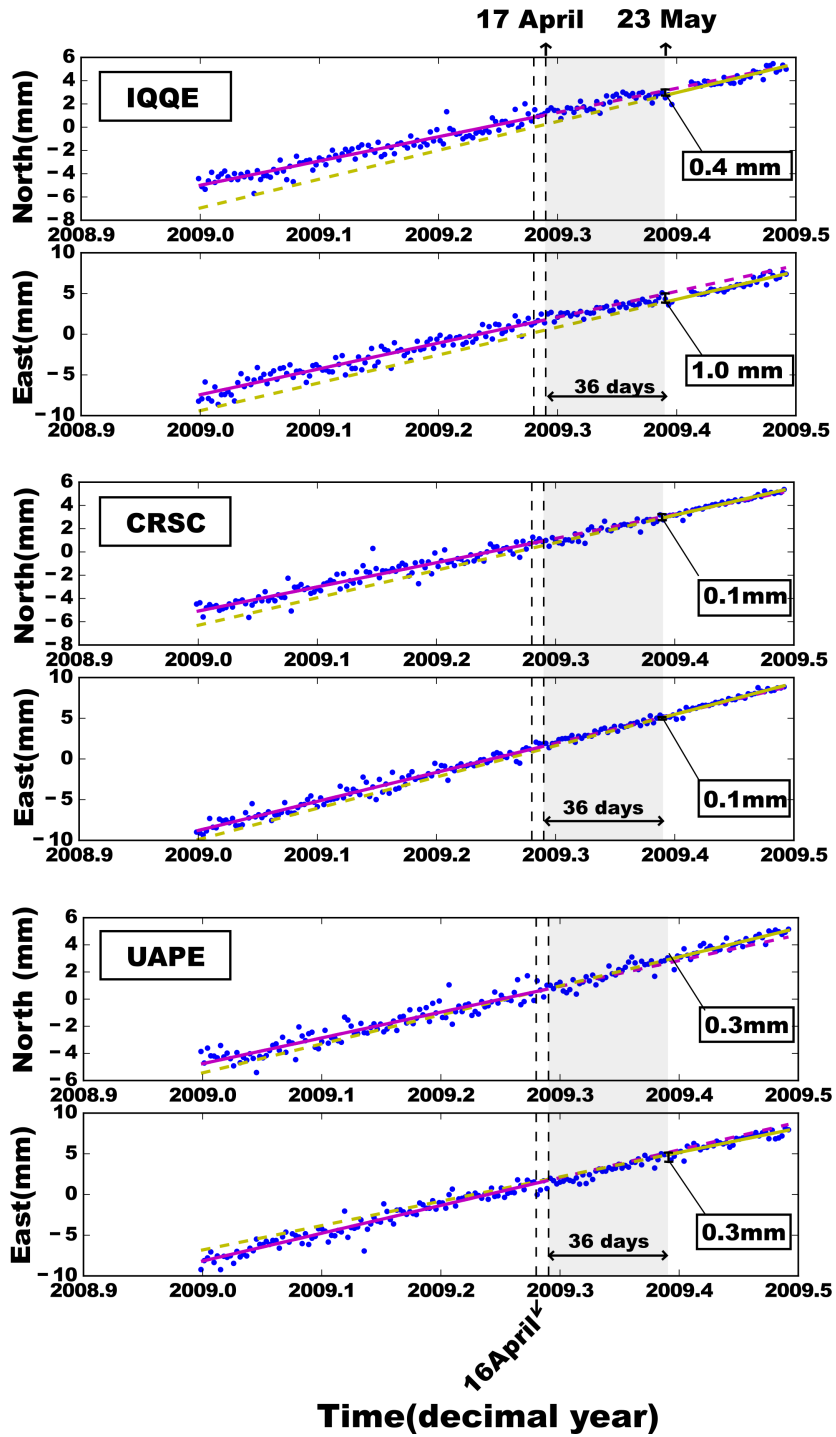


Figure 2.26: Time series from IQQE, CRSC and UAPE cGPS sites including the period when a transient event is detected during 2009 (shaded rectangle). While it is possible to estimate a total displacement during these 36 days for IQQE, CRSC and UAPE does not detect any transient signal (less than 1 mm). 2 earthquakes with magnitude over M_w 5.5 are indicated with vertical dashed lines.

The total displacements during these 36 days at the stations detecting this transient signal are shown in figure (2.27). The fact that the coastal station IQQE sees a smaller displacement than stations inland and the null observations (less than 1 mm) at several other stations (i.e. CRSC, UAPE) does not allow to adjudicate these observations to slow slip at the usual seismic depth on the subduction interface, like in 2014. However, the signal detected at PB01 and HMBS is measurable and coherent, possibly indicating a deeper event, below the transition zone and therefore showing up on inland records rather than on coastal records.

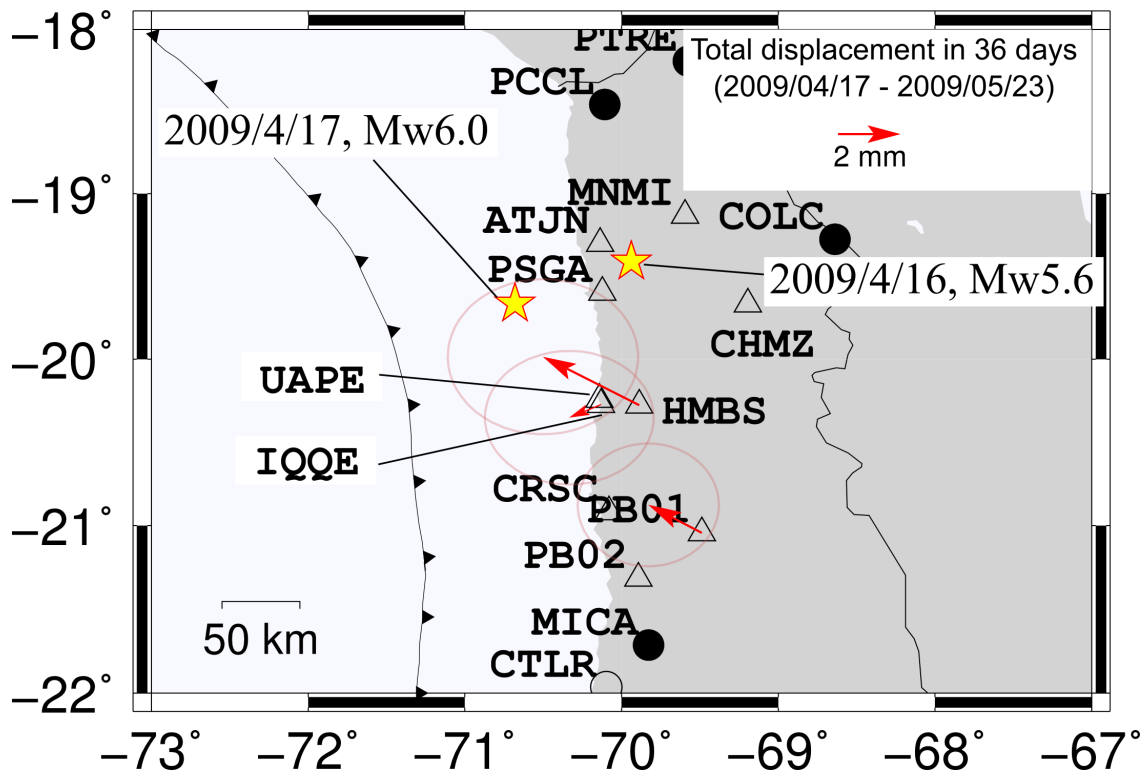


Figure 2.27: 3 vectors for the stations IQQE, HMBS and PB01 representing the total transient displacement detected between 17 April and 23 May of 2009. Displacements for UAPE and CRSC are not shown for being smaller than 1 mm. 2 earthquakes occurring at the beginning of this period are symbolized as yellow stars (Chilean Seismological Service location). Error ellipses are included for each case.

Case 5: Transient event in front of Pisagua in 2011

Between May and October 2011, a transient event with same duration than the one found in 2009 (36 days) is detected near the station PSGA (Pisagua). 3 stations (PSGA, CHMZ, PCHA) located at around the same latitude, recorded up to 2 mm of a transient displacement to the west. In contrast, the north components do not show any clear transient (see figure 2.28).

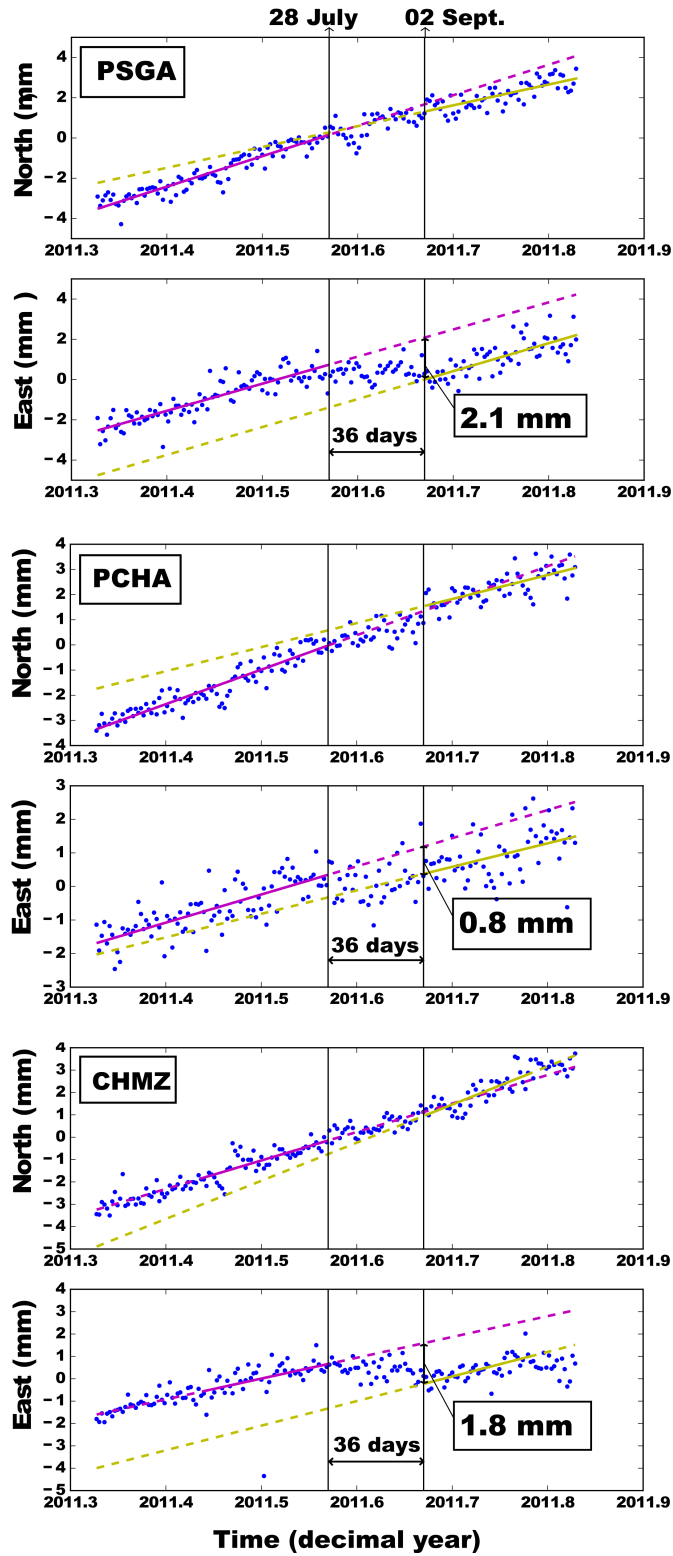


Figure 2.28: Time series from PSGA, PCHA and CHMZ (west to east) detecting a westward transient displacement in 2011 (May-October 6-months window). The limits of the period when this displacement takes place are indicated as vertical black lines. Trend before and after the event are represented by purple and yellow lines respectively.

Setting of the stations for this period and the westward displacements found at these 3 stations are shown in figure 2.29. Only 2 earthquakes (yellow stars) with magnitudes over M_w 5.5 occur during these 6 months. They have depths exceeding 90 km and they are located at more than 200 km far away from the stations recording a transient signal. Thus, this transient is not linked to any seismic crisis.

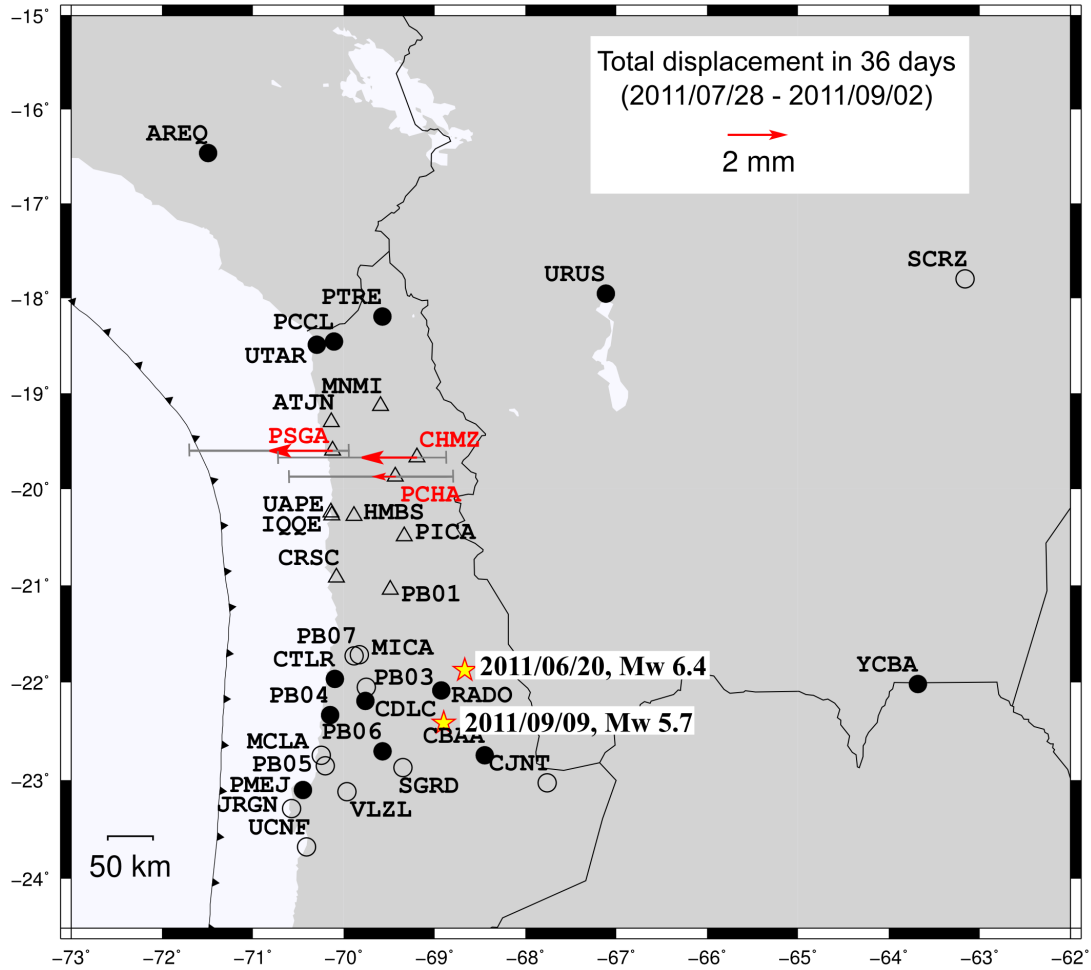


Figure 2.29: Reference (black dots) and corrected cGPS stations (triangles). Other stations not included in the calculations are symbolized as open circles. Transient displacements recorded for 3 stations (red) are indicated as vectors pointing to the east (north component remains undetectable). Errors for the east component are represented by horizontal bars in gray.

2.6.3 Conclusion

After an exhaustive revision of 35 six-month windows of GPS time series recording during the period spanned between 2000 and 2015, we have found several transient events occurring in Chile, only 4 recorded by more than 2 stations. Contrary to Mexico or New Zealand, most of these events have very small amplitudes (up to ~ 3 mm) and durations of no more than several days. Small amplitudes and few recording stations make difficult to determine the source of 3 of these 4 events and thus, they remain only as candidates to correspond to SSE. The signal with the largest amplitude (fourth event) occurs simultaneously to the foreshock seismic crisis preceding Iquique 2014 earthquake. The sensitivity and resolution of the available tiltmeter instrument allow to identify several SSE rather than only one general motion. This corresponds to a more realistic situation than the long-term slow displacement found by other authors in the same region. Finally, thanks to GPS and tiltmeter instruments recording the foreshock activity of Iquique earthquake, we confirm that this precursory phase is accompanied by slow slip, and that it can be described more precisely as a sequence of several slow slip events.

Chapter 3

A long term change on the deformation accumulation

3.1 Introduction

The Earth's surface deforms very rapidly during and very shortly after an earthquake (co-seismic deformation), but also during the days and years following the earthquake (postseismic deformation). In the last decades, since geodetic and seismic instruments have been monitoring subduction zones, these postseismic signals have been widely analyzed for shallow (Shen *et al.* [1994]; Pollitz *et al.* [2001]) and megathrust events (e.g.: Bedford *et al.* [2013]; Klein *et al.* [2016]) (figure 3.1). Postseismic deformation is commonly explained as the combination of 3 principal mechanisms: creep or afterslip at the down- and up-dip of the coseismic rupture, viscoelastic relaxation of the mantle and poroelastic relaxation. The latest mechanism is related with fluids motion (transient pore pressure) in different areas of a subduction zone after an earthquake. This transport of fluids modifies mechanical properties on rocks and thus becomes an important factor to consider in Coulomb stress changes in a time lapse from weeks to months (Detournay & Cheng [1995]; Hughes *et al.* [2010]). Afterslip and viscoelastic relaxation are the most common mechanisms explaining longer-term deformation. While afterslip is related with deformation neighboring the fault, relaxation of the stress triggered by an earthquake in the mantle, affects wider areas of several thousands of kilometers around the earthquake producing deformation for even decades. The viscoelastic relaxation of the mantle is directly related to its rheology, normally associated to Maxwell or Burgers bodies that better represent the viscoelas-

ticity of the asthenosphere, and therefore to viscosities that can follow simple linear behavior. Apart from mega-thrust earthquakes, subduction zones are affected by large intermediate-depth events. Because of their location, inside the subduction plate and below the down-dip end of the seismogenic zone (~ 50 km depth), the way they interact with the asthenosphere differs from subduction earthquakes, which makes the analysis of deformations following intraslab earthquakes an interesting topic. Even though these types of events are subject of many studies, these mostly attempt to establish a relation between interplate and intraplate events (Astiz *et al.* [1988]; Kato [2004]; Nakajima *et al.* [2013]; Bouchon *et al.* [2013]; Jara *et al.* [2017]). For instance, Bouchon *et al.* [2013] find synchronization between intermediate-depth seismicity occurring previous to large mega-earthquakes as the M_w 9.0 Tohoku-oki (Japan) or M_w 8.2 Iquique (Chile), and shallow foreshock activity, arguing that this interaction may be an indicator of the nucleation of mega-thrust earthquakes. Nevertheless, only few works make an analysis of the spatiotemporal evolution of postseismic crustal displacements caused by intermediate depth earthquakes (Yoshioka & Tokunaga [1998]; Bie *et al.* [2017]), probably due to the small magnitude of displacements induced at the surface, but also because they are less frequent than subduction earthquakes. These few studies emphasize the feasibility of using intermediate-depth earthquakes of large magnitudes in realistic 3D models to provide/reinforce information about the rheology of subduction zones inferred from thrust earthquakes studies.

In June 2005, a large intermediate-depth earthquake magnitude M_w 7.7 took place in the Tarapaca region in north Chile. It occurred in the middle of a recognized seismic gap, commonly associated to the 1877 tsunamigenic earthquake (M_w 8.8) described by Kausel [1986] (see Métois *et al.* [2013b] for a different interpretation). As most of the intraplate earthquakes, the source mechanism of Tarapaca 2005 corresponds to a slab-pull, related with extensional stresses downdip the coupled seismogenic zone (Lemoine *et al.* [2002]). Located at ~ 100 km depth, with a rupture area of approximately $60 \text{ km} \times 30 \text{ km}$ and an average slip of 10 m, this event is particular because of its slow effective rupture velocity and its nearly horizontal fault plane (Peyrat *et al.* [2006]). This low dipping plane was determined from the aftershock sequence following the main event (Peyrat *et al.* [2006]; Delouis & Legrand [2007]) and from seismic waveform inversion (Delouis & Legrand [2007]). The figure 3.2 shows the focal mechanism of the mainshock and 21 days of aftershocks in a plan view and cross-section, outlining the rupture extension.

A scenario where this earthquake modifies the coupling on the subduction interface enough to trigger interplate transient slow slip, which in turn prepares the conditions for the large sub-

duction earthquake of Iquique 2014, has been recently proposed by Jara *et al.* [2017]. This interpretation is supported by a change in the deformation gradient in the upper plate, detected right after the earthquake in cGPS time series available at these dates in northern Chile. This change corresponds to a decrease in the velocity with respect to the interseismic rate established before this intermediate-depth earthquake.

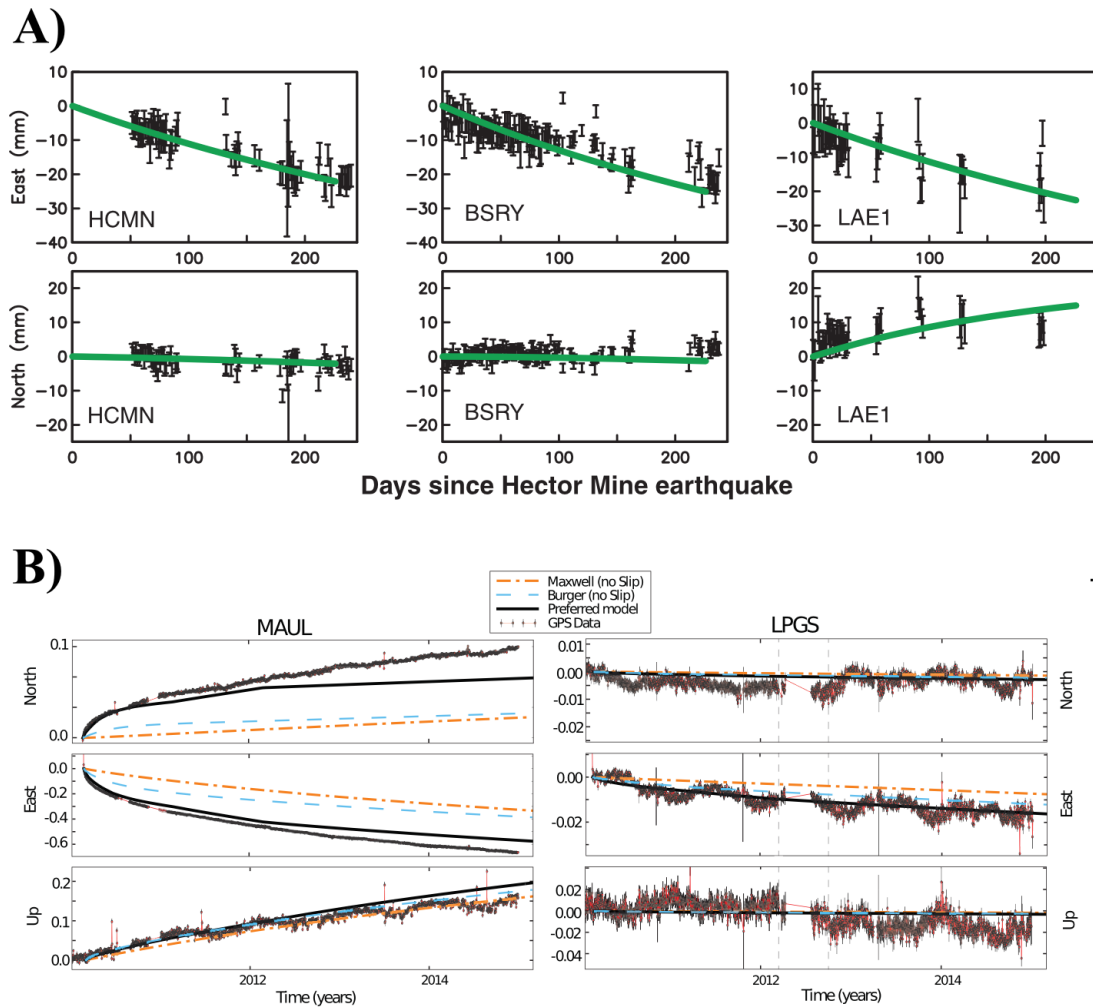


Figure 3.1: Prediction of 2 viscoelastic models contrasted with observations of deformation for A) 1999 Hector mine shallow earthquake and B) the subduction earthquake of Maule in 2010. Both figures correspond to modified versions from Pollitz *et al.* [2001] and Klein *et al.* [2016] respectively.

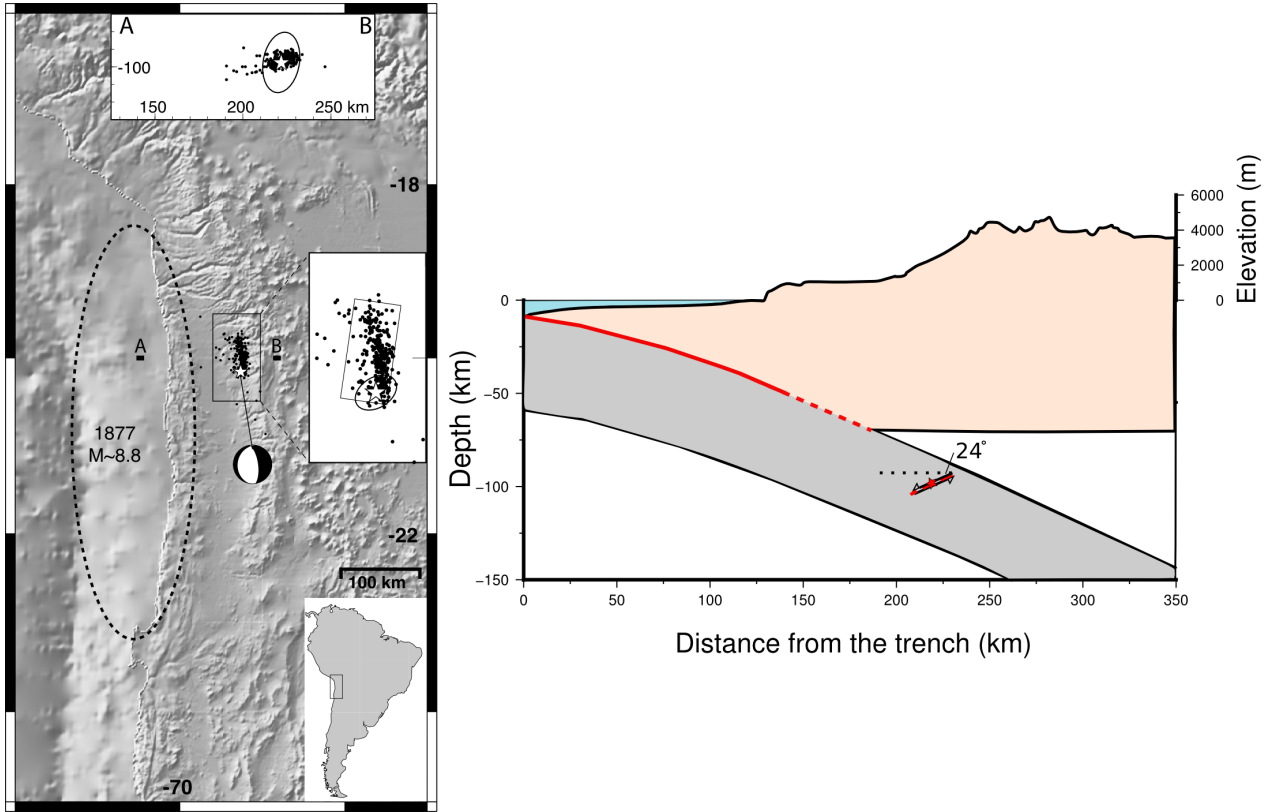


Figure 3.2: Left: Modified figure from Peyrat *et al.* [2006] showing the mainshock location (white star), its focal mechanism and 21 days of aftershocks (black dots) for Tarapaca 2005 event. A cross section view for the profile A-B is included (upper box). The larger rupture area of the mega 1877 earthquake is shown by a dashed ellipse. Right: Cross-section scheme at 20.5° S and parallel to the convergence, showing the rupture plane width (30 km) and dip angle (24°) in relation with a realistic representation of the slab (slab top USGS version 1.0) of 50 km width. Seismogenic zone is shown as a continuous red line.

Starting from the same observation, in this chapter we are interested in elucidating the origin of this velocity decrease. In the first part of this chapter we show different factors affecting the stability of the trend calculation on GPS time series, present the methods applied to decrease the noise and we quantify the change of velocity due to Tarapaca earthquake. Finally, the second part is dedicated to find an explanation for these observations by using numerical modeling techniques.

3.2 Improving precision on GPS time series of 15 years duration

The exhaustive GPS time series analysis performed in the previous chapter is useful to detect transient signals of no more than several weeks of duration. The strategy followed there is no longer suitable in the case of the study of transient deviations exceeding the previously used 6-month window. For long time spans of several years, we have time series corresponding to positions calculated with respect to the ITRF reference frame. These time series contain high frequency noise and non-tectonic signals related to mass redistribution over the Earth's surface. Unlike high frequency noise, hydrological signals might have a strong effect on the stability of the trend during several years. The latter lead us to examine in first place this phenomenon which could alter our observations regarding long term variations on deformation accumulation, and evaluate the best way to remove it.

3.2.1 The Mass distribution effect

The hydrosphere is equivalent to the water content in the Earth located underground, on its surface and in the air. The water redistribution phenomenon deforms the Earth and this effect can be detected by space geodetic methods as the Global Navigation Satellite Systems (GNSS). The gravity variation induced by the redistribution of hydrological loads is measured by the Gravity and Recovery Climate Experiment (GRACE). Both methods measure accurately this surface deformation, which is a response of the Earth to the loading phenomenon determined by its composition. Both techniques highly improved during the last decade and became an important tool to infer the rheology of the planet. On one side, continuous geodetic records obtained by the Global Positioning System (GPS) (most known GNSS system) show local seasonal signals, especially evident (large amplitude) on the vertical components. On the other hand, GRACE makes use of the gravity variations (with an accuracy of 2-3 mm) detected by twin satellites to infer the global distribution of water in Earth's surface and sub-surface (Tapley *et al.* [2004]). The GRACE estimation of the global masses redistribution is necessary to model the loading seasonal signal detected locally by GPS instruments. Modeled seasonal oscillations can be used either to infer Earth's viscoelastic structure or to improve the quality of GPS time series by removing hydrology effects. It is a very common practice for geodesists to approximate these

annual oscillations by a four-term Fourier series consisting in 2 semi-annual and 2 annual terms (Bevis & Brown [2014]). This strategy assumes apriori fixed amplitudes and periods for the hydrological signal which is not always what is observed in reality. Figure (3.3) shows an example for this approximation and the seasonal variations modeled with GRACE for a station in northern Chile. Although annual oscillations models based on truncated Fourier series apparently represent a very good fit to the observations, a more realistic curve will include different local phenomena inducing water mass variation with a recurrence period longer than one year, as for instance are “el niño” or “la niña” climate patterns. They affect the east-central Equatorial Pacific, resulting in large scale hydrological oscillations in the continent with variable amplitudes and wavelengths as it is seen in signals modeled with GRACE. In this work, we take advantage of the seasonal signals available in the region product of the combination between GPS observations and GRACE. This correction is essential if we want to avoid a bias in the identification of tectonic signals in continuous position records.

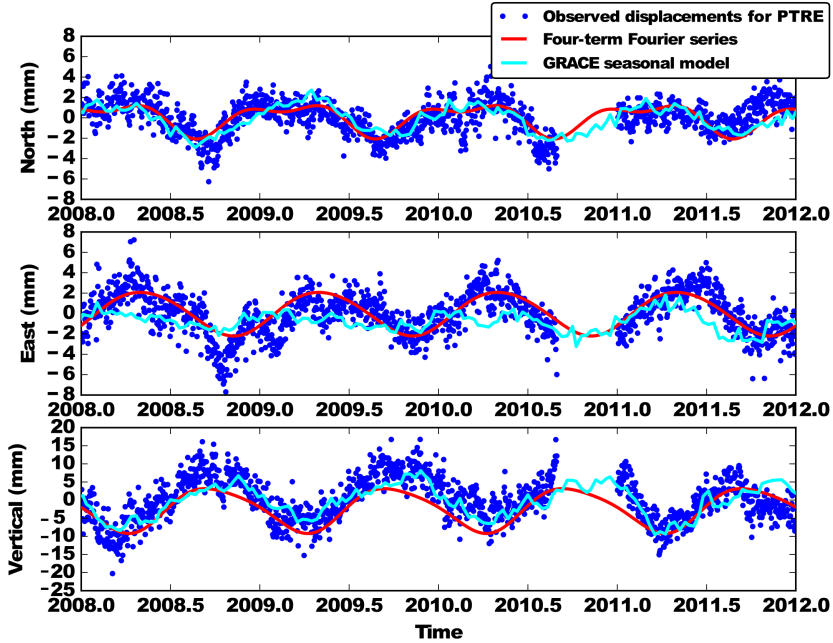


Figure 3.3: Positions recorded by the GPS station PTRE in Northern Chile (blue dots) and 2 signals representing hydrological seasonal cycles: 4-terms Fourier series (red) and predicted oscillations with GRACE (cyan).

3.2.2 Seasonal variations observed in Northern Chile

In this work we study the region corresponding to the Northern part of Chile: the Atacama desert. This zone is known for being the most arid in the world with mean annual precipitation increasing from 0 mm for the Absolute Desert (< 1000 m height) to 230 mm at heights up to 4500 m corresponding to Altiplano-Puna region (Betancourt *et al.* [2000]). As a result, Northern Chile observed variations are not strongly related with local pluviometric variations but mostly to variations of rainfall in the Amazon basin. The amazonian basin is very far from north Chile (~ 2000 km), but the seasonal change of mass is so large and at such large scale, that the crustal deformation generated is still measurable in Chile. The figure 3.4 shows 3 components of hydrological signal calculated with GRACE for 11 GPS stations located up to 500 km apart. Distant GPS stations show very similar hydrological pattern showing that local precipitation regime remains small compared with the larger scale Amazon basin variations.

The seasonal signals obtained for GPS sites located in northern Chile have been calculated following the method exposed in Chanard *et al.* [2018]. In this study, they show the importance of properly including degree one loads in order to achieve a good prediction of the displacements induced by hydrology. The improvement is both in the amplitude and phase of the predicted signals, and the predictions of the horizontal displacements are particularly improved.

3.2.3 Hydrological correction for northern Chile GPS time series

GPS time series to be corrected correspond to 15 years-long records starting in 2000 from 40 permanent sites located in northern Chile and southern Peru. Their location and availability during the period of interest are shown in figure 3.4 and table 3.1 respectively. These time series are produced by GAMIT/GLOBK process described in 2.1. Unlike the short term method detailed in chapter 2, the daily coordinates are mapped in the ITRF (GLRED module) using a large set of globally distributed stations.

We used best model from K. Chanard (Per. Comm.) to predict seasonal variation at the locations of our 40 stations in northern Chile. Unfortunately, GRACE modeled seasonal signals are available only between 11/08/2002 to 20/07/2012 because the satellites were launched in March 2002. In order to remove them from our raw time series they have been daily interpolated. The figure 3.5 shows horizontal and vertical velocities before and after the seasonal correction for

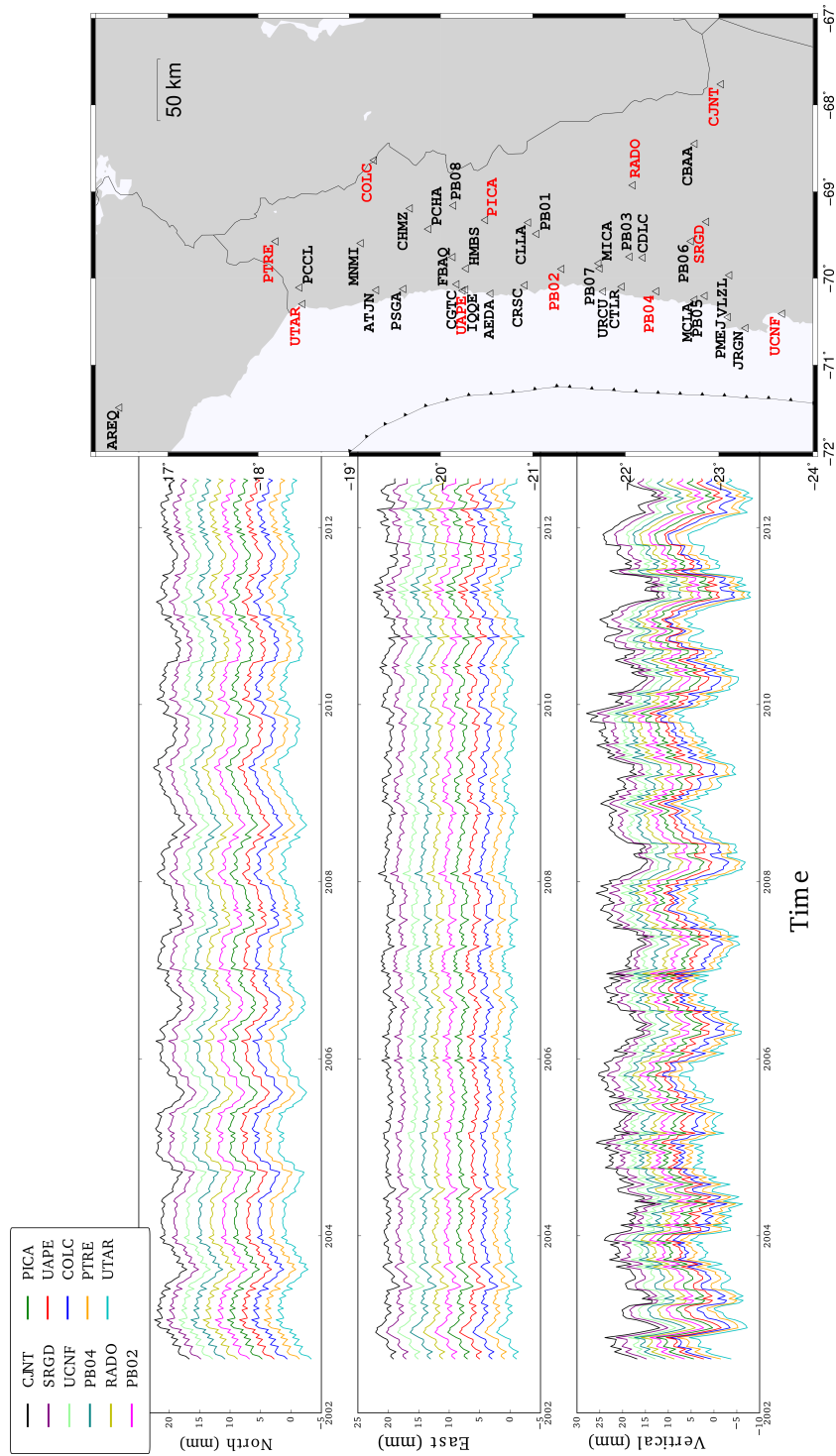


Figure 3.4: Hydrological signals (north, east and vertical components) for 11 GPS stations highlighted in red from the complete North Chile GPS network. Almost the same hydrological pattern is observed for stations separated by more than 600 km.

Station	2000 (366)	2001 (365)	2002 (365)	2003 (365)	2004 (366)	2005 (365)	2006 (365)	2007 (365)	2008 (366)	2009 (365)	2010 (365)	2011 (365)	2012 (366)	2013 (365)	2014 (365)	2015 (318)
AREQ	99	94	54	95	95	100	74	99	100	98	100	99	99	100	100	99
IQQE	0	0	40	60	55	99	11	0	51	98	95	100	100	99	100	85
CJNT	0	0	0	0	0	17	100	100	100	81	97	45	24	50	35	14
CBAA	0	0	0	0	0	0	25	18	100	100	100	100	100	83	99	29
COLC	0	0	0	0	0	0	0	15	26	100	92	22	99	100	99	54
RADO	0	0	0	0	0	0	0	7	100	100	75	100	98	92	80	70
PB08	0	0	0	0	0	0	0	0	0	17	70	21	86	44	86	0
CHMZ	0	0	0	0	0	0	0	46	100	100	100	89	23	91	91	0
SRGD	0	0	0	0	0	0	13	99	100	100	100	100	100	83	99	29
CLLA	0	0	0	0	0	0	0	0	0	0	100	0	72	83	61	15
PCHA	0	0	0	0	0	47	100	100	93	0	54	100	100	81	62	0
PB01	0	0	0	0	0	0	0	10	100	90	78	90	99	51	91	0
PB06	0	0	0	0	0	0	0	0	0	10	77	98	51	66	81	0
PTRE	0	0	0	0	0	19	100	100	100	100	66	100	42	56	29	0
MNMI	0	0	0	0	0	0	0	37	66	98	92	95	100	100	23	83
CDLC	0	0	0	0	0	0	24	17	100	100	98	100	99	78	52	24
MICA	0	0	0	0	0	0	0	0	92	100	89	90	22	0	0	0
VLZL	0	0	0	0	0	0	26	99	99	84	88	55	98	83	96	0
CGTC	0	0	0	0	0	0	0	0	0	0	100	0	33	98	99	0
CRSC	0	0	0	0	0	14	100	100	100	100	100	100	100	100	88	51
CTLR	0	0	0	0	0	0	0	47	100	100	100	100	39	73	26	0
PCCL	0	0	0	0	0	20	100	100	100	100	100	66	78	100	98	0
PSGA	0	0	0	0	0	0	0	73	81	100	89	100	100	100	100	83
ATJN	0	0	0	0	0	18	100	100	100	100	100	100	100	100	99	0
UAPF	88	89	93	91	79	61	100	98	100	100	100	99	99	75	93	46
PB04	0	0	0	0	0	0	0	10	78	95	89	100	95	96	100	0
MCLA	0	0	0	0	0	16	100	100	100	100	100	99	100	83	99	24
UTAR	0	0	0	7	98	100	90	64	91	12	100	87	100	100	100	74
UCNF	0	0	0	0	0	67	0	0	92	73	98	100	100	73	99	47
PMEJ	0	0	0	6	98	99	76	74	94	100	100	100	99	100	100	49
JRGN	0	0	0	0	0	16	100	100	100	100	93	98	100	82	99	23
FBAQ	0	0	0	19	34	73	76	26	6	0	0	0	8	6	62	17
AEDA	0	0	0	6	62	60	91	91	92	0	0	0	7	100	99	72
PB03	0	0	0	0	0	0	0	10	72	0	0	28	90	64	100	0
PB07	0	0	0	0	0	0	0	0	0	16	16	66	99	96	77	0
PB02	0	0	0	0	0	0	0	10	99	76	0	11	98	96	98	0
PB05	0	0	0	0	0	0	0	10	72	74	0	26	91	96	100	0
HMBS	0	0	0	0	0	0	0	55	67	100	33	74	0	0	0	68
URCU	0	0	0	0	0	0	0	8	84	0	0	0	0	0	0	0
PICA	90	13	46	40	51	66	81	55	0	10	100	100	100	63	98	22

Table 3.1: Percentage of registered days per year for 40 GPS sites with available hydrological data. This value is calculated respect to the total number of days per year which is shown next to each year.

each one of the 40 stations. The velocities have been calculated during a stable part of the interseismic period before Iquique earthquake. This time window varies in duration depending on the events affecting the station (up to 5 years). Special attention was given to the reported changes of material (antenna and receiver) for every station producing offsets in the data. It is clear that the component showing more important differences is the vertical. Unlike horizontal components, the amplitude of this component is comparable with the amplitude showed by seasonal variations. The correction then becomes fundamental if we want to include this component in our analysis.

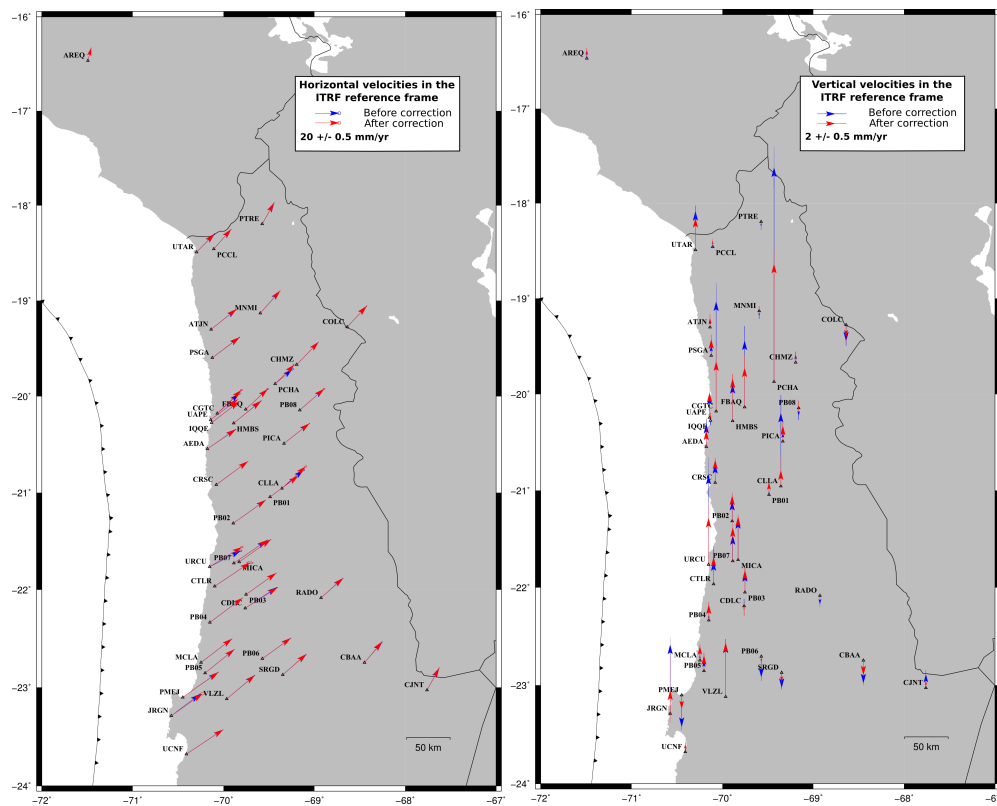


Figure 3.5: Horizontal (left) and vertical (right) velocities for the interseismic period before Iquique earthquake 2014. The figure shows the difference between velocities calculated before (blue) and after (red) the hydrological correction. The error is shown as 95% confidence ellipses. All velocities are calculated in the ITRF terrestrial reference frame.

3.2.4 GPS time series correction

Before eliminating hydrological variations to obtain reliable time series, it is necessary to correct tectonic and instrumental offsets perturbing the expected linear trend of the positions. In this region, large earthquakes might affect the stations during the period where hydrological data is available (2002/08/11 - 2012/07/20). Apart from Tarapaca 2005, these include Tocopilla 2007 M_w 7.7 (2007/11/14), Maule 2010 M_w 8.8 (2010/02/27) and a local earthquake of M_w 6.4 occurred in 2009 (2009/11/10). In addition to this, 4 of the 5 stations (AEDA, UAPE, IQQE, FBAQ and PICA) contain several data offsets related with documented antenna and receiver changes. The figure 3.6 shows the very raw time series of these 4 stations.

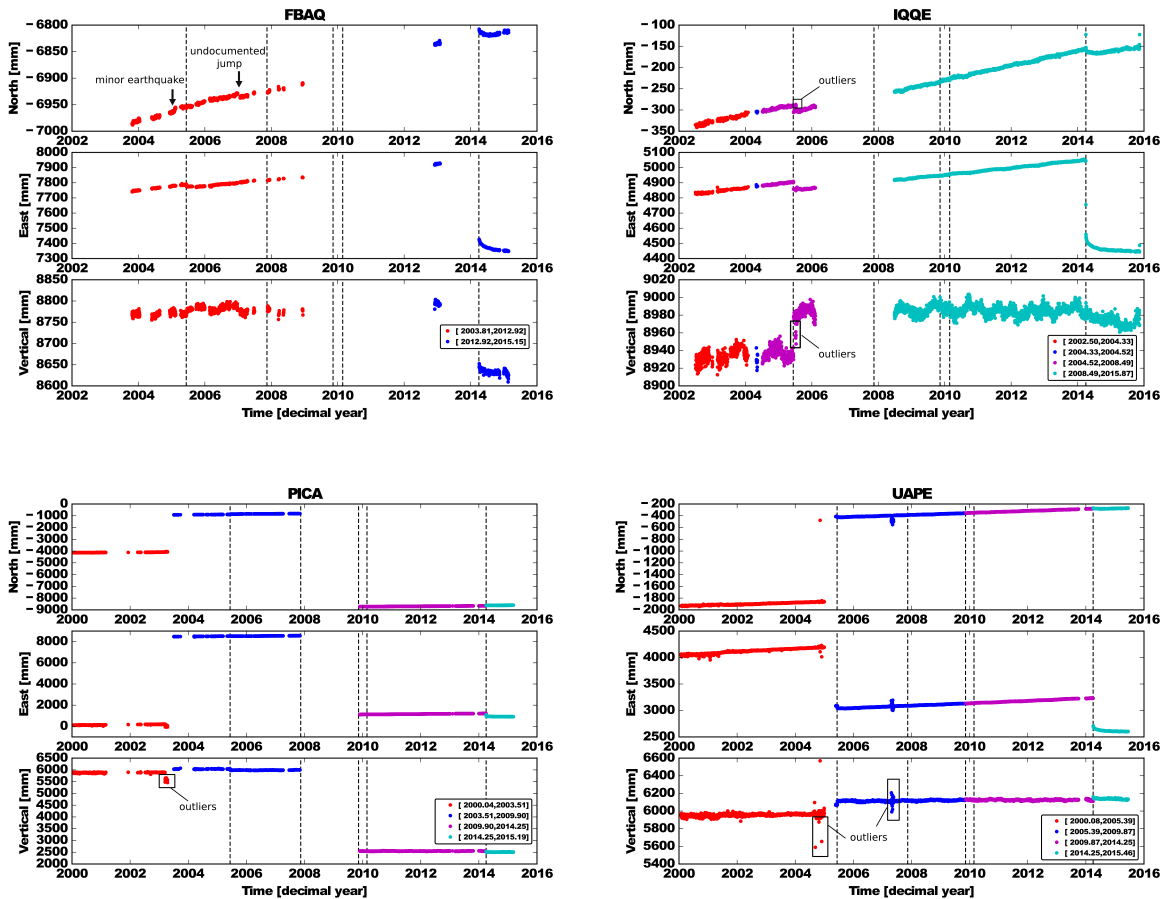


Figure 3.6: Instrument changes affecting 4 of the 5 studied stations are shown in different colors for different periods. Earthquakes that could have been detected by the stations occurred in the dates: 2005.44 (Tarapaca), 2007.87, 2009.86, 2010.16 and 2014.24. These events are marked with dashed vertical black lines. Outliers and offsets in the data are shown as example for some stations.

In the figure, equipment changes that may or may not have induced jumps in the time series are indicated as color changes. Seismic events are represented by dashed vertical lines, and outliers positions (enclosed in rectangles for some components as an example) together with some particular characteristics for the station FBAQ are written specifically in each case. Every time a jump is detected and attributed to instrumental change, we do a very simple correction: an offset is calculated between the continuous records, by shifting the difference at the time of the jump between linear fits of the data before and after it. Thus, a very large data gap between 2 different periods as well as too short data periods can lead to unsuitable results and it is necessary to keep this in mind for velocity calculation.

Finally, resulting time series have been corrected by hydrological terms described in section 3.2.3 and estimated with respect to a stable South American plate. Velocity for this plate at (70° S, 20° S), by using the SOAM ITRF 2000 rotation pole (-21.457, -134.631, 0.113), is -2.6 mm/yr and 10.6 mm/yr in the east and north directions. After the corrections described above, time series still contain several gaps that increase the inaccuracy of velocity calculation, specially for the pre-Tarapaca period. In order to correct this, we first eliminated high frequency noise of the signals re-sampling all time series to 1 position every 10 days. Due to the proximity of IQQE and UAPE sites (see figure 3.6), we decided to combine both stations in one. The resulting merged station (UAIQ), characterized for containing no data gaps, can be seen in figure 3.7 together with the rest of the stations sampled every 10 days. The remaining 3 stations still contain data gaps.

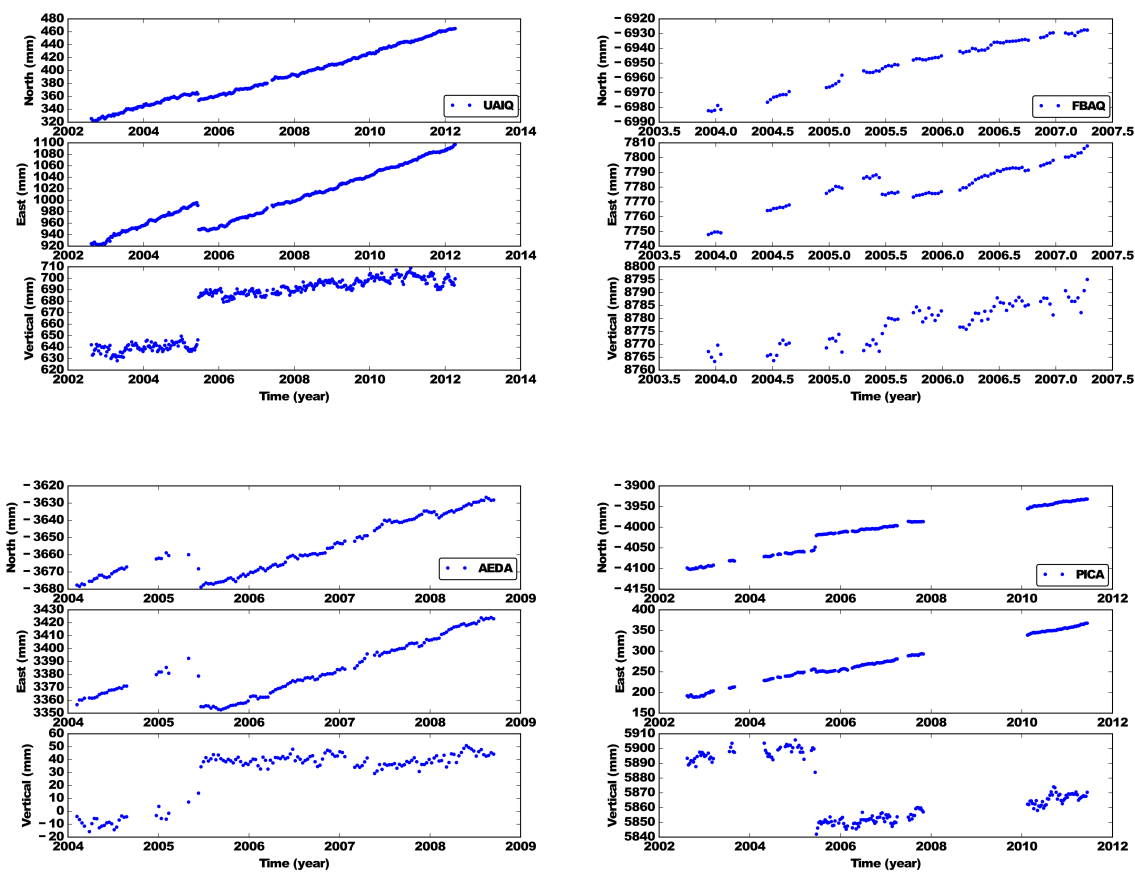


Figure 3.7: New combined site UAIQ and the rest of time series sampled every 10 days. Positions are corrected for hydrological signals.

We need to obtain the most accurate pre- and post-Tarapaca trends to determine the post-seismic signal produced by the earthquake. Therefore, it is fundamental to increase the trend stability before Tarapaca for these sites. Appealing to the proximity of the stations and the presence of common mode, we subtract UAIQ signal from all other time series already detrended using the pre-Tarapaca velocity found at UAIQ. Then, the new pre-Tarapaca trend for the stations FBAQ, AEDA and PICA corresponds to the trend calculated for these time series plus the pre-Tarapaca trend at UAIQ. Resulting signals with pre-Tarapaca trend eliminated (postseismic signal only due to the earthquake) are shown in figure 3.9 in the results section.

3.2.5 Velocity error estimation and the concepts of white and colored noise

As it was discussed briefly in chapter 2, the GPS noise spectrum is very wide. Mismodeled phenomena like atmospheric perturbation, satellite orbits and antenna phase center as well as reference frame issues, multipath effects, mismodeling of the hydrological loading and instrumental performance, are sources of error affecting the calculated positions at different time scales. Thus, it is important to categorize the noise in order to know how to reduce it when it is possible and to estimate uncertainties accurately. A useful distinction is the contrast between noise which maintains the same characteristics in time (white) and noise that is time-correlated (colored).

Certainly for GPS time series, the standard error of its rate calculated by linear regression is underestimated. The latest because this basic calculation assumes that every individual position is not related with each other as it is common in several other geophysical data. In this case, daily positions are affected by *white noise* which varies randomly in time. The correct assumption for geodetic measurements is that there is a combination between white and time correlated or *colored noise*. For simplicity, mostly only two types of colored noise are commonly modeled as sources of error in the deformation rate calculation: random walk and flicker noise (Hackl *et al.* [2011]). The first is related to the drift of the geodetic monument, which induces noise with characteristics of a random walk process and can be an important source of error (Johnson & Agnew [1995]). Flicker noise on the other hand, is related to electronic devices involved in the measuring process, as indicated by several studies (Zhang *et al.* [1997]; Mao *et al.* [1999]) and is a predominant signal in GPS time series. Mao *et al.* [1999] studied the noise spectra using 3 years long daily position time series of 23 globally distributed GPS sites. Applying spectral analysis and Maximum Likelihood Estimation (MLE) they found a combination of white and flicker noise to best fit the data. Based on this model, they argue that GPS time series velocity calculations based on a pure white noise model are underestimated by an average factor varying between 5 and 11, depending on the location and component of the station.

In order to obtain a maximum value for the velocity uncertainty range, in this work we use Mao *et al.* [1999] approximation, adapted to our case. Underestimation factor are calculated using average noise amplitude values obtained for their closer station to our study area (SANT) and a 2 years time span, resulting in factors of (5, 5, 6) for north, east and vertical components. In the case of our time series, corrected for hydrological variations (see section 3.2.3), re-sampled

and combined as it is described in section 3.2.4, velocity uncertainties might range somewhere in between the standard error (only due to white noise) and a maximum value, product of the amplification of this lower uncertainty limit by the calculated factors. From now on, we assign this higher limit to our uncertainties. However, it is important to think about this value as a maximum, and not as a definitive velocity uncertainty.

3.3 Results: Long term velocity change detected by geodetic instruments

Out of our 40 GPS sites (see figure 3.4), 8 recorded enough data before 2005 (see table 3.1). 5 of these 8 stations (AEDA, UAPE, IQQE, FBAQ and PICA), all of them located around latitude 20.5° S, show an apparent decrease on the horizontal velocity of several millimeters after this date (see figure B.1, annexe B). The change coincides with the occurrence of the intermediate-depth earthquake M_w 7.7 which occurred in the region of Tarapaca (see 3.2). This velocity decrease, calculated from our final time series (figure 3.7) product of the improvement method detailed in 3.2.4, is represented in figure 3.8.

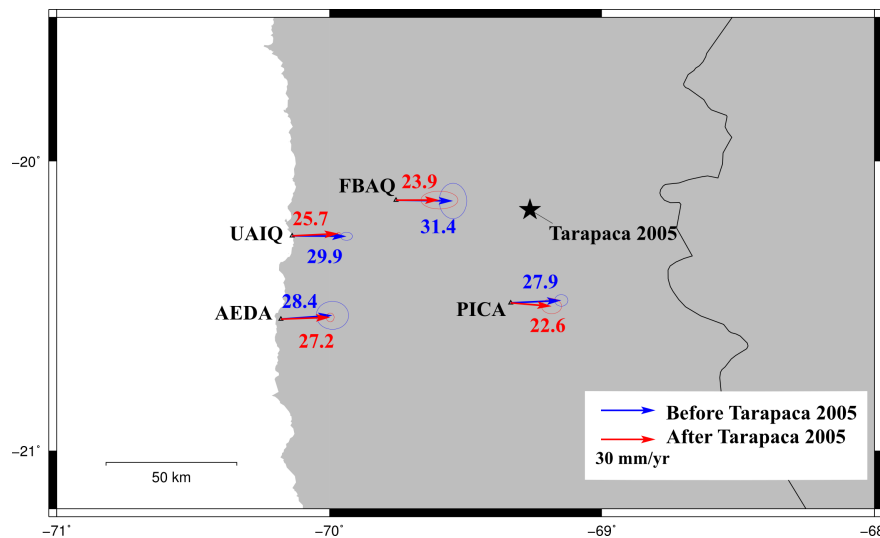


Figure 3.8: 3 real cGPS sites and one merged from 2 coastal stations (UAIQ) showing velocities (in mm/yr) pre- (blue) and post- (red) Tarapaca 2005 earthquake. Velocities are expressed in a stable South American plate and error ellipses correspond to 95 % confidence considering white and flicker noise. The velocity decrease is a constant for all stations.

The chosen time window for velocity calculation varies depending on the site. In the case of FBAQ the time window before the event is interrupted several months before Tarapaca earthquake by a jump, specially large on the north component. This offset, apparently not related with a seismic event, nor to a registered instrument change, leaves isolated from the rest of data some few datapoints right before the earthquake, which are impossible to correct and thus will be ignored hereafter. In addition, a not documented jump has been identified and corrected at this station around 2007 (see figure 3.6), leaving few isolated and incongruent points after this date, which lead us to eliminate as well all positions after this date. Similarly, the selection of only a part of the corrected data after Tarapaca earthquake for PICA is related to the unsuccessful correction of the post Tarapaca offset. This inaccurate offset correction is probably due to Tocopilla 2007 earthquake occurring in the middle of a data gap. Other time series anomalies identified as artifacts that were not successfully eliminated, have not been considered in velocity calculation. An example of this are: the signal at the end of 2007 of unknown origin observed in the north component of almost all stations, and the apparent strong northern displacement that shows the combined site UAIQ (acquired from UAPE and IQQE) starting from February 2010. Additionally, four months after Tarapaca earthquake have been excluded on velocity calculation for all stations to eliminate the initial short-term non-linear change on the deformation following the earthquake. Thus, the obtained time series postseismic velocity is shown in figure 3.9. Additional statistic information related with velocity determination is summarized in table B.1 from annexe B.

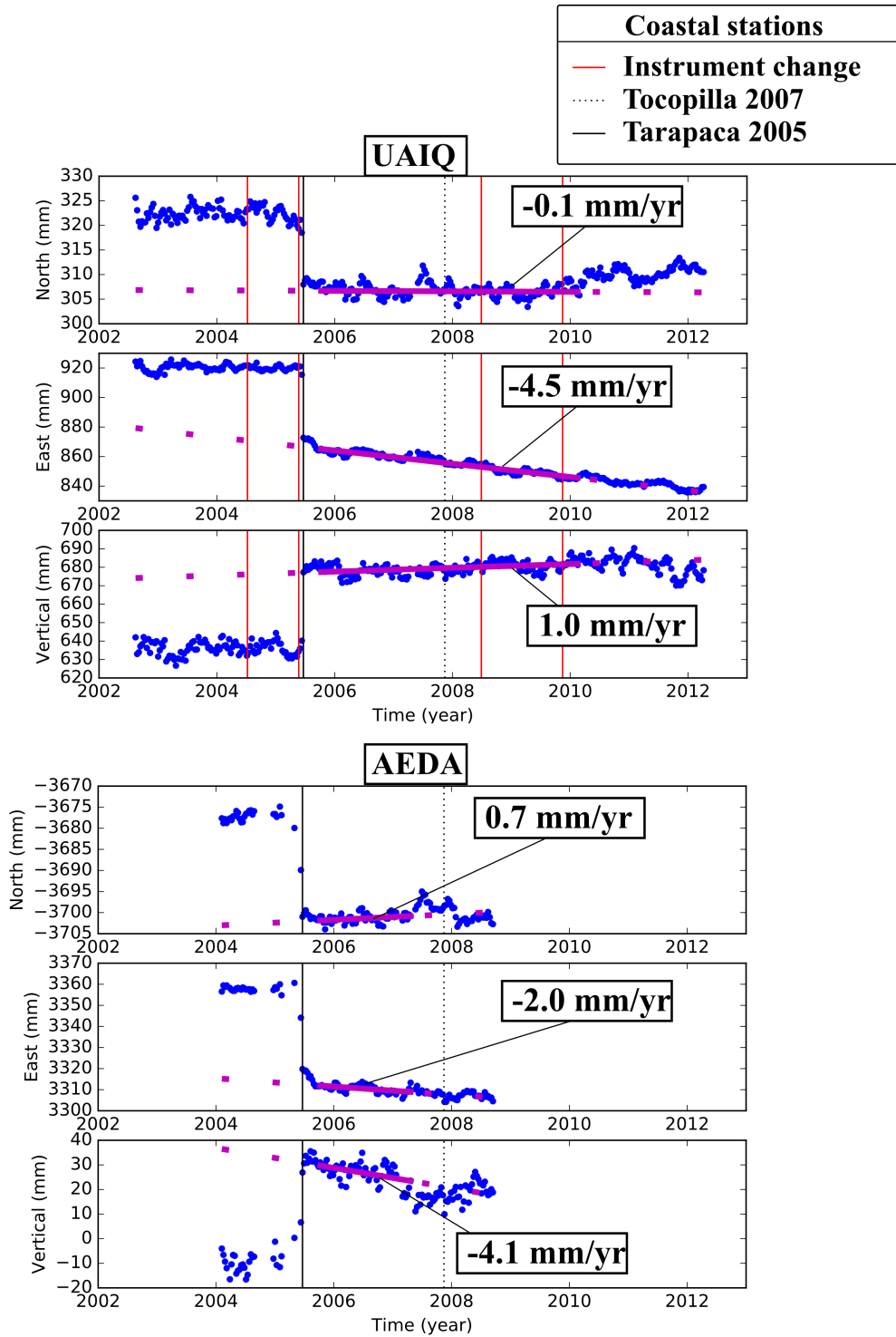


Figure 3.9: Observed postseismic signal (blue circles) and postseismic velocities (purple line) for combined and rest of the stations. Values for postseismic velocities are indicated for each station and component. Other parameters as specific times when velocities were measured, errors and standard deviation (σ) for calculation periods are detailed in table B.1 in Annexe B. Unfilled blue dots represent data not included in velocity calculations.

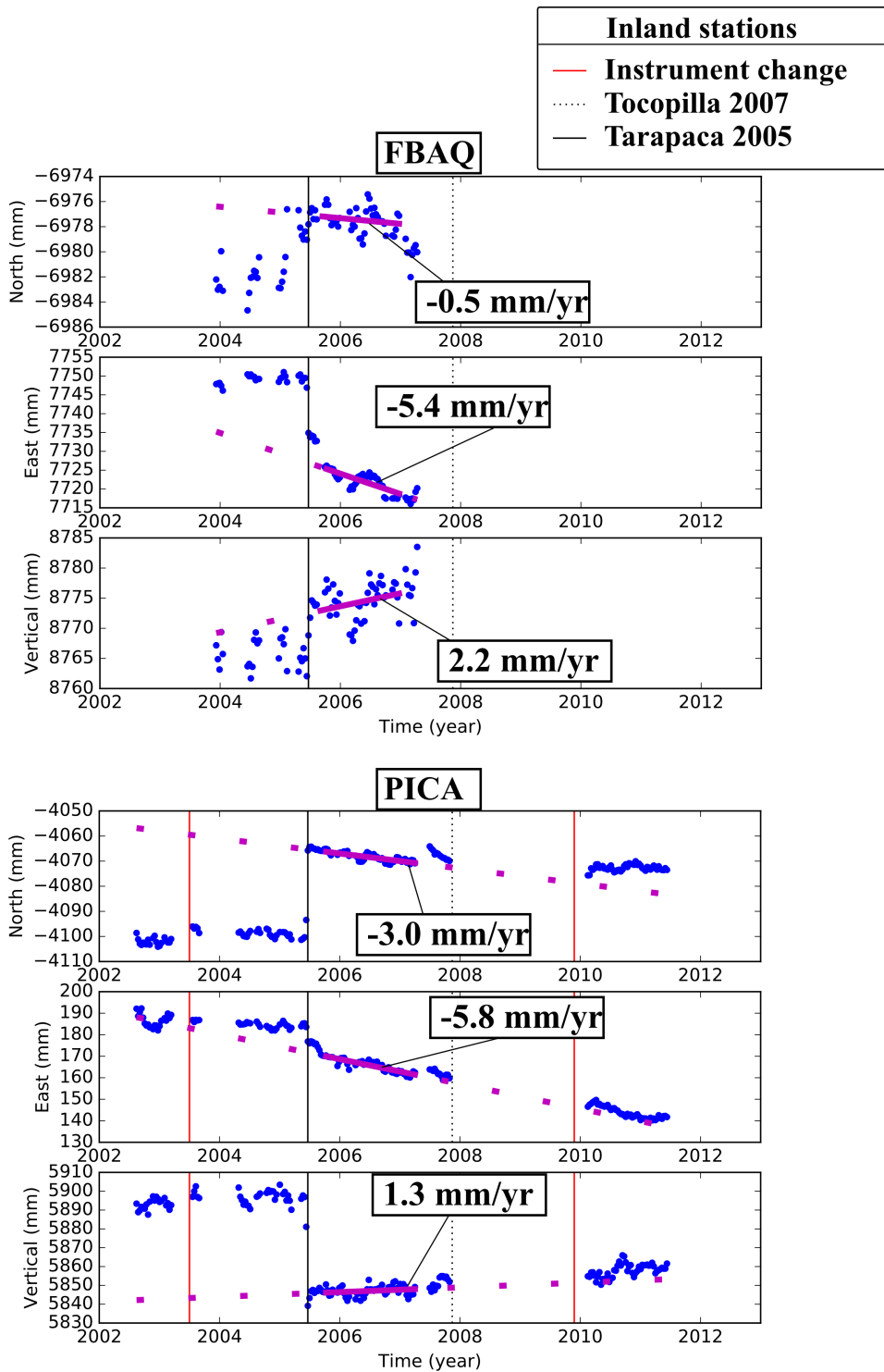


Figure 3.9: (Continued.) Observed postseismic signal of 2 inland stations.

3.4 Possible phenomena explaining the velocity change observed

In the following we will analyze the signal associated to the intermediate depth Tarapaca 2005 earthquake recorded by GPS instruments located in its vicinity. Only GPS stations which have acquired data before 2005 are considered. Postseismic displacements associated to Tarapaca 2005 correspond to observed displacements after the mainshock once the interseismic velocity before the earthquake is subtracted. It is important to make clear at this point that the use of the term interseismic velocity here refers to the characteristic velocity calculated at the end of the interseismic period, and this can differ with the interseismic trend calculated for a longer period.

Because the accuracy of this trend, and then the accuracy of the postseismic deformation, depends strongly on the stability of the period previous the earthquake, the final signals obtained in section (3.2.4) are the best possible time series we can obtain from the available data, and then they will be used in all subsequent calculations.

Three phenomena are considered as possible explanations for this postseismic signal detected as a long term change on the velocity trend: afterslip on Tarapaca fault plane, slow slip on the subduction fault plane and/or viscoelastic relaxation of the asthenosphere after Tarapaca earthquake. The first scenario, yields a simple correlation between the postseismic signal and the coseismic signal. The second scenario implies that the postseismic signal would look like slip on a fault plane located in the seismogenic zone. Thus, the post-seismic pattern would be in agreement with the coseismic signal produced by a subduction earthquake. Assuming a linear longterm postseismic velocity calculated from our new improved time series (see figure 3.9), a contrast between these 2 scenarios and the postseismic displacement observed after 2 years is shown in the figure 3.10. Left part of the figure representing the case of afterslip on Tarapaca fault plane, shows the observed coseismic signal (in red) and the postseismic signal (2 years) (in blue) from Tarapaca 2005 earthquake. Afterslip on Tarapaca fault then, will be perceived as a west-upward movement for all the stations except for PICA, the eastern station and the closest to the event. At this station the displacement corresponds to a vector pointing to the rupture. Post-seismic displacements on the contrary are all directed away from the earthquake. Also FBAQ post-seismic is much larger than its coseismic, an indicator than the postseismic deformation is not of the same origin than the coseismic deformation. Scenario 1 seems invalidated. The

second scenario (figure 3.10, right), represents the pattern expected for slow slip taking place in the seismogenic zone, mimicked by the actual Iquique 2014 coseismic slip observed at 3 extra stations included here because of their stability and alignment at a similar latitude. What we see is an obvious and progressive decrease in the magnitude of the displacement which is not present in the postseismic pattern observed after Tarapaca 2005, because inland points have a larger motion than coastal points. In spite of these observations, it is not possible to completely discard scenarios 1 and 2 because of the simplicity of the analysis and the uncertainties in velocity calculation. However, these results give preliminary information supporting the relevance on evaluating the third scenario proposed, which requires the use of a viscoelastic finite element model.

In the following, a two-dimensional viscoelastic finite element model reproducing the intermediate depth earthquake of Tarapaca 2005 is described. Then, because its results are in agreement with the postseismic signal observed, this 2D approach will be the starting point of a three-dimensional model with realistic geometry according the north part of the Chilean subduction zone.

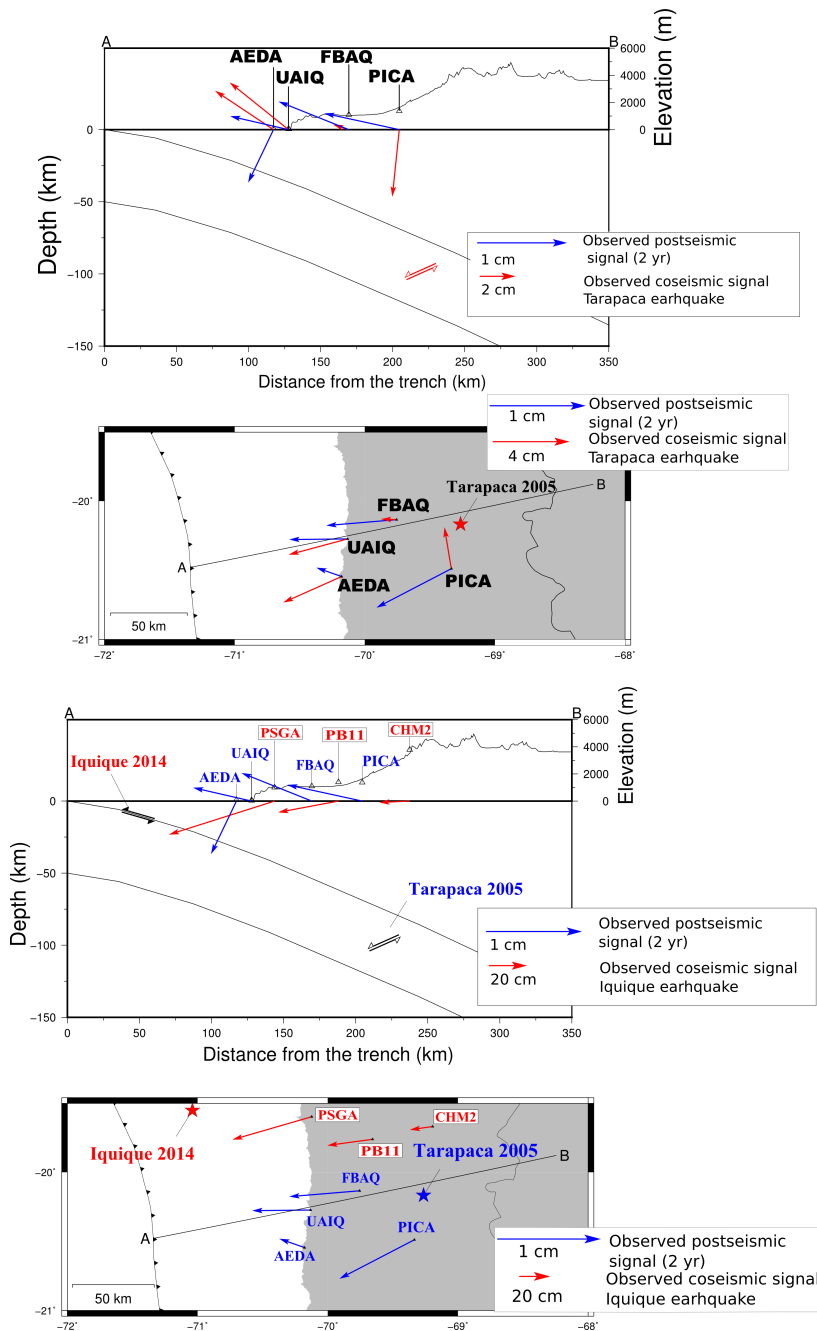


Figure 3.10: 4 GPS stations showing a comparison between postseismic displacements from Tarapaca earthquake after 2 years and coseismic displacements from different types of earthquakes. All vectors are shown in plain (bottom) and cross-section A-B (top) views. Top: Postseismic (blue) and coseismic displacements (red) from the intermediate depth earthquake of Tarapaca 2005. Bottom: Postseismic from Tarapaca 2005 (blue) and coseismic displacements corresponding to the subduction Iquique 2014 earthquake (red) for 3 extra stations (PSGA, PB11, CHMZ) aligned at similar latitude. Ellipse errors are not included in order to simplify the scheme.

3.5 Two-dimensional viscoelastic finite-element model of an intermediate-depth earthquake

3.5.1 Description of the model

We have chosen the finite element software Z-set/ZéBuLoN (<http://www.zset-software.com/products/zebulon/>) created for École des Mines de Paris in collaboration with ONERA (French aerospace laboratory), a toolkit composed by several integrated modules including a finite element solver and an advanced material representation program, to create a two-dimensional viscoelastic model that reproduces the intermediate-depth earthquake of Tarapaca M_w 7.7 occurred in 2005.

The geometry of our 2D model is represented in the figure 3.11. It is composed by an overriding and subducted plate of 70 km and 50 km thickness respectively (thermal thickness), the latest extending down to a 500 km depth in the mantle. These values are appropriate for the northern part of the Chilean subduction zone (Sodoudi *et al.* [2011]). The limits of the box are chosen large enough to avoid any deformation on the boundaries and all the domain has been discretized to 6-nodes 2D triangular linear elements. The upper limit is controlled by a counteracting vertical force given by $F_z = -\rho g U_z$, where ρ is the density, g is the gravity and U_z represents any vertical displacement on the surface. This force is imposed to simulate the gravity response to any vertical displacement. The rest of boundaries are imposed to zero velocity. In this manner, we define a model that does not include tectonic plate motion (see Trubienko *et al.* [2013]).

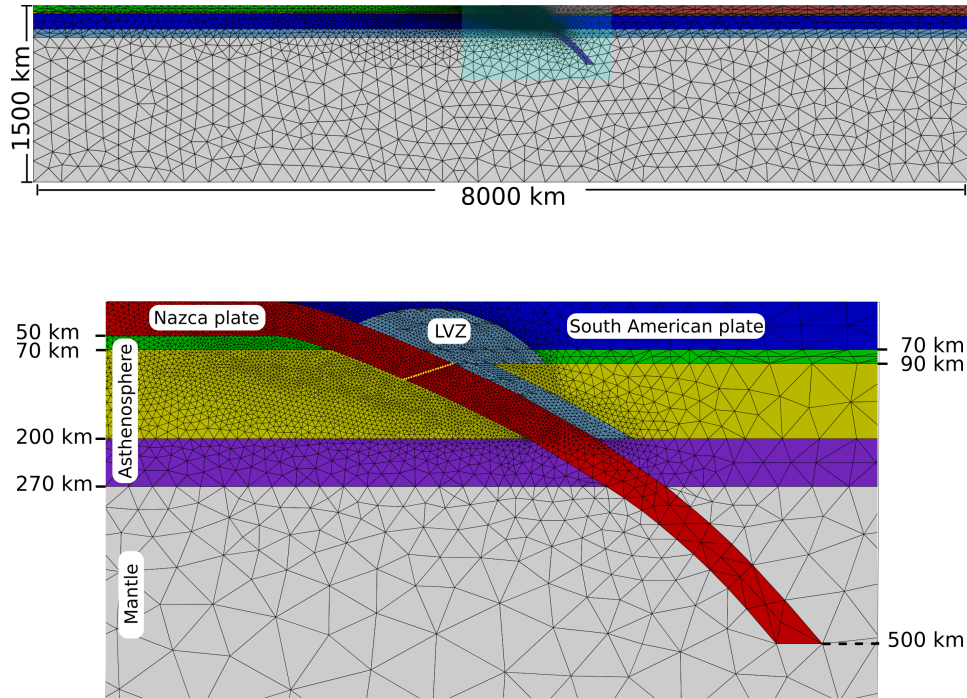


Figure 3.11: Top: Complete grid discretized by triangular elements for our two-dimensional viscoelastic finite element model. Large dimensions are intended to avoid border effects. Bottom: Zoom showing details of the geometry of the modeled subduction zone. Only asthenosphere and the low viscosity zone (LVZ) are modeled with viscoelastic behavior, the rest are considered as elastic bodies. The fault is indicated as a yellow dotted line into the slab. Colors vary respect to the figure on top but the unities are exactly the same.

In the zoomed part of the figure we see clearly Nazca and South American plates above an asthenosphere confined between 2 transition zones 20 and 70 km thick which permit to vary the thickness of the lithosphere. The top of the slab has been drawn by using the one provided for USGS at 20.5° S in its 1.0 version. In addition, the figure shows the deep mantle (> 270 km), and a zone of an approximate area of 140 km width times 50 km in order to simulate, if necessary, a plausible mantle wedge underlying the hot volcanic arc, often associated to a weak behavior (van Keken [2003]). The model includes a long subduction channel of approximately 28 km width which reaches a depth of 200 km as another weak zone, following the results of Klein *et al.* [2016] for a southern part of the Chilean subduction zone. Thus, wedge and channel are labeled in the figure as a whole low viscosity zone (LVZ) and sub-divided in more than 30 elements allowing us to model different shapes and viscosity heterogeneities on it. Each area in the model is associated to a material depending on the case of study. Both plates and deep mantle are always modeled as linear elastic bodies, in contrast with the asthenosphere

considered as viscoelastic. The LVZ, when not considered as part of the overriding plate or continental asthenosphere for the simplest configurations, is modeled as a viscoelastic body with low viscosity. Shear (G) and bulk (K) moduli describing elastic behavior, increase with depth for the whole model according to PREM. Moho discontinuity has been fixed at 30 km depth and maintained constant for the whole model. Elastic parameters for viscoelastic materials are identical to those of elastic materials (see table 3.2). The mesh has been refined nearby the Tarapaca fault plane (nodes highlighted in yellow) and in the zones where we want to measure displacements. Far from these areas of interest the mesh is less refined in order to reduce the calculation time.

The rupture of the earthquake, a normal fault at 100 km depth dipping to the west and 37 km width (Peyrat *et al.* [2006]; Delouis & Legrand [2007]), is initiated as a given instantaneous and uniform slip following the method proposed by Melosh & Raefsky [1981] which duplicates the nodes in the fault plane. Thus, the coseismic slip on Tarapaca fault is kinematically generated as a relative displacement of 6.5 m tangential to the interface, as Peyrat *et al.* [2006] indicated as the average slip for Tarapaca 2005. This “single-event model” used in this work does not include the steady subduction effect, and only aims to represent the postseismic crustal deformation associated exclusively to Tarapaca 2005 in a decadal timescale. Ignoring the steady, long time-scale deformation when studying the shorter time-scale deformation linked to the seismic cycle is sound as long as the rheologies are linear (Maxwell or Burger viscoelasticity but no power-law creep) (see Trubienko *et al.* [2013] for more details).

Depth [km]	G [Pa]	K [Pa]
-3.00×10^3	2.94×10^{11}	6.56×10^{11}
-2.89×10^3	2.94×10^{11}	6.56×10^{11}
-1.25×10^3	1.93×10^{11}	3.73×10^{11}
-6.71×10^2	1.55×10^{11}	3.00×10^{11}
-6.60×10^2	1.25×10^{11}	2.42×10^{11}
-4.06×10^2	9.06×10^{10}	1.76×10^{11}
-4.01×10^2	8.24×10^{10}	1.60×10^{11}
-2.21×10^2	6.56×10^{10}	1.27×10^{11}
-60	68×10^9	130×10^9
-30	68×10^9	130×10^9
-30	26×10^9	52×10^9
10	26×10^9	52×10^9

Table 3.2: Depth dependence of elastic moduli (G (shear) and K (bulk)) used for elastic and viscoelastic materials. These parameters increase with depth according to PREM with a modified crust on continents.

3.5.2 Viscoelastic mantle rheology

The term rheology, referred to a particular material, can be defined as its characteristic mode to relate stress and strain by constitutive equations. Each rock, depending on its location in the Earth, will respond to stress most commonly following a linear-elastic, viscous or brittle deformation. The rheology of viscoelastic materials can be phenomenologically represented as a combination of elements as springs (linear-elastic) and dashpots (linear-viscous), resulting for instance in simple viscoelastic rheologies, as the Maxwell and Kelvin-Voigt bodies (see figure 3.12). The difference between these 2 rheological models relies on the steady state response of the former and the transient nature of the latest. Because these 2 states characterize strain at high temperatures (Yuen *et al.* [1986]), a combination of both elements is often invoked as a more realistic approximation of mantle rheology: the viscoelastic Burgers body.

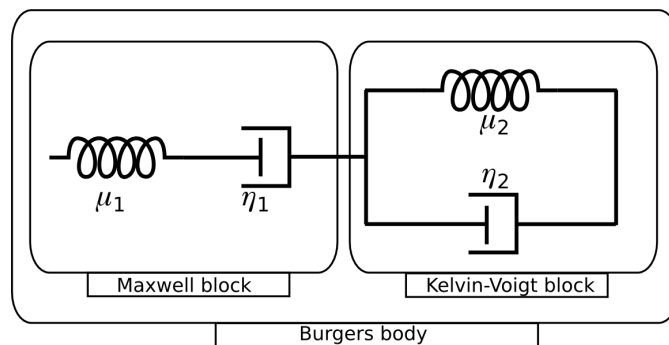


Figure 3.12: Springs and dashpots represent elastic and viscous material properties respectively. Subscripts 1,2 in shear modulus (μ) and viscosity (η) correspond to Maxwell and Kelvin-Voigt bodies. Both connected in series define the viscoelastic Burgers rheology.

The deformation of a Maxwell body as a response to a given stress, is governed by an equation where strains (of each element) are additive, resulting in the following equation:

$$\dot{\epsilon} = \frac{\dot{\sigma}}{2\mu_1} + \frac{\sigma}{2\eta_1}$$

Where ϵ is the shear strain, σ is the stress and μ_1 and η_1 are the shear modulus and viscosity respectively. This type of material which evolves from an instantaneous elastic response to a fluid behavior, responds to stress with an exponential relaxation with a characteristic time of

$$\tau = \frac{\eta_1}{\mu_1}.$$

In a Kelvin-Voigt material the additive quantities are the stresses, giving as a result the following constitutive equation:

$$\sigma = 2\dot{\epsilon}\eta_2 + 2\epsilon\mu_2$$

Where the transient creep will be characterized by one relaxation time dependent of short-term rigidity and viscosity ($\tau = \frac{\eta_2}{\mu_2}$).

The bi-viscous Burgers body (only one Kelvin-Voigt element), as a combination of both rheologies described above, deforms following the equation (Bürgmann & Dresen [2008]):

$$\eta_2\ddot{\epsilon} + \mu_2\dot{\epsilon} = \frac{\eta_2}{\mu_1}\ddot{\sigma} + \left(1 + \frac{\mu_2}{\mu_1} + \frac{\eta_2}{\eta_1}\right)\dot{\sigma} + \frac{\mu_2}{\eta_1}\sigma$$

Where subscripts (1, 2) indicate Maxwell and Kelvin parameters respectively and $\dot{\epsilon}$ corresponds to the engineering shear strain (twice the shear strain rate).

A Burgers body has more than one relaxation time ($\tau_{i=1,2} = \frac{\eta_i}{\mu_i}$), being more accurate to describe a non-homogeneous material.

This rheology is characterized in first place by an instantaneous elastic response (elastic component Maxwell) followed by a phase of transient creep (Ivins & Sammis [1996]) represented by a Kelvin-Voigt element, to finally present a long-term viscous behavior (viscous component Maxwell) with constant strain rate. Its long-term creep-rate relaxation time is proportional to the inverse of the steady-state viscosity μ_1 . In general, a typical steady-state viscosity in the asthenosphere deduced from the postseismic response after large earthquakes is of the order of 10^{18-19} (Pa s) (Hu *et al.* [2004]; Klein *et al.* [2016]; Wang *et al.* [2012]), much lower than 10^{20} (Pa s) which represents the typical global average viscosity of the upper mantle. Note that these low viscosities permit to explain the observed large postseismic velocity in the far-field at distances of more than 1000 km from the subduction. They are therefore a general characteristic of the asthenosphere, at least in non-cratonic areas. They are not a particular feature of the mantle wedge.

3.6 Results: 2D-model sensitivity to geometrical and rheological parameters

We used the 2D model described in 3.5.1 to study the postseismic surface deformation associated to Tarapaca 2005 earthquake, including the relaxation of a viscoelastic asthenosphere. The curves shown on figure 3.13 (top) correspond to the postseismic deformation produced at ~ 120 and 200 km from the trench in a time lapse of 10 years after the earthquake. Postseismic signal was obtained using the more basic configuration of the model (bottom part, figure 3.13) including oceanic and continental plates, deep mantle and an asthenosphere with 3 different viscoelastic rheologies:

1. Maxwell ($\eta_M = 3 \times 10^{19}(\text{Pa} \cdot \text{s})$)
2. Maxwell ($\eta_M = 3 \times 10^{18}(\text{Pa} \cdot \text{s})$)
3. Burgers ($\eta_M = 4.8 \times 10^{18}(\text{Pa} \cdot \text{s}); \eta_K = 1 \times 10^{17}(\text{Pa} \cdot \text{s}); \mu_K/\mu_M = 3.9$)

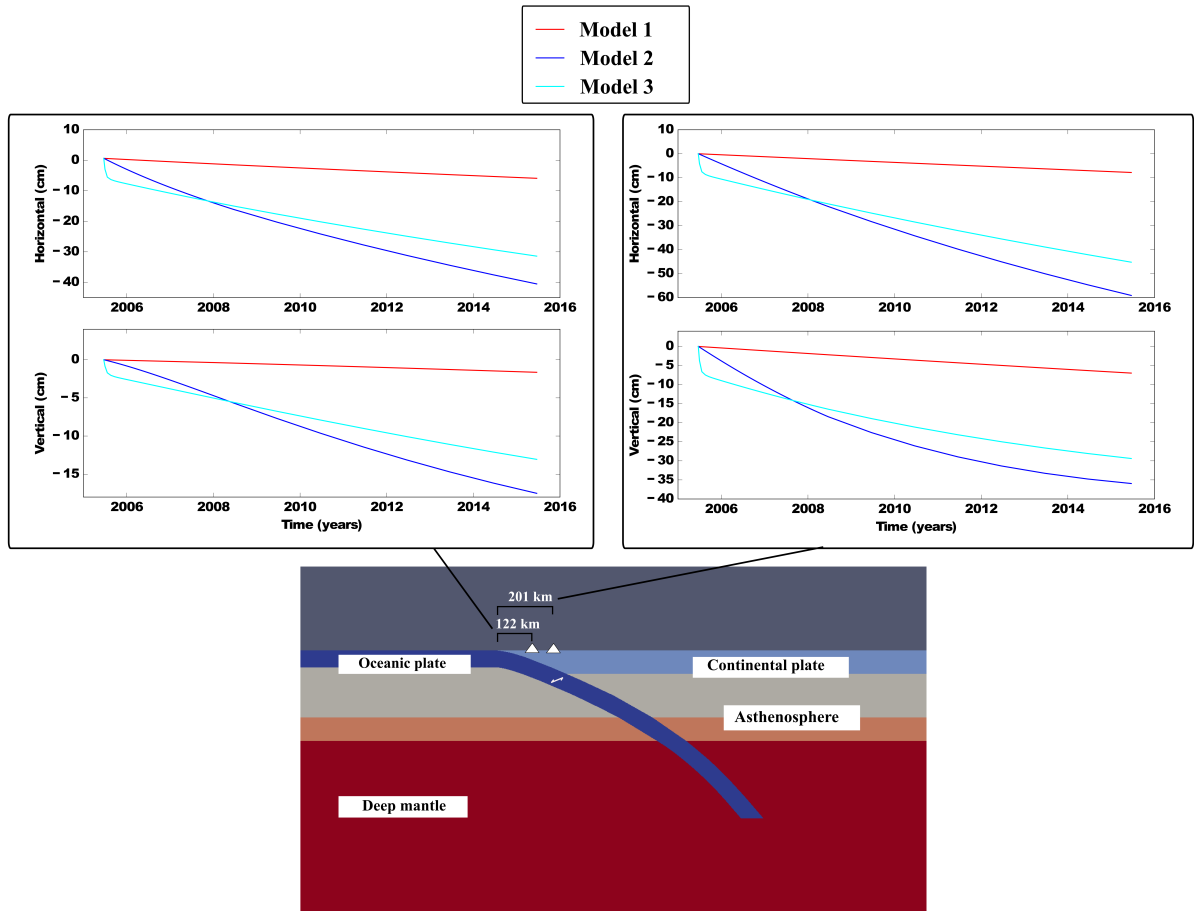


Figure 3.13: Top: Postseismic deformation curves for 2 inland locations at approximately 120 and 200 km from the trench. Each curve represents a different viscoelastic rheology of the asthenosphere (see text for model parameters). Bottom: Basic model used to obtain the postseismic deformation shown on top. It consists on oceanic and continental crusts, deep mantle and asthenosphere. Only the latest is modeled as a viscoelastic body. For this model, the transition zone between deep mantle and shallower mantle is considered as part of the asthenosphere.

The first 2 cases correspond to Maxwell rheologies with typical long-term viscosities assigned to the asthenosphere in subduction zones. In the figure 3.13, a higher viscosity (red curve) is characterized by a lower creep-rate compared to the smaller viscosity case (blue curve). The former exhibits a practically linear behavior during the first years, as well as for time scales comparable with the seismic cycle (~ 100 years), as it has been shown by several authors (Trubienko *et al.* [2013]; Klein [2015]). A lower viscosity (as the one of model 2) has been proposed to be more appropriated, not only in the case of southern Chile (Klein *et al.* [2016]), but also for all studies of deformation after large earthquakes (Trubienko [2012]). Nevertheless, observations from several subduction zones after megathrusts earthquakes demon-

strate the existence of a clear transient phase, which is product of the afterslip process occurring in the surroundings of the thrust fault and/or a fast initial creep characteristic of an asthenosphere with Burgers rheology. Burgers rheology specified in case 3 corresponds to the one used in the preferred model of Maule earthquake in Chile (2010) proposed by Klein *et al.* [2016], which shows a clear but short transitory phase. cGPS time series recording first months after Tarapaca 2005 then give important information about the feasibility of a Burgers rheology for this subduction zone.

Also suggested for the Chilean margin (Klein *et al.* [2016]) is the existence of a narrow low viscosity channel, going along with the top of the subducted slab and reaching more than 100 km depth. We added this new element to our geometry creating a low viscosity area of ~ 28 km width starting at 50 km depth, and we tried with 3 different lengths: 40, 60 and 80 km. Figure 3.14 depicts observed deformation in time at 120 and 200 km from the trench, for a geometry including 2 viscous elements: low viscosity channels (3 different lengths) and an asthenosphere, both with a Burgers rheology. The curve labeled as "only asthenosphere" corresponds to model 3 in 3.13, and is included in order to compare these new results with the ones obtained for a simple geometry. The rheological parameters of the low viscosity channel and the asthenosphere are:

1. Low viscosity channel ($\eta_M = 2.6 \times 10^{18} (Pa \cdot s)$; $\eta_K = 1.2 \times 10^{17} (Pa \cdot s)$; $\mu_K/\mu_M = 3.9$)
2. Asthenosphere ($\eta_M = 4.8 \times 10^{18} (Pa \cdot s)$; $\eta_K = 1 \times 10^{17} (Pa \cdot s)$; $\mu_K/\mu_M = 3.9$)

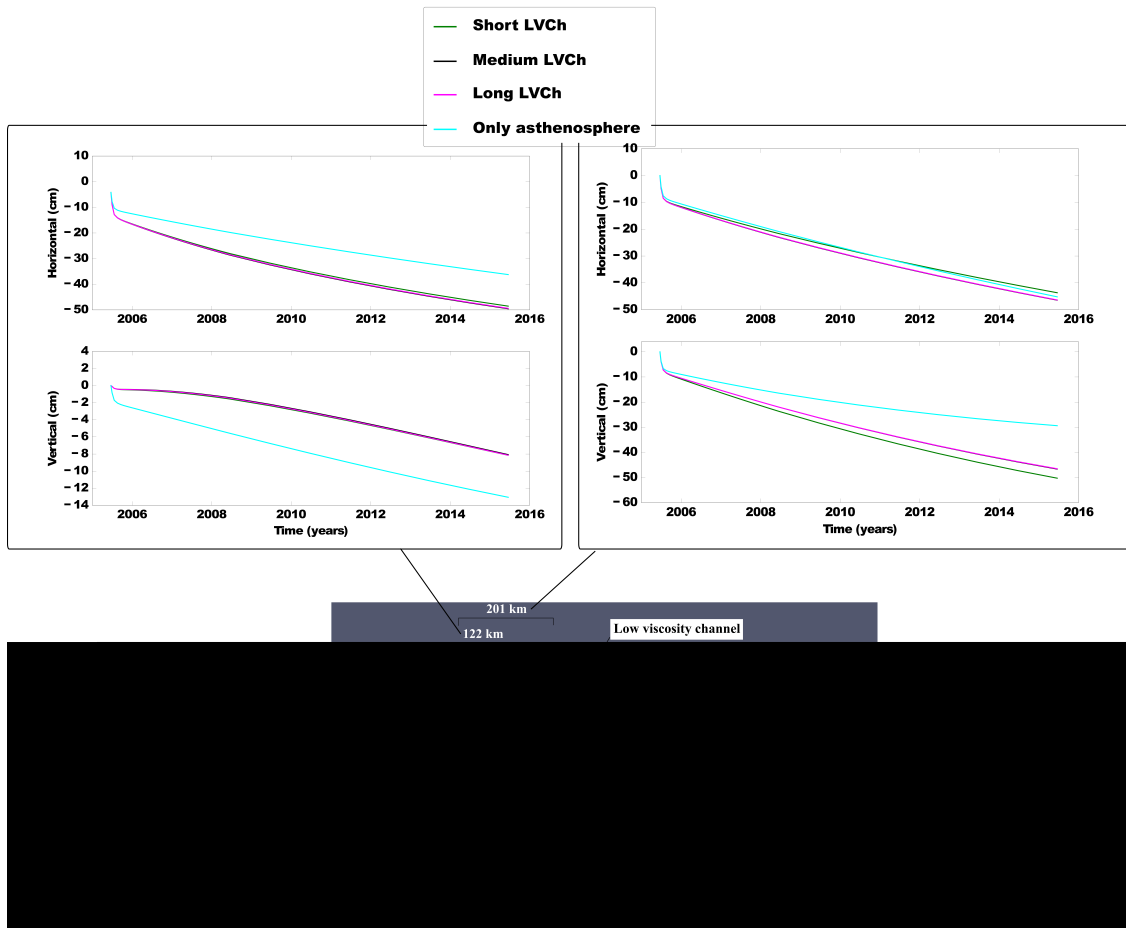


Figure 3.14: Top: Horizontal and vertical postseismic deformation (at approximately 120 and 200 km inland) for a model with a Burgers viscoelastic asthenosphere, without (cyan) and with (other colors) a low viscosity channel. A Burgers viscoelastic rheology is assigned to the asthenosphere and channel (see label with parameters), the latest changing in longitude. Bottom: 3 different longitudes for the low viscosity channel: 1 (short), 1+2 (medium), 1+2+3 (long). Tarapaca fault is indicated with white arrows into the slab.

Differences between deformation curves corresponding with models with channels of 3 different lengths are minimal, at least for the 2 chosen observation points. Instead, we observe significant differences between predicted displacements of model 3 and those of models including a viscoelastic channel, depending if the observation point is directly above of the low viscosity area or not. A particular situation is produced in the case of the station the furthest from the trench, for which the low viscosity channel does not seem to have much effect on the horizontal component.

3.7 Three-dimensional viscoelastic finite element model of Tarapaca 2005 earthquake

The two-dimensional model presented in the previous section gives the first insight about a viscoelastic relaxation process as the main phenomenon causing a velocity decrease after the intraplate earthquake of Tarapaca 2005. Nevertheless, in order to measure the real extension, shape and amplitude of the deformation produced by this intermediate depth earthquake, it is necessary to add some complexity to the model to make it more realistic. A three-dimensional viscoelastic finite element model is constructed, starting from a simplified version of the 2D geometry described in 3.5.1 (see scheme in figure 3.11) which does not include the deeper part of the narrow low viscosity channel. Details about model setup and results concerning three-dimensional postseismic deformation due to Tarapaca earthquake triggered as a single-event, will be introduced in a publication format in the following.

3.7.1 Abstract

The northern part of the Chilean subduction zone was recognized for a long time as a seismic gap since the last larger rupture (M_w 8.5) which occurred in 1877. The fact that Iquique earthquake 2014 (M_w 8.1) broke only part of this region, raise questions about the characteristic mechanisms of stress release of this zone. Several GPS time series over more than 15 years show a consistent decrease of the upper plate velocity after the intermediate depth earthquake of Tarapaca 2005. This large event M_w 7.7 affected the same region as Iquique earthquake, however its rupture occurs at ~ 100 km depth into the slab. Possible explanations for this velocity change could be: a decrease of the locking on the subduction interface, afterslip on the fault of Tarapaca, viscoelastic response of the mantle to this earthquake or a combination of all these mechanisms caused by this intraplate earthquake. We demonstrate that the velocity perturbation is best explained by the viscoelastic relaxation of the mantle excited by this intraslab earthquake. We study the interaction between this type of earthquake and a viscous asthenosphere by using an spherical 3D finite-element model. We compare our results with the observed postseismic displacements of 5 permanent GPS stations with long enough record before Tarapaca. A very good fit of the horizontal components of the postseismic signal is obtained when we assign a

simple bi-viscous Burgers rheology to the asthenosphere with a long term viscosity of 1.9×10^{18} Pa s, transient viscosity of 7.3×10^{17} Pa s and ratio $\mu_k/\mu_M = 2.8$. Similarly, the prediction of this model fit well the observed vertical components corresponding to the longest time series. Fast short-term deformation occurring for some months after the earthquake, a characteristic feature of models involving a bi-viscous rheology, is clearly visible in all EW components.

3.7.2 Introduction

Geodetic observations and numerical models representing the asthenosphere as a viscoelastic material have helped to elucidate important characteristics of deformation during the seismic earthquake cycle (SEC) in subduction zones. For instance, new viscoelastic models including the most invoked processes explaining the SEC postseismic deformation, as the relaxation of the upper mantle (including transient rheology), afterslip and re-locking of the fault, have been able to explain different observed crustal deformation patterns from different subduction zones as different parts of the same seismic process (Wang *et al.* [2012]; Hu & Wang [2012]). Three-dimensional viscoelastic models are fundamental nowadays in order to allow for all the complexities of SEC, as the direct scaling that exist between transient and steady-state relaxation times and the rupture length of the earthquake. All recent studies seem to confirm the lower value of the continental upper mantle viscosity respect to its oceanic part, distinctive of a zone that has been hydrated by the released fluids from the subducted slab. Nevertheless, what it is still debated is how low is this viscosity. Particularly for the subduction zone in Chile, viscoelastic models for Maule earthquake in 2010 predict continental upper mantle viscosities varying significantly. For instance, Bedford *et al.* [2016] estimates a viscosity range of 2×10^{19} - 4×10^{19} Pa s for the continental mantle, the best fit for a model including afterslip, a non-instantaneous re-locking of the fault and the long-term viscoelastic relaxation of the mantle. In contrast, the Maule model of Klein *et al.* [2016] considers afterslip and mantle relaxation produced by both: coseismic slip and afterslip. A long low viscosity channel is included which explains a large percentage of mid-term deformation, and a bi-viscous Burgers mantle rheology (includes a transient relaxation component) with a long-term viscosity 10 times lower than the one proposed by Bedford *et al.* [2016], gives a good fit of mid- and long-field deformation. Discrepancies in the near-field are attributed to a rather insufficient afterslip pattern. For the same

subduction zone, another viscoelastic model using transient rheology for Valdivia 1960 (Wang *et al.* [2012]), deduce a lower long-term viscosity of the continental upper mantle in Chile compared with models for other regions as Sumatra 2004, or the Cascadia $M_w \sim 9.0$ occurred in 1700. This low long-term viscosity has been explained for Klein *et al.* [2016] as a transient viscosity "active" in a decadal time span more than the real long-term viscosity suitable for a complete SEC.

Contrary to the large number of studies concerning the surface displacement pattern product of the interaction between earthquakes occurring in the seismogenic zone and a viscous asthenosphere, intraslab earthquakes of intermediate depth have not been widely studied. The first attempt is the work of Yoshioka & Tokunaga [1998], which uses a three-dimensional rectangular finite-element model with a viscoelastic asthenosphere to determine its interaction with the large intermediate 1993 Koshiro-oki earthquake $M_w=7.8$ (Japan). Assigning a Maxwell rheology to the asthenosphere, they study principally the spatio-temporal distribution of coseismic and postseismic displacements founding symmetry in relation with the orientation of the semi-horizontal fault. On the contrary, they do not find any correlation between elastic or viscoelastic deformation on the surface and the realistic heterogeneous slip distribution assigned to the fault, appealing to the large depth of the event. For this model, the postseismic displacements after 20 years of the earthquake are on the order of one tenth of the elastic deformation due to the earthquake, characterized by SSE-uplift and north-subsidence of some centimeters distributed seaward and landward over the fault region respectively. Unfortunately there were not GPS data to compare with observations, although previous tidal and leveling data (Hashimoto *et al.* [1993]) reveals same vertical patterns but with different magnitudes.

There are two recent publications studying the intraslab earthquake of Tarapaca 2005. The first one is from Bie *et al.* [2017], which uses InSAR and survey GPS data together with a 3D viscoelastic relaxation model considering lateral and vertical heterogeneities of the mantle viscosity, to determine rheological parameters of separate units: the continental asthenosphere, a strong forearc and a weaker layer below the volcanic arc. They find a good azimuthal fit between data and modeled postseismic displacements for a continental asthenosphere with a Maxwell viscosity ranging between $4 - 8 \times 10^{18}$ Pa s, coinciding with the low value found by Klein *et al.* [2016] for this subduction zone. Additionally, after calculating the Coulomb stress produced by co- and post-seismic deformation of Tarapaca 2005 in the seismogenic zone, they suggest that this intraslab earthquake might be related with the foreshock sequence of 2014, triggering the

large foreshock of March 16 and then indirectly causing the large intraslab of Iquique 2014. On the other hand, Jara *et al.* [2017] makes an exhaustive analysis of the seismicity in time before and after the earthquake, finding an increase on the deep and shallow background seismicity after the intraslab event. They associate these events (occurring in pulses) with a decoupling in the subduction zone supported by an eastward decrease of the GPS velocities, arguing that is not possible to observe the characteristic exponential shape of the deformation in time produced by the viscoelastic relaxation of the mantle for such a deep earthquake. Finally, they found certain synchrony between deep and shallow seismic activity which is interpreted as a slow stress transfer between the slab and the interplate zone, leading to the large thrust event of April 2014 in front of Iquique.

The present work focuses on modeling the postseismic signal of the intraslab earthquake of Tarapaca 2005 with a three-dimensional spherical FEM model including an elastic slab and the viscoelastic relaxation of the mantle. We take advantage of the availability of time series of 5 permanent GPS stations recording interseismic and postseismic daily positions (see figure 3.15) to contrast modeled and observed surface deformation.

3.7.3 Tarapaca 2005 earthquake and GPS observations

A large intraslab event of intermediate depth

Several intermediate depth intraslab earthquakes causing large damage and deaths have occurred on the Chilean subduction zone. A good example of these damaging events are the Chillan 1939 M_s 7.8 (near Concepcion) and Antofagasta 1950 M_s 8.0 earthquakes (Madariaga [1998]), both with typical tensional mechanisms and associated near vertical fault planes of rupture. In the northern part of the Chilean margin, one uncommon intraslab earthquake of large magnitude M_w 7.8 (National Earthquake Information Center - NEIC) occurred in 2005. With an extensional focal mechanism and located at 100 km depth, this event is characterized by a sub-horizontal rupture plane slightly dipping to the west, inferred from the foreshock sequence distribution (Peyrat *et al.* [2006]; Delouis & Legrand [2007]). Figure 3.15-A shows ruptures of Tarapaca 2005 and Tocopilla 2007, 2 large events occurring before the Iquique subduction earthquake in 2014. The figure includes the array of permanent stations recording before and after 2005. 3.15-B corresponds to an schematic cross-section that illustrates an average hypocenter

location of the earthquake, its fault plane dipping to the west with a low angle of 24° and rupture width of 30 km.

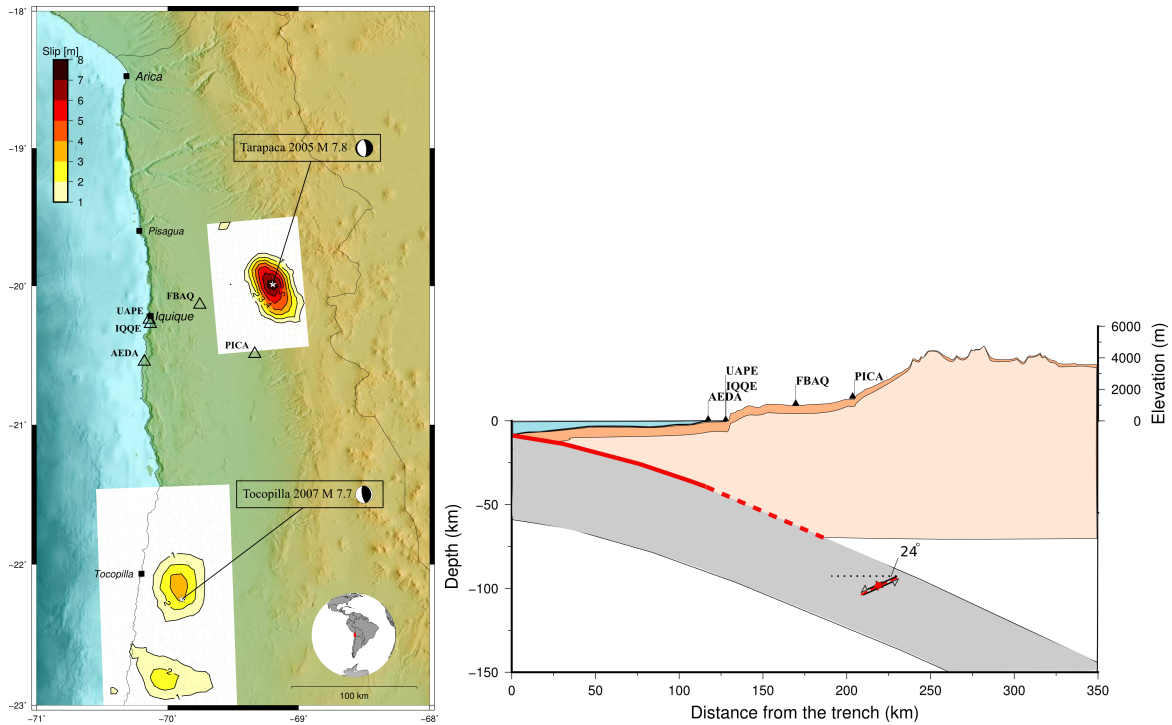


Figure 3.15: Left: cGPS stations recording before and after Tarapaca 2005. Ruptures of large earthquakes are depicted in the figure. Right: Cross-section of a profile starting in the trench at latitude 20.48 S and following the plates convergence direction. A longitudinal view of the rupture of Tarapaca 2005 shows a fault of 30 km width dipping to the west, as is modeled in this study.

GPS time series

In the northern part of the Chilean subduction zone, 7 permanent GPS stations (IQQE, UAPE, AEDA, FBAQ, PICA, QUIL, COLL) recorded daily positions both before and after Tarapaca 2005 earthquake. We consider insufficient the amount of positions recorded by the latest 2 stations and we do not include them in the analysis (see figure XX in annexe B). We calculated relative positions by using the double-difference technique performed by the first module of the combination software GAMIT-GLOBK (King & Bock [1999]). In a posterior stage (GLOBK), these daily free solutions are expressed with respect to a stable reference frame. During this process we first enlarge our local network to a regional scale, including stations from Argentina (RAMSAC), Brasil (RBMC) and Bolivia, increasing the stability of the solution. The next and final step consists in mapping our free coordinates in the global International Terrestrial

Reference Frame version 2008 (ITRF08) (Altamimi *et al.* [2011]), by combining our regional solutions with the International GNSS Service (IGS) solutions (SOPAC processing), to subsequently perform a Helmert transformation using 43 global stations with well known positions. Positions expressed in a regional reference frame use the SOAM ITRF 2000 rotation pole (-21.457, -134.631, 0.113) which provides a velocity of -2.6 mm/yr east and 10.6 mm/yr north at 20.5° S for the South American plate. We corrected these time series from seasonal displacements induced by hydrological loads using the signals computed from GRACE gravity signal by Chanard *et al.* [2018]. This signal deduced from GRACE is available between 2002 and 2012. Jumps due to instrument changes were corrected, although large data gaps can make this correction inaccurate. 2 of the 5 stations analyzed in this work were merged in one due to their proximity (~ 3.5 km) forming the fictitious station UAIQ (from the sites UAPE and IQQE), the one with the longest and most reliable time series. In order to decrease the low frequency noise we first re-sample the positions every 10 days. Because postseismic signals depend strongly on the stability of the pre-Tarapaca trend, the new record (UAIQ) is used to improve the trend of the pre-Tarapaca signal for the rest of the stations (with many data gaps) by subtracting the UAIQ residual signal from the other time series. In a posterior step this velocity is restored to each site, resulting in new time series with more accurate interseismic trends. Postseismic signal for each of these new time series is shown in figure 3.17.

3.7.4 Velocity decrease after Tarapaca earthquake

Time series obtained for UAIQ, AEDA, FBAQ and IQQE show a decrease in the horizontal component of the velocity after Tarapaca 2005. Velocities before and after the earthquake, obtained by a regression analysis, are drawn in blue and red respectively in figure 3.16. Error ellipses represent a 95% confidence, and include white and flicker noise. Velocity errors were calculated following Mao *et al.* [1999] approach, which obtains underestimation factors of velocity errors varying between 5 and 11 respect to a model with pure white noise (rate standard error). We estimate factors of (5, 5, 6) for north, east and vertical components, using noise parameters from Mao *et al.* [1999] for their closest station to our region (SANT) in a 2 years time span. Although the difference between pre- and post-Tarapaca deformation rates does not exceed 1 cm/yr (uncertainties order), we have to consider that the given uncertainties were esti-

mated as an upper limit. In addition, the fact that all stations consistently exhibit a diminution maintained for several years, leads us to think on this intraslab earthquake as the responsible for a non negligible impact on the postseismic deformation field.

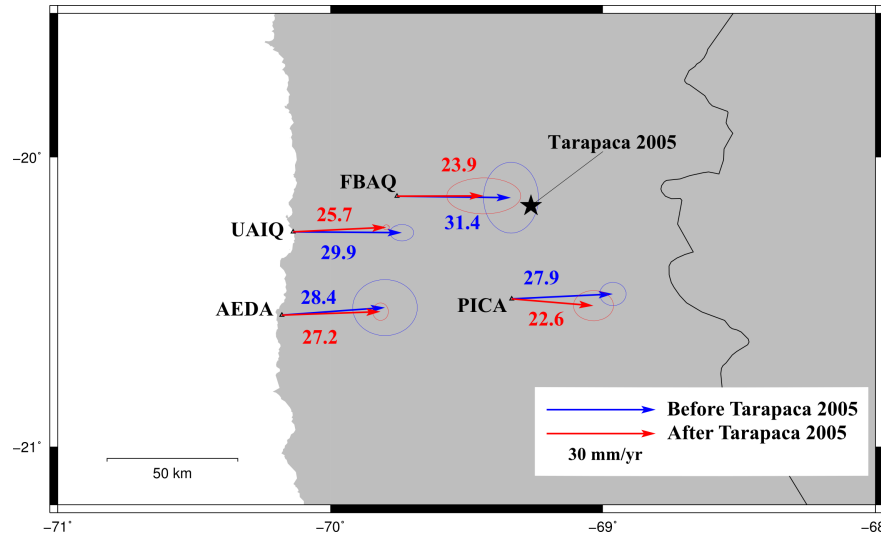


Figure 3.16: 3 real cGPS sites and one merged from 2 real stations (UAIQ) showing velocities (in mm/yr) pre- (blue) and post- (red) Tarapaca 2005 earthquake. Velocities are expressed in a stable South American plate and error ellipses correspond to 95 % confidence considering white and flicker noise. The velocity decrease is a constant for all stations.

Observed coseismic displacement and postseismic deformation in time related to Tarapaca 2005 earthquake is shown in figure 3.17 for 2 coastal and 2 inland stations ordered by latitude. The observed postseismic signal is calculated as the observed displacement after the pre-Tarapaca trend is removed. Despite a common mode error is visible at all stations, we decided not to remove this signal due to the small number of stable reference stations during the period of interest, a limitation that might lead to the removal of tectonic displacements. However, a trend is visible for each component, specially in the EW component: all stations show postseismic westward displacements with larger % deformation rates on inland sites. The north-south component is practically null for UAIQ, AEDA and FBAQ (between ± 1 mm/yr), with a more detectable southern trend for PICA (3 mm/yr). The vertical component of postseismic signal in all sites is very small and presumably hidden by the noise, although is possible to infer practically null displacements for coastal stations (UAIQ, AEDA) in the first years after the mainshock, with AEDA disrupted by a downward offset which is not associated to antenna changes or/and seismic events. In contrast, inland stations show uplift with velocities up to 2.2

mm/yr. All postseismic velocities and associated uncertainties are indicated in table B.1 in an-
 nexa B.

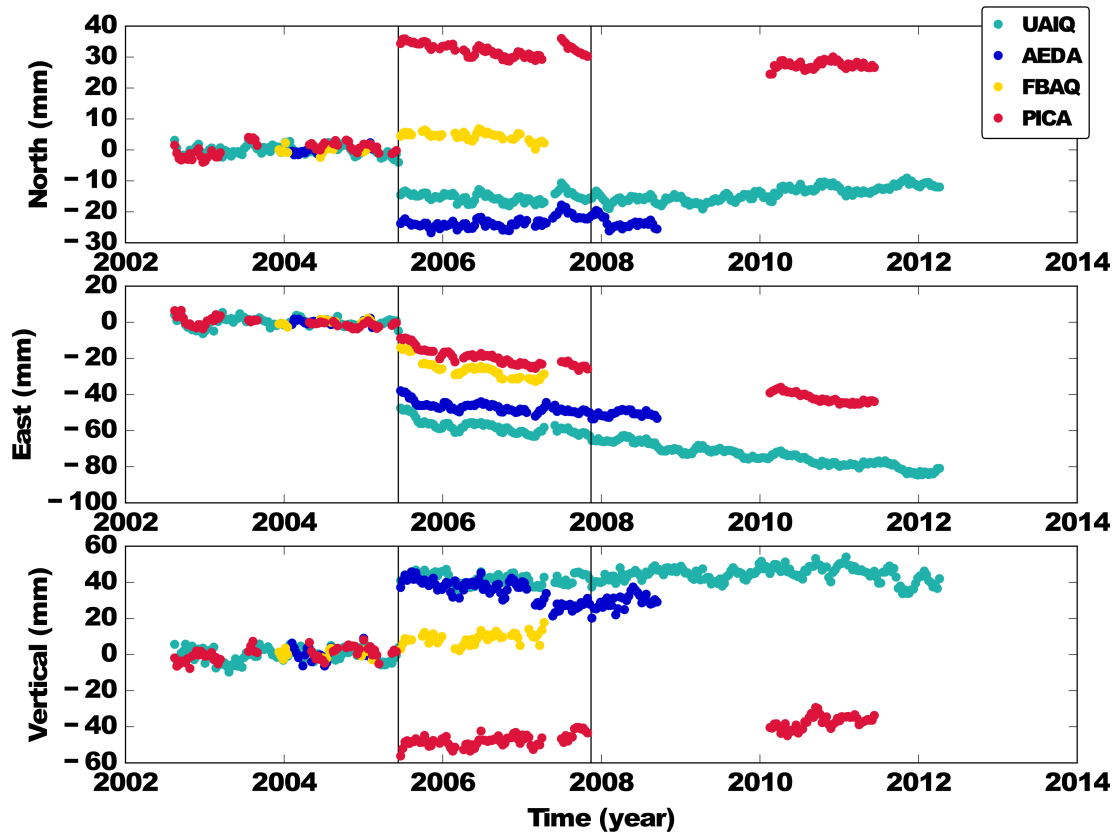


Figure 3.17: 3 components of postseismic deformation associated to Tarapaca 2005 recorded by 2 coastal (cool colors) and 2 inland (warm colors) cGPS stations. Plan view depicting geometrical array of stations can be seen in figure 3.21.

Three phenomena could explain this change in the long-term deformation rate: afterslip on the fault plane of Tarapaca earthquake, slow slip on the subduction fault plane and/or viscoelastic relaxation of the asthenosphere after Tarapaca. We decided to focus on the evaluation of the third scenario, after analyzing the signature of the observed postseismic signal. Figure 3.18 compares 2 years of postseismic displacements (blue) with coseismic displacements (red) corresponding to Tarapaca 2005 (left) and Iquique 2014 (right). The coseismic displacements of Tarapaca and Iquique are indicative of the deformation pattern which would be induced by long-term slip on their respective fault planes. The fact that postseismic displacement for the station right above

the rupture points away from it, and that horizontal postseismic displacements do not decrease progressively landward, makes dubious the possibility that slip on Tarapaca fault and slow slip on the seismogenic zone could be the right explanation for the post-Tarapaca perturbation of the velocity field. Although we do not discard the possibility of a minor contribution of fault-slip in the observed pattern, we decide to test the possible effect of viscoelastic relaxation. For that, we build a three-dimensional viscoelastic finite element model of the intraplate earthquake of Tarapaca 2005, whose characteristics and results are detailed in the following sections.

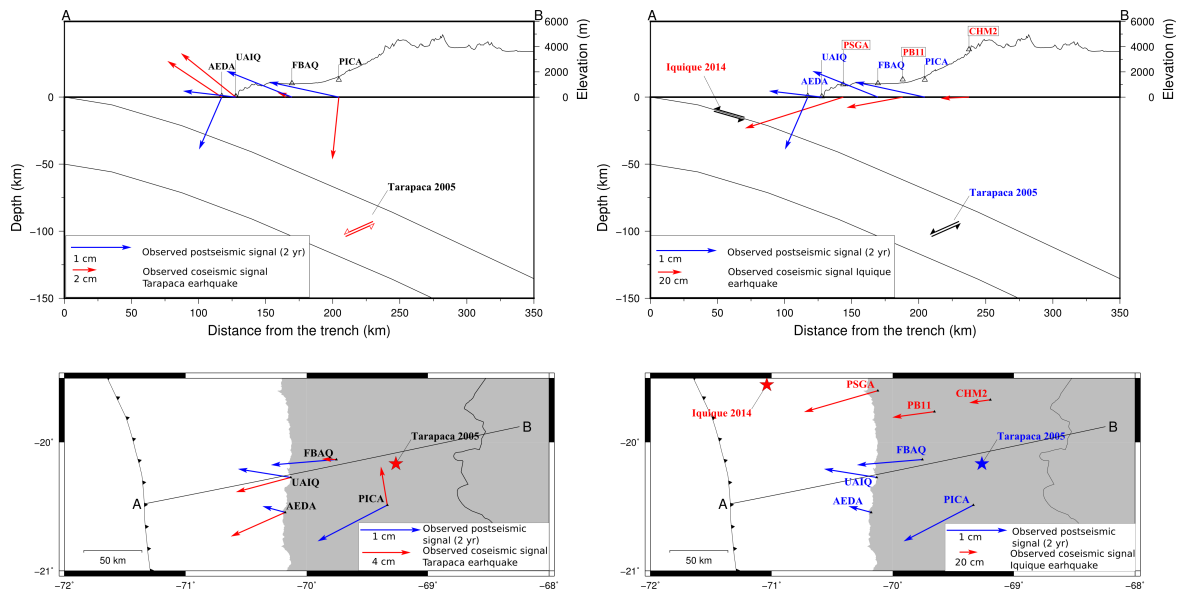


Figure 3.18: Comparison between postseismic displacements after 2 years associated to Tarapaca earthquake and displacement patterns representing afterslip and slow slip on Tarapaca and subduction faults respectively. Left: Postseismic (blue) and coseismic displacements (red) from the intermediate depth earthquake of Tarapaca 2005. Right: Postseismic from Tarapaca 2005 (blue) and coseismic displacements corresponding to the subduction Iquique 2014 earthquake (red) for 3 extra stations (PSGA, PB11, CHMZ) aligned at similar latitude. Ellipse errors are not included to simplify the scheme.

3.7.5 Finite element modeling

Mesh geometry

Our 3D mesh represents a spherical portion of the Earth excluding the core (see figure 3.19-A). Centered on Tarapaca 2005 earthquake, its surface extents over an area of $8000\text{km} \times 6000\text{km}$ and reaches 2800km down to the core-mantle boundary, dimensions kept large enough to prevent any boundary effect. Figure 3.19-B corresponds to a zoom to the inner part of the grid. It

shows the geometry used in detail: Nazca (including Tarapaca fault) and South American plates lying over an asthenosphere of 200 km thickness whose upper 20 km layer is created to use it as a transition zone. The overriding and subducted plate have 70 km and 50 km thickness respectively, the latest subducting down to 500 km depth into the mantle. These values, corresponding to the lithospheric thickness, are appropriate for the northern part of the Chilean subduction zone (Sodoudi *et al.* [2011]). The region between 30 and 90 km adjacent to the top of the slab represents a low viscosity zone that has been sub-divided in order to study the effect on the longitude of a narrow channel with lower viscosity than the surroundings proposed by Klein *et al.* [2016]. The top of the slab has been drawn by using the data provided for USGS at 20.5° S in its 1.0 version (Hayes *et al.* [2012]). The surface of the model is controlled by a counteracting vertical force simulating the gravity response given by $F_z = -\rho \cdot g \cdot U_z$, where ρ is the density, g the gravity and U_z represents the vertical displacement of the surface. The rest of boundaries are imposed to zero velocity, appropriate for the postseismic modeling of a single event. All the domain has been discretized in 314.753 three-dimensional lineal tetrahedral elements and 56.192 nodes, with an increased density around the earthquake fault and the region where the instruments are located. The finite element computations have been done with the finite element software Z-set/ZeBuLoN (Missoum-benziame *et al.* [2011]).

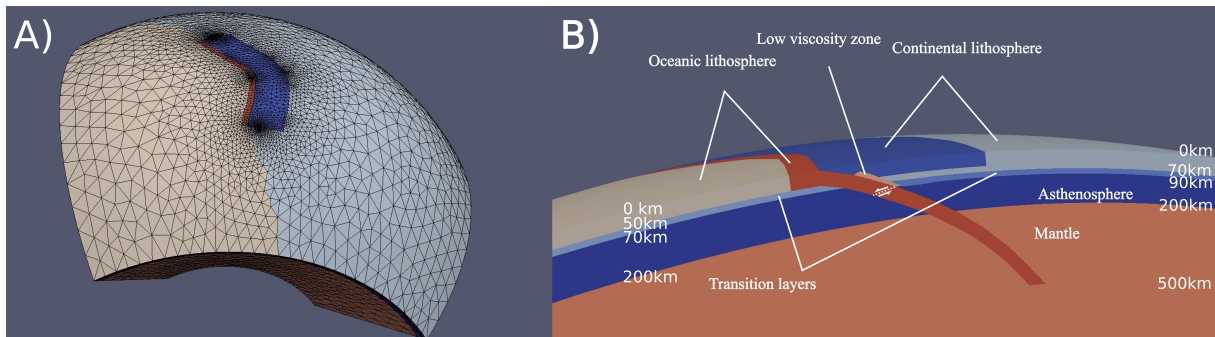


Figure 3.19: A) Three-dimensional grid used to model with finite element techniques the intraslab earthquake of Tarapaca occurred in 2005 in Chile. The surface of the grid clearly shows the distinction between oceanic (left) and continental (right) plates. B) Cross-section in the middle of the grid showing the geometry used for the model. South American and Nazca plates with 70 and 50 km thickness lie over an asthenosphere reaching 200 km depth. Other elements added to enable a more complex analysis are a mantle wedge (LVW) and 2 layers of 20 km separating lithosphere from asthenosphere. A schematic representation of Tarapaca fault is included, where the west dipping plane and the sense of slip are indicated as a white dashed line and white arrows respectively.

Rheology of different model units

In this work, both plates and deep mantle are modeled with a linear elastic behavior, with shear and bulk moduli increasing with depth, following the one-dimensional Preliminary Reference Earth Model (PREM). Other units as the asthenosphere, the low viscosity channel and transition layers under the lithosphere are modeled (or not, depending on the test) with a viscoelastic behavior. These linear viscoelastic rheologies are commonly represented by Maxwell and Burgers bodies. Due to its simplicity, the most used viscoelastic rheology is Maxwell (left diagram, figure 3.20), a combination between an instantaneous elastic response (μ_M) and a long term viscous behavior (η_M). A more complex rheology it is the Burgers rheology, governed by an initial instantaneous response and a posterior long term behavior determined by the Maxwell block, with an intermediate transient phase represented by the Kelvin-Voigt element (see right diagram, figure 3.20).

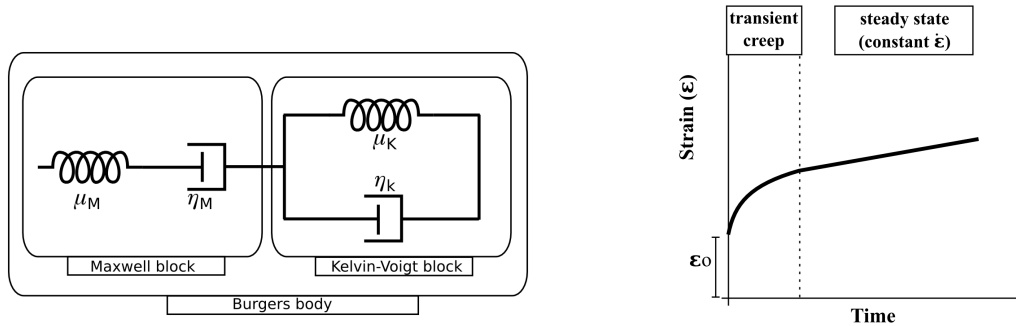


Figure 3.20: Left: diagram of a simple Burgers body described as a combination of 2 other material behaviors: Maxwell and Kelvin-Voigt (see the 2 elements enclosed by frames and connected in series). The figure shows schematically viscoelastic constitutive stress-strain relationships for different materials, symbolized by multiple combinations of springs and dashpots representing elastic and viscous behavior respectively. Right: Time evolution of strain under a constant stress loading for a simple burgers rheology. It is characterized by an initial elastic deformation ϵ_o followed by a fast transient creep phase and a steady-state phase with constant deformation rate.

3.7.6 Coseismic displacement from Tarapaca earthquake

The coseismic slip is prescribed by instantaneous relative displacement between duplicated nodes on the fault plane following the split-node method (Melosh & Raefsky [1983]). Based

on the studies of Tarapaca earthquake of Peyrat *et al.* [2006] and Delouis & Legrand [2007], we have built a fault plane into the slab centered at 101 km depth and dipping to the west with an angle of 18° , extending along strike for the whole model. We have chosen a rupture area of 30x60 km contained in this plane and centered in the hypocenter given by (69.2° S, 20° S, 99 km). We take advantage of the accurate geometry and realistic elastic parameters used in our model to obtain our own coseismic slip distribution. For that, we inverted observed displacements of the 5 permanent GPS stations used in this study, adding 3 extra stations: 2 nearby the rupture (QUIL, COLL) and another one further to the north (UTAR). Coseismic displacements of the stations QUIL and COLL were obtained from Peyrat *et al.* [2006], the rest was calculated as the difference between positions given by the trends obtained right before and right after the earthquake (table B.2, annexe B). The chosen inversion method uses least-square technique on green functions calculated with Z-set/ZeBuLoN (Missoum-benziame *et al.* [2011]) for each one of the 5 nodes contained in the rupture area. The resulting slip pattern is shown in figure 3.21. The comparison between observed (red) and modeled (blue) surface coseismic displacements product of the inverted slip distribution of Tarapaca earthquake (5 nodes with different slip assigned) is shown in the figure 3.21. The error represented as an ellipse in the figure corresponds to the sum of statistical errors from both trends. The coseismic pattern is characterized by 2 blocks of horizontal displacements converging-to and diverging-from the rupture zone separated by a nodal line passing through the middle of 2 of our stations. Maximum values reach 7 cm of westward movement nearby the rupture area. For the vertical displacement we can see seaward moderate uplift and landward subsidence of up to 15 cm.

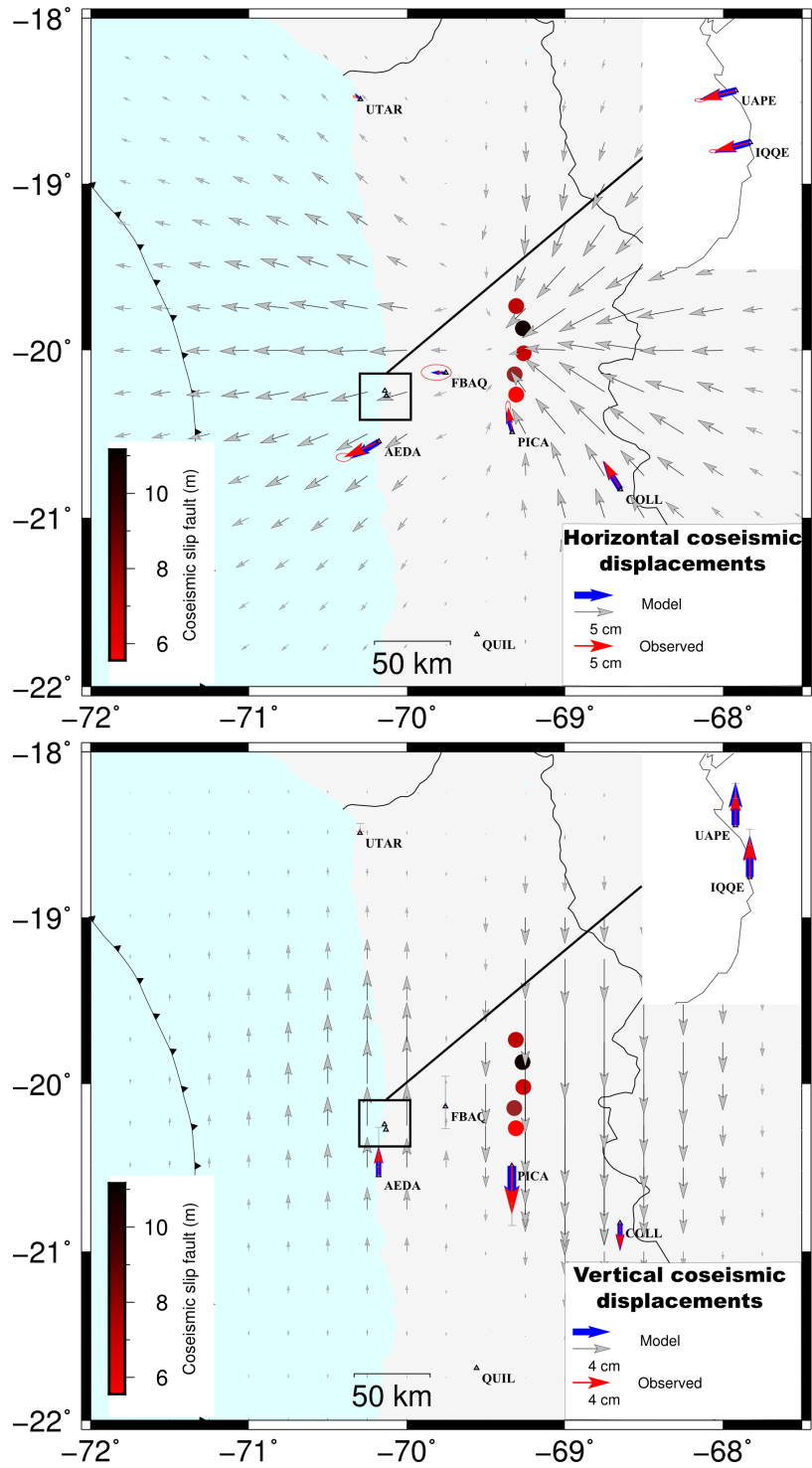


Figure 3.21: Coseismic displacement observations (red) and viscoelastic model results (blue, gray) for the inverted slip depicted in the figure for each of the 5 slipping nodes representing Tarapaca 2005 fault (5 circles aligned vertically). Observations errors are represented by ellipses of 95% confidence (details of its calculation on the text); vertical bars represent same error in vertical components. Results for 2 stations (UAPE, IQQE) are shown apart for clarity due to their proximity. Coseismic values for stations COLL and QUIL were obtained from the study of Peyrat *et al.* [2006]; errors has not been included for this reason.

3.7.7 Results: viscoelastic deformation after Tarapaca Earthquake

We performed several tests varying the rheology and geometry of a basic setting. This starting model is composed by oceanic and continental plates represented by 2 elastic bodies of 50 and 70 km thickness overlying a viscoelastic asthenosphere. We selected 4 representative models (detailed in table 3.3), one including a low viscosity channel adjacent to the top of the slab. The predictions of the 4 models as well as the observed displacement time-series are depicted in Figure 3.22.

Model	Asthenosphere				Low viscosity channel			
	Rheology	η_M [Pa s]	η_K [Pa s]	μ_K/μ_M	Rheology	η_M [Pa s]	η_K [Pa s]	μ_K/μ_M
Model 1	Maxwell	4.8e+18	-	-	-	-	-	-
Model 2	Burgers	1.6e+18	7.32e+17	2.8	-	-	-	-
Model 3	Burgers	4.8e+18	7.32e+17	2.8	Maxwell	1e+18	0.8e+27	3.9
Model 4	Burgers	3.5e+18	7.32e+17	5.6	-	-	-	-

Table 3.3: Rheological parameters of 4 principal viscoelastic models performed in this study.

Model configuration including a low viscosity channel is identified as model 3, and emulates the best three-dimensional viscoelastic model for Maule 2010 proposed by Klein *et al.* [2016]. Parameters used in our model 3 are the same used for southern Chile, however, the low viscosity zone is shorter, ending at 90 km depth. Rest of the models consist on one single viscous region (asthenosphere) with different rheologies: Model 1 represents an upper mantle with Maxwell rheology, and models 2 and 4 use 2 different Burgers rheologies, the former with approximately the half of the long-term viscosity of the latest.

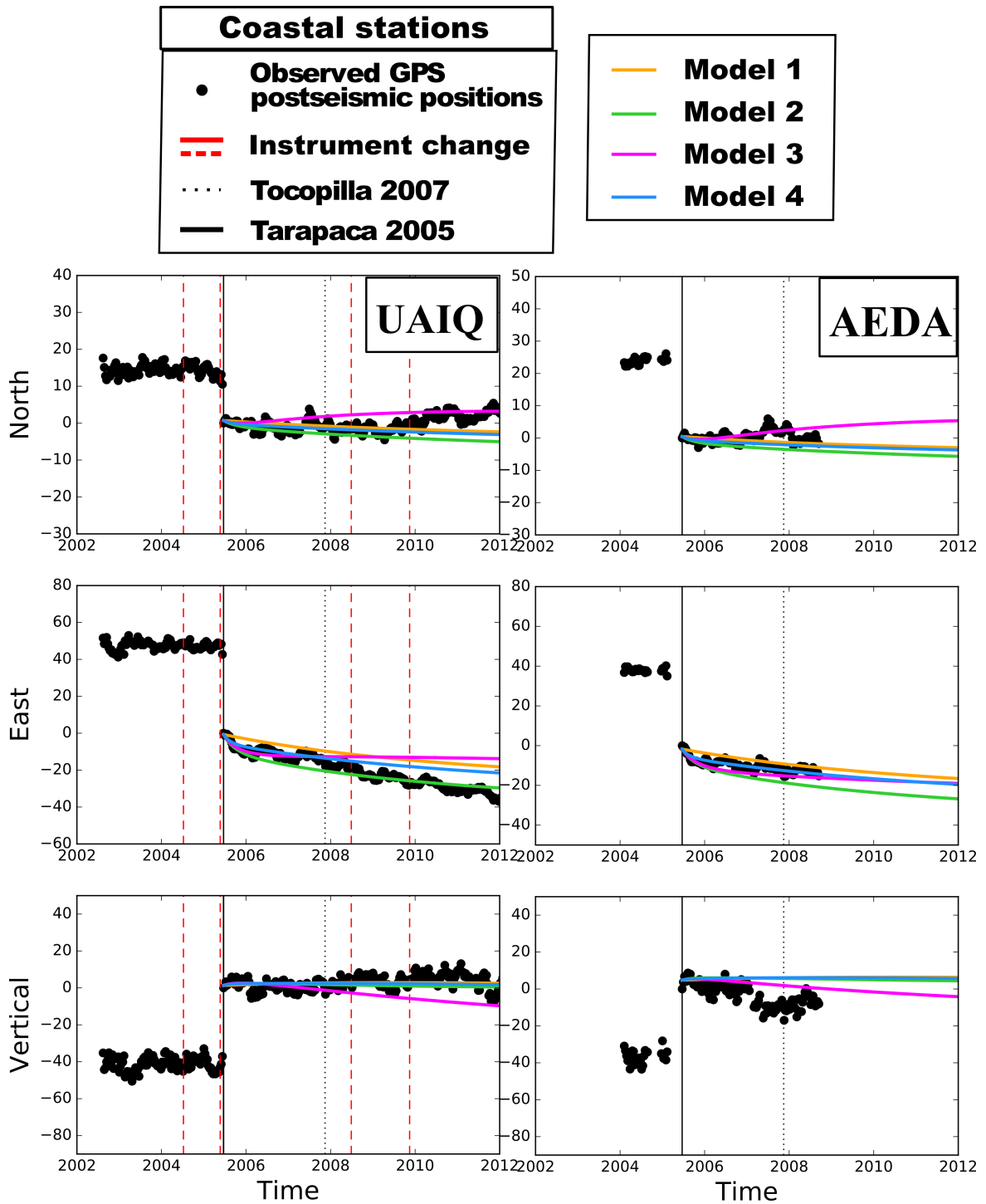


Figure 3.22: Positions recorded by 2 coastal sites surrounding the rupture of Tarapaca 2005 (black circles) and surface deformation produced by 4 models detailed in table 3.3 (colored curves). Tarapaca 2005 and Tocopilla 2007 are indicated on each component by continuous and dashed vertical black lines respectively. Red vertical lines indicate the exact date when a change of instrument is registered on the site. Instrument changes for the combined station UAIQ come from 2 different stations and thus they are displayed as dashed lines.

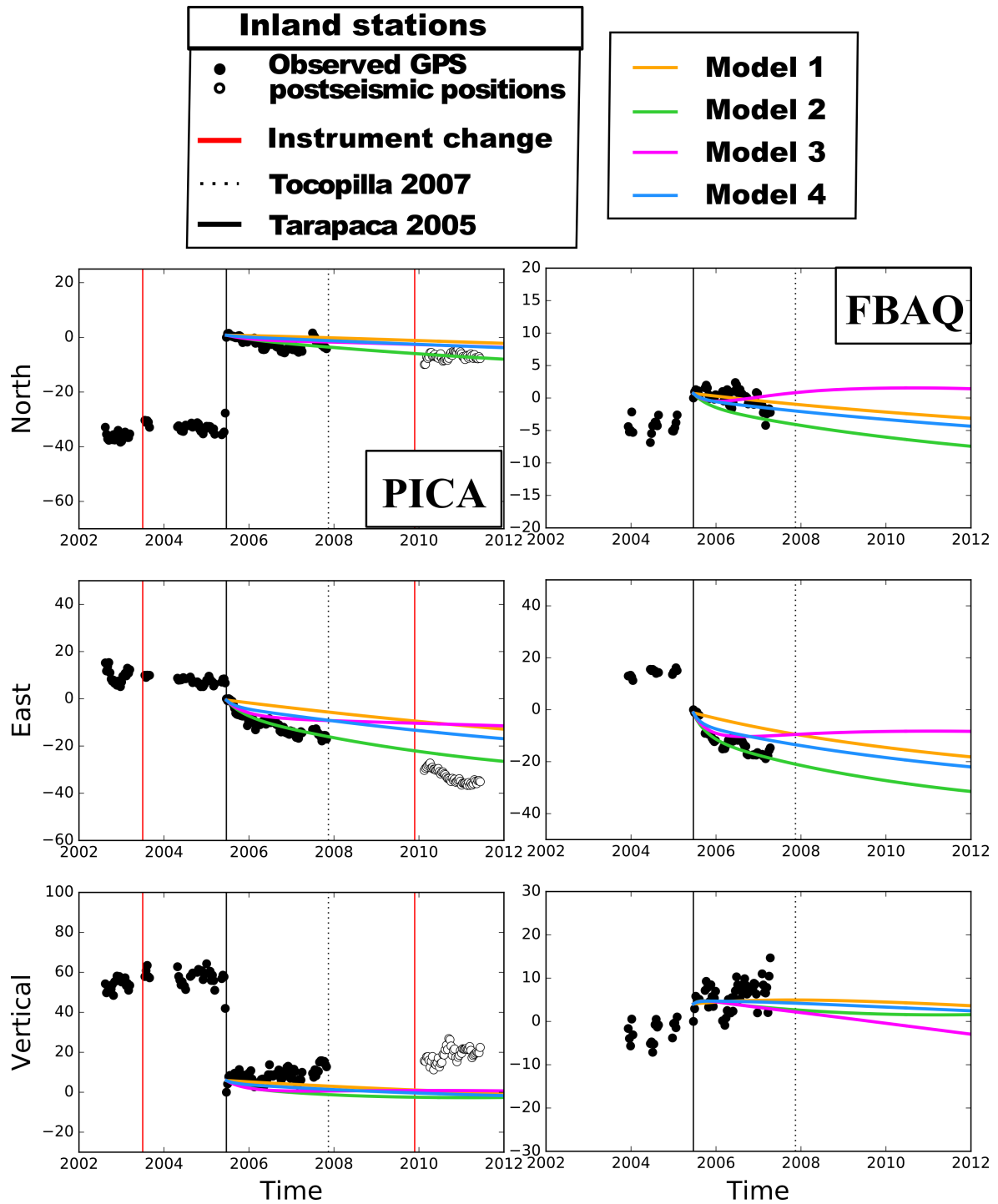


Figure 3.22: (*Continued.*) Observed positions in this case correspond to 2 inland stations. Open circles at PICA station were not used in the calculations.

The first important feature we can infer from figure 3.22 is how Burgers rheology assigned to the asthenosphere, better describe the first years of viscoelastic relaxation compared with a Maxwell rheology. This is particularly obvious on EW components, where initial recorded po-

sitions seem to depict what is known as the fast transient phase of a Burgers material, instead a linear relaxation associated with Maxwell rheologies. The figure shows as well the very good fit between observations and model 1 for horizontal components of all sites. While for the vertical component the fit for all models is not obvious due to the larger dispersion of the positions, in the longest time series corresponding to the site UAIQ, slow progressive uplift predicted by the model is in agreement with observed deformation. Thus, rheological parameters of model 1 seem to be more appropriate compared with model 4. The characteristic change on the sense of deformation some months after the mainshock and fast deceleration of horizontal components produced by model 3 is not a trend we observe clearly on the data. As a consequence, and to obtain the best fit, we chose 11 viscosities varying around the steady-state viscosity of model 1 in order to produce 11 new postseismic deformation curves by forward modeling. Figure 3.23 shows the resultant RMS misfit for each model, with components weighted by standard deviation and calculated for the same periods than for the calculation of the observed postseismic velocity. An anomalous signal between May 2007 and the beginning of 2008, visible in almost all stations, is considered an artifact and is not considered for this calculation. The particular abrupt northward signal after February 2010 shown by time series of the site UAIQ can not be confirmed by the rest of the stations. Consequently, RMS calculation for this station includes data up to this date. As a result, our preferred model corresponds to a Burgers asthenosphere with Maxwell long-term viscosity $\eta_M = 1.9e+18$ Pa s, $\mu_K/\mu_M = 2.8$ and $\eta_K = 7.32e+17$ Pa s.

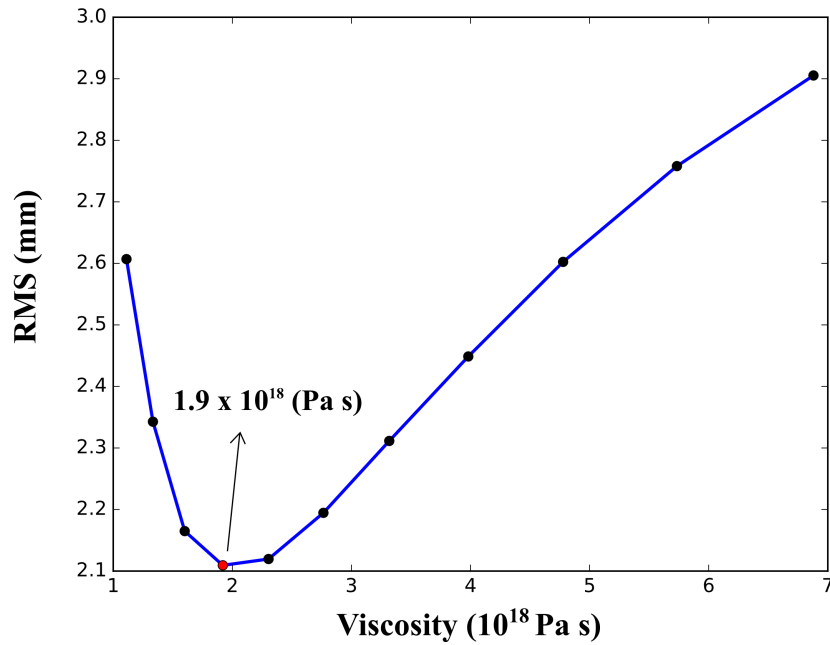


Figure 3.23: RMS misfit curve for 11 models using Burgers rheology for the asthenosphere with long-term viscosities ranging between 1×10^{18} Pa.s and 7×10^{18} Pa.s. Maxwell viscosity of the best model is represented by a red circle.

Figure 3.24 shows a plan view of the horizontal and vertical postseismic velocities corresponding to our preferred model, calculated between the first and second year after the earthquake (blue and gray arrows). Red arrows represent observed postseismic velocities. Finally, this modeled signal is contrasted with postseismic observations in figure 4.6.

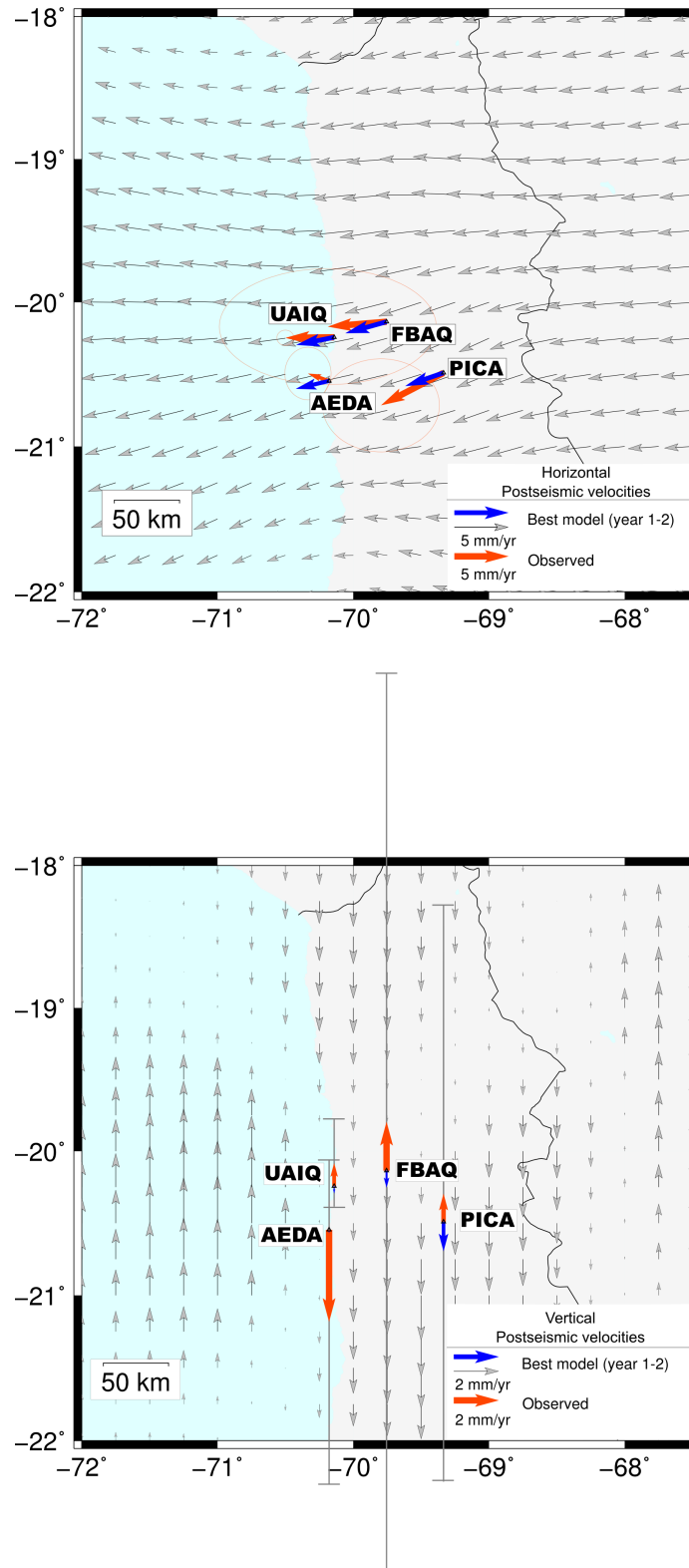


Figure 3.24: Observed (red) and modeled postseismic velocities (blue) between the first and the second year after Tarapaca 2005. Modeled postseismic velocity field (between years 1 and 2 after the earthquake) is represented by gray arrows. Error ellipses of 95% confidence correspond to horizontal error. Vertical error is shown as vertical bars.

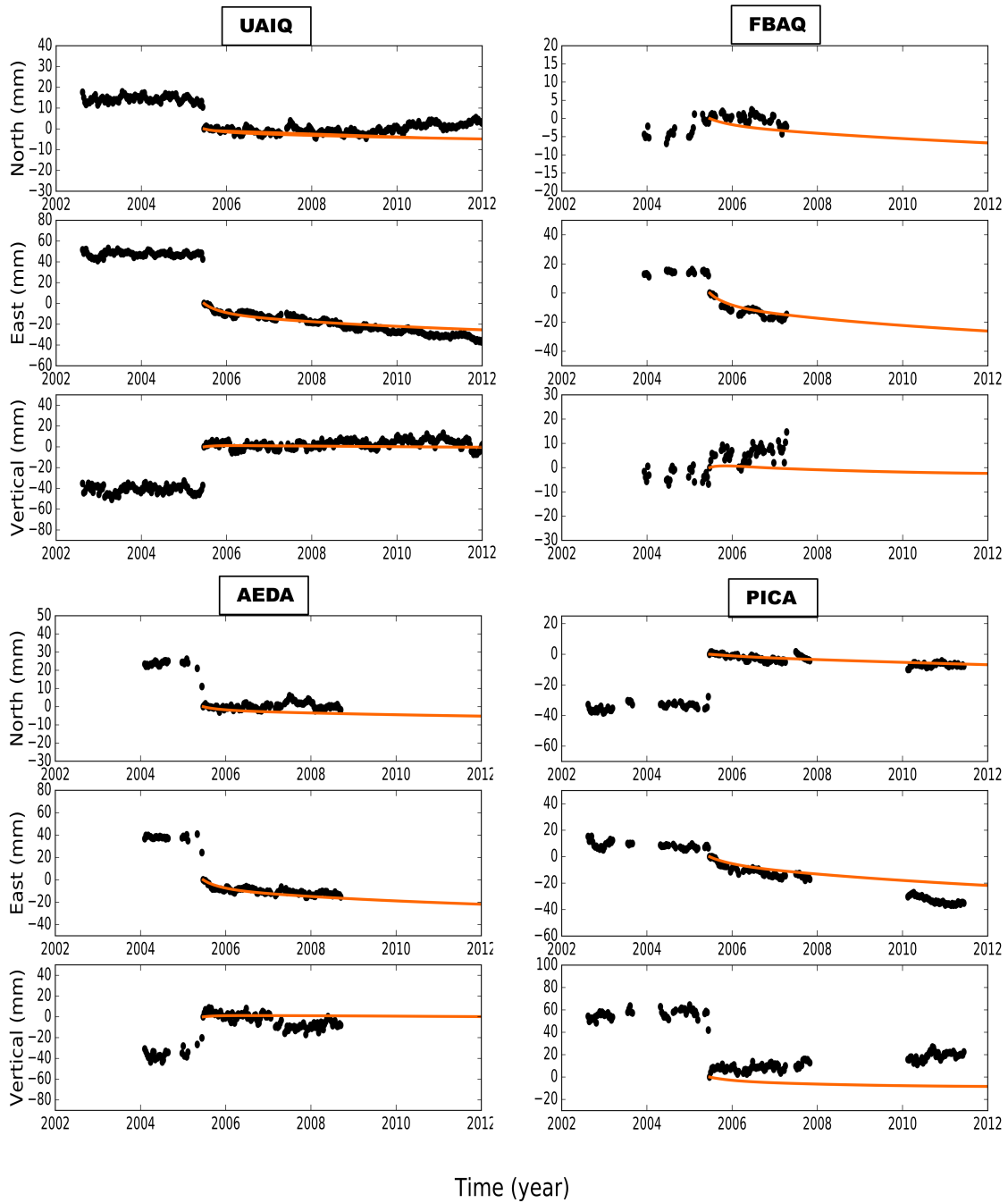


Figure 3.25: Observations (black circles) and the best model (blue) representing the postseismic signal produced by Tarapaca earthquake and a viscoelastic asthenosphere with Burgers rheology and a long-term viscosity of 1.9×10^{18} Pa.s.

3.7.8 Discussion

Previous viscoelastic models of subduction earthquakes in Chile favored low asthenosphere viscosities of the order of the value obtained in this study (Trubienko *et al.* [2013]; Klein *et al.*

[2016]), however not many have inferred rheological parameters analyzing the postseismic signal of an intermediate-depth earthquake. One of these few studies corresponds to Bie *et al.* [2017], who analyzed the viscoelastic relaxation of Tarapaca 2005 using 4 years of observations from Envisat satellite and GPS campaign data. Based on the information post-Tarapaca from 135 interferograms, they determine that the velocity decrease shown by sGPS positions is in part due to the viscoelastic relaxation process of a continental upper mantle with viscosity between $4 - 8 \times 10^{18}$. Regardless the similarity of this viscosity range with our results, the large and systematic difference in amplitude between observed horizontal displacements and the ones predicted by their preferred model, leads us to speculate that a viscosity of 8×10^{18} is too large, and thus the predicted deformation is underestimated. We think that this problem might be the result of considering a null interseismic signal. Azimuthal misfits associated with the lower limit of their optimal viscosity range are not observed in our case, difference that could be explained by discrepancies between models. Tarapaca intraslab earthquake was studied as well by Jara *et al.* [2017]. In this study is performed an exhaustive seismic analysis which leads to establish a connexion between deep and shallow background seismicity following the earthquake. They relate this seismic synchronization with the decoupling of the seismogenic interface (Bouchon *et al.* [2013]), phenomenon that is supported by the velocity decrease detected by GPS instruments. Coincidentally with Jara *et al.* [2017], we detect this change of deformation rate and we attribute it to Tarapaca earthquake. However, the good predictions of our model, together with the fact that inland cGPS stations show larger postseismic displacements than stations along the coast, support the idea of viscoelastic relaxation inducing deformation instead of a change in the friction state of the seismogenic zone.

On the other hand, Klein *et al.* [2016] proposed a steady-state Maxwell viscosity of $\eta_K = 4.8 \times 10^{18}$ Pa s based on a model for the large Maule subduction earthquake occurring in the same subduction zone but more than 1500 km to the south. They make emphasis on interpreting such low value as a “transient” steady-state viscosity because it leads to underestimate deformations in the long-term (tens of years). This problem is solved assigning a more complex Burgers structure (more realistic situation), and the bi-viscous Burgers rheology with such a low viscosity remains a very good approximation for the first years following a subduction earthquake. In the same way, we think that the obtained viscosity, that might be common to all the margin, would explain only short-term observations, and that a longer deformation monitoring period will be necessary to determine a more accurate Burgers rheology for the asthenosphere.

3.7.9 Conclusion

We built a three-dimensional viscoelastic model of an intraslab earthquake occurring at 100 depth, to determine the incidence of this earthquake on the velocity change detected by GPS instruments. For this, we use a suitable geometry for north Chile subduction and a basic configuration including an elastic lithosphere and a viscoelastic asthenosphere with Burgers rheology. We demonstrate that an intraplate earthquake triggering the viscoelastic relaxation of the upper mantle with a low steady-state viscosity of $\eta_M = 1.9 \times 10^{18}$ Pa s, produce deformations of the order of the recorded postseismic signal up to 7 years after the event. These results support other studies that obtained low viscosity values for this subduction zone but using large megathrust earthquakes. In addition, the model proposed here predicts that an intermediate-depth earthquake produce deformation of the order of ~ 1.5 mm/yr after 7 years. We set 7 years as a maximum time span in which model predictions are reliable; predicted deformation after several decades might be overestimated. Finally, the very good fit between observations and modeled displacements makes us to propose the viscoelastic mantle relaxation as the most likely process explaining the detected velocity change, questioning the occurrence of large long-term locking changes in the seismogenic zone.

Chapter 4

Instrumental gap between Central and North Chile is filled: new results regarding coupling complexities and the Andean sliver motion

The deployment of GPS instruments along more than 2000 km along the Chilean subduction zone from Arica to the south, started more than 20 years ago. Whether in the beginning measurements of deformation had mainly the propose of monitoring the Andean evolution, soon was possible to determine interseismic velocities with higher precision as more positions were accumulated in mostly annual GPS campaigns (one site position per year). Several authors (Moreno *et al.* [2011]; Béjar-Pizarro *et al.* [2013]; Métois *et al.* [2016]) use this interseismic velocity field to obtain by inversion the coupling distribution along this subduction interface. Coupling distribution determined by elastic inversion of interseismic velocities considering the rotation of a rigid sliver (Métois *et al.* [2016]), results in a highly segmented pattern, with several large patches of high coupling alternated with low coupling zones (LCZ) (see figure 4.1). The importance on determining the degree of coupling in zones prone to break, as the ones identified as seismic gaps, lies in the good correspondence founded between ruptures of large earthquakes and areas of high coupling (Moreno *et al.* [2010]; Vigny *et al.* [2011]; Ruiz *et al.* [2014]; Métois *et al.* [2016]; Klein *et al.* [2017]). For instance, the region between (25° S - 30° S) is considered of high seismic hazard because it corresponds to an important seismic gap with no

mega earthquakes taking place since the last 1922 M_w 8.4 (Lomnitz [2004]). Here, the coupling distributes as 2 recognized high coupled zones (Métois *et al.* [2013ba 2016]), separated by a low coupled region at 28° S. Nevertheless, the northern identified asperity contains a low resolution gap (Taltal region) due to the lack of velocity measurements (see blurry zone in figure 4.1-right).

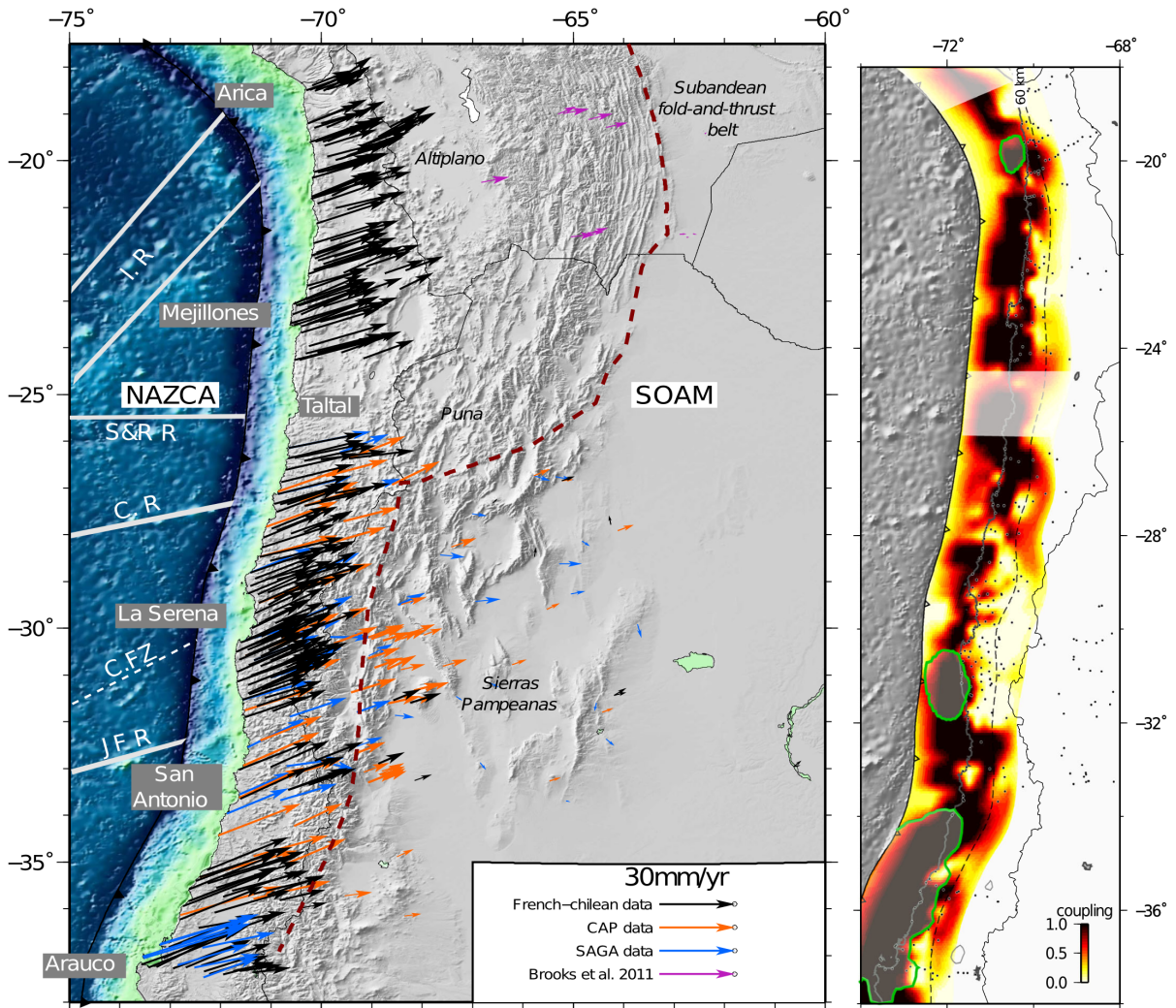


Figure 4.1: Modified figure from Métois *et al.* [2016]. Left: Horizontal interseismic velocities respect to South American plate product of continuous and campaign GPS data. Right: Coupling distribution obtained inverting for Andean sliver motion and coupling amount simultaneously. Green contours represent large recent rupture areas from north to south: Iquique 2014 (M_w 8.1), Illapel 2015 (M_w 8.4) and Maule 2010 (M_w 8.8).

The evolution since 2010 of the non-permanent GPS network in the northern part of this zone (figure 4.2) shows how the velocity gap corresponding to the region of Taltal is filled progressively. Today, new data is available for this zone product of several GPS campaigns started in 2013. Two of these campaigns were part of fieldwork activity we performed during this thesis. The first GPS campaign in April 2015 had a duration of 22 days. 21 instruments were deployed in 57 sites from Vallenar to Taltal (see figure 4.3). Our activities coincided with a large landslide that hit the whole region some weeks before, product of anomalous meteorological phenomena affecting the desert region. Despite the difficulties due to the damage that this event produced in several roads, obstructing the access to the stations, we succeed to measure 98% of the markers. Another successful campaign in the same region was performed during May/June 2016 with a duration of 16 days.

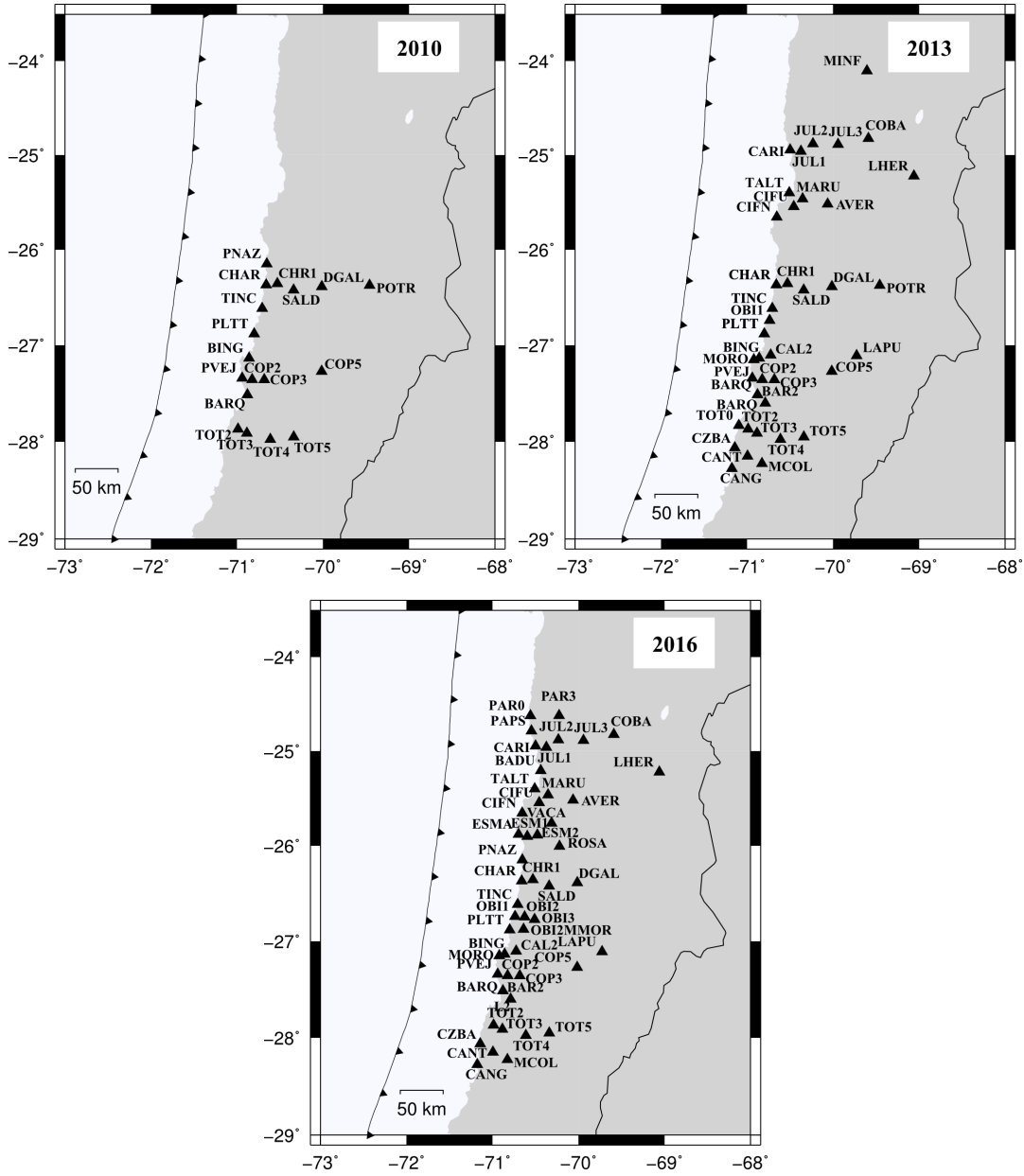


Figure 4.2: Evolution of the network of non-permanent markers between the regions of Atacama (south) y Taltal (north) from 2010 until today.

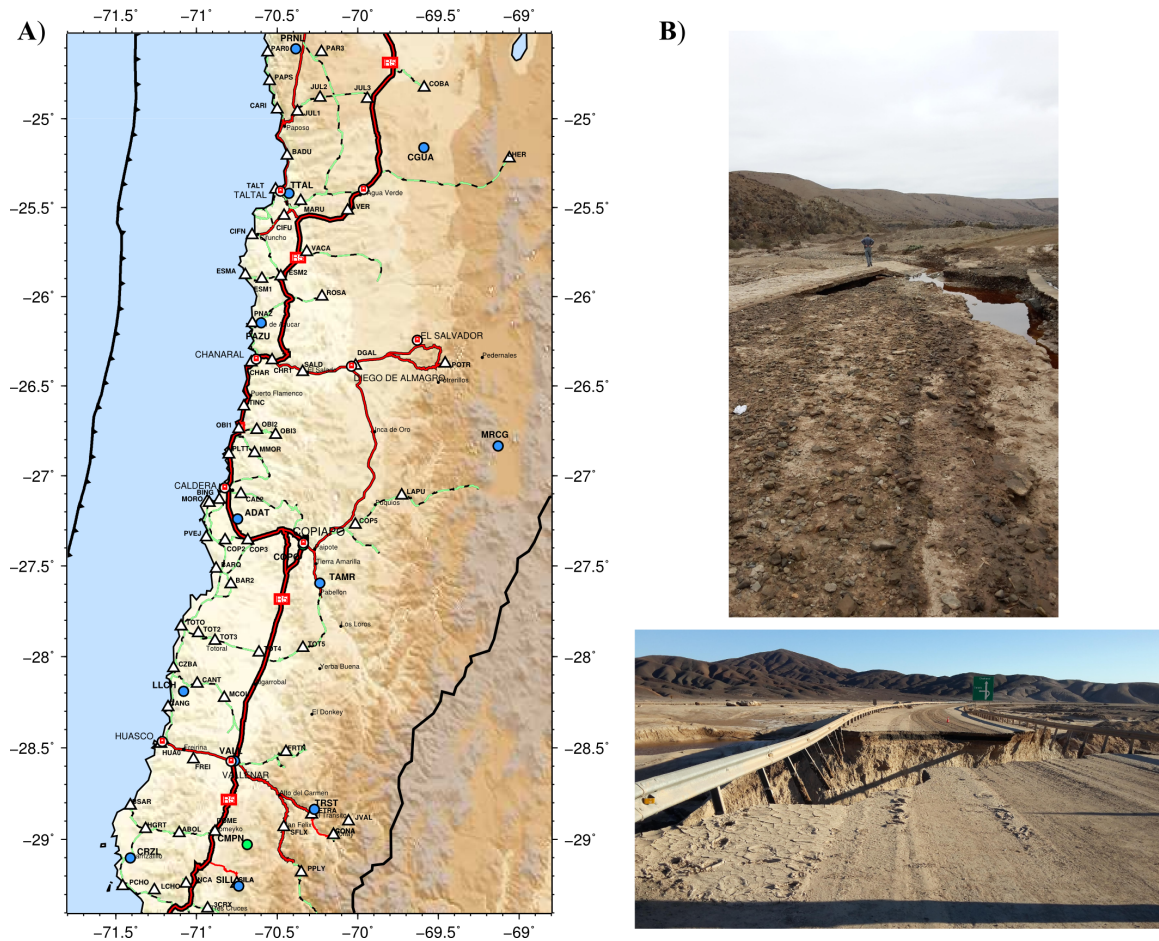


Figure 4.3: A: GPS network of the regions of Atacama and south Antofagasta. GPS markers are indicated as white triangles, while continuous sites are represented as blue circles. Relevant cities are indicated with red/white circles. B: Evidence of the damage produced by the landslide of 2015 in Atacama region. Many principal roads were blocked and a sector of the highway near Copiapo was cut in two.

Position measurements obtained from these 2 GPS surveys helped to obtain the first velocities for the region of Taltal. The new coupling pattern including these new vectors is obtained and analyzed in Klein *et al.* [2018]. This study gives insight regarding seismic hazard of one of the important seismic gaps of the Chilean subduction: the Atacama region. In the next pages, we add this publication and its supplementary information. We end the chapter with a brief review of the principal findings of this work.

Bridging the gap between North and Central Chile: insight from new GPS data on coupling complexities and the Andean sliver motion

E. Klein,^{1,2,*} M. Métois,³ G. Meneses,¹ C. Vigny¹ and A. Delorme⁴

¹Laboratoire de géologie, Département de Géosciences, ENS, CNRS, UMR 8538, PSL research University, F-75231 Paris CEDEX 5, France. E-mail: emklein@ucsd.edu

²Institut de Physique du Globe; UMR 7516, Université de Strasbourg/EOST, CNRS, F-67084 Strasbourg cedex, France

³Laboratoire de géologie de Lyon, Université de Lyon 1, ENS de Lyon, CNRS, UMR 5276 LGL-TPE, F-69622 Villeurbanne, France

⁴Institut de Physique du Globe de Paris, UMR 7154, F-75238 Paris cedex 05, France

Accepted 2018 March 8. Received 2018 March 6; in original form 2017 September 14

SUMMARY

GPS surveys have been extensively used over the past 20 yr to quantify crustal deformation associated with the Andean subduction zone in Chile. Such measurements revealed the coupling variations associated with the seismic segmentation of the subduction. However, because of data gaps mostly due to access difficulties, the Atacama–Antofagasta regions of North Chile remain poorly known. We present here an upgraded interseismic velocity field aggregating new data acquired between 2012 and 2016 in the region of Taltal (24°S–26°S), over a small-scale network of 20 benchmarks. This denser data set reveals a new complexity regarding the modelling methodology commonly used. We first show that a large-scale rigid Andean sliver, running from central to North Chile, does not allow to explain the velocities measured near the cordillera in the region of Taltal. This region exhibits an additional coherent block motion of almost 8 mm yr⁻¹ with respect to the inland motion generated by the rotation of the sliver proposed by, for example, Brooks *et al.* 2003; Métois *et al.* 2013, 2014, which works well everywhere else. Second, once this local block motion is taken into account, the coupling in the Taltal area is refined, which brings new insights about the subduction segmentation there. The Taltal area shows as a relative low in coupling (although coupling values are still high), potentially cutting a long section of the subduction into two independent highly coupled segments: the Paranal segment—north of Taltal, between 23°S and 25°S—and the Chañaral segment—south of Taltal, between 26°S and 28°S. These segments may rupture individually with magnitude ~8 earthquakes or simultaneously which would produce a larger earthquake, especially if a third segment (Atacama—more to the south—between 28°S and 29°S) is also involved.

Key words: Satellite geodesy; Seismic cycle; South America; Earthquake hazards; Subduction zone processes.

1 INTRODUCTION

Twenty years of GPS campaign carried out along the Chilean subduction interface allowed to estimate a very dense and quasi-continuous interseismic velocity field from the Peninsula of Arauco (38°S) up to Arica (18°S) (Klotz *et al.* 2001; Khazaradze *et al.* 2002; Brooks *et al.* 2003; Ruegg *et al.* 2009; Vigny *et al.* 2009; Chlieh *et al.* 2011; Métois *et al.* 2012, 2014, 2016). Interseismic velocities are commonly modelled as a combination of elastic deformation of the upper plate due to coupling on the subduction interface and the

rigid rotation of an Andean sliver block (Brooks *et al.* 2003; Chlieh *et al.* 2011; Métois *et al.* 2016). The coupling variations reveal a clear segmentation of the interface: long highly coupled segments separated by shorter low coupled zones (LCZs) (Moreno *et al.* 2011; Métois *et al.* 2012; Béjar-Pizarro *et al.* 2013; Métois *et al.* 2016). LCZs seem to behave as barriers to the propagation of megathrust ruptures and highly coupled segments correlate very well with the rupture zones of the recent megathrust earthquakes: Maule (M_w 8.8 2010, Moreno *et al.* 2010; Vigny *et al.* 2011; Métois *et al.* 2012), Iquique (M_w 8.2 2014, Schurr *et al.* 2014; Ruiz *et al.* 2014) and Illapel (M_w 8.3 2015, Ruiz *et al.* 2016; Métois *et al.* 2016; Klein *et al.* 2017). Moving forward, a challenging possibility opened by recent geodetic measurements in poorly known areas is to identify the potential location and extent of future large earthquakes. The last three megathrust earthquakes (2010, 2014, 2015) left three

* Now at: Institute of Geophysics and Planetary Physics, Scripps Institution of Oceanography, University of California, San Diego, La Jolla, CA 92093-0225, USA.

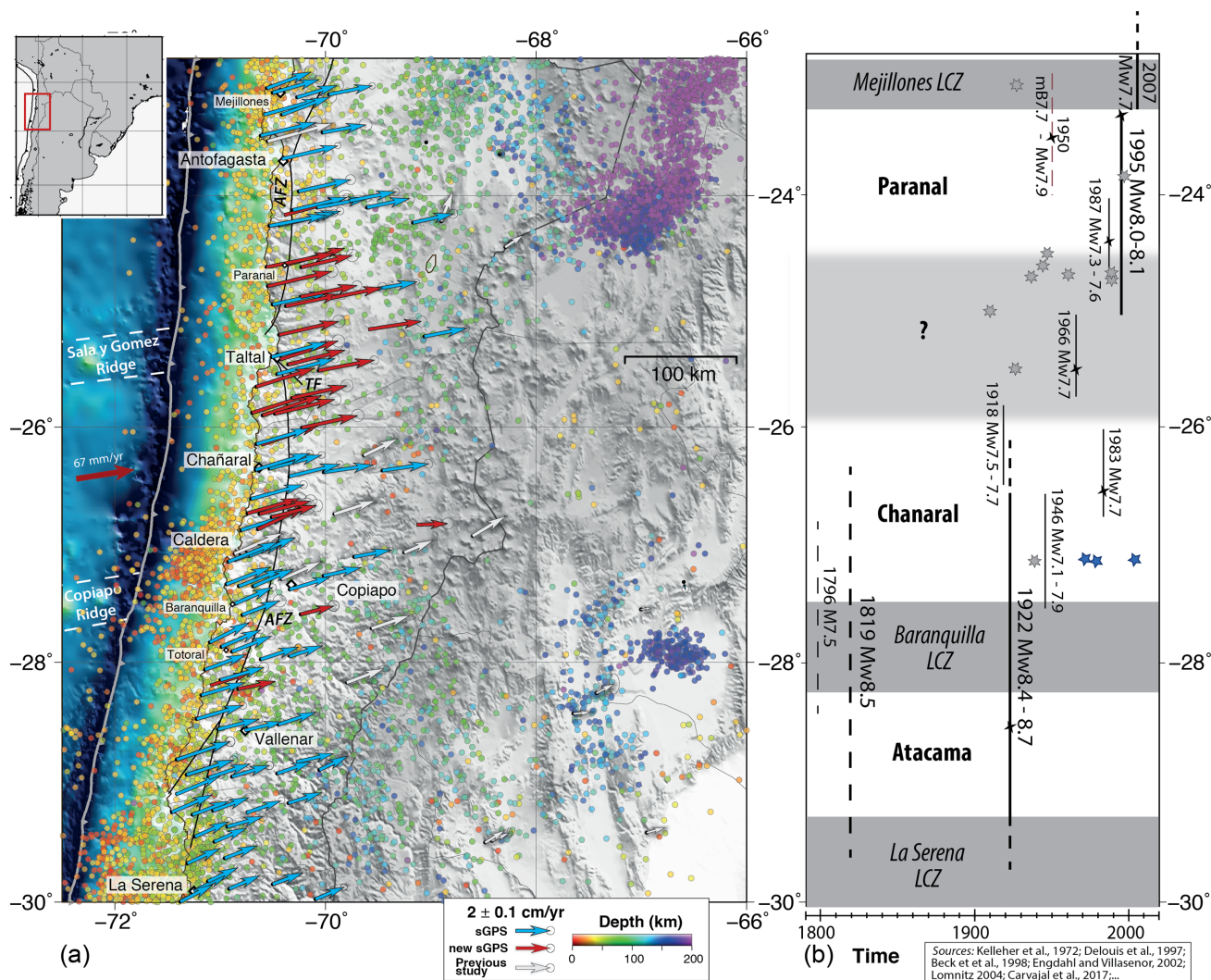


Figure 1. Inset: localization of the study; (a) interseismic velocity field (mm yr^{-1}) combined between 2010 and 2016 relative to stable South America. Background seismicity (1973–2017) from USGS, represented in colour scale as function of depth. Topography and bathymetry from ETOPO5, white lines represent the main bathymetric features of the Nazca plate (Álvarez *et al.* 2015). Black lines depict the Atacama Fault Zone (AFZ) and the Taltal Fault (TF) (Lemke *et al.* 1968; Armijo & Thiele 1990). (b) Segmentation (Métois *et al.* 2016) and historical seismicity as function of time, $M_w \sim 7$ earthquake epicentres are depicted by grey stars, seismic swarms by blue pentagrams. Black lines represent rupture zones of historical (dashed) and instrumental (continuous) of major events, their epicentres are depicted by black crosses.

apparent seismic gaps: (i) the Metropolitan region offshore Valparaiso (from 32°S to 34°S , last ruptured in 1906 and 1985); (ii) North Chile (between 20.5°S and 23°S unruptured since 1877); (iii) the Atacama region (between 30°S and 25°S). There, a seismic cycle of about a century seems to emerge with the occurrence of two $M+ 8.5$ earthquake in 1819 and 1922 (Lomnitz 2004; Engdahl & Villaseñor 2002; Fig. 1). A range of magnitudes have been proposed for the last 1922 earthquake: M_s 8.3 (Abe 1981), M_w 8.4 (Lomnitz 2004), recently re-evaluated to M_w 8.5–8.6 by (Carvajal *et al.* 2017).

This variety may also relate to a real complexity of the seismic sources. The 1819 earthquake is in fact a triple event occurring several days apart (3, 4 and 11 April) and the 1922 earthquake is also described as two great shocks following each other within 8 min (Lomnitz 1970). Possibly in adequacy with this complexity, GPS measurements in this region revealed high coupling values between 30°S and 23°S , but with a complex coupling pattern and at least two identified segments between 30°S and 25°S : Atacama and Chañaral (see Fig. 1b; Métois *et al.* 2016). Going north, another highly coupled segment has been imaged by the GPS data south of 23°S ,

the Paranal segment, where the 1995 M_w 8 Antofagasta earthquake could have broken only the deepest portion of the interface (Ruegg *et al.* 1996; Chlieh *et al.* 2004; Métois *et al.* 2013). Because of the late human settlement in this desertic region, whether and when the last megathrust rupture occurred there remains unknown.

The boundary between Atacama and Chañaral segments is marked by a low coupling portion, the Baranquilla LCZ (see Fig. 1b; Métois *et al.* 2014, 2016). By contrast, a boundary between Chañaral and Paranal segments may exist somewhere in the region of the city of Taltal (25.4°S) but is not clearly identified since this area remained one of the last data gap with only four geodetic markers installed and surveyed over a 200 km long area until now (Klotz *et al.* 2001). Therefore, the northern limit of the Chañaral segment and the southern limit of the Paranal segment remain unclear and the behaviour of the portion of interface in front of Taltal unknown, opening ways for two distinct scenarios. First, an LCZ separates the Chañaral and Paranal segments, behaving as a barrier to the propagation of past earthquake ruptures (1819 and 1922 along the Atacama segment and 1995 along the Paranal segment). This LCZ

could act similarly for future large earthquakes, occurring on either sides. This hypothesis could be supported by the presence of a known geological structure, the Sala y Gomez Ridge, which is subducted beneath the South American plate offshore the Taltal bay (see Fig. 1). Such a correlation between bathymetric structures and LCZs was already observed in Chile but remains debated (i.e. the Copiapó Ridge faces the LCZ of Baranquilla and the Challenger Fracture Zone faces the LCZ of La Serena, Métois *et al.* 2016; Collet *et al.* 2017). The second scenario implies a single and continuous 500–700 km long segment, highly coupled, capable of producing a giant earthquake of $M_w +9$, and only partially broken by the last known earthquakes. Such an earthquake, breaking the two segments of Chañaral and Paranal (and possibly a third one, Atacama, if going across the Baranquilla LCZ also), could trigger a major tsunami with devastating impact along a very large section of the Chilean coastline.

Here we present new interseismic velocities acquired in the area since 2012 and that help arbitrate between both hypothesis.

2 SEISMOTECTONIC CONTEXT

In this study, we focus on the Taltal area (24°S–26°S). At these latitudes, the Nazca plate subducts beneath the South American plate with a convergence rate of 67 mm yr⁻¹ (Angermann *et al.* 1999; Vigny *et al.* 2009). This area is characterized by the presence of one of the main crustal fault system in Chile, the Atacama Fault Zone (AFZ; Fig. 1a). Extending over more than 1000 km, it separates the uplifting Coastal Cordillera from the compressional fore-arc, but is characterized by very little seismic activity to date and most probably presently inactive (e.g. Arabasz 1968; Okada 1971; Armijo & Thiele 1990). It is divided in two segments cut at the latitude of the Taltal bay by the eponymous NW-SE fault, corresponding also to the latitude where the Sala y Gomez Ridge enters the subduction (Fig. 1). In the region of Taltal, maybe due to the limited completeness and historical continuity of the catalogue, only one major event is known, a M_w 7.7 earthquake in 1966 but several events of M_w close to 7 have occurred in the last century (Deschamps *et al.* 1980, Fig. 1). In the whole area considered here, the shallowest part of the interface shows little background seismicity, at the exception of the repeated occurrence of seismic swarms offshore Caldera (in 1973, 1979 and 2006; Holtkamp *et al.* 2011, Fig. 1b). On the contrary, the deep seismic activity appears very heterogeneous: we observe a clear gap of deep seismicity (>100 km depth) between 27°S and 25°S, contrasting with the northernmost part where intense deep seismicity is observed.

3 INTERSEISMIC VELOCITY FIELD

3.1 GPS data acquisition and processing

We installed and surveyed the first markers in the Atacama region immediately after the Maule earthquake of 2010 (Métois *et al.* 2014). Starting in 2012, 20 additional benchmarks were installed in the region of Taltal and measured annually. We also remeasured three CAP (Central Andes GPS Project, see Brooks *et al.* 2003) and eight SAGA (South America Geodynamic Activities, see Klotz *et al.* 2001) markers in the area, building a data set of almost 70 points. Overall, all included sites were measured at least three times and up to seven times (see Supporting Information Table S3).

We also include observations from the recently installed regional continuous stations operated by the Chilean National Seismolog-

ical Center (CSN) and from a selection of well-distributed permanent stations across the South American continent [IGS (Beutler *et al.* 1999), Red Argentina de Monitoreo Satelital Continuo (RAM-SAC) and Rede Brasileira de Monitoramento Continuo (RBMC) networks]. This data set is processed using the GAMIT/GLOBK software following the classical MIT methodology (Herring *et al.* 2010a,b). Daily solutions are combined using a global stabilization approach because of the post-seismic deformation following the Maule earthquake which affects many reference stations on the South American continent (see the Supporting Information and Klein *et al.* 2016). Plotted relative to the South American Plate defined by the NNR-Nuvel-1A model (25.4°S, 124.6°W, 0.11° Myr⁻¹, DeMets *et al.* 1994), estimated velocities of stations located on the stable part of the South American continent present a systematic northward residual of about 2 mm yr⁻¹ (see Supporting Information Fig. S1a). Therefore, we map our solution in a new Stable South America reference frame. The Euler pole location and angular velocity of this plate (20.9°S, 128.6°W, 0.122° Myr⁻¹) were inverted using a subset of seven sites that exhibit rigid block motion with respect to the ITRF2008 (Altamimi *et al.* 2012, Supporting Information Fig. S1b).

Interseismic velocities from Métois *et al.* (2013) north of the Peninsula of Mejillones are combined with this data set by applying the rotation vector estimated in this study. Note that data from previous and older studies (Klotz *et al.* 2001; Brooks *et al.* 2003, represented in Fig. 1) were not included in the solution for consistency purpose. We also excluded 2016 position measurements at several sites between Copiapó (27.3°S) and Chañaral (26.4°S) because they seemed to have been affected by a transient deformation of unknown origin occurring in this area between the two measurement campaigns of 2015 and 2016. Finally, we excluded 2016 measurements south of Copiapó to avoid any contamination due to the post-seismic deformation following the 2015 Illapel earthquake and the time-series of sites in the region of interest show that they are not contaminated further north (see Supporting Information Fig. S3). Because the 2014 Iquique earthquake that occurred at more than 400 km from the north of our network was only $M_w \sim 8.1$, we are confident that no post-seismic motion associated with this distant quake could contaminate our data set.

As mentioned previously, post-seismic deformation at continental scale has been highlighted following the 2010 Maule earthquake, not only directly in front of the rupture zone up to the east coast of Argentina, but also north of the rupture zone (Klein *et al.* 2016). This effect was indeed measurable in the region of the 2015 Illapel earthquake, where an increase of north-eastward velocity of some 2 mm yr⁻¹ was reported between 2010 and 2015 (Ruiz *et al.* 2016). Yet, north of La Serena (30°S), the residual velocities between pre-2010 and post-2010 velocities no longer show any consistent pattern expected from such processes, especially from campaign measurements (*cf.* fig. 4 in Ruiz *et al.* 2016). The studied region is located even further north, that is, some 1000 km from the Maule rupture zone. Time-series of both continuous stations and campaign sites are provided to confirm their linearity and therefore the quality of velocities estimation, also regarding seasonal signals (see Supporting Information Figs S2 and S3). A prediction of the viscoelastic model of post-seismic deformation following the Maule earthquake (Klein *et al.* 2016) also shows that this effect is not any more affecting significantly the surface deformation at these latitude (*cf.* Supporting Information Fig. S5).

Therefore, our data set encompasses only the linear trend determined at all sites over a relatively short time window (6 yr) but constrained with yearly measurements (up to 7 positions), hopefully

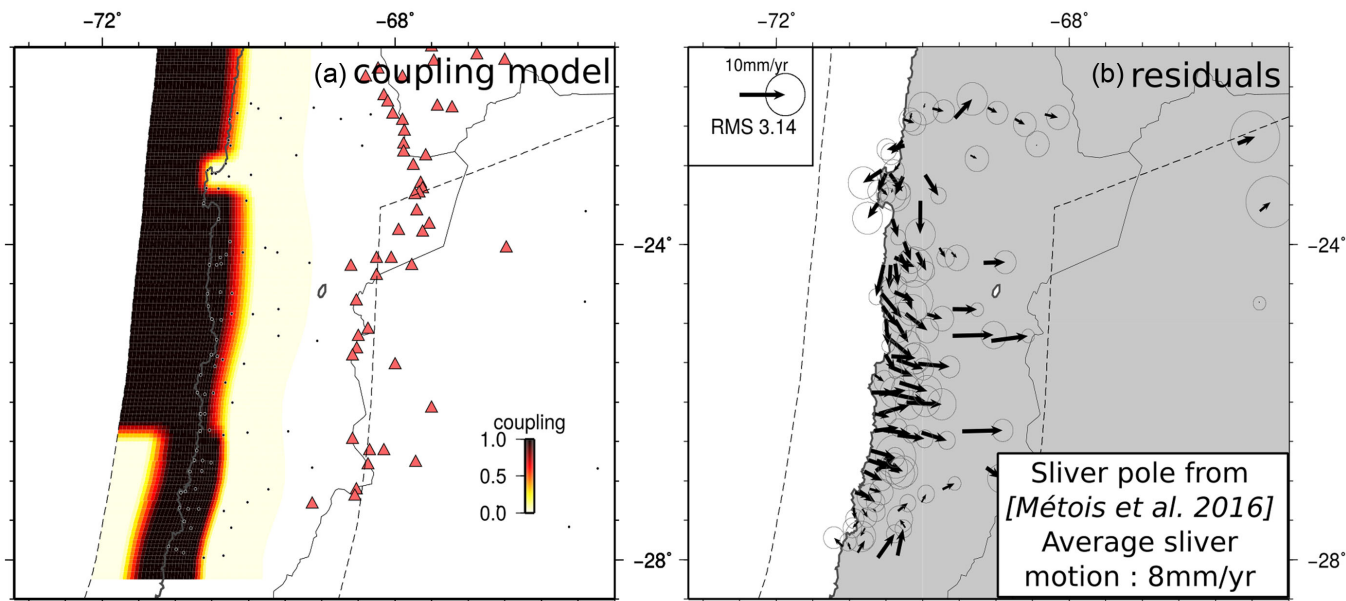


Figure 2. (a) Simplified forward coupling model derived from the best-model obtained by Métois *et al.* (2016) without the newly acquired data in the Taltal zone. The Mejillones LCZ is mimicked by an abrupt shallowing of the highly coupled zone. The Andean sliver (dashed grey lines) is moving around the Euler pole (56.37°S , 41.27°W and $-0.12^{\circ}\text{Myr}^{-1}$) and produces a 8 mm yr^{-1} northeastward motion. Red triangles are the active volcanoes. (b) Residuals (observations-predictions) and normalized root mean square.

representative of long term inter-seismic deformation. The vertical component of GPS data being less precise and more strongly affected by any hydrological signal than the horizontal component, a longer time span or the knowledge of the long-term hydrological signal derived from neighbouring cGPS stations is necessary to constrain a robust vertical velocity field. Therefore, since very few and recent cGPS stations are in place in the study area, we do not use vertical velocities in this study.

3.2 Velocity field description

In general, velocities show a typical interseismic loading pattern, with a north-eastern orientation and coastal vectors roughly parallel to the plate convergence direction (Fig. 1a). We observe the usual clockwise rotation and decrease of amplitude going inland. However, the velocity gradient varies along strike. A very strong gradient of almost 10 mm yr^{-1} over the first 30 km off the coast is detected between Caldera (27°S) and Chañaral (26.3°S) (*cf.* Supporting Information Fig. S6—profile E) when a much weaker gradient is observed north of (26.3°S). Moreover, coastal velocities increase significantly from 25 mm yr^{-1} in the south of the network (Totoral— 27.8°S , Supporting Information Fig. S6—profile G), to 40 mm yr^{-1} in the north (Paranal— 24.6°S , Supporting Information Fig. S6—profile B) while distance to the trench remains constant ($\sim 80\text{ km}$). Additionally, in the region of Taltal (25.5°S), inland velocities do not show the typical amplitude decrease and remain high with almost 30 mm yr^{-1} 200 km away from the trench (Supporting Information Fig. S6—profile C), compared to less than 20 mm yr^{-1} at the same distance from the trench but few hundreds of kilometres to the south (Supporting Information Fig. S6—profile F). This atypical pattern (weak gradient associated with high velocities) does not correspond to the standard elastic accumulation model and has often been interpreted as due to the motion of a uniformly rigid block in the Andes. However, other unidentified deformational processes could also be invoked such as distributed deformation on crustal faults over the mountain belt.

4 INTERSEISMIC COUPLING ALONG THE TALTAL AREA (24°S – 26°S)

Using the TDEFNODE code developed by McCaffrey (2015) (version 2015.04.20), the SLAB1.0 geometry (Hayes *et al.* 2012) and the modelling settings described in the supplementary material and in Métois *et al.* (2016), we first calculate the residuals produced by a simple bimodal coupling model (zero or 100 per cent coupling) derived from the previously published large-scale models by Métois *et al.* 2016; Fig. 2). In this model, the upper-crust deformation is mimicked by the combination of elastic deformation due to partial locking of the Nazca–South America megathrust together with the rigid motion of an Andean sliver relative to the stable interior of South America. The sliver motion is described by the Euler pole determined by Métois *et al.* (2016) and located in the South Atlantic ocean (56.37°S , 41.27°W) with an angular velocity of $-0.12^{\circ}\text{Myr}^{-1}$. It generates an average 8 mm yr^{-1} northeastward motion in our study area and nearly 10 mm yr^{-1} northeastward motion over the Bolivian fold-and-thrust belt front, consistently with the few GPS velocities available in the far-field (Brooks *et al.* 2011; Weiss *et al.* 2016).

This Andean sliver is a widely used modelling trick to remove from the observed velocity field the atypical translation-like motion observed in the middle to far field, that is, in the main cordillera, and that is roughly parallel to the convergence velocity between the Nazca and South American plates (Chlieh *et al.* 2011; Nocquet *et al.* 2014; Métois *et al.* 2016). Since the eastern boundaries of such a sliver remain vague and that it is rather likely that the Chilean upper plate deforms in a more complex way than a purely rigid body, we call for caution in interpreting such sliver motion. This coarse first-order model presented in Fig 2 highlights the defining feature of the Taltal area, while the residuals are small north of the Mejillones Peninsula (23.1°S) and south of Caldera (27°S), large ($>5\text{ mm yr}^{-1}$) and systematic eastward pointing residuals are observed over the Taltal area (24.5°S – 25.5°S , see Fig. 2). The transition between the residuals on the edges and those in the centre of the zone draw two counter-clockwise rotation cells. Such residuals demonstrate

that the 8 mm yr^{-1} translation-like motion attributed to the large scale Andean sliver motion is not sufficient to explain the large eastward velocities observed inland in the Taltal area. Whatever the coupling distribution used on the seismogenic zone (0–80 km depth), no acceptable fit could be obtained for the inland velocities at the latitude of Taltal if keeping a 8 mm yr^{-1} eastward moving sliver (see Supporting Information Fig. S8). Instead, a locally faster rotation of the Andean sliver relative to stable South America seems to be needed, thus challenging the sliver rigidity assumption used in previous studies (Chlieh *et al.* 2011; Nocquet *et al.* 2014; Métois *et al.* 2016).

Such a pattern of residuals could also suggest a viscous effect related to post-seismic deformation due to distant earthquakes. The viscoelastic relaxation following the Maule earthquake indeed predicts a whirlpool effect on both sides of the rupture zone (Klein *et al.* 2016): a clockwise rotation in the north of the rupture zone which ends with eastward velocities roughly aligned with inter-seismic velocities in the Illapel region (Ruiz *et al.* 2016), and a counter-clockwise rotation in the south of the Maule rupture zone. In the present case, two events would be necessary to explain the observed residuals: one in the north responsible for the counter-clockwise part of the rotation, and a second in the south generating the clockwise rotation (Fig. 2b). The amplitude of the residuals would imply recent and large events (no more than 50 yr ago and $M_w \sim 8.5$) for which we do not have any historical record. The 1922 Atacama earthquake occurred about a century ago, which is too long ago to produce such an effect. The 1995 Antofagasta earthquake that occurred 22 yr ago could only explain the residuals in the northern part of our study area (between Antofagasta and Taltal) but not south of Taltal. Therefore, the unusually large middle to far field eastward velocities observed in the Taltal area could not be simply explained by post-seismic rebound induced by any of the known seismic events in the area (1922 Atacama or 1995 Antofagasta).

To date, too few GPS velocities spanning the inner cordillera deformation are available to build a consistent alternative model of the Andes deformation (Brooks *et al.* 2003; McFarland *et al.* 2017). Therefore, the rigid-sliver modelling trick remains the simplest assumption in the frame of a purely elastic modelling strategy, to account for the non-elastic deformation of the Chilean upper plate and correctly invert for the coupling distribution on the megathrust (see Supporting Information Fig. S10). Since this cannot be done here with a single large scale rigid sliver over the entire margin (38 to 18°S), we chose to model the velocity field observed in the Taltal area by inverting simultaneously for the coupling distribution on the megathrust and the Euler pole of a local sliver. Fig. 3 presents three models obtained with varying constraints on the coupling distribution: (i) imposed down-dip decrease, (ii) Gaussian distribution of coupling with depth inverting for amplitude, central depth and width of the Gaussian, and (iii) independent functions of coupling with depth. All three distributions lead to reasonable fit to the data with nRMS < 1.7 and non-systematic residuals.

All three models (Fig. 3) highlight significant along-strike and along-dip changes in the amount and distribution of coupling on the subduction plane north and south of the Taltal bay (25.5°S). First, when coupling is forced to decrease with depth, the best model exhibits a highly coupled zone offshore the Paranal segment, while coupling is lower and deepens in the Chañaral segment. When coupling varies as a Gaussian function of depth, the fit to the data is slightly improved by reducing the sliver motion to 16.6 mm yr^{-1} and by allowing full coupling on the deep part of the seismogenic zone, from 20 to 60 km, in the Chañaral segment. When only a 2-D smoothing is applied on nodes following the shape spread

smoothing technique proposed by McCaffrey (2015), the nRMS is reduced (1.57 versus 1.69 and 1.65 for previous models), the best sliver motion is $\sim 16 \text{ mm yr}^{-1}$, and the same shallowing of the highly coupled zone is observed in the Paranal segment compared to the Chañaral segment. Increasing step by step the complexity of the coupling distribution brings out the common and robust features that are really required to fit the data and helps defining a reliable segmentation of the margin: two highly coupled segments named after Métois *et al.* (2016), the Paranal segment from 23°S to 25°S where the highly coupled zone is shallow, and the Chañaral segment from 25°S to 27°S where the highly coupled zone is deeper, are separated by an anomalous low in coupling in the Taltal bay.

5 DISCUSSION

Several aspects of the best model (thus corresponding to the third model presented on the previous section) showed in Fig. 5(c) have to be considered carefully: first, coupling is not resolved over the first 10 km depth of the slab (see sensitivity map in Fig. 4 and checker board tests in Supporting Information Fig. S7) preventing us from interpreting the value of the very shallow coupling in terms of tsunami hazard for instance. Second, the hypothesis of a local rigid sliver distinct from a large scale Andean micro-plate is questionable (see Section 5.1). However, all models agree on two major points: (i) the observed velocities in the Taltal area require the local Andean sliver to rotate around a Euler pole still located in the South Atlantic ocean but producing a $16\text{--}17 \text{ mm yr}^{-1}$ northeastward translation towards South America, that is, more than 8 mm yr^{-1} higher than the rigid motion expected by Métois *et al.* (2016); (ii) the Taltal bay (25.5°S) is a transition zone between two highly coupled segments: the Paranal segment to the north and the Chañaral segment to the south.

5.1 The Andean sliver: one rigid block?

There is a trade-off between the amount of coupling, its distribution with depth on one side and the amplitude of the sliver rotation on the other side: inverting for coupling variations only while using the predicted 8 mm yr^{-1} Andean sliver motion in the area would fail to retrieve the observed velocities and would require a deep and probably unrealistic highly coupled zone (down to $\sim 70 \text{ km}$ depth, nRMS 2.39; see Supporting Information Fig. S8). Opposite, a larger than 16 mm yr^{-1} Andean sliver motion would decrease the average coupling and reduce the highly coupled zones to the shallowest portion of the slab. This trade-off has been explored in details by several authors (for instance in Chlieh *et al.* 2011; Métois *et al.* 2013, 2016). Therefore, our main finding showing a shallowing of the highly coupled zone in the Paranal segment compared to the deepening of the southernmost Chañaral segment when using a local homogeneous sliver rotation could also result from a progressive increase in the back-arc rotation amount from north to south, between 25°S and 27°S . As stated before, too few GPS velocities are still available in the medium to far field away from the subduction zone to untangle this issue. It is to note however that the published velocity fields spanning the eastern front of the Andes so far (Brooks *et al.* 2011; McFarland *et al.* 2017) are consistent with the average motion predicted locally by our rigid-Andes approach.

To the best of our knowledge, our study raises a new concern: a simple large scale rigid Andean sliver scheme does not provide a satisfactory physical model for describing the large scale straining of the Andes. Indeed, no common Euler motion could retrieve

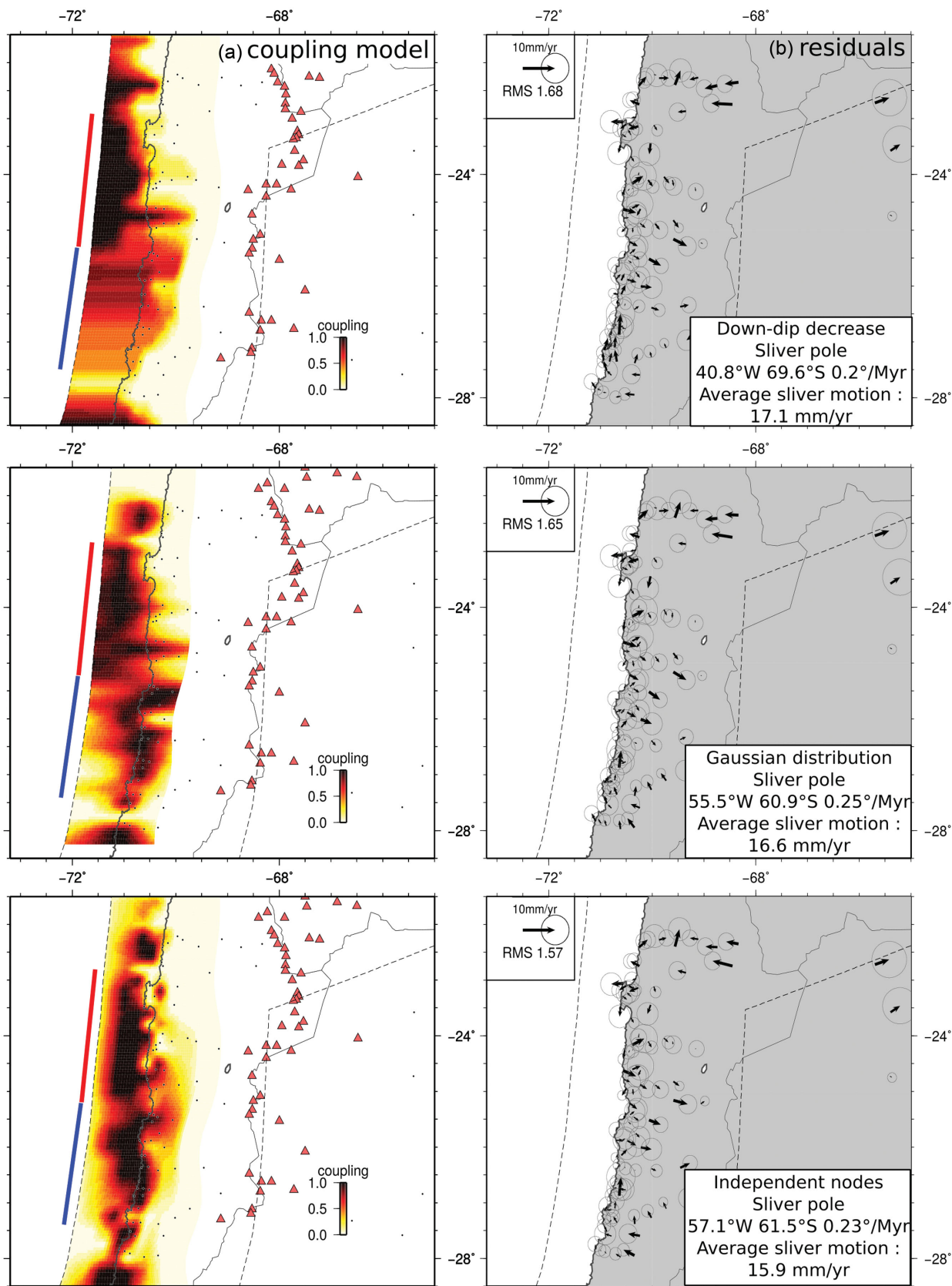


Figure 3. Coupling distributions (a), associated residuals and sliver motion (b) inverted using increasing constrains on the coupling variation with depth. a: coupling is colour-coded, red triangles are active volcanoes. Red and blue lines delineate the Paranal and Chañaral segments. b: normalized RMS is plotted on the upper left corner while the Euler pole position and average motion induced on the sliver are indicated on the lower-right corner. Top : coupling is forced to decrease with depth. Centre : coupling follows a Gaussian distribution with depth (amplitude and width are inverted). Down: coupling is independent on each nodes but 2-D smoothing is applied to avoid numerical instabilities.

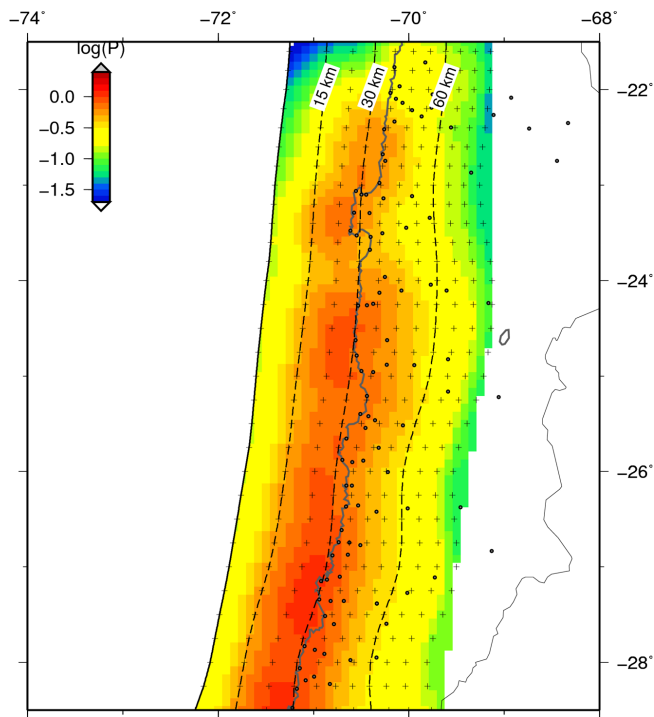


Figure 4. Sensitivity of the velocity observed in our network to unit coupling on each node of the slab. Each subfault of the interface is coloured by the log of the sum of the displacements (P in mm yr^{-1}) at GPS stations (dots) due to unit slip on the nearest grid node. The highest the displacement produced by unit slip on one subfault, the highest the sensitivity of the network to coupling/slip on this subfault (see Loveless & Meade 2011, for further details on the method). Black crosses are slab nodes projection at surface.

the surface velocities observed on the western cordillera front in North Chile and metropolitan area together with the ones observed in the Taltal region. The motions for each of these zones inverted by (Métois *et al.* 2013, 2014) and this study imply a 10 mm yr^{-1} north-eastward motion of the North Chile area (from 18°S to 24°S , confirmed by the recent velocities acquired by Weiss *et al.* (2016) in Bolivia), $\sim 16 \text{ mm yr}^{-1}$ in the Taltal area (24°S to 27°S , confirmed by the recent paper by McFarland *et al.* (2017) and less than 5 mm yr^{-1} south of La Serena (30°S). No large or small scale shear zone, parallel to the convergence velocity and that could accommodate such gradients on the long-term has been detected to date. A possible explanation for this discrepancy is that the so-called ‘Andean sliver’ which north and south boundaries remain furthermore unclear, is rather straining in a more distributed way that remains to be understood. This study therefore challenges the commonly used rigid Andean sliver hypothesis.

Another possibility would be that part of the motion interpreted so far as sliver-related would result from the improper elastic assumption used in our modelling. Previous studies showed that viscoelastic assumption of the asthenosphere properties would predict significantly larger horizontal velocities in the medium field at the end of the cycle (e.g. in the Indonesian subduction zone or in North Chile, Trubienko *et al.* 2013; Li *et al.* 2015). Therefore, at least part of the deformation associated with rigid blocks in previous elastic models (eg Simons *et al.* 2007; Métois *et al.* 2016) could actually be related to the seismic cycle on the subduction interface, assuming viscoelastic properties of the asthenosphere. This hypothesis, going beyond the scope of the present work, will be further investigated in future studies. It is to note that assuming a purely elastic behaviour

rather than a viscoelastic behaviour impacts only very slightly the along-strike coupling variations that depends on the strain rate in the very near field of the fault ($<150 \text{ km}$ from the trench, see for instance Li *et al.* 2015). We are therefore confident that our analysis in terms of kinematic segmentation of the margin remains correct.

5.2 The Taltal transition zone

The Taltal bay marks in all models a depth transition between the highly coupled segments of Chañaral and Paranal (Fig. 5b). Indeed, the average depth of the highly coupled zone is close to 20 km depth for the Paranal segment and 30 km depth (close to being under the coastline) for the Chañaral segment, as highlighted in Fig. 5(a). The shallower locking depth in the Paranal segment compared to the Chañaral segment could result from the 1995 Antofagasta event that may have increased the stress on the unruptured shallowest part of the interface in the case the rupture did not reach the trench, which remains debated (Ruegg *et al.* 1996; Delouis *et al.* 1997). The Taltal area presents also a local minimum in the average coupling calculated on the convergence direction on 20 km along-strike wide sliding windows, whatever the depth interval chosen to integrate the coupling coefficient (see Fig. 5b). However, it is to note that the average coupling in the Taltal area remains high (~ 50 per cent) compared to many low coupling zones (LCZ) previously identified (e.g. the Mejillones LCZ (23.1°S) or the Baranquilla LCZ (27.5°S); Métois *et al.* 2016, see Fig. 5c). As stated in Section 1, the Taltal bay is the place where (i) the Sala y Gomez volcanic ridge, roughly parallel to the convergence direction, subducts (Fisher & Norris 1960; Maksymowicz 2015), (ii) the Antofagasta segment of the Atacama Fault Zone ends (Arabasz 1968; Armijo & Thiele 1990), (iii) several seismic events of $M_w < 7$ (Deschamps *et al.* 1980) occurred in the past, and (iv) the 1995 Antofagasta and the 1922 Copiapó earthquakes stopped (see Figs 1b and 5d). The whole Taltal region correlates also with a deficit in very deep seismicity compared to the La Serena and North Chile area (Fig. 1a).

Together, these observations confirm that the Taltal bay (25.5°S) plays an important role in the segmentation of the megathrust interface and opens the question of the physical control of the coupling coefficient. Indeed, the Taltal low coupling anomaly could either be controlled by the subducting sea mounts of the Sala y Gomez ridge, which is supported by the apparent parallelism between the low coupling area and the ridge orientation, or controlled by the upper-plate properties and complexities like the Atacama Fault Zone for instance. A detailed analysis of the background seismicity and in-depth imaging of the margin would be required to untangle these controlling factors (interface roughness, fluid amount, connection between crustal faults and the subduction plane etc.).

5.3 Plausible scenarios for future ruptures

Better understanding the coupling distribution from the Mejillones LCZ (23.1°S) to the Baranquilla LCZ (27.5°S) has a direct impact on rupture scenarios that could be assessed for the region. Previous studies had detected the onset of the Paranal and Chañaral segments by imaging high coupling in front of Antofagasta (Métois *et al.* 2013) and north of Copiapó (Métois *et al.* 2014). However, whether these two segments were continuous and therefore able to rupture with a very large earthquake or separated by an LCZ capable of blocking rupture propagation was unknown. Our results show that the Taltal area has a unique behaviour in terms of kinematics, seismicity and morphology and that a narrow low in coupling is

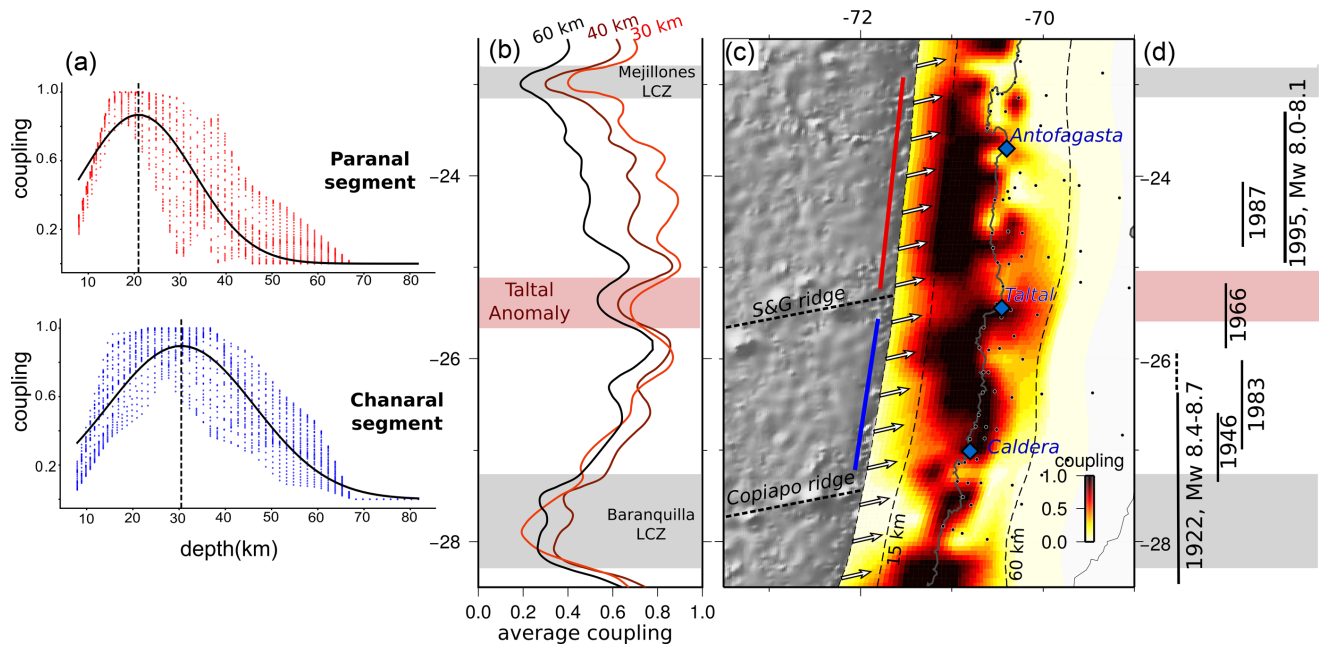


Figure 5. Best coupling model characteristics. (a) Variation of the coupling coefficient with depth along the Paranal (red dots, up) and Chañaral segments (blue dots, down) and best-fit Gaussian (black curve). (b) Average coupling variation with latitude. The average coupling is calculated on 20 km along-strike wide sliding windows in the convergence direction and every 10 km along the trench. Coupling is either integrated from 10 to 30 km (red curve), from 10 to 40 km (brown curve) and on the entire seismogenic zone (from 10 to 60 km, black curve). (c) Coupling model presented in Fig. 3 with 2-D smoothing applied on independent nodes. Dashed curves: 15 and 60 km depth slab contours. White arrows: Nazca–South America convergence direction. Red and blue bold lines depict the extent of the Paranal and Chañaral segments, respectively as in Fig. 3. Dashed bold lines: main bathymetric features, aseismic ridges. Black dots: GPS stations used in this study. (d) Recall of the historical ruptures extends. Reddish area: Taltal low coupling area.

observed in the Taltal bay. This Taltal anomaly could result from a more velocity-strengthening behaviour of the interface under the bay, therefore able to creep during the interseismic period and to slow-down or stop a rupture coming from the neighbouring segments depending on its size. However, the average coupling under the Taltal bay is ~ 50 per cent, that is, higher than other LCZ detected along the margin, suggesting that this zone may not be fully free to creep during the interseismic period. Rather, we suggest that this intermediate coupling area is apparently partially locked due to the stress shadows associated with the neighbouring velocity-weakening and highly locked asperities (see Métois *et al.* 2012; Hetland & Simons 2010, for discussion).

These highly coupled segments north and south of the Taltal bay could therefore rupture alone with an M_w 8+ earthquake that would be stopped by the Taltal velocity-strengthening area, alike the 1819, 1922, 1987 and 1995 earthquakes; or jointly, if the rupture would propagate through the Taltal LCZ.

Such a velocity-strengthening narrow zone surrounded by velocity-weakening asperities is also a good candidate for nucleation and initiation of a rupture since stress is prone to accumulate more in these zones of mechanical transition. At least two of the three recent megathrust earthquakes that stroke Chile since 2010 nucleated in a zone of intermediate coupling, that is, at the transition between velocity-strengthening and velocity-weakening behaviour: the 2010 Maule earthquake nucleated in an area that experienced very high rates of aftershocks and large post-seismic slip (Vigny *et al.* 2011; Métois *et al.* 2012) and the 2014 Iquique earthquake nucleation sequence developed in the Iquique LCZ and around the Camarones segment (Ruiz *et al.* 2014; Schurr *et al.* 2014).

These observations suggest that the Taltal bay could very probably host the nucleation point of a future megathrust earthquake that could therefore propagate north and south, rupturing the Paranal and

Chañaral segments jointly. Such megathrust earthquake rupturing the interface from Mejillones to Baranquilla (i.e. 525 km) would reach at least a magnitude close to M_w 8.5, and possibly even larger if it also cuts across the Baranquilla LCZ and involves the Atacama segment.

The two previous megathrust earthquakes of 1819 and 1922 likely ruptured the two southern segments of Atacama and Chañaral. Their ruptures were complex, involving two or three main shocks (Willis 1929), which is compatible with simultaneous or rapidly subsequent ruptures of several segments, first Atacama, then Chañaral. Since no damages were reported north of the city of Taltal, we conclude that the rupture was probably stopped by the Taltal LCZ and did not propagate north of it, into the Paranal segment. A repeat of these earthquakes is plausible to occur soon, since both segments are fully coupled and have accumulated enough deformation since 1922 to produce M_w 8+ earthquakes. However, a propagation across the Taltal LCZ into the northern most segment of Paranal is a distinct possibility given its relative weakness. Another scenario of a northern rupture involving only Paranal and Chañaral segments but not Atacama is also plausible even though not supported by any known historical earthquake, because of the presence of the stronger Baranquilla LCZ to the south. Any of these two scenarios involving rupture of the Paranal segment (on top of other segments) would not only increase the magnitude of the expected earthquake but more importantly the magnitude of the subsequent tsunami, since the coupling in this northernmost segment seems to extend at shallow depths. Recently, (Carvajal *et al.* 2017) have revised the magnitude of the 1922 earthquake to M_w 8.6 based on far-field tsunami data. A large tsunami produced by the rupture of the Atacama and Chañaral segments could result from coupling extending to shallower depth before 1922 than presently in the ruptured segments (Atacama and Chañaral) implying either (i) temporal variations of the coupling coefficient during the seismic cycle or (ii) underestimated coupling

in these shallow area due to low sensitivity of our data, or could result from dynamic propagation of the rupture up to the trench.

In all cases, because of the poor knowledge of historical megathrusts in the region, the Taltal area offers a unique opportunity to test the capability of coupling models alone to sustain correct rupture scenarios.

ACKNOWLEDGEMENTS

This work was performed in the frame of the French-Chilean LiA ‘Montessus de Ballore’ with financial support of the French Agence Nationale de la Recherche (ANR-2012-BS06-004) and the European Marie Curie Initial Training Network *Zooming in between plates* (ITN FP7 Grant Agreement no.: 604713). We are also thankful to the French Institut National des Sciences de l’Univers (INSU-CNRS) and the Réseau Sismologique & Géodésique Français (RESIF) for providing the geodetic instruments for all campaigns. We would like to warmly thank E. Saldaño, M.C. Valderas-Bermejo and all the CSN personnel, for their precious help for the field work. We thank M. Moreno for access to previous data sets on GFZ benchmarks that were remeasured for this study. We finally thank our two anonymous reviewers for their constructive comments, which helped to improve this manuscript.

REFERENCES

Abe, K., 1981. Magnitudes of large shallow earthquakes from 1904 to 1980, *Phys. Earth planet. Inter.*, **27**(1), 72–92.

Altamimi, Z., Métivier, L. & Collilieux, X., 2012. ITRF2008 plate motion model, *J. geophys. Res.*, **117**(B7), B07402, doi:10.1029/2011JB008930.

Álvarez, O., Gimenez, M., Folguera, A., Spagnotto, S., Bustos, E., Baez, W. & Braitenberg, C., 2015. New evidence about the subduction of the Copiapó ridge beneath South America, and its connection with the Chilean–Pampean flat slab, tracked by satellite GOCE and EGM2008 models, *J. Geodyn.*, **91**, 65–88.

Angermann, D., Klotz, J. & Reigber, C., 1999. Space-geodetic estimation of the Nazca–South America euler vector, *Earth planet. Sci. Lett.*, **171**(3), 329–334.

Arabasz, W.J., 1968. Geologic structure of the Taltal area, northern Chile, in relation to the earthquake of December 28, 1966, *Bull. seism. Soc. Am.*, **58**(3), 835–842.

Armijo, R. & Thiele, R., 1990. Active faulting in northern Chile: ramp stacking and lateral decoupling along a subduction plate boundary?, *Earth planet. Sci. Lett.*, **98**(1), 40–61.

Béjar-Pizarro, M., Socquet, A., Armijo, R., Carrizo, D., Genrich, J. & Simons, M., 2013. Andean structural control on interseismic coupling in the North Chile subduction zone, *Nat. Geosci.*, **6**(6), 462–467.

Beutler, G., Rothacher, M., Schaer, S., Springer, T., Kouba, J. & Neilan, R., 1999. The International GPS Service (IGS): an interdisciplinary service in support of earth sciences, *Adv. Space Res.*, **23**(4), 631–653.

Brooks, B.A., Bevis, M., Smalley, R., Kendrick, E., Manceda, R., Lauría, E., Maturana, R. & Araujo, M., 2003. Crustal motion in the southern Andes (26°–36° S): do the Andes behave like a microplate?, *Geochem. Geophys. Geosyst.*, **4**(10), doi:10.1029/2003GC000505.

Brooks, B.A. et al., 2011. Orogenic-wedge deformation and potential for great earthquakes in the central Andean backarc, *Nat. Geosci.*, **4**(6), 380–383.

Carvajal, M., Cisternas, M., Gubler, A., Catalán, P., Winckler, P. & Wesson, R., 2017. Reexamination of the magnitudes for the 1906 and 1922 Chilean earthquakes using Japanese tsunami amplitudes: implications for source depth constraints, *J. geophys. Res.*, **122**(1), 4–17.

Chlieh, M., de Chabaliér, J., Ruegg, J., Armijo, R., Dmowska, R., Campos, J. & Feigl, K.L., 2004. Crustal deformation and fault slip during the seismic cycle in the north Chile subduction zone, from GPS and InSAR observations, *Geophys. J. Int.*, **158**, 695–711.

Chlieh, M. et al., 2011. Interseismic coupling and seismic potential along the central Andes subduction zone, *J. geophys. Res.*, **116**, doi:10.1029/2010JB008166.

Collot, J.-Y. et al., 2017. Subducted oceanic relief locks the shallow megathrust in central Ecuador, *J. geophys. Res.*, **122**(5), 3286–3305.

Delouis, B. et al., 1997. The $M_w = 8.0$ Antofagasta (northern Chile) earthquake of 30 July 1995: a precursor to the end of the large 1877 gap, *Bull. seism. Soc. Am.*, **87**(2), 427–445.

DeMets, C., Gordon, R.G., Argus, D.F. & Stein, S., 1994. Effect of recent revisions to the geomagnetic reversal time scale on estimates of current plate motions, *Geophys. Res. Lett.*, **21**(20), 2191–2194.

Deschamps, A., Lyon-Caen, H. & Madariaga, R., 1980. Etude du tremblement de terre de Taltal (Chili, 1966) à partir des ondes sismiques de longue période, *Ann. Geophys.*, **36**(2), 179–190.

Engdahl, E.R. & Villaseñor, A., 2002. 41 Global seismicity: 1900–1999, *Int. Geophys.*, **81**, 665–690.

Fisher, R.L. & Norris, R.M., 1960. Bathymetry and geology of Sala y Gomez, southeast Pacific, *Bull. geol. Soc. Am.*, **71**(4), 497–502.

Hayes, G.P., Wald, D.J. & Johnson, R.L., 2012. Slab1.0: A three-dimensional model of global subduction zone geometries, *J. geophys. Res.*, **117**(B1), doi:10.1029/2011JB008524.

Herring, T., King, R. & McClusky, S.C., 2010a. GAMIT: GPS analysis at MIT, release 10.4.

Herring, T., King, R. & McClusky, S.C., 2010b. GLOBK: Global Kalman filter VLBI and GPS analysis program release 10.4.

Hetland, E. & Simons, M., 2010. Post-seismic and interseismic fault creep II: transient creep and interseismic stress shadows on megathrusts, *Geophys. J. Int.*, **181**(1), 99–112.

Holtkamp, S.G., Pritchard, M.E. & Lohman, R.B., 2011. Earthquake swarms in South America, *Geophys. J. Int.*, **187**(1), 128–146.

Khazaradze, G., Wang, K., Klotz, J., Hu, Y. & He, J., 2002. Prolonged post-seismic deformation of the 1960 great Chile earthquake and implications for mantle rheology, *Geophys. Res. Lett.*, **29**(22), doi:10.1029/2002GL015986.

Klein, E., Fleitout, L., Vigny, C. & Garaud, J., 2016. Afterslip and viscoelastic relaxation model inferred from the large scale postseismic deformation following the 2010 M_w 8.8 Maule earthquake (Chile), *Geophys. J. Int.*, **205**(3), 1455–1472.

Klein, E., Vigny, C., Fleitout, L., Grandin, R., Jolivet, R., Rivera, E. & Métois, M., 2017. A comprehensive analysis of the 2015 M_w 8.3 Illapel Earthquake from GPS and InSAR data, *Phys. Earth planet. Inter.*, **469**, 123–134.

Klotz, J., Khazaradze, G., Angermann, D., Reigber, C., Perdomo, R. & Cifuentes, O., 2001. Earthquake cycle dominates contemporary crustal deformation in central and southern Andes, *Earth planet. Sci. Lett.*, **193**(3), 437–446.

Lemke, R.W., Dobrovolsky, E., Alvarez, S. L. & Ortiz, O. F., 1968. Geologic and related effects of the Taltal earthquake, Chile, of December 28, 1966, *Bull. seism. Soc. Am.*, **58**(3), 851–859.

Li, S., Moreno, M., Bedford, J., Rosenau, M. & Oncken, O., 2015. Revisiting visco-elastic effects on interseismic deformation and locking degree: a case study of the Peru–North Chile subduction zone, *J. geophys. Res.*, **120**(6), 4522–4538.

Lomnitz, C., 1970. Major earthquakes and tsunamis in Chile during the period 1535 to 1955, *Geol. Rundsch.*, **59**(3), 938–960.

Lomnitz, C., 2004. Major earthquakes of Chile: a historical survey, 1535–1960, *Seismol. Res. Lett.*, **75**, 368–378.

Loveless, J.P. & Meade, B.J., 2011. Spatial correlation of interseismic coupling and coseismic rupture extent of the 2011 $M_w = 9.0$ Tohoku-Oki earthquake, *Geophys. Res. Lett.*, **38**(17), doi:10.1029/2011GL048561.

Maksymowicz, A., 2015. The geometry of the Chilean continental wedge: Tectonic segmentation of subduction processes off Chile, *Tectonophysics*, **659**, 183–196.

McCaffrey, R., 2015. Tdefnode user’s manual version 2015.07. 30.

McFarland, P.K., Bennett, R.A., Alvarado, P. & DeCelles, P.G., 2017. Rapid geodetic shortening across the eastern cordillera of NW Argentina observed by the Puna-Andes GPS array, *J. geophys. Res.*, **122**(10), 8600–8623.

- Métois, M., Vigny, C. & Socquet, A., 2012. Interseismic coupling, segmentation and mechanical behavior of the central Chile subduction zone, *J. geophys. Res.*, **662**, 120–131.
- Métois, M. *et al.*, 2013. Revisiting the north Chile seismic gap segmentation using GPS-derived interseismic coupling, *Geophys. J. Int.*, **194**(3), 1283–1294.
- Métois, M., Vigny, C., Socquet, A., Delorme, A., Morvan, S., Ortega, I. & Valderas-Bermejo, C.-M., 2014. GPS-derived interseismic coupling on the subduction and seismic hazards in the Atacama region, Chile, *Geophys. J. Int.*, **196**(2), 644–655.
- Métois, M., Vigny, C. & Socquet, A., 2016. Interseismic coupling, megathrust earthquakes and seismic swarms along the Chilean subduction zone (38–18° S), *Pure appl. Geophys.*, **173**(5), 1431–1449.
- Moreno, M., Rosenau, M. & Oncken, O., 2010. 2010 Maule earthquake slip correlates with pre-seismic locking of Andean subduction zone, *Nature*, **467**(7312), 198–202.
- Moreno, M. *et al.*, 2011. Heterogeneous plate locking in the South–Central Chile subduction zone: building up the next great earthquake, *Earth planet. Sci. Lett.*, **305**, 413–424.
- Nocquet, J.-M. *et al.*, 2014. Motion of the continental slivers and creeping subduction in the northern Andes, *Nat. Geosci.*, **7**(4), 287–291.
- Okada, A., 1971. On the neotectonics of the Atacama Fault Zone region. preliminary notes on late Cenozoic faulting and geomorphic development of the coast range of northern Chile, *Bull. Dep. Geogr. Kyoto Univ.*, **3**, 47–65.
- Ruegg, J.-C. *et al.*, 1996. The $M_w = 8.1$ Antofagasta (North Chile) earthquake of July 30, 1995: first results from teleseismic and geodetic data, *Geophys. Res. Lett.*, **23**(9), 917–920.
- Ruegg, J.-C. *et al.*, 2009. Interseismic strain accumulation measured by GPS in the seismic gap between constitucion and conception in Chile, *Phys. Earth planet. Inter.*, **175**(1–2), 78–85.
- Ruiz, S. *et al.*, 2014. Intense foreshocks and a slow slip event preceded the 2014 Iquique M_w 8.1 earthquake, *Science*, **345**(6201), 1165–1169.
- Ruiz, S. *et al.*, 2016. The seismic sequence of the 16 September 2015 M_w 8.3 Illapel, Chile, earthquake, *Seism. Res. Lett.*, **87**(4), 789–799.
- Schurr, B. *et al.*, 2014. Gradual unlocking of plate boundary controlled initiation of the 2014 Iquique earthquake, *Nature*, **512**(7514), 299–304.
- Simons, W. *et al.*, 2007. A decade of GPS in southeast Asia: resolving sundaland motion and boundaries, *J. geophys. Res.*, **112**(B6), doi:10.1029/2005JB003868.
- Trubienko, O., Fleitout, L., Garaud, J.-D. & Vigny, C., 2013. Interpretation of interseismic deformations and the seismic cycle associated with large subduction earthquakes, *Tectonophysics*, **589**, 126–141.
- Vigny, C., Rudloff, A., Ruegg, J.C., Madariaga, R., Campos, J. & Alvarez, M., 2009. Upper plate deformation measured by GPS in the Coquimbo Gap, Chile, *Phys. Earth planet. Inter.*, **175**(1), 86–95.
- Vigny, C. *et al.*, 2011. The 2010 M_w 8.8 Maule megathrust earthquake of central Chile, monitored by GPS, *Science*, **332**(6036), 1417–1421.
- Weiss, J.R. *et al.*, 2016. Isolating active orogenic wedge deformation in the southern subandes of bolivia, *J. geophys. Res.*, **121**(8), 6192–6218.
- Willis, B., 1929. *Studies in Comparative Seismology: Earthquake Conditions in Chile*, no. 382, Carnegie Institution of Washington.

SUPPORTING INFORMATION

Supplementary data are available at [GJI](https://doi.org/10.1002/gji.1111) online.

Table S1: Stations used to define our reference frame. The first 7 are located in South-America, ISPA and GLPS are located on the Nazca plate. Velocities are indicated with respect to ITRF08. Others stations are located worldwide.

Table S2: Nazca-South America relative angular velocities and respective predicted velocities on the Chilean trench at 28°S.

Table S3: Table of measurements for campaigns in the two regions (III Atacama - left and II Antofagasta - right) used in this study, starting in 2010

Figure S1: Horizontal velocities (mm/yr) with respect to stable South-America a) defined in NNR-Nuvel-1A (DeMets *et al.* 1994); b) estimated in this study (20.9°S; 128.6°W; 0.122° Myr⁻¹). Red numbers indicate the velocity in mm/yr, red dots highlight the stations used to estimate the rotation vector (KOUR, BRFT/FORT, SAVO, TOPL, BRAZ, CHPI, CUIB), ellipses depict the region of 99% confidence

Figure S2: Horizontal time series in ITRF of stations located on the brazilian craton that were used to estimate the rotation vector (Fig. S1).

Figure S3: Horizontal time series in ITRF of A) cGPS stations COPO (Copiapó), UCNF (Antofagasta), TUCU (Argentina); B) campaign sites. All stations and sites are located on Fig. S4.

Figure S4: Location map of permanent stations and campaign sites for which time series are presented on Fig. S3.

Figure S5: Prediction of Klein *et al.* (2016) viscoelastic model of post-seismic deformation following the 2010 Maule earthquake: amplitude of horizontal velocity in the area of interest during the same period (2010–2016). The dashed line highlights the limit north of which less than 1 mm/yr of postseismic signal is predicted.

Figure S6: Left: Interseismic velocity field (mm/yr) relative to stable South America (same as in Fig. 1 of the main text). Right: Profiles of horizontal velocities (mm/yr) as function of distance from the trench (km) along 7 profiles. The corresponding profiles are depicted on the map.

Figure S7: Checker board resolution tests. Left: synthetic checker board coupling distributions showing large scale (top, 80 × 30 km) or small scale (bottom 40 × 30 km) checkers. Centre: coupling distribution inverted using the synthetic velocities. Right: coupling distribution inverted using the synthetic velocities plus white noise

Figure S8: Left: Best coupling distributions obtained when imposing the Andean sliver motion to the one proposed by Métois *et al.* (2016), with (bottom) or without (upper) allowing deeper than 60 km depth coupling. Right: associated residuals and nRMS.

Figure S9: Left: Best coupling distributions obtained when fixing the Nazca-South America relative pole to the new value calculated in this study (53.9°N, 86.1°W, 0.605° Myr⁻¹). Right: associated residuals and nRMS. The coupling distribution is very similar to the best “model” presented in Figure 5 of the main text

Figure S10: Decomposition of the modelled velocity field: adding the translation like motion associated to the Andean sliver rotation (left) to the deformation produced by elastic loading only (centre) gives the overall modelled velocity field (right).

Figure S11: Sketch presenting the Andean rigid rotation inverted for three distinct regions of the margin: North Chile only Métois *et al.* (2013), Metropolitan and Atacama (Métois *et al.* 2014, 2016), and Taltal area (this study). The inverted Euler poles are all located in South Atlantic, and the rotation produced over the margin is close to be parallel to the South America-Nazca convergence velocity. However, the amount of this sliver-induced motion significantly varies from North to South without any active structure able to accommodate these along-strike variations being identified. Therefore, the current study presenting new GPS data in the Taltal area challenges the hypothesis of an Andean belt rigidly deforming.

Please note: Oxford University Press is not responsible for the content or functionality of any supporting materials supplied by the authors. Any queries (other than missing material) should be directed to the corresponding author for the paper.

Supporting information for Bridging the gap between North and Central Chile : insight from new GPS data on coupling complexities and the Andean sliver motion

E. Klein^{1,2,*}, M. Métois³, G. Meneses¹, C. Vigny¹, A. Delorme⁴

¹ *Laboratoire de géologie, Département de Géosciences, ENS, CNRS, UMR 8538, PSL research University, Paris, France*

² *Institut de Physique du Globe ; UMR 7516, Université de Strasbourg/EOST, CNRS ; Strasbourg, France*

^{*} *now at Institute of Geophysics and Planetary Physics, Scripps Institution of Oceanography, University of California, S*

³ *Univ Lyon, Université Lyon 1, ENS de Lyon, CNRS, UMR 5276 LGL-TPE, Villeurbanne, France*

⁴ *Institut de Physique du Globe de Paris, UMR 7154, Paris, France*

6 March 2018

GPS processing The whole dataset described in the main paper is processed using the GAMIT/GLOBK softwares (Herring et al. 2010a,b) following the classical MIT methodology. The horizontal (resp. vertical) components of the calculated relative position vectors have repeatabilities of 1-3 (resp. 3-5) mm. Because the post-seismic deformation induced by the Maule earthquake (Mw 8.8, 2010) contaminates a very wide area, including almost the whole Argentina, Uruguay and Southern Brazil (Klein et al. 2016), a "regional stabilization" approach is no longer sufficient to provide a stable reference frame. Therefore, we map our solution in a global reference frame, by combining our daily solution with daily global H-files produced at SOPAC. The daily solution is combined using Helmert transformations to estimate translation, and rotation. This procedure estimates the positions and velocities in the International Terrestrial Reference Frame 2008 (ITRF08, Altamimi et al. 2012) for a set of 7 well-determined stations unaffected by the Maule earthquake in the stable part of the South American Continent, 2 stations on the Nazca plate and 33 world wide stations (table S1). The misfit to these "stabilization" stations is less than 4 mm in position and 0.9 mm/yr

in velocity.

Definition of stable South America reference frame The angular velocity of the South American plate was inverted using a subset of 7 sites (KOUR, BRFT/FORT, SAVO, TOPL, BRAZ, CHPI, CUIB) that behave rigidly together (Fig. S1) and are not contaminated by the large scale post-seismic deformation following the 2010 Maule earthquake (see their time series (Fig. S2)). Note that data from BRAZ and CUIB after 2013 were excluded from the process because of equipment issues (frequent antenna change for example) or the presence of unexplained signal. This pole, located at (20.9°S, 128.6°W), presents a rotation rate of 0.122°/Myr, which is coherent with the rate proposed by the ITRF08 (Altamimi et al. (2012)) and previous studies (Vigny et al. 2009), (Nocquet et al. 2014). The residuals on the Brazilian craton are lower than 1 mm/yr with no systematic direction (fig.S1-b). Finally, like previous geodetic study, the corresponding relative Nazca/South America angular velocity predicts a plate convergence rate of the order of 67 mm/yr at the latitude of our network (table S2). The predicted azimuth (82°N) is slightly different from the one predicted by others studies (78°N), which is probably due to the selection of stations used in the rate estimation. Unlike previous cases, we excluded stations located West of Brazil and South of 25°S, in order to avoid a possible contamination of postseismic deformation following megathrust earthquake (the 2010 Maule earthquake, but potentially also the 2001 Arequipa earthquake). The fact that stations located on the east coast of Argentina, south of 25°S are significantly affected by the postseismic deformation following the Maule earthquake (Klein et al. 2016) tends to imply that the rigid block, used to estimate the stable South America reference frame in previous studies, is smaller and that a large part of the continent, believed to represent the stable tectonic plate, actually deforms even weakly.

We provide an additional document with the table of the horizontal velocity field, given in the ITRF08 and also relative to our stable South America reference frame.

Evaluation of the impact of the postseismic deformation for the Maule earthquake and oth-

ers non linear signals Being located at more than 1000 km from the Maule rupture zone and despite its large scale postseismic response, we are confident in interpreting the presented velocity field as interseismic signal, free of postseismic deformation. To prove this statement, we present here the time series of 3 permanent stations circling the area of interest (Fig. S3-A): COPO in Copiapó, ie south of the area, UCNF in Antofagasta, ie north of the area and TUCU in the far east of the network, in Argentina (location map Fig.S4). Additionally, using the preferred model of Klein et al. (2016), we predict the amplitude of horizontal velocities due to the postseismic deformation on a 0.25° grid over the whole region considered in this study (Fig. S5). This prediction is computed over the same period as the campaign measurements, that started in May 2010. We can thus predict until what latitude postseismic deformation is still measurable and could contaminate measurements. The model predicts postseismic deformation of less than 1 mm/yr north of Copiapó (27.3°S) and less than 0.5 mm/yr at the latitude of Taltal. The precision of GPS and especially of survey GPS could not allow to detect such small signal. We also present here the time series of 7 campaign sites (Fig. S3-B) spanning the region (Fig. S4). As explained in the paper, measurements there started between 2010 and 2012, it is therefore not possible to compare the present estimated velocities with the pre-Maule period. Nevertheless, according to the permanent stations (Fig. S3-A) and visco-elastic modelling (Fig. S5), we are confident that the postseismic deformation following the Maule earthquake do not contaminate velocity estimation this region. Moreover, the linearity of time series can be appreciated, showing that no significant seasonal signals or others non linear signal can explain the anomaly reporting in the region of Taltal.

Model set-up and resolution We use the Tdefnode code developed by McCaffrey (2015) (version 2015.04.20) to simultaneously invert for coupling on the subduction megathrust and the motion of the Andean rigid block. The megathrust fault is discretized into 30 along-strike and 8 along-dip nodes (every 0.2° and 7.5 km depth, from surface to 60 km depth) based on the Slab 1.0 geometry. We choose to use the ITRF2008 Nazca-South America relative pole (55.057°N , 94.013°W , $0.603^\circ/\text{Myr}$) for the models presented in the main text for consistency purposes with the previously published studies North and South of our area of interest (Métois et al. 2013; Métois et al. 2016). However, an alternative inversion conducted using the newly defined Nazca-South America rel-

ative pole is presented in Fig.S9. In all cases, we invert for the location and angular velocity of the Andean sliver pole. We therefore invert for 243 parameters, using 176 independent observations (east and north component of GPS velocities). To avoid numerical instabilities, we impose a 2D (both along strike and dip) smoothing regularization that allows for the best compromise between small-scale coupling variations and fit to the data (*spread smoothing* technique proposed by McCaffrey 2015). To limit the number of free parameters, we force the rake of the back-slip component to be parallel to the plate convergence velocity. We plot on Fig. S10 the contributions of both the rigid sliver rotation and the elastic coupling effects to the modelled velocity field. The inverted rotation motion of the Andean sliver locally produces a ~ 16 mm/yr eastward translation-like motion, roughly parallel to the Nazca-South America convergence velocity (Fig. S11).

The main issue in retrieving the coupling coefficient in subduction zones with respect to continental active faults is the lack of data in the vicinity of the trench, i.e. over the first kilometres depth of the fault interface. Furthermore, we sample the deformation on the upper plate only. In order to assess the resolution of our models, we follow Loveless & Meade (2011) and calculate the sensitivity of our network to each unit slip dislocation on the plate interface, i.e. we calculate the displacements produced at each station by a unit slip on one subfault of the interface and sum them over the whole network. This process gives us the power P of the network to resolve this unit slip (see Fig. 4 of the main text). Our network is unable to resolve coupling on the first 10 km depth of the interface. The resolution is low at the edges of the model but overall, our network is sufficiently dense to resolve the coupling pattern between 10 and 60 km depth.

We also provide standard checker board tests in supplementary Fig. S7 that show the capability of the network to capture large (80 x 30 km) and small (40 km x 30 km) scales in the coupling distribution, with or without random noise added to the synthetic data. While large scale variations of the coupling are well retrieved over almost all the subduction plane, smaller variations are only captured by the network in the 10 to 60 km depth range.

Alternative models Fig. S8 shows the best-models obtained by inverting the coupling distribution on the megathrust interface only while the Andean sliver motion is fixed to the one proposed by Métois et al. (2016) (i.e. Andean sliver's Euler pole located at 56.37°S , 41.27°W and $-0.12^\circ/\text{Myr}$).

Lon(°)	Lat(°)	Vlon	Vlat	Station	Lon(°)	Lat(°)	Station	Lon(°)	Lat(°)	Station
312.1221	-15.9475	-3.77	12.55	BRAZ	40.44	-3.95	VILL	-43.96	-176.57	CHAT
321.5745	-3.8774	-4.68	12.42	FORT/BRFT	40.43	-4.25	MADR	-36.60	174.83	AUCK
307.1940	5.2522	-5.24	12.15	KOUR	27.76	-15.63	MASP	-77.84	166.67	MCM4
321.5677	-12.9392	-4.56	12.30	SAVO	-63.32	-57.90	OHIG	-54.50	158.94	MAC1
315.0148	-22.6871	-3.64	12.62	CHPI	32.37	-64.70	BRMU	-35.40	148.98	TIDB
303.930	-15.555	-3.11	14.18	CUIB	76.54	-68.83	THU1	-42.80	147.44	HOB2
292.2489	-53.7855	3.27	11.98	RIOG/RIO2	42.61	-71.49	WES2	13.59	144.87	GUAM
311.669	-10.171	-4.75	12.29	TOPL	39.02	-76.83	GODE	-31.80	115.89	PERT
250.6556	-27.1250	67.24	-5.99	ISPA	45.96	-78.07	ALGO	52.22	104.32	IRKT
269.6963	-0.7430	51.24	10.28	GLPS	30.68	-104.01	MDO1	-68.58	77.97	DAV1
					34.30	-108.12	PIE1	-49.35	70.26	KERG
					62.48	-114.48	YELL	39.14	66.88	KIT3
					35.42	-116.89	GOLD	40.65	16.70	MATE
					49.32	-119.63	DRAO	47.07	15.49	GRAZ
					64.98	-147.50	FAIR	52.38	13.07	POTS
					22.13	-159.66	KOKB	57.40	11.93	ONSA
								78.93	11.87	NYAL

Table S1. Stations used to define our reference frame. The first 7 are located in South-America, ISPA and GLPS are located on the Nazca plate. Velocities are indicated with respect to ITRF08. Others stations are located worldwide.

Whether coupling is fixed to 0 under 60 km (upper Fig. S8) or not (bottom), the nRMS remains high (higher than 2) and systematic eastward pointing residuals are observed in the Taltal area, similar to what is described in Fig.2 of the main text. These models clearly indicate that the GPS velocities require inverting for the local amplitude of the Andean sliver motion together with the coupling distribution on the fault.

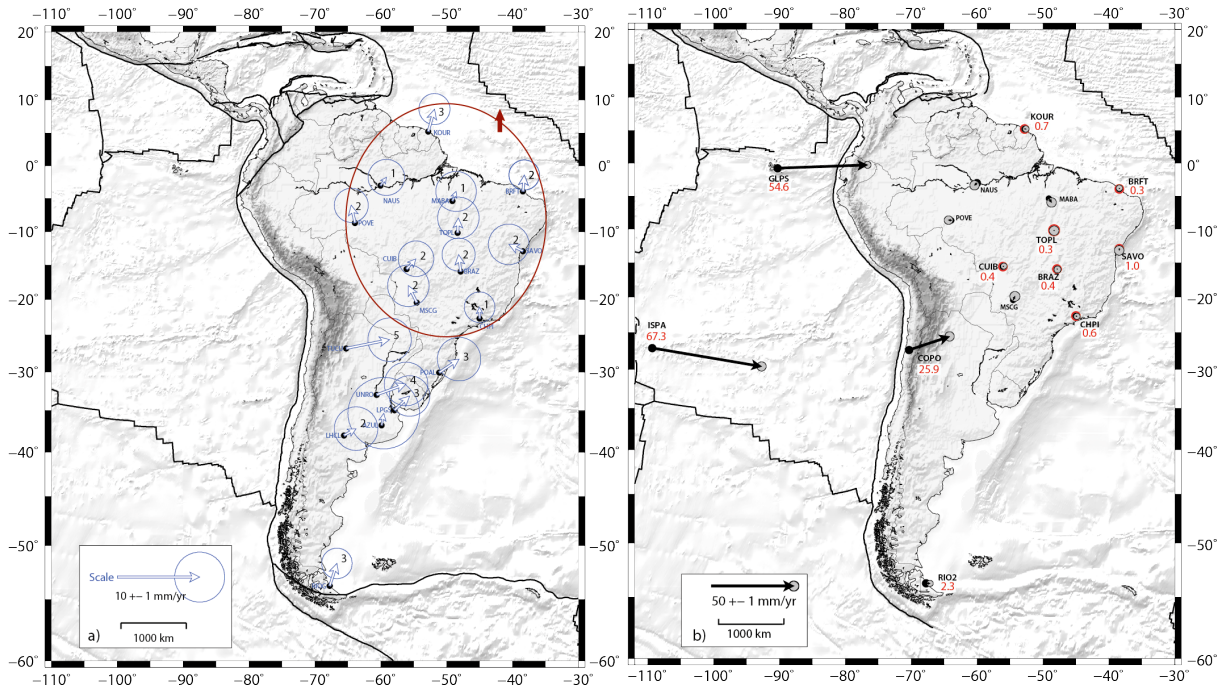


Figure S1. Horizontal velocities (mm/yr with respect to stable South-America **a**) defined in NNR-Nuvel-1A (DeMets et al. 1994); **b**) estimated in this study (20.9°S ; 128.6°W ; $0.122^{\circ}/\text{Myr}$). Red numbers indicate the velocity in mm/yr, red dots highlight the stations used to estimate the rotation vector (KOUR, BRFT/FORT, SAVO, TOPL, BRAZ, CHPI, CUIB), ellipses depict the region of 99 % confidence

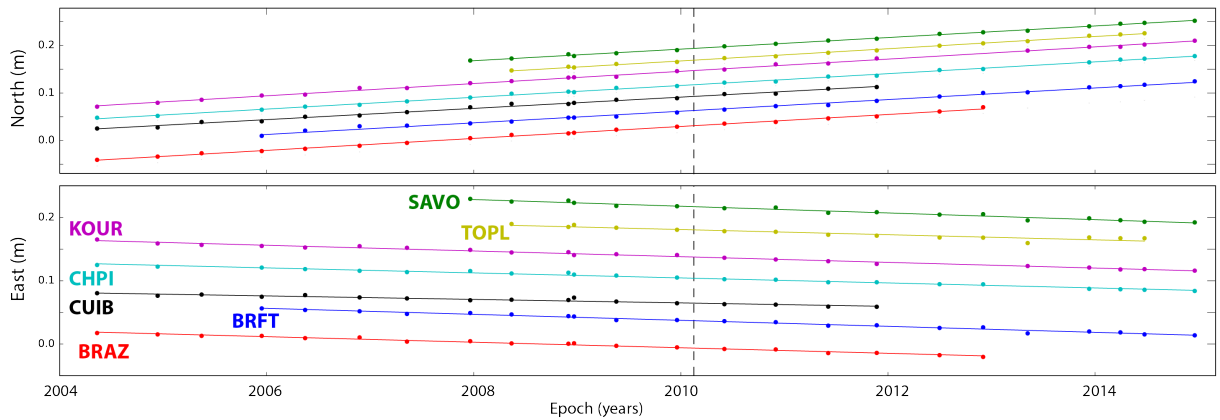


Figure S2. Horizontal time series in ITRF of stations located on the Brazilian craton that were used to estimate the rotation vector S1

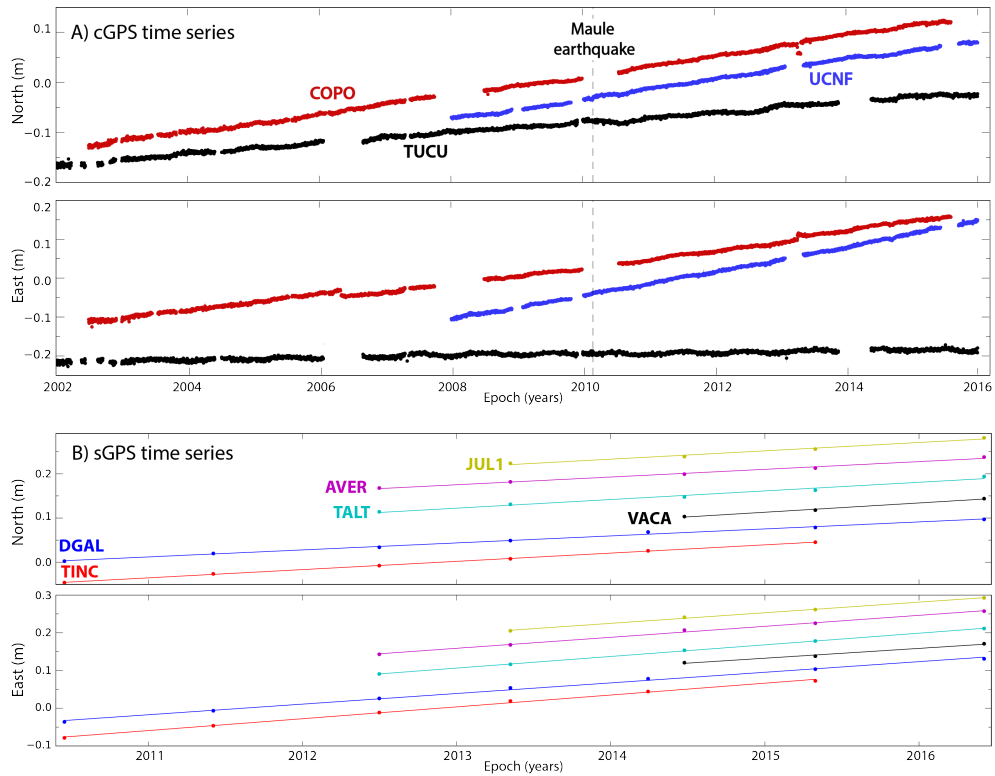


Figure S3. Horizontal time series in ITRF of A) cGPS stations COPO (Copiapó), UCNF (Antofagasta), TUCU (Argentina); B) campaign sites. All stations and sites are located on Fig. S4.

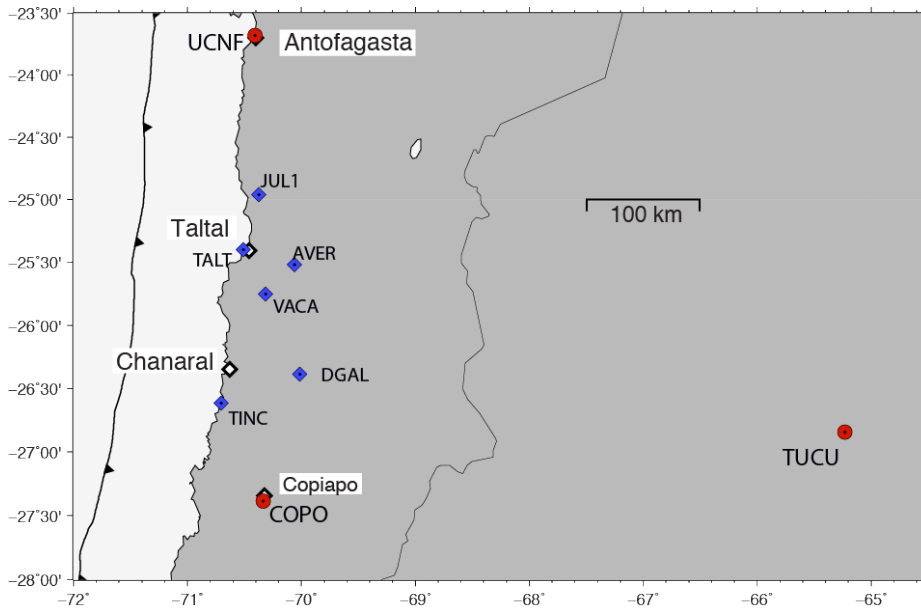


Figure S4. Location map of permanent stations and campaign sites for which time series are presented on Fig. S3

	Angular velocity			Predicted velocity at 28°S	
	Latitude	Longitude	Rotation	Convergence	Azimet
Nuvel-1A	56°N	94°W	0.72°/Myr	80 mm/yr	78°N
Larson et al. (1997)	43.8°N	84.8°W	0.74°/Myr	79 mm/yr	80°N
Angermann et al. (1999)	48.8°N	91.7°W	0.59°/Myr	64 mm/yr	77°N
Norabuena et al. (1998)	47.4°N	93.7°W	0.624°/Myr	68 mm/yr	75°N
Sella et al. (2002)	52.1°N	91.2°W	0.633°/Myr	70 mm/yr	78°N
Kendrick et al. (2003) Brooks et al. (2003)	61°N	94.4°W	0.57°/Myr	63 mm/yr	79°N
ITRF2005 Altamimi et al. (2011)	53.9°N	87.5°W	0.605°/Myr	67 mm/yr	81°N
Vigny et al. (2009)	55.9°N	95.2°W	0.61°/Myr	68 mm/yr	77°N
ITRF2008 Altamimi et al. (2012)	55.1°N	94°W	0.603°/Myr	67 mm/yr	78°N
Marotta et al. (2013)	61°N	91.4°W	0.569°/Myr	63 mm/yr	81°N
Kreemer et al. (2014)	59.7°N	84.3°W	0.57°/Myr	68 mm/yr	77°N
Nocquet et al. (2014)	54.5°N	92.6°W	0.601°/Myr	67 mm/yr	78°N
This study	53.9°N	86.1°W	0.605°/Myr	67 mm/yr	82°N

Table S2. Nazca-South America relative angular velocities and respective predicted velocities on the Chilean trench at 28°S.

REFERENCES

- Altamimi, Z., Collilieux, X., & Métivier, L., 2011. ITRF2008: An improved solution of the International Terrestrial Reference Frame, *Journal of Geodesy*, **85**(8), 457–473.
- Altamimi, Z., Métivier, L., & Collilieux, X., 2012. ITRF2008 plate motion model, *Journal of Geophysical Research: Solid Earth*, **117**(B7), n/a–n/a, B07402.
- Angermann, D., Klotz, J., & Reigber, C., 1999. Space-geodetic estimation of the Nazca-South America euler vector, *Earth and Planetary Science Letters*, **171**(3), 329 – 334.
- Brooks, B. A., Bevis, M., Smalley, R., Kendrick, E., Manceda, R., Lauría, E., Maturana, R., & Araujo, M., 2003. Crustal motion in the southern Andes (26°–36° S): Do the Andes behave like a microplate?, *Geochemistry, Geophysics, Geosystems*, **4**(10).
- DeMets, C., Gordon, R. G., Argus, D. F., & Stein, S., 1994. Effect of recent revisions to the geomagnetic reversal time scale on estimates of current plate motions, *Geophysical Research Letters*, **21**(20), 2191–

Sites	2010	2011	2012	2013	2014a	2014b	2015	2016
BAR2	-	-	-	X	X	-	X	X
BARQ	X	X	X	X	X	-	X	X
BING	X	X	X	X	X	-	X	X
CAL2	-	-	X	X	X	-	X	X
CANG	-	X	X	X	X	-	X	X
CANT	-	-	-	X	X	-	X	X
CHAR	X	X	X	X	X	-	X	X
CHR1	X	X	X	X	X	-	X	X
COP2	X	X	X	X	X	-	X	X
COP3	X	X	X	X	X	-	X	X
COP5	X	X	X	X	X	-	-	X
CZBA	-	X	X	X	X	-	X	X
DGAL	X	X	X	X	X	-	X	X
LAPU	-	X	X	X	X	-	-	X
MCOL	-	-	-	X	X	-	X	X
MMOR	-	-	-	-	X	-	X	X
MORO	-	-	X	X	X	-	X	X
OBI1	-	-	-	X	X	-	X	X
OBI2	-	-	-	X	-	X	X	X
OBI3	-	-	-	X	-	X	X	X
PLTT	X	X	X	X	X	-	X	X
PNAZ	X	X	X	X	-	X	-	X
POTR	X	X	X	X	X	-	-	-
PVEJ	X	X	X	X	X	-	X	X
SALD	X	X	X	X	X	-	X	X
TINC	X	X	X	X	X	-	X	X

Sites	2010	2011	2012	2013	2014a	2014b	2015	2016
TOT0	-	-	X	X	-	-	-	-
TOT2	X	X	X	X	X	-	X	X
TOT3	X	X	X	X	X	-	X	X
TOT4	X	X	X	X	X	-	X	X
TOT5	X	X	X	X	X	-	-	X
AVER	-	-	X	X	-	X	X	X
BADU	-	-	-	-	-	X	X	X
CARI	-	-	-	X	-	X	X	X
CIFU	-	-	X	X	-	X	X	X
CIFN	-	-	X	X	-	X	X	X
COBA	-	-	-	X	-	X	X	X
ESMA	-	-	-	-	-	X	X	X
ESM1	-	-	-	-	-	X	X	X
ESM2	-	-	-	-	-	X	X	X
JUL1	-	-	-	X	-	X	X	X
JUL2	-	-	-	X	-	X	X	X
JUL3	-	-	-	X	-	X	X	X
LHER	-	-	X	X	X	-	X	X
MARU	-	-	X	X	-	X	X	X
MINF	-	-	-	X	-	-	-	-
PAPS	-	-	-	-	-	X	X	X
PAR0	-	-	-	-	-	X	X	X
PAR3	-	-	-	-	-	X	X	X
ROSA	-	-	-	-	-	X	X	X
TALT	-	-	X	X	X	X	X	X
VACA	-	-	-	-	-	X	X	X

Table S3. Table of measurements for campaigns in the two regions (III Atacama - left and II Antofagasta - right) used in this study, starting in 2010

2194.

Herring, T., King, R., & McClusky, S. C., 2010a. *GAMIT : GPS Analysis at MIT, release 10.4.*

Herring, T., King, R., & McClusky, S. C., 2010b. *GLOBK : Global Kalman filter VLBI and GPS analysis program release 10.4.*

Kendrick, E., Bevis, M., Smalley, R., Brooks, B., Vargas, R. B., Lauria, E., & Fortes, L. P. S., 2003. The nazca–south america euler vector and its rate of change, *Journal of South American Earth Sciences*, **16**(2), 125–131.

Klein, E., Fleitout, L., Vigny, C., & Garaud, J., 2016. Afterslip and viscoelastic relaxation model inferred

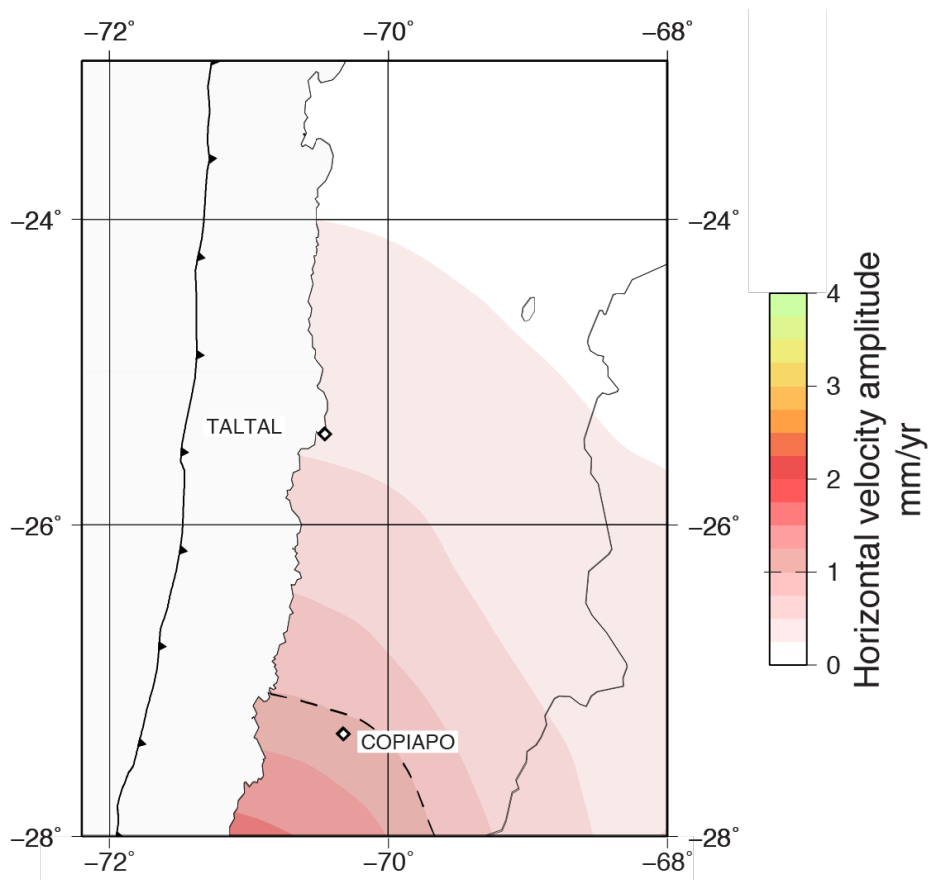


Figure S5. Prediction of Klein et al. (2016) visco-elastic model of postseismic deformation following the Maule earthquake: amplitude of horizontal velocity in the area of interest during the same period (2010–2016). The dashed line highlights the limit north of which less than 1 mm/yr of postseismic signal is predicted.

from the large scale postseismic deformation following the 2010 Mw 8.8 Maule earthquake (Chile), *Geophysical Journal International*, **205**(3), 1455–1472.

Kreemer, C., Blewitt, G., & Klein, E. C., 2014. A geodetic plate motion and global strain rate model, *Geochemistry, Geophysics, Geosystems*, pp. n/a–n/a.

Larson, K., Freymuller, J., & Philipson, S., 1997. Global consistent rigid plate velocities from GPS, *J. Geophys. Res.*, **102**, 9961–9981.

Loveless, J. P. & Meade, B. J., 2011. Spatial correlation of interseismic coupling and coseismic rupture extent of the 2011 Mw = 9.0 Tohoku-Oki earthquake, *Geophysical Research Letters*, **38**(17), n/a–n/a.

Marotta, G. S., França, G. S., ao Francisco Galera Monico, J., Fuck, R. A., & de Araújo Filho, J. O., 2013. Strain rate of the South American lithospheric plate by sirgas-con geodetic observations, *Journal of South American Earth Sciences*, **47**(0), 136 – 141.

McCaffrey, R., 2015. Tdefnode user’s manual version 2015.07. 30.

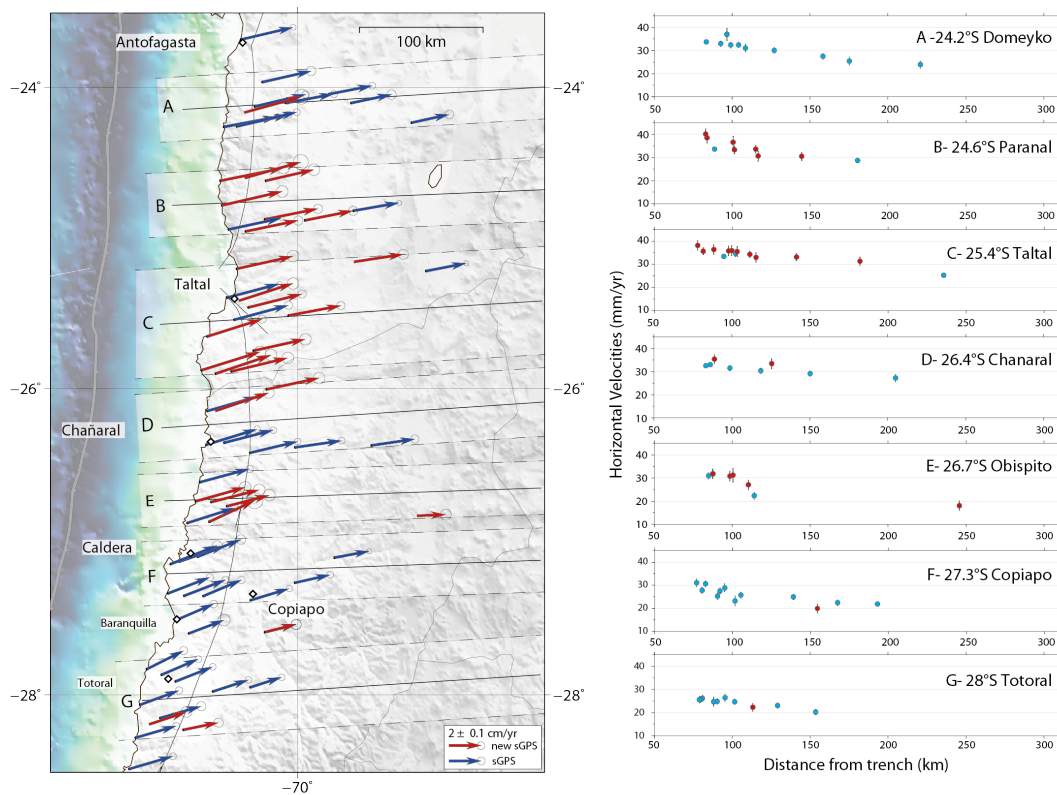


Figure S6. Left: Interseismic velocity field (mm/yr) relative to stable South America (same as in fig.1 of the main text). Right: Profiles of horizontal velocities (mm/yr) as function of distance from the trench (km) along 7 profiles. The corresponding profiles are depicted on the map.

Métois, M., Socquet, A., Vigny, C., Carrizo, D., Peyrat, S., Delorme, A., Maureira, E., Valderas-Bermejo, M.-C., & Ortega, I., 2013. Revisiting the north Chile seismic gap segmentation using GPS-derived interseismic coupling, *Geophysical Journal International*, **194**(3), 1283–1294.

Métois, M., Vigny, C., Socquet, A., Delorme, A., Morvan, S., Ortega, I., & Valderas-Bermejo, C.-M., 2014. GPS-derived interseismic coupling on the subduction and seismic hazards in the atacama region, Chile, *Geophysical Journal International*, **196**(2), 644–655.

Métois, M., Vigny, C., & Socquet, A., 2016. Interseismic coupling, megathrust earthquakes and seismic swarms along the Chilean subduction zone (38–18° S), *Pure and Applied Geophysics*, **173**(5), 1431–1449.

Nocquet, J.-M., Villegas-Lanza, J.-C., Chlieh, M., Mothes, P., Rolandone, F., Jarrin, P., Cisneros, D., Alvarado, A., Audin, L., Bondoux, F., et al., 2014. Motion of the continental slivers and creeping subduction in the northern Andes, *Nature Geosciences*, **7**(4), 287.

Norabuena, E., Leffler-Griffin, L., Mao, A., Dixon, T., Stein, S., Sacks, I. S., Ocola, L., & Ellis, M., 1998. Space geodetic observations of Nazca-South America convergence across the central Andes, *Science*,

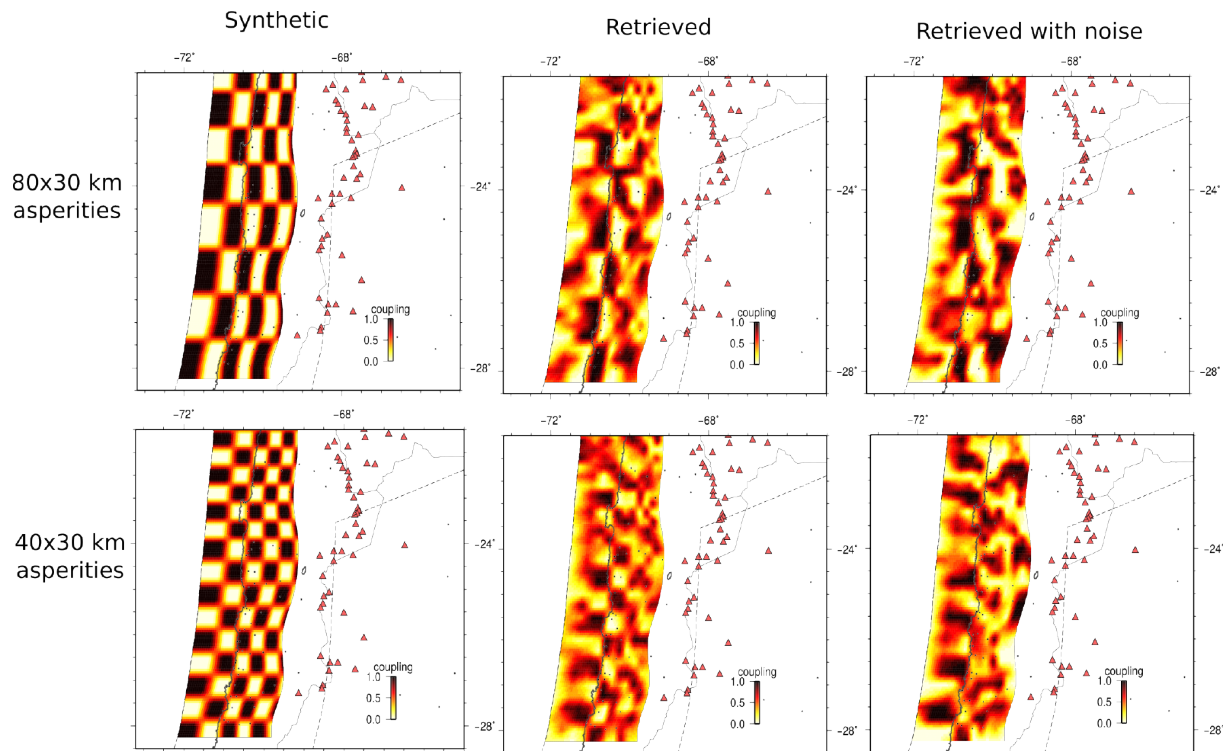


Figure S7. Checker board resolution tests. Left : synthetic checker board coupling distributions showing large scale (top, 80 x 30 km) or small scale (bottom 40 x 30 km) checkers. Centre : coupling distribution inverted using the synthetic velocities. Right : coupling distribution inverted using the synthetic velocities plus white noise.

279(5349), 358–362.

Sella, G., Dixon, T., & Mao, A., 2002. Revel: A model for recent plate velocities from space geodesy, *Journal of Geophysical Research*, **107**(B4).

Vigny, C., Rudloff, A., Ruegg, J. C., Madariaga, R., Campos, J., & Alvarez, M., 2009. Upper plate deformation measured by GPS in the Coquimbo Gap, Chile, *Physics of the Earth and Planetary Interiors*, **175**(1), 8695.

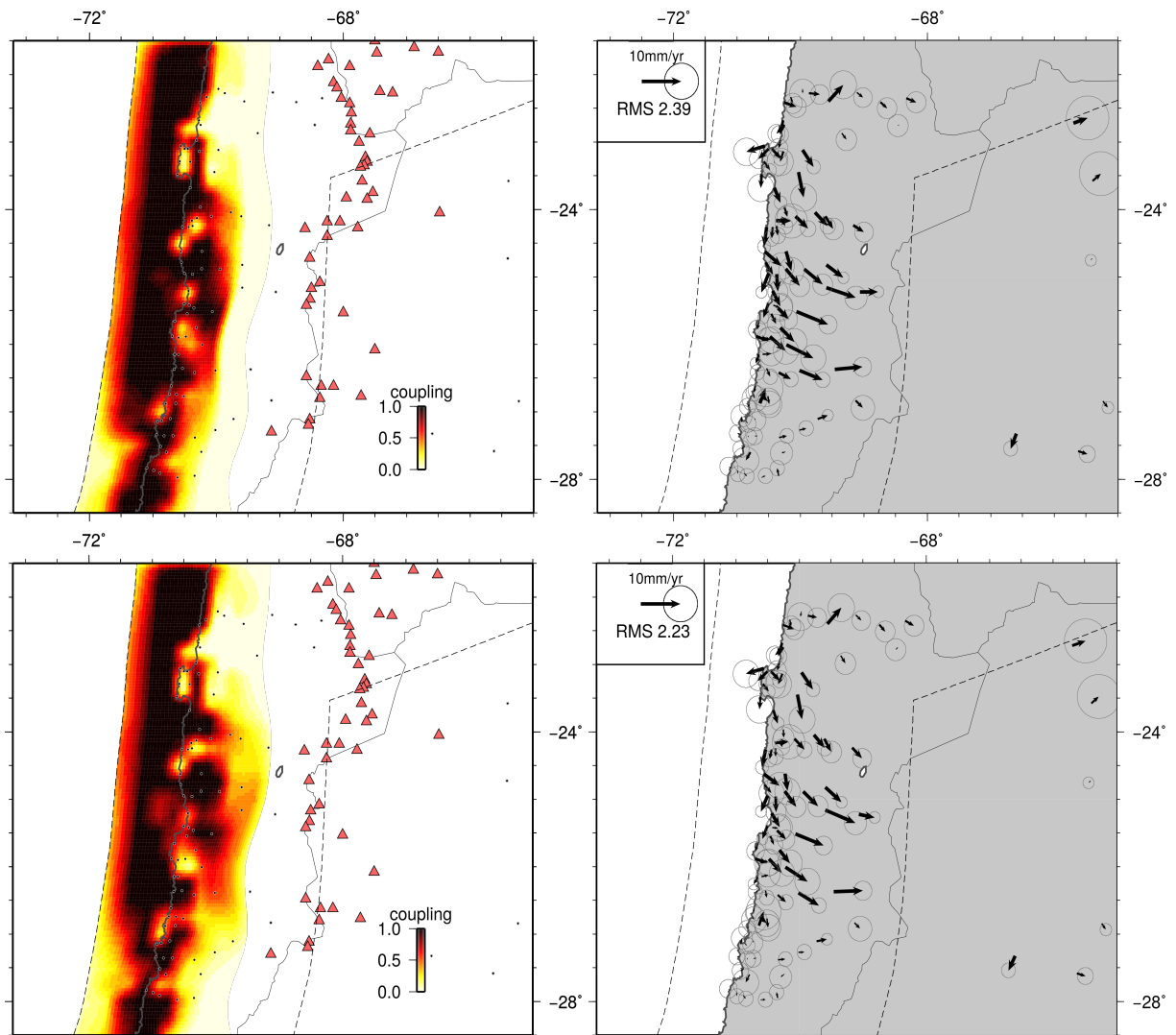


Figure S8. Left: Best coupling distributions obtained when imposing the Andean sliver motion to the one proposed by Métois et al. (2016), with (bottom) or without (upper) allowing deeper than 60 km depth coupling. Right : associated residuals and nRMS.

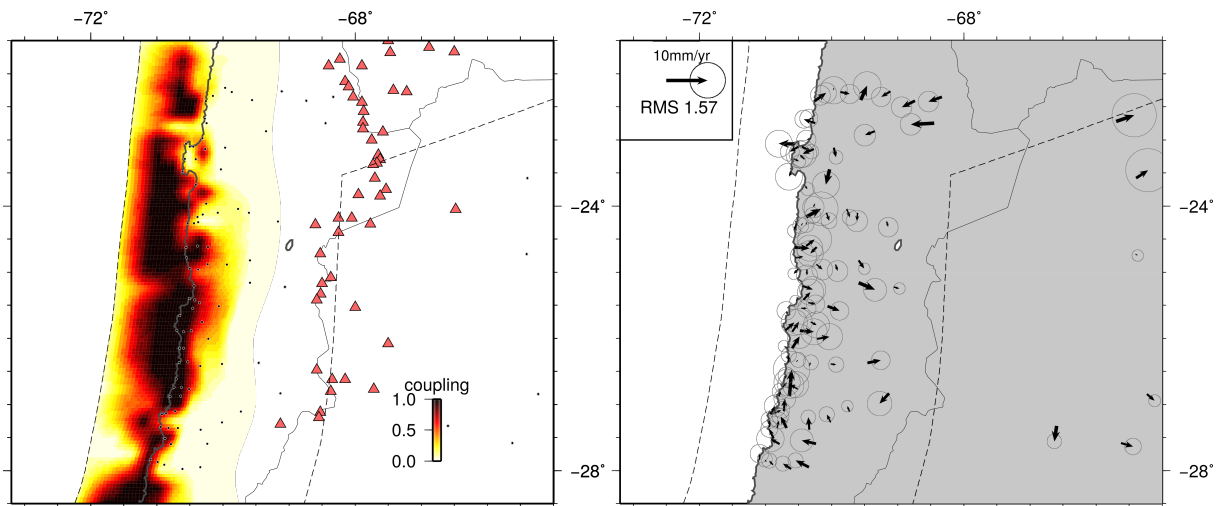


Figure S9. Left: Best coupling distributions obtained when fixing the Nazca-South America relative pole to the new value calculated in this study (53.9°N , 86.1°W , $0.605^{\circ}/\text{Myr}$). Right : associated residuals and nRMS. The coupling distribution is very similar to the 'best model' presented in Figure 5 of the main text.

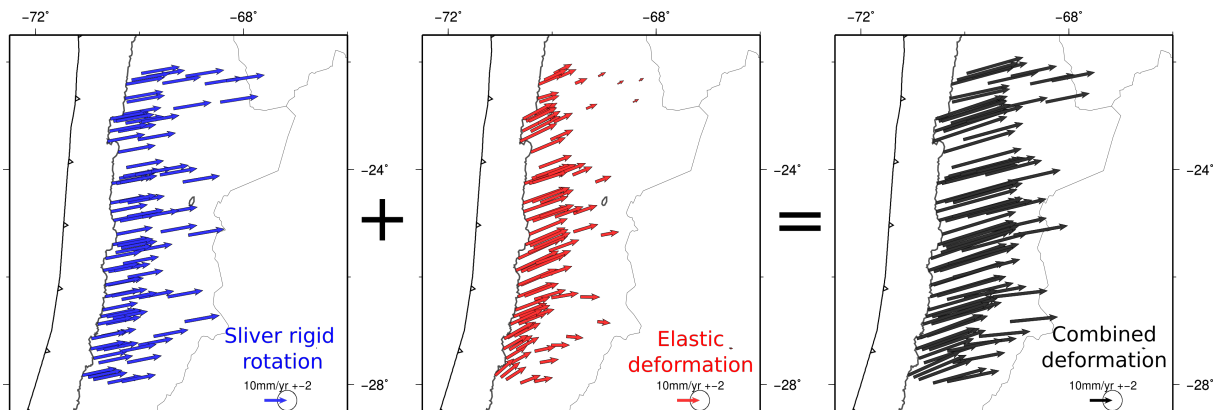


Figure S10. Decomposition of the modelled velocity field : adding the translation like motion associated to the Andean sliver rotation (left) to the deformation produced by elastic loading only (centre) gives the overall modelled velocity field (right).

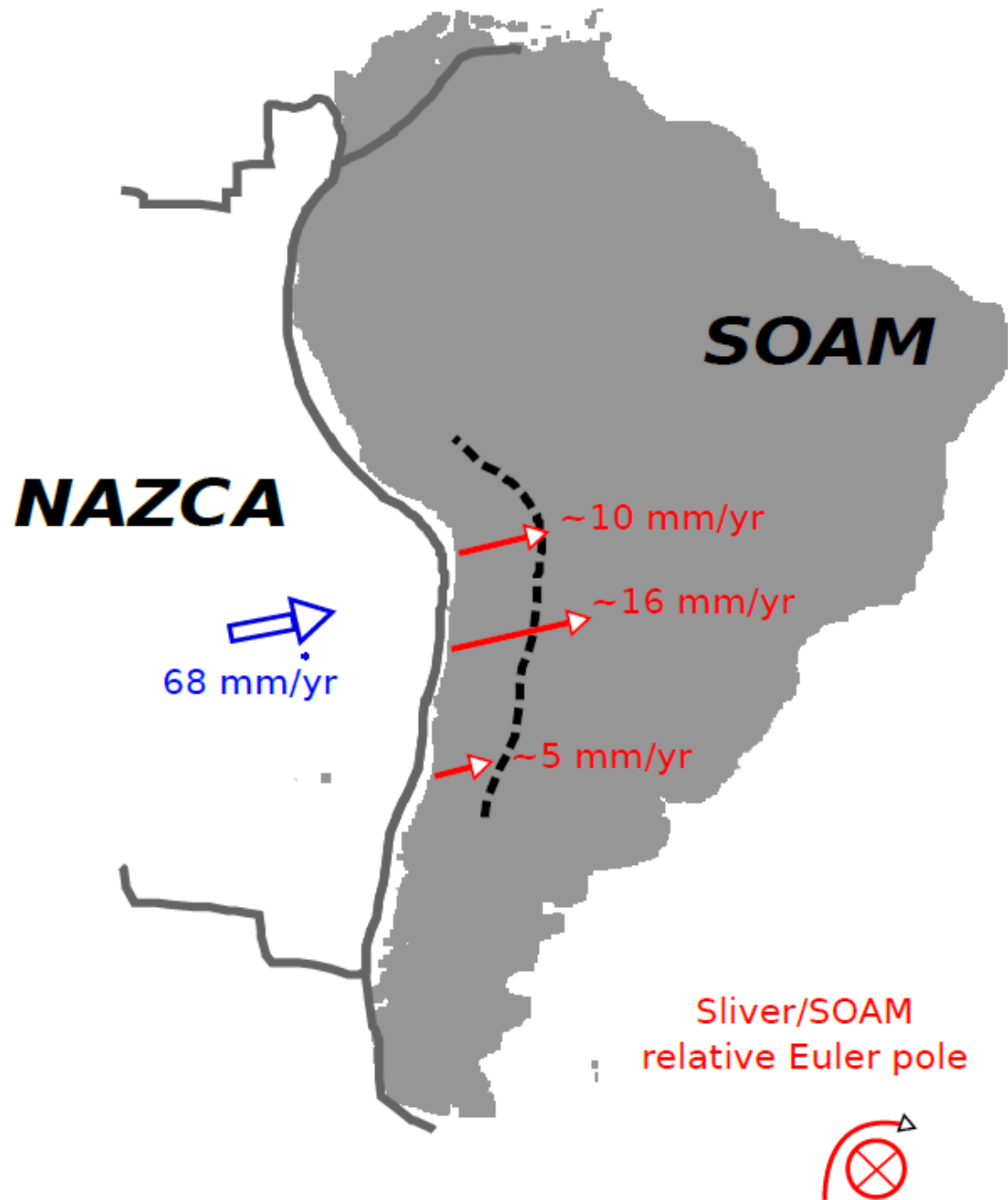


Figure S11. Sketch presenting the Andean rigid rotation inverted for three distinct regions of the margin : North Chile only (Métois et al. 2013), Metropolitan and Atacama (Métois et al. 2014; Métois et al. 2016), and Taltal area (this study). The inverted Euler poles are all located in South Atlantic, and the rotation produced over the margin is close to be parallel to the South America-Nazca convergence velocity. However, the amount of this sliver-induced motion significantly varies from North to South without any active structure able to accommodate these along-strike variations being identified. Therefore, the current study presenting new GPS data in the Taltal area challenges the hypothesis of an Andean belt rigidly deforming.

Supporting information for Bridging the gap between North and
Central Chile: Insight from new GPS data on coupling complexities
and the Andean sliver motion

Sites	Position		ITRF08		stable SOAM		Uncertainties		r
	Lon	Lat	Vlon	Vlat	Vlon	Vlat	Siglon	Siglat	
3CRX	289.068	-29.376	19.90	16.50	20.79	5.80	1.02	1.02	0.000
ABOL	288.893	-28.967	22.94	18.69	23.87	8.01	1.02	1.02	0.000
AVER	289.937	-25.518	30.97	16.95	32.48	6.15	1.05	1.04	0.000
BADU	289.561	-25.208	33.35	18.56	34.87	7.81	1.48	1.47	0.000
BAR2	289.212	-27.601	20.58	18.98	21.74	8.26	1.55	1.47	0.007
BARQ	289.121	-27.514	21.98	20.68	23.14	9.97	0.95	0.95	0.000
BING	289.141	-27.134	27.75	20.63	28.97	9.92	0.94	0.94	0.000
BSAR	288.589	-28.816	30.19	21.10	31.11	10.47	1.18	1.17	0.000
CALC	289.468	-24.264	25.61	21.39	33.17	6.23	0.76	0.76	0.001
CAL2	289.275	-27.102	31.52	16.98	26.84	10.67	1.23	1.22	-0.001
CANG	288.824	-28.277	24.06	17.96	25.08	7.29	0.92	0.92	0.000
CANT	289.004	-28.149	24.28	18.04	25.34	7.35	1.18	1.17	0.000
CARI	289.501	-24.947	31.26	17.82	32.82	7.07	0.65	0.65	0.001
CERZ	289.386	-23.476	30.54	18.39	32.30	7.65	1.53	1.52	0.000
CGUA*	290.41	-25.163	29.38	15.60	30.96	4.75	1.30	1.29	0.000
CHAR	289.339	-26.369	30.21	20.41	31.55	9.68	0.85	0.85	0.000
CHR1	289.469	-26.357	29.10	18.66	30.45	7.91	0.85	0.85	0.000
CIFN	289.345	-25.656	32.55	21.51	33.99	10.78	1.04	1.04	0.000
CIFU	289.543	-25.546	32.13	19.80	33.61	9.04	1.04	1.04	0.000
COBA	290.411	-24.824	26.55	15.79	28.19	4.93	0.65	0.65	0.001
COP2	289.177	-27.357	24.51	20.65	25.70	9.94	0.94	0.94	0.000
COP3	289.317	-27.358	22.43	20.74	23.63	10.01	0.94	0.94	0.000
COP5	289.984	-27.271	20.58	15.69	21.85	4.88	0.86	0.85	0.000
COPO*	289.662	-27.385	22.61	18.00	23.84	7.23	0.82	0.82	0.000
CRIS*	289.613	-24.168	33.94	20.60	35.62	9.83	1.91	1.90	0.000
CRZL	288.59	-29.102	24.87	21.38	25.75	10.74	0.82	0.82	0.001
CZBA	288.857	-28.063	23.01	19.53	24.06	8.86	0.93	0.92	0.000
DGAL	289.986	-26.387	27.37	14.97	28.76	4.16	0.86	0.86	0.000
DO10	289.56	-24.26	30.46	18.02	32.12	7.26	0.89	0.89	0.000
DO20	289.627	-24.244	29.84	18.04	31.51	7.27	0.90	0.90	0.000
DO30	289.692	-24.127	29.88	18.20	31.57	7.43	0.90	0.90	0.003
DO40	289.92	-24.105	27.84	16.36	29.55	5.56	0.90	0.89	0.000
DO50	290.231	-24.045	25.17	16.05	26.91	5.22	0.89	0.89	0.000
DO60	290.834	-24.236	21.57	16.05	23.33	5.15	1.11	1.10	0.000
DOME	289.114	-28.959	20.77	17.27	21.72	6.57	1.03	1.02	0.000
ESM1	289.406	-25.901	33.03	22.31	34.43	11.58	1.48	1.48	0.001
ESM2	289.522	-25.887	33.55	19.13	34.97	8.39	1.48	1.47	0.000
ESMA	289.303	-25.879	35.01	22.06	36.41	11.34	1.48	1.47	0.000
ETRA	289.714	-28.865	18.11	13.31	19.13	2.53	1.34	1.33	0.003
FREI	288.98	-28.564	22.95	16.62	23.95	5.93	0.89	0.88	0.000
FRTN	289.555	-28.522	20.68	17.87	21.73	7.11	0.99	0.99	0.000
HGRT	288.684	-28.944	26.39	19.26	27.30	8.61	1.03	1.02	0.000
HORN	288.688	-29.679	18.36	19.52	19.17	8.87	1.03	1.02	-0.001
HUA0	288.778	-28.478	26.01	18.59	27.00	7.93	0.89	0.89	0.000
INCA	288.935	-29.242	20.04	18.27	20.93	7.60	1.03	1.02	0.000
JRGN*	289.425	-23.289	30.90	19.83	32.69	9.09	0.74	0.74	0.000
JUL1	289.626	-24.961	31.02	17.57	32.59	6.82	1.18	1.18	-0.001
JUL2	289.766	-24.881	31.34	17.39	32.93	6.61	1.17	1.17	0.000

JUL3	290.058	-24.887	28.19	16.73	29.80	5.93	1.17	1.17	0.000
JVAL	289.942	-28.903	15.47	18.84	16.50	8.04	1.22	1.19	-0.010
LAPU	290.273	-27.109	20.17	14.87	21.49	4.03	0.65	0.65	0.003
LCHO	288.739	-29.277	20.50	18.57	21.37	7.91	1.02	1.02	0.000
LHER	290.94	-25.223	23.16	15.75	24.79	4.83	0.65	0.65	0.001
LIVE	289.747	-23.964	28.56	17.64	30.28	6.86	1.21	1.20	0.000
LLCH*	288.919	-28.19	22.33	18.42	23.38	7.74	1.38	1.38	0.000
LOBO	289.443	-23.062	23.95	20.22	25.77	9.48	1.53	1.52	0.000
MABL	289.972	-23.448	23.42	15.21	25.22	4.40	1.53	1.52	-0.001
MARU	289.646	-25.464	31.76	19.12	33.26	8.35	1.04	1.04	0.000
MCOL	289.172	-28.226	20.71	15.22	21.77	4.51	1.21	1.18	0.002
MEJ0	289.501	-23.102	25.32	18.47	27.14	7.72	1.06	1.06	0.000
MINF	290.394	-24.105	23.18	16.12	24.93	5.27	1.21	1.21	0.000
MMOR	289.36	-26.874	26.94	23.92	28.22	13.19	2.06	2.04	-0.002
MORO	289.078	-27.15	27.64	22.20	28.85	11.50	1.24	1.23	-0.001
MRCG*	290.87	-26.835	16.64	11.58	18.06	0.67	1.39	1.38	0.000
OBI1	289.262	-26.74	29.33	19.39	30.61	8.67	1.48	1.47	0.000
OBI2	289.374	-26.745	28.52	18.34	29.81	7.60	1.48	1.48	0.001
OBI3	289.49	-26.772	24.85	17.58	26.15	6.83	1.48	1.48	0.001
PAPS	289.453	-24.787	35.83	19.36	37.40	8.63	1.48	1.48	0.000
PAR0	289.441	-24.624	37.77	18.66	39.36	7.93	1.48	1.47	0.000
PAR3	289.773	-24.623	28.14	17.62	29.75	6.85	1.49	1.48	0.000
PAZU*	289.401	-26.148	32.05	22.08	33.44	11.33	1.39	1.38	0.000
PCHO	288.542	-29.254	22.57	20.76	23.43	10.12	1.02	1.02	0.000
PLTT	289.2	-26.881	28.15	20.05	29.41	9.34	0.95	0.94	0.000
PMEJ	289.552	-23.101	28.97	18.12	30.79	7.36	0.82	0.81	0.000
PNAZ	289.346	-26.148	29.85	19.80	31.22	9.07	0.65	0.65	0.002
POTR	290.542	-26.374	25.39	14.82	26.83	3.95	1.06	1.06	0.000
PPLY	289.649	-29.18	18.36	16.92	19.33	6.15	1.15	1.14	0.000
PRNL*	289.616	-24.605	33.45	20.74	35.07	9.98	1.91	1.90	0.000
PVEJ	289.06	-27.341	24.68	20.68	25.86	9.98	0.94	0.94	0.000
ROSA	289.778	-26.006	31.17	17.81	32.59	7.05	1.48	1.48	0.000
SALD	289.658	-26.423	28.09	17.81	29.45	7.04	0.85	0.85	0.000
SFLX	289.542	-28.933	18.80	17.46	19.79	6.70	1.14	1.13	-0.001
SILL*	289.261	-29.255	19.00	17.67	19.92	6.95	0.80	0.80	0.000
SMRD	289.733	-23.14	21.46	17.67	23.29	6.89	1.55	1.53	0.001
TALT	289.491	-25.4	30.82	19.28	32.31	8.53	0.65	0.65	0.001
TAMR	289.765	-27.594	18.08	15.60	19.29	4.82	1.30	1.29	0.000
TINC	289.294	-26.615	29.37	18.97	30.67	8.24	0.94	0.94	0.000
TOT1	288.904	-27.832	21.79	22.14	22.89	11.46	1.05	1.04	-0.001
TOT2	289.012	-27.87	21.74	20.50	22.84	9.81	0.85	0.85	0.000
TOT3	289.115	-27.912	21.88	19.75	22.98	9.05	0.85	0.85	0.000
TOT4	289.387	-27.977	20.80	17.90	21.92	7.16	0.85	0.85	0.000
TOT5	289.66	-27.951	18.14	17.04	19.28	6.27	0.85	0.85	0.001
TRST*	289.726	-28.836	20.72	15.65	21.74	4.87	1.98	1.98	-0.002
TTAL*	289.574	-25.421	32.34	21.58	33.83	10.84	1.47	1.47	0.000
UCNF*	289.591	-23.679	30.66	18.36	32.40	7.60	0.74	0.74	0.000
VACA	289.683	-25.751	30.70	17.91	32.15	7.16	1.47	1.47	0.000
VALL*	289.236	-28.572	20.37	15.72	21.39	5.00	0.74	0.74	0.001
VLZL*	290.035	-23.117	23.32	15.87	25.18	5.06	0.78	0.78	0.000

Horizontal velocities in mm/yr, given in the ITRF08 reference frame (col.4-5) and relative to the stable South America reference frame reestimated (col. 6-7). (col. 8-9 indicate the associated uncertainties and col.10 the correlation between the 2 components). Sites marked by a star are continuous stations.

4.1 Brief review of the principal results of the study

4.1.1 Anomalies of the interseismic velocity pattern

The new study from Klein *et al.* [2018] assemble all new interseismic velocities for the region of the Chilean subduction zone delimited between 23° S and 30° S. Horizontal velocity vectors (figure 4.4-A), were calculated from annual positions (from 3 to 7 measurements per year) given by campaigns performed in a 6-years time span starting in 2010. They are plotted respect to a stable South American plate defined by an Euler pole inverted for this study. The figure depicts typical features of the interseismic velocity field: velocities following the convergence direction and the progressive decrease in magnitude and clockwise rotation starting from the trench. However, is clear from the figure an increase of velocity magnitudes from south to north, and an anomalous pattern in the Taltal region ($\sim 25.5^\circ$ S). The typical inland reduction of the velocity amplitudes is not seen in this zone, with the large value of $\sim 30 \text{ mm yr}^{-1}$ at 200 km from the trench (20 mm yr^{-1} is a typical value for southern sites). Figure 4.5 shows residuals between observed deformations and the ones produced by a model including a bimodal coupling (0 or 100 percent coupled) thrust zone and the rigid motion of an Andean sliver proposed by Métois *et al.* [2016] before Taltal velocities were available.

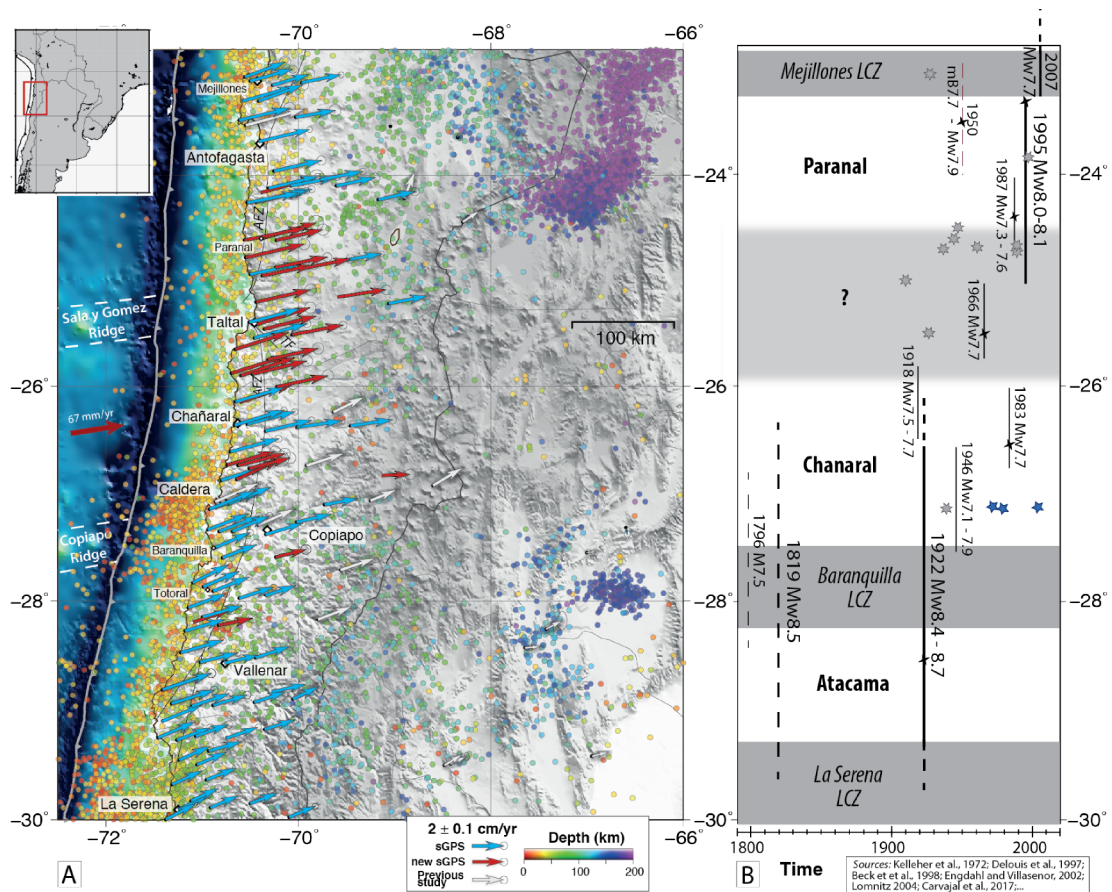


Figure 4.4: Figure from Klein *et al.* [2018]. Inset: localization of the study; (a) interseismic velocity field (mm yr^{-1}) combined between 2010 and 2016 relative to stable South America. Background seismicity (1973–2017) from USGS, represented in colour scale as function of depth. Topography and bathymetry from ETOPO5, white lines represent the main bathymetric features of the Nazca plate (Álvarez *et al.* [2015]). Black lines depict the Atacama Fault Zone (AFZ) and the Taltal Fault (TF) (Lemke *et al.* [1968]; Armijo & Thiele [1990]). (b) Segmentation (Métouis *et al.* [2016]) and historical seismicity as function of time, Mw \sim 7 earthquake epicentres are depicted by gray stars, seismic swarms by blue pentagrams. Black lines represent rupture zones of historical (dashed) and instrumental (continuous) of major events, their epicentres are depicted by black crosses.

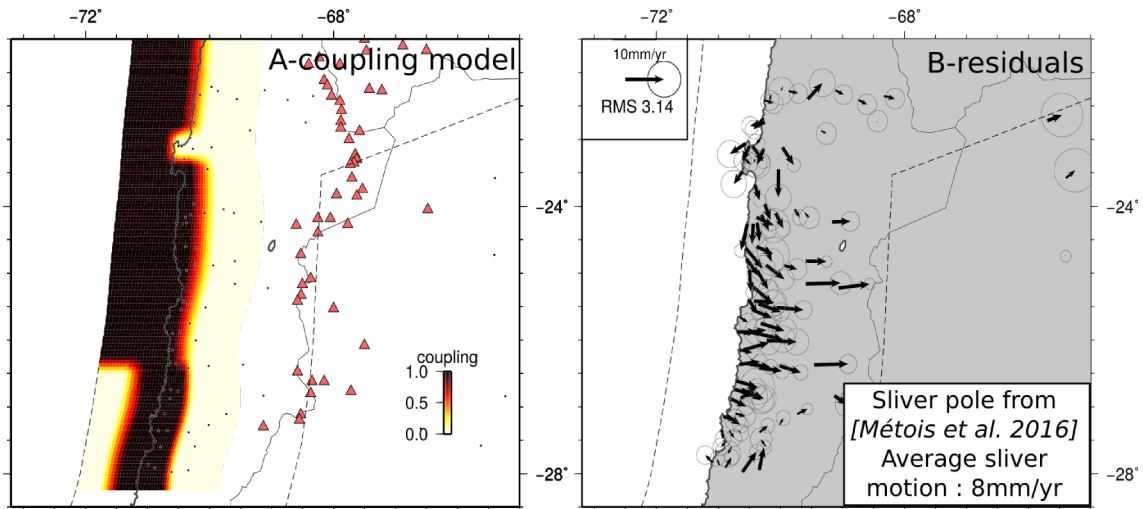


Figure 4.5: Figure from Klein *et al.* [2018]. (a) Simplified forward coupling model derived from the best-model obtained by Métois *et al.* [2016] without the newly acquired data in the Taltal zone. The Mejillones LCZ is mimicked by an abrupt shallowing of the highly coupled zone. The Andean sliver (dashed gray lines) is moving around the Euler pole (56.37°S , 41.27°W and $-0.12^{\circ}\text{Myr}^{-1}$) and produces a 8mmyr^{-1} northeastward motion. Red triangles are the active volcanoes. (b) Residuals (observations-predictions) and normalized root mean square.

Residuals due to the model shown in figure 4.5 are large and systematic at the region of Taltal, with north-east directions at the center and clockwise rotation at the southern and northern ends. Viscoelastic relaxation triggered by earthquakes surrounding this area might be causing such rotation, however, the possibility that 2 recent large earthquakes taking place in the vicinity (one on each side) produce such effect was evaluated and discarded. Furthermore, several coupling models were tested maintaining the same sliver, with no acceptable fit obtained. As a result, a model that explains the deformation of Taltal would require the rotation of the sliver, which challenge the rigidity assumption proposed by previous studies (Chlieh *et al.* [2011]; Nocquet *et al.* [2014]; Métois *et al.* [2016]).

4.1.2 The new local sliver hypothesis and the coupling distribution founded for Taltal

Interpreting the velocity pattern of Taltal requires an accurate model of the Andean deformation, region with insufficient velocity measurements up to date in order to determine its complexity. Considering that the concept of sliver corresponds to a modeling mechanism that allows

to give account for non-elastic deformation in a pure elastic model, then it seems necessary in this case to refine the large scale rigid block modeled for the zone. Thus, the preferred model was obtained inverting simultaneously the coupling distribution and a local sliver (figure 4.6).

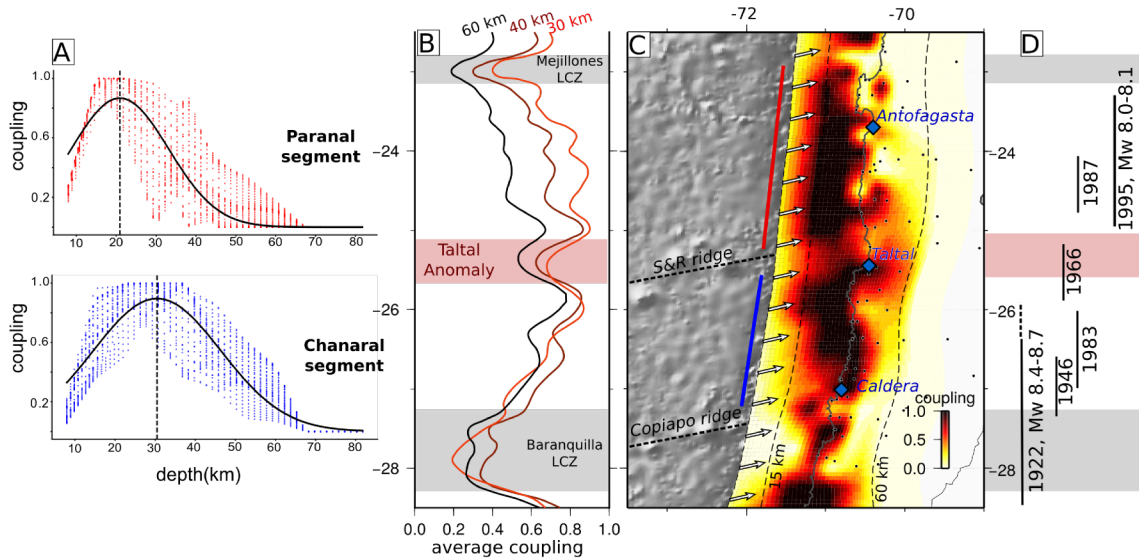


Figure 4.6: Figure from Klein *et al.* [2018]. Best coupling model characteristics. (a) Variation of the coupling coefficient with depth along the Paranal (red dots, up) and Chañaral segments (blue dots, down) and best-fit Gaussian (black curve). (b) Average coupling variation with latitude. The average coupling is calculated on 20 km along-strike wide sliding windows in the convergence direction and every 10 km along the trench. Coupling is either integrated from 10 to 30 km (red curve), from 10 to 40 km (brown curve) and on the entire seismogenic zone (from 10 to 60 km, black curve). (c) Coupling model with 2-D smoothing applied on independent nodes. Dashed curves: 15 and 60 km depth slab contours. White arrows: Nazca-South America convergence direction. Red and blue bold lines depict the extent of the Paranal and Chañaral segments. Dashed bold lines: main bathymetric features, aseismic ridges. Black dots: GPS stations used in this study. (d) Recall of the historical ruptures extends. Reddish area: Taltal low coupling area.

The new preferred coupling distribution is characterized by 2 blocks of marked high coupling separated by a lower coupled zone that coincides with Taltal area. Northern segment named Paranal (23° - 25°) has a shallower high coupling distribution compared with the southern segment Chañaral (25° - 27°). The inversion gives as a result a new local Andean sliver, with an Euler pole still located in the South Atlantic, but moving northeastward respect to South America with a velocity of 16 mm yr^{-1} , 8 mm yr^{-1} more than large scale micro-plate deduced in previous studies. Is important to notice that this apparent forced local sliver is just a representation of a more complex deformation process that can not be determined with the actual available data. In fact, a progressive increase from north to south of the back-arc rotation might be equiv-

alent to the local rigid micro-plate hypothesis. Finally, results from all models performed in this study show the area of Taltal as a low coupled transition zone which divides the region on 2 high coupling patches which might correlate with shallower and deeper seismic ruptures for the north and south segments respectively.

4.1.3 Interseismic velocity calculation

In order to obtain the GPS velocity field of a region it is necessary to express the displacements in a stable reference frame. In general, reference stations for velocities calculated in the Chilean subduction zone correspond to stable sites located at the Amazonian Craton, far from the plates contact where the deformation is strong. Nevertheless, during the time span analyzed here, some of these stations were affected by the mega-earthquake of Maule 2010 (M_w 8.8) which broke more than 500 km along the subduction margin Vigny *et al.* [2011]. This situation forces to enlarge this reference system to a global scale: 42 stations with well known positions (7 of them in South American continent) from ITRF2008 which are not affected for Maule 2010 (see figure 4.7). The mapping of these velocities to a stable South American reference frame is performed by using a new plate with Euler pole (20.9° S, 128.6° W, 0.122° /Myr) calculated for this work. This is necessary due to the high residuals founded for station on the craton using the Euler pole defined by the NNR-Nuvel-1A model DeMets *et al.* [1994].

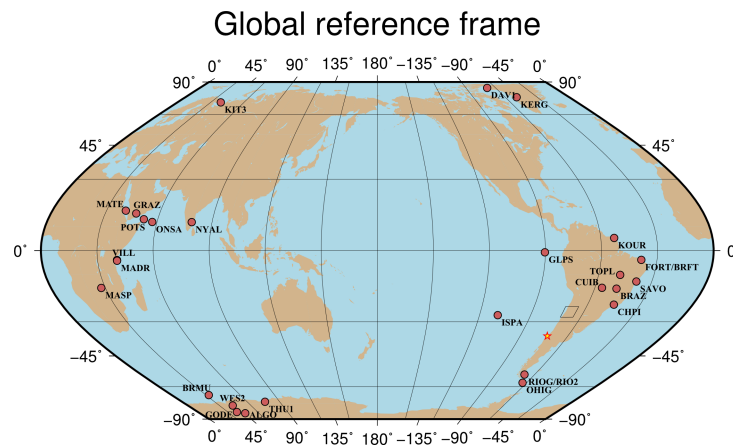


Figure 4.7: Global reference stations used in the calculation of interseismic velocities at the region of study (black rectangle). Epicenter of Maule mega-earthquake is represented by a yellow star.

4.1.4 Do Taltal velocities represent the interseismic period?

It is common to think that with the occurrence of large earthquakes as Maule, the complete Chilean territory is affected by its postseismic signal, although it is important to consider the entire longitude of this margin (more than 4000 km in length) as well as the variation of the magnitude of the postseismic deformation depending on the distance to the event. In this case, in spite of the large co- and post-deformation field produced by this earthquake, the horizontal velocity is less than 1 mm/yr in the region of study at the time that the campaign measurements were performed. This zone is located at more than 900 km from the epicenter. The small amplitude of this deformation at these latitudes was obtained from the viscoelastic relaxation model for Maule 2010 from Klein *et al.* [2016]. The complete postseismic deformation pattern at the region of Taltal obtained from that model is shown in figure 4.8. Additionally, time series from stations surrounding the zone (see figure 4.9) do not exhibit the well known postseismic decay related with afterslip and/or relaxation of the asthenosphere. This confirms that the velocity field for the region is not contaminated by large scale postseismic deformation following Maule 2010, and therefore corresponds to interseismic velocities.

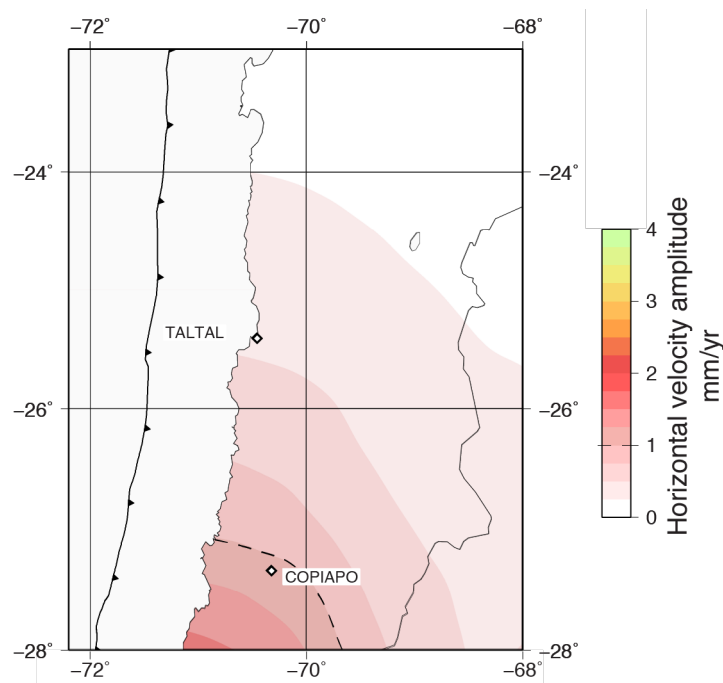


Figure 4.8: Horizontal velocity field for the zone of Taltal obtained by using the viscoelastic relaxation model for Maule 2010 from Klein *et al.* [2016]. Velocities in this region are less than 1mm/yr, and then are not detected due to the precision of GPS time series.

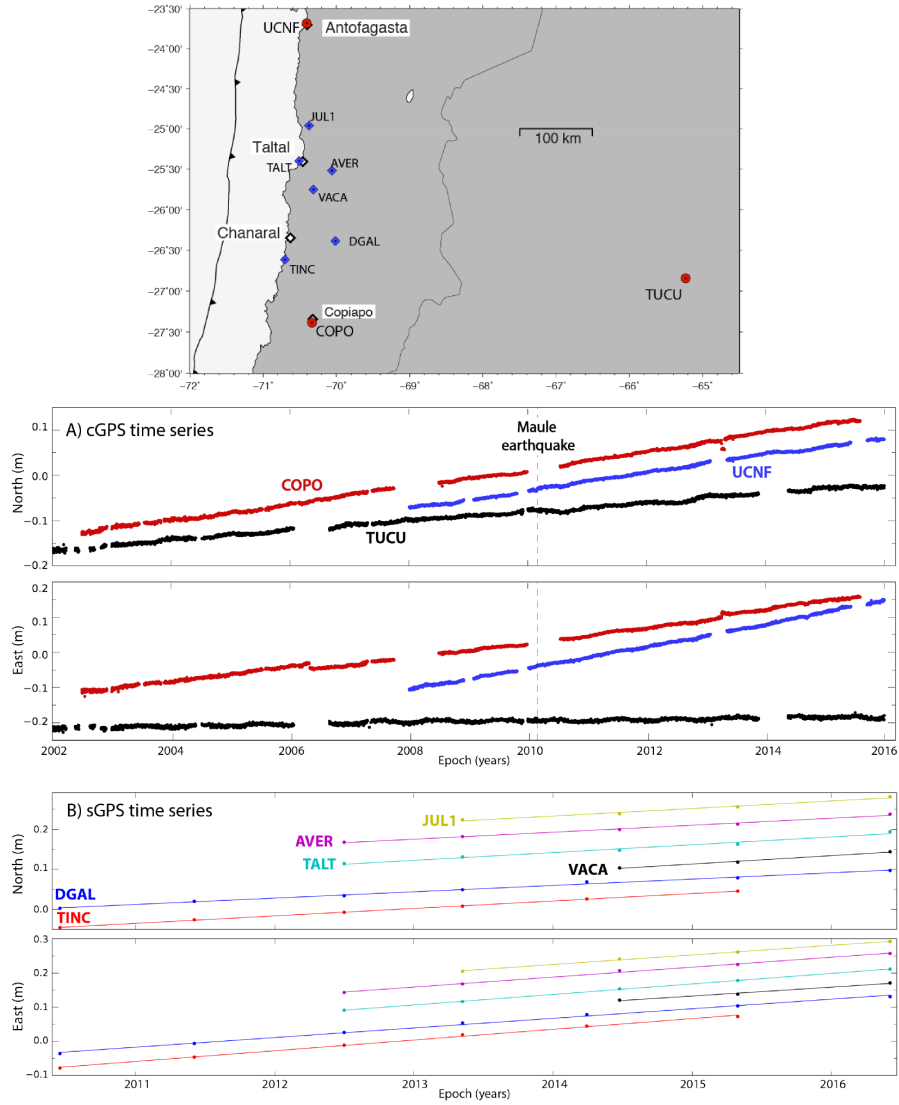


Figure 4.9: Horizontal components of time series (ITRF reference frame) for stations located at the studied region, corresponding to A: continuous time series and B: survey GPS sites. Location of the sites is shown on the map above.

Conclusions

The northern part of the Chilean subduction zone had no large interplate events during almost 150 years after the mega-thrust earthquake of 1877. This seismic silence was interrupted in April 2014, when an interplate earthquake M_w 8.2 broke this seismic gap, although only its northern part. Despite this partial rupture gave some additional information about the current seismic hazard of the region, accounting for possible aseismic slip taking place in this subduction zone is necessary to evaluate the real degree of locking between the plates. Consequently, we used 15 years of continuous GPS time series from this zone to perform short- (days - months) and long-term (years) analyses in the search of aseismic transient deformation.

Because there is no previous evidence of aseismic events in Chile, we performed a new filtering method in our time series, in case the amplitude of these events was too small to be detected with regular noise filtering techniques. We considered critical removing the high frequency noise in a way that ensures a minimal manipulation of the signal. Thus, to remove the common mode error from our time series we used Pyacs, a toolkit able to express raw GPS solutions in a local reference frame. This method is based on the fact that there is some similar spatially correlated noise at a local scale. The short-term analysis revealed only few small amplitude transient signals with durations of up to several weeks. With Pyacs, we obtained a significant improvement in the precision of the time series, especially in horizontal components. The median RMS decreases its value by 27% in comparison to raw time series, reaching 0.6 mm as average between north and east components. This important improvement favors the authenticity of the transitory signals of few millimeters detected in our corrected time series. The largest of these transients occurred simultaneously to the precursory seismicity associated to the M_w 8.2 Iquique earthquake in 2014.

This intense seismic activity, starting several months before the mainshock, was well monitored by seismic and geodetic instruments and also recorded by a higher resolution instrument: a tiltmeter. Our filtered time series together with the analysis of tiltmeter data (F. Boudin, Per. Comm.), allowed to detect 4 different consecutive slow slip events striking the zone at the same time as the foreshock crisis leading to Iquique 2014. Thus, we confirm that slow slip takes place in North Chile subduction zone.

The filtering strategy used in the first part of this study was no longer suitable in the case of our long-term analysis. In the case of the long-term analysis, since high frequency noise does not considerably affect the trend over several years, we did not apply any common mode error filter. However, all sorts of corrections were performed to estimate a purely tectonic long term velocity. For this matter, the effect of the mass variation on Earth's surface was taken into account, and hydrological signals estimated using satellite gravimetry (GRACE) (Chanard *et al.* [2018]) were removed from each of our time series. These filtered positions revealed a clear velocity decrease after Tarapaca 2005 intraslab earthquake observed by 5 stations recording before and after the event. The possibility that such type of earthquake modifies the friction properties of the seismic zone was evaluated in a recent study (Jara *et al.* [2017]). In contrast, we analyzed the viscoelastic behavior of the mantle using a three dimensional finite element model accomplished by the finite element software Z-set/ZéBuLoN. We performed several models combining Maxwell and Burgers rheologies with 2 different geometric configurations. One of them includes a low viscosity region (channel) as the one proposed for southern Chile (Klein *et al.* [2016]), and the second consists on a basic asthenosphere-lithosphere configuration. Our results show that the velocity decrease after Tarapaca earthquake is well explained by models excluding regions with localized low viscosity. In particular, the best fit is produced using a model with a bi-viscous Burgers asthenosphere defined by a low steady-state viscosity of $\eta_M = 1.9e+18$ Pa.s. Therefore, we demonstrate that this detectable interseismic velocity change is well explained by the viscoelastic relaxation of the mantle excited by this 100 km depth intraslab earthquake. Additionally, these results support recent studies analyzing postseismic signals after mega-earthquakes that infer low mantle viscosities in subduction zones (Trubienko *et al.* [2013]; Klein *et al.* [2016]). Since coupling change of the thrust fault is still a plausible phenomenon to explain interseismic velocity reduction, it is fundamental as a next step to contrast both hypothesis considering their very different implications.

The principal contribution of this thesis is to provide new insight on the roll played by large intermediate-depth earthquakes in the seismic cycle, and demonstrate that deep ruptures (~ 100 km) can be used in order to constrain the rheology of subduction zones. Certainly, better recorded (higher quality and more numerous records) intermediate-depth events in the future will allow to obtain more precise results to contrast with our current findings.

Bibliography

- Altamimi, Zuheir, Collilieux, Xavier, & Métivier, Laurent. 2011. ITRF2008: an improved solution of the international terrestrial reference frame. *Journal of Geodesy*, **85**(8), 457–473.
- Álvarez, Orlando, Gimenez, Mario, Folguera, Andres, Spagnotto, Silvana, Bustos, Emilce, Baez, Walter, & Braitenberg, Carla. 2015. New evidence about the subduction of the Copiapó ridge beneath South America, and its connection with the Chilean-Pampean flat slab, tracked by satellite GOCE and EGM2008 models. *Journal of Geodynamics*, **91**, 65–88.
- Angermann, D, Klotz, J, & Reigber, Ch. 1999. Space-geodetic estimation of the Nazca-South America Euler vector. *Earth and Planetary Science Letters*, **171**(3), 329–334.
- Armijo, Rolando, & Thiele, Ricardo. 1990. Active faulting in northern Chile: ramp stacking and lateral decoupling along a subduction plate boundary? *Earth and Planetary Science Letters*, **98**(1), 40–61.
- Astiz, Luciana, Lay, Thorne, & Kanamori, Hiroo. 1988. Large intermediate-depth earthquakes and the subduction process. *Physics of the Earth and Planetary interiors*, **53**(1-2), 80–166.
- Avouac, Jean-Philippe. 2015. From geodetic imaging of seismic and aseismic fault slip to dynamic modeling of the seismic cycle. *Annual Review of Earth and Planetary Sciences*, **43**, 233–271.
- Beck, Susan, Barrientos, Sergio, Kausel, Eduardo, & Reyes, M. 1998. Source characteristics of historic earthquakes along the central Chile subduction. *Journal of South American Earth Sciences*, **11**(2), 115–129.
- Bedford, Jonathan, Moreno, Marcos, Baez, Juan Carlos, Lange, Dietrich, Tilmann, Frederik, Rosenau, Matthias, Heidbach, Oliver, Oncken, Onno, Bartsch, Mitja, Rietbrock, Andreas,

- et al.* . 2013. A high-resolution, time-variable afterslip model for the 2010 Maule Mw= 8.8, Chile megathrust earthquake. *Earth and Planetary Science Letters*, **383**, 26–36.
- Bedford, Jonathan, Moreno, Marcos, Schurr, Bernd, Bartsch, Mitja, & Oncken, Onno. 2015. Investigating the final seismic swarm before the Iquique-Pisagua 2014 Mw 8.1 by comparison of continuous GPS and seismic foreshock data. *Geophysical Research Letters*, **42**(10), 3820–3828.
- Bedford, Jonathan, Moreno, Marcos, Li, Shaoyang, Oncken, Onno, Baez, Juan Carlos, Bevis, Michael, Heidbach, Oliver, & Lange, Dietrich. 2016. Separating rapid relocking, afterslip, and viscoelastic relaxation: An application of the postseismic straightening method to the Maule 2010 cGPS. *Journal of Geophysical Research: Solid Earth*, **121**(10), 7618–7638.
- Béjar-Pizarro, Marta, Socquet, Anne, Armijo, Rolando, Carrizo, Daniel, Genrich, Jeff, & Simons, Mark. 2013. Andean structural control on interseismic coupling in the North Chile subduction zone. *Nature Geoscience*, **6**(6), 462.
- Beroza, Gregory C, & Ide, Satoshi. 2011. Slow earthquakes and nonvolcanic tremor. *Annual review of Earth and planetary sciences*, **39**, 271–296.
- Betancourt, JL, Latorre, Claudio, Rech, JA, Quade, Jay, & Rylander, KA. 2000. A 22,000-year record of monsoonal precipitation from northern Chile's Atacama Desert. *Science*, **289**(5484), 1542–1546.
- Bevis, Michael, & Brown, Abel. 2014. Trajectory models and reference frames for crustal motion geodesy. *Journal of Geodesy*, **88**(3), 283–311.
- Bie, Lidong, Ryder, Isabelle, & Métois, Marianne. 2017. Deep postseismic viscoelastic relaxation excited by an intraslab normal fault earthquake in the Chile subduction zone. *Tectonophysics*, **712**, 729–735.
- Bouchon, Michel, Durand, Virginie, Marsan, David, Karabulut, Hayrullah, & Schmittbuhl, Jean. 2013. The long precursory phase of most large interplate earthquakes. *Nature geoscience*, **6**(4), 299.
- Boudin, F, Bernard, P, Longuevergne, Laurent, Florsch, Nicolas, Larmat, C, Courteille, C, Blum, P-A, Vincent, T, & Kammentaler, M. 2008. A silica long base tiltmeter with high stability and resolution. *Review of Scientific Instruments*, **79**(3), 034502.

- Bürgmann, Roland, & Dresen, Georg. 2008. Rheology of the lower crust and upper mantle: Evidence from rock mechanics, geodesy, and field observations. *Annual Review of Earth and Planetary Sciences*, **36**.
- Chanard, Kristel, Fleitout, Luce, Calais, Eric, Barbot, Sylvain, & Avouac, Jean-Philippe. 2018. Constraints on transient viscoelastic rheology of the asthenosphere from seasonal deformation. *Geophysical Research Letters*, **45**(5), 2328–2338.
- Chlieh, M, De Chabalier, JB, Ruegg, JC, Armijo, R, Dmowska, R, Campos, J, & Feigl, KL. 2004. Crustal deformation and fault slip during the seismic cycle in the North Chile subduction zone, from GPS and InSAR observations. *Geophysical Journal International*, **158**(2), 695–711.
- Chlieh, Mohamed. 2003. *Le cycle sismique décrit avec les données de la géodésie spatiale (interférométrie SAR et GPS différentiel): variations spatio-temporelles des glissements stables et instables sur l'interface de subduction du Nord Chili*. Ph.D. thesis, Paris, Institut de physique du globe.
- Chlieh, Mohamed, Perfettini, Hugo, Tavera, Hernando, Avouac, Jean-Philippe, Remy, Dominique, Nocquet, Jean-Mathieu, Rolandone, Frédérique, Bondoux, Francis, Gabalda, Gerninal, & Bonvalot, Sylvain. 2011. Interseismic coupling and seismic potential along the Central Andes subduction zone. *Journal of Geophysical Research: Solid Earth*, **116**(B12).
- Comte, Diana, & Pardo, Mario. 1991. Reappraisal of great historical earthquakes in the northern Chile and southern Peru seismic gaps. *Natural hazards*, **4**(1), 23–44.
- Delouis, Bertrand, & Legrand, Denis. 2007. Mw 7.8 Tarapaca intermediate depth earthquake of 13 June 2005 (northern Chile): Fault plane identification and slip distribution by waveform inversion. *Geophysical Research Letters*, **34**(1).
- DeMets, Charles, Gordon, Richard G, Argus, Donald F, & Stein, Seth. 1994. Effect of recent revisions to the geomagnetic reversal time scale on estimates of current plate motions. *Geophysical research letters*, **21**(20), 2191–2194.
- Detournay, Emmanuel, & Cheng, Alexander H-D. 1995. Fundamentals of poroelasticity. *Pages 113–171 of: Analysis and design methods*. Elsevier.

- Dieterich, James H. 1979. Modeling of rock friction: 1. Experimental results and constitutive equations. *Journal of Geophysical Research: Solid Earth*, **84**(B5), 2161–2168.
- Dragert, H, Wang, K, & Rogers, G. 2004. Geodetic and seismic signatures of episodic tremor and slip in the northern Cascadia subduction zone. *Earth, planets and space*, **56**(12), 1143–1150.
- Fedotov, SA, Sobolev, GA, Boldyrev, SA, Gusev, AA, Kondratenko, AM, Potapova, OV, Slavina, LB, Theophylaktov, VD, Khramov, AA, & Shirokov, VA. 1977. Long-and short-term earthquake prediction in Kamchatka. *Tectonophysics*, **37**(4), 305–321.
- Hackl, M, Malservisi, R, Hugentobler, U, & Wonnacott, R. 2011. Estimation of velocity uncertainties from GPS time series: Examples from the analysis of the South African TrigNet network. *Journal of Geophysical Research: Solid Earth*, **116**(B11).
- Hashimoto, M, Sagiya, T, Ozawa, S, & Tada, T. 1993. Fault models for the crustal movements associated with the 1993 Off Koshiro earthquake and the 1993 Southwestern Off Hokkaido earthquake and their tectonic significance. *Proceedings of the CRCM*, **93**, 57–64.
- Hayes, Gavin P, Wald, David J, & Johnson, Rebecca L. 2012. Slab1.0: A three-dimensional model of global subduction zone geometries. *Journal of Geophysical Research: Solid Earth*, **117**(B1).
- Hirose, Hitoshi, & Obara, Kazushige. 2005. Repeating short-and long-term slow slip events with deep tremor activity around the Bungo channel region, southwest Japan. *Earth, planets and space*, **57**(10), 961–972.
- Hu, Y, Wang, K, He, J, Klotz, J, & Khazaradze, G. 2004. Three-dimensional viscoelastic finite element model for postseismic deformation of the great 1960 Chile earthquake. *Journal of Geophysical Research: Solid Earth*, **109**(B12).
- Hu, Yan, & Wang, Kelin. 2012. Spherical-Earth finite element model of short-term postseismic deformation following the 2004 Sumatra earthquake. *Journal of Geophysical Research: Solid Earth*, **117**(B5).
- Hughes, Kristin LH, Masterlark, Timothy, & Mooney, Walter D. 2010. Poroelastic stress-triggering of the 2005 M8. 7 Nias earthquake by the 2004 M9. 2 Sumatra–Andaman earthquake. *Earth and Planetary Science Letters*, **293**(3-4), 289–299.

- Ide, Satoshi, Beroza, Gregory C, Shelly, David R, & Uchide, Takahiko. 2007. A scaling law for slow earthquakes. *Nature*, **447**(7140), 76.
- Ito, Yoshihiro, Obara, Kazushige, Shiomi, Katsuhiko, Sekine, Shutaro, & Hirose, Hitoshi. 2007. Slow earthquakes coincident with episodic tremors and slow slip events. *Science*, **315**(5811), 503–506.
- Ivins, Erik R, & Sammis, Charles G. 1996. Transient creep of a composite lower crust: 1. Constitutive theory. *Journal of Geophysical Research: Solid Earth*, **101**(B12), 27981–28004.
- Jara, Jorge, Socquet, Anne, Marsan, David, & Bouchon, Michel. 2017. Long-Term Interactions Between Intermediate Depth and Shallow Seismicity in North Chile Subduction Zone. *Geophysical Research Letters*, **44**(18), 9283–9292.
- Johnson, Hadley O, & Agnew, Duncan Carr. 1995. Monument motion and measurements of crustal velocities. *Geophysical Research Letters*, **22**(21), 2905–2908.
- Kaneko, Yoshihiro, Avouac, Jean-Philippe, & Lapusta, Nadia. 2010. Towards inferring earthquake patterns from geodetic observations of interseismic coupling. *Nature Geoscience*, **3**(5), 363.
- Kato, Aitaro, & Nakagawa, Shigeki. 2014. Multiple slow-slip events during a foreshock sequence of the 2014 Iquique, Chile Mw 8.1 earthquake. *Geophysical Research Letters*, **41**(15), 5420–5427.
- Kato, Naoyuki. 2004. A possible effect of an intermediate depth intraslab earthquake on seismic cycles of interplate earthquakes at a subduction zone. *Earth, planets and space*, **56**(6), 553–561.
- Kausel, E. 1986. Los terremotos de agosto de 1868 y mayo de 1877 que afectaron el sur del Perú y norte de Chile. *Boletín de la Academia Chilena de Ciencias*, **3**(1), 8–13.
- King, RW, & Bock, Y. 1999. Documentation for the GAMIT GPS analysis software. *Mass. Inst. of Technol., Cambridge Mass*, **9**.
- Klein, E, Fleitout, L, Vigny, C, & Garaud, JD. 2016. Afterslip and viscoelastic relaxation model inferred from the large-scale post-seismic deformation following the 2010 M w 8.8 Maule earthquake (Chile). *Geophysical Journal International*, **205**(3), 1455–1472.

- Klein, E, Métois, M, Meneses, G, Vigny, C, & Delorme, A. 2018. Bridging the gap between North and Central Chile: insight from new GPS data on coupling complexities and the Andean sliver motion. *Geophysical Journal International*, **213**(3), 1924–1933.
- Klein, Emilie. 2015 (Dec.). *Post-seismic deformation after the Maule earthquake (Mw8.8, Chile, 2010) : GPS measurements and finite element modeling for a viscoelastic asthenosphere*. Theses, Ecole normale supérieure - ENS PARIS.
- Klein, Emilie, Vigny, Christophe, Fleitout, Luce, Grandin, Raphael, Jolivet, Romain, Rivera, Efrain, & Métois, Marianne. 2017. A comprehensive analysis of the Illapel 2015 Mw8. 3 earthquake from GPS and InSAR data. *Earth and Planetary Science Letters*, **469**, 123–134.
- Lemke, Richard W, Dobrovolny, Ernest, Alvarez S, Leonardo, & Ortiz O, Francisco. 1968. Geologic and related effects of the Taltal earthquake, Chile, of December 28, 1966. *Bulletin of the Seismological Society of America*, **58**(3), 851–859.
- Lemoine, A, Madariaga, R, & Campos, J. 2002. Slab-pull and slab-push earthquakes in the Mexican, Chilean and Peruvian subduction zones. *Physics of the Earth and Planetary Interiors*, **132**(1-3), 157–175.
- Lomnitz, Cinna. 2004. Major earthquakes of Chile: a historical survey, 1535-1960. *Seismological Research Letters*, **75**(3), 368–378.
- Madariaga, Raúl. 1998. Sismicidad de Chile. *Física de la Tierra*, 221.
- Mao, Ailin, Harrison, Christopher GA, & Dixon, Timothy H. 1999. Noise in GPS coordinate time series. *Journal of Geophysical Research: Solid Earth*, **104**(B2), 2797–2816.
- Melosh, HJ, & Raefsky, A. 1981. A simple and efficient method for introducing faults into finite element computations. *Bulletin of the Seismological Society of America*, **71**(5), 1391–1400.
- Melosh, HJ, & Raefsky, A. 1983. Anelastic response of the Earth to a dip slip earthquake. *Journal of Geophysical Research: Solid Earth*, **88**(B1), 515–526.
- Métois, M, Vigny, C, Socquet, A, Delorme, A, Morvan, S, Ortega, I, & Valderas-Bermejo, C-M. 2013a. GPS-derived interseismic coupling on the subduction and seismic hazards in the Atacama region, Chile. *Geophysical Journal International*, **196**(2), 644–655.

- Métois, M, Vigny, C, & Socquet, A. 2016. Interseismic coupling, megathrust earthquakes and seismic swarms along the Chilean subduction zone (38–18 S). *Pure and Applied Geophysics*, **173**(5), 1431–1449.
- Métois, Marianne. 2012. *Quantification du couplage au long de la subduction chilienne*. Ph.D. thesis, Université Paris 7-Denis Diderot; Institut de Physique du Globe de Paris (IPGP), France.
- Métois, Marianne, Socquet, Anne, Vigny, Christophe, Carrizo, Daniel, Peyrat, Sophie, Delorme, A, Maureira, E, Valderas-Bermejo, M-C, & Ortega, I. 2013b. Revisiting the North Chile seismic gap segmentation using GPS-derived interseismic coupling. *Geophysical Journal International*, **194**(3), 1283–1294.
- Missoum-benziame, D, Chiaruttini, V, Garaud, JD, Feyel, F, Foerch, R, Osipov, N, Quilici, S, Rannou, J, Roos, A, & Ryckelynck, D. 2011. Z-set. In: *ZeBuLoN: Une Suite Logicielle Pour La Mécanique Des Matériaux et Le Calcul de Structures, 10e colloque national en calcul des structures*, vol. 8.
- Moreno, M, Melnick, Daniel, Rosenau, M, Bolte, John, Klotz, Jan, Echtler, H, Baez, J, Bataille, K, Chen, J, Bevis, M, *et al.* . 2011. Heterogeneous plate locking in the South–Central Chile subduction zone: Building up the next great earthquake. *Earth and Planetary Science Letters*, **305**(3), 413–424.
- Moreno, Marcos, Rosenau, Matthias, & Oncken, Onno. 2010. 2010 Maule earthquake slip correlates with pre-seismic locking of Andean subduction zone. *Nature*, **467**(7312), 198.
- Nakajima, Junichi, Yoshida, Keisuke, & Hasegawa, Akira. 2013. An intraslab seismic sequence activated by the 2011 Tohoku-oki earthquake: Evidence for fluid-related embrittlement. *Journal of Geophysical Research: Solid Earth*, **118**(7), 3492–3505.
- Nocquet, Jean-Mathieu, Villegas-Lanza, JC, Chlieh, Mohamed, Mothes, PA, Rolandone, Frédérique, Jarrin, P, Cisneros, D, Alvarado, A, Audin, Laurence, Bondoux, Francis, *et al.* . 2014. Motion of continental slivers and creeping subduction in the northern Andes. *Nature Geoscience*, **7**(4), 287.
- Peng, Z, & Gomberg, J. 2010. An integrative perspective of coupled seismic and aseismic slow slip phenomena. *Nature Geosci*, **3**, 599–607.

- Perfettini, Hugo, Avouac, Jean-Philippe, Tavera, Hernando, Kositsky, Andrew, Nocquet, Jean-Mathieu, Bondoux, Francis, Chlieh, Mohamed, Sladen, Anthony, Audin, Laurence, Farber, Daniel L, *et al.* . 2010. Seismic and aseismic slip on the Central Peru megathrust. *Nature*, **465**(7294), 78.
- Peyrat, S, Campos, J, De Chabalier, Jean-Bernard, Perez, A, Bonvalot, S, Bouin, M-P, Legrand, D, Necessian, Alexandre, Charade, Olivier, Patau, G, *et al.* . 2006. Tarapacá intermediate-depth earthquake (Mw 7.7, 2005, northern Chile): A slab-pull event with horizontal fault plane constrained from seismologic and geodetic observations. *Geophysical research letters*, **33**(22).
- Pollitz, Fred F, Wicks, Chuck, & Thatcher, Wayne. 2001. Mantle flow beneath a continental strike-slip fault: Postseismic deformation after the 1999 Hector Mine earthquake. *Science*, **293**(5536), 1814–1818.
- Radiguet, Mathilde, Cotton, Fabrice, Vergnolle, Mathilde, Campillo, Michel, Valette, Bernard, Kostoglodov, Vladimir, & Cotte, Nathalie. 2011. Spatial and temporal evolution of a long term slow slip event: the 2006 Guerrero Slow Slip Event. *Geophysical Journal International*, **184**(2), 816–828.
- Reid, Harry Fielding. 1910. The mechanism of the earthquake, The California earthquake of April 18, 1906. *Report of the Research Senatorial Commission, Carnegie Institution, Washington, DC*, **2**, 16–18.
- Rogers, Garry, & Dragert, Herb. 2003. Episodic tremor and slip on the Cascadia subduction zone: The chatter of silent slip. *Science*, **300**(5627), 1942–1943.
- Ruegg, JC, Rudloff, A, Vigny, C, Madariaga, R, De Chabalier, JB, Campos, J, Kausel, E, Barrientos, S, & Dimitrov, D. 2009. Interseismic strain accumulation measured by GPS in the seismic gap between Constitución and Concepción in Chile. *Physics of the Earth and Planetary Interiors*, **175**(1-2), 78–85.
- Ruina, Andy. 1983. Slip instability and state variable friction laws. *Journal of Geophysical Research: Solid Earth*, **88**(B12), 10359–10370.

- Ruiz, S, Metois, M, Fuenzalida, A, Ruiz, J, Leyton, F, Grandin, R, Vigny, C, Madariaga, R, & Campos, J. 2014. Intense foreshocks and a slow slip event preceded the 2014 Iquique Mw 8.1 earthquake. *Science*, **345**(6201), 1165–1169.
- Schmidt, DA, & Gao, H. 2010. Source parameters and time-dependent slip distributions of slow slip events on the Cascadia subduction zone from 1998 to 2008. *Journal of Geophysical Research: Solid Earth*, **115**(B4).
- Scholz, Christopher H. 1998. Earthquakes and friction laws. *Nature*, **391**(6662), 37.
- Schurr, Bernd, Asch, Günter, Hainzl, Sebastian, Bedford, Jonathan, Hoechner, Andreas, Palo, Mauro, Wang, Rongjiang, Moreno, Marcos, Bartsch, Mitja, Zhang, Yong, *et al.* . 2014. Gradual unlocking of plate boundary controlled initiation of the 2014 Iquique earthquake. *Nature*, **512**(7514), 299.
- Shen, Zheng-Kang, Jackson, David D, Feng, Yanjie, Cline, Michael, Kim, Mercedes, Fang, Peng, & Bock, Yehuda. 1994. Postseismic deformation following the Landers earthquake, California, 28 June 1992. *Bulletin of the Seismological Society of America*, **84**(3), 780–791.
- Shimazaki, Kunihiko, & Nakata, Takashi. 1980. Time-predictable recurrence model for large earthquakes. *Geophysical Research Letters*, **7**(4), 279–282.
- Socquet, Anne, Valdes, Jesus Piña, Jara, Jorge, Cotton, Fabrice, Walpersdorf, Andrea, Cotte, Nathalie, Specht, Sebastian, Ortega-Culaciati, Francisco, Carrizo, Daniel, & Norabuena, Edmundo. 2017. An 8 month slow slip event triggers progressive nucleation of the 2014 Chile megathrust. *Geophysical Research Letters*, **44**(9), 4046–4053.
- Sodoudi, F, Yuan, X, Asch, G, & Kind, R. 2011. High-resolution image of the geometry and thickness of the subducting Nazca lithosphere beneath northern Chile. *Journal of Geophysical Research: Solid Earth*, **116**(B4).
- Tapley, Byron D, Bettadpur, Srinivas, Ries, John C, Thompson, Paul F, & Watkins, Michael M. 2004. GRACE measurements of mass variability in the Earth system. *Science*, **305**(5683), 503–505.
- Trubienko, Olga. 2012. Déformation pré et post-sismique dans la région de Sumatra et le cycle sismique.

- Trubienko, Olga, Fleitout, Luce, Garaud, Jean-Didier, & Vigny, Christophe. 2013. Interpretation of interseismic deformations and the seismic cycle associated with large subduction earthquakes. *Tectonophysics*, **589**, 126–141.
- Turcotte, DL, & Schubert, G. 2002. *Geodynamics*, 456 pp.
- van Keken, Peter E. 2003. The structure and dynamics of the mantle wedge. *Earth and planetary science letters*, **215**(3-4), 323–338.
- Vigny, C, Socquet, A, Peyrat, Sophie, Ruegg, J-C, Métois, M, Madariaga, R, Morvan, S, Lancieri, M, Lacassin, R, Campos, J, *et al.* . 2011. The 2010 Mw 8.8 Maule megathrust earthquake of Central Chile, monitored by GPS. *Science*, **332**(6036), 1417–1421.
- Vigny, Christophe, Rudloff, Alain, Ruegg, Jean-Claude, Madariaga, Raul, Campos, Jaime, & Alvarez, Manuel. 2009. Upper plate deformation measured by GPS in the Coquimbo Gap, Chile. *Physics of the Earth and Planetary Interiors*, **175**(1-2), 86–95.
- Wang, Kelin, & Dixon, Timothy. 2004. “Coupling” semantics and science in earthquake research. *Eos, Transactions American Geophysical Union*, **85**(18), 180–180.
- Wang, Kelin, Hu, Yan, & He, Jiangheng. 2012. Deformation cycles of subduction earthquakes in a viscoelastic Earth. *Nature*, **484**(7394), 327.
- Yoshioka, SHOICHI, & Tokunaga, Y. 1998. Numerical simulation of displacement and stress fields associated with the 1993 Kushiro-oki, Japan, earthquake. *pure and applied geophysics*, **152**(3), 443–464.
- Yuen, David A, Sabadini, Roberto CA, Gasperini, Paolo, & Boschi, Enzo. 1986. On transient rheology and glacial isostasy. *Journal of Geophysical Research: Solid Earth*, **91**(B11), 11420–11438.
- Zhang, Jie, Bock, Yehuda, Johnson, Hadley, Fang, Peng, Williams, Simon, Genrich, Joachim, Wdowinski, Shimon, & Behr, Jeff. 1997. Southern California Permanent GPS Geodetic Array: Error analysis of daily position estimates and site velocities. *Journal of Geophysical Research: Solid Earth*, **102**(B8), 18035–18055.

Appendix A

Appendix A (chapter 2)

Reference stations	RMS North [mm]	RMS East [mm]	RMS Vertical [mm]				
AREQ	3.3	3.3	5.3				
PTRE	4.5	4.0	5.6				
PCCL	4.2	4.3	4.6				
MICA	4.1	5.5	4.1				
RADO	3.9	4.1	6.1				
CDLC	3.9	5.1	4.2				
PB04	4.0	5.5	4.5				
MCLA	4.1	5.0	3.9				
JRGN	4.0	5.4	3.9				
CBAA	3.9	3.7	3.9				
CJNT	3.9	3.8	3.4				
Corrected stations	RMS North [mm] before correction	RMS East [mm] before correction	RMS Vertical [mm] before correction	RMS North [mm] after correction	RMS East [mm] after correction	RMS Vertical [mm] after correction	Possible event dates
MNMI	1.6	3.0	6.0	0.5	0.7	4.9	2008.91
UAPE	1.8	2.8	3.4	0.5	0.7	2.0	-
HMBS	1.8	3.2	6.6	0.6	0.9	5.3	2008.91
PB01	1.6	3.0	3.3	0.4	0.6	2.6	-
ATJN	1.7	3.0	3.4	0.6	0.6	2.1	-
PSGA	1.6	3.0	3.8	0.5	0.8	2.5	2008.91
COLC	-	-	-	-	-	-	-
CHMZ	1.6	3.0	3.3	0.4	0.5	1.8	-
PCHA	-	-	-	-	-	-	-
FBAQ	-	-	-	-	-	-	-
IQQE	1.7	3.0	3.3	0.4	0.7	2.3	-
AEDA	-	-	-	-	-	-	-
CRSC	1.6	3.0	3.2	0.4	0.5	1.7	-
PB02	1.8	3.0	3.3	0.5	0.7	2.3	-

Table A.1: RMS values for reference and Pyacs corrected stations for a 6-months window spanning September 2008 to February 2009.

Reference stations	RMS North [mm]	RMS East [mm]	RMS Vertical [mm]				
AREQ	1.8	3.1	3.6				
PTRE	1.2	2.1	3.5				
PCCL	2.2	2.4	3.6				
UTAR	2.5	2.2	4.1				
COLC	2.4	2.5	4.8				
CTLR	2.8	2.6	3.4				
MCLA	2.8	2.6	3.3				
SRGD	2.5	2.3	3.6				
CBAA	2.6	2.4	3.8				
CJNT	2.5	2.5	3.8				
PMEJ	3.4	2.7	4.1				
UCNF	3	3.1	3.7				
Corrected stations	RMS North [mm] before correction	RMS East [mm] before correction	RMS Vertical [mm] before correction	RMS North [mm] after correction	RMS East [mm] after correction	RMS Vertical [mm] after correction	Possible event dates
ATJN	1.7	2.3	3.3	0.5	0.4	1.5	nul
CHMZ	1.7	2.2	3.3	0.3	0.5	1.3	2010.75
CGTC	1.7	2.2	3.3	0.3	0.4	1.2	nul
UAPE	1.7	2.5	4.2	0.4	0.8	2.8	2010.55
PICC	1.8	2.3	3.6	0.3	0.5	1.9	2010.55
CRSC	1.7	2.2	3.4	0.3	0.4	1.2	nul
CLLA	1.8	2.3	3.4	0.3	0.4	1.4	nul
MNMI	1.6	2.3	3.4	0.5	0.8	2.1	2010.57
COLC	1.8	2.5	4.4	0.9	1.5	3.1	nul
PSGA	1.8	2.4	4.2	0.4	0.6	3	nul
PCHA	1.4	2.5	3.2	0.5	0.7	3.1	2010.6
PB08	1.8	2.3	4.3	0.6	0.9	2.7	nul
IQQE	1.7	2.2	3.7	0.3	0.5	1.9	2010.56
PB01	1.7	2.2	4.2	0.3	0.4	2.2	nul

Table A.2: RMS values for reference and Pyacs corrected stations for a 6-months window spanning May to October 2010.

Appendix B

Appendix B (chapter 3)

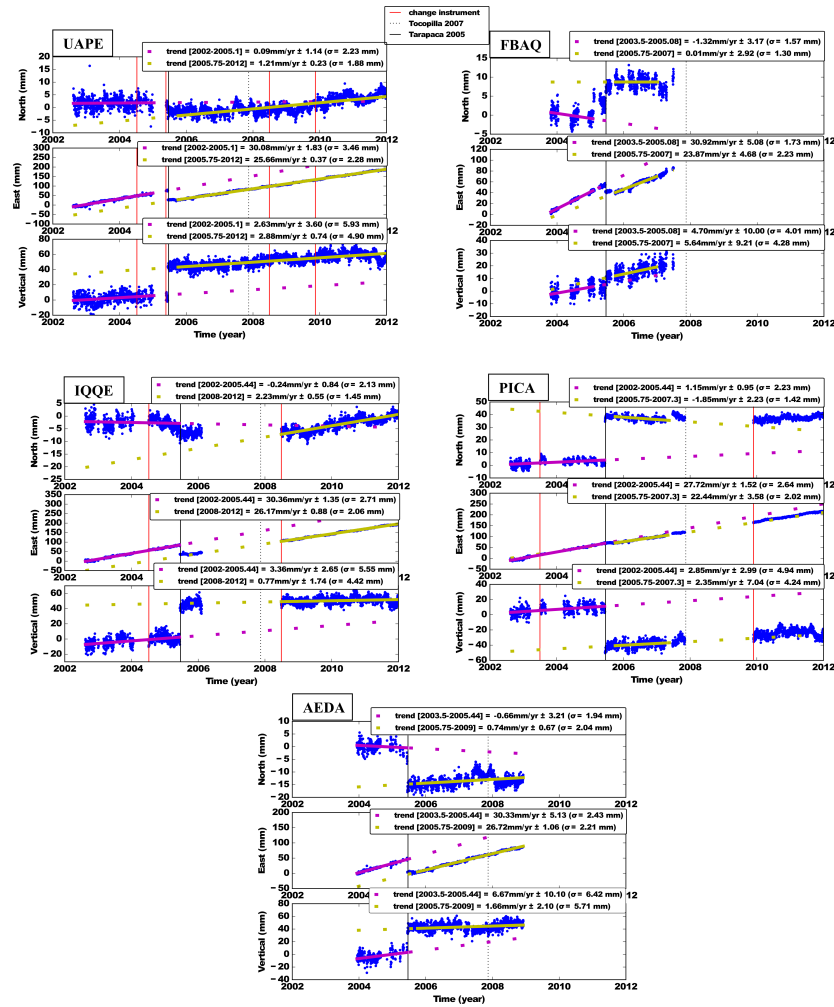


Figure B.1: Velocity calculation before and after Tarapaca 2005 for 5 stations located around 20°S. Positions observed between 2002 and 2012 are represented as blue dots. Trends before (magenta) and after (yellow) are shown as a continuous line for the calculation period. Labels contain information about the trends as errors and standard deviation (σ) for each period. Tarapaca earthquake can be identified as the uncorrected jump in the figure. The layout of the figures is presented as the real station locations on a plan view.

Site	date _{start}	date _{end}	V _n	ΔV _n	V _e	ΔV _e	V _v	ΔV _v	σ _n	σ _e	σ _v
AEDA	01/10/2005	16/05/2007	0.7	1.65	-2.0	2.5	-4.1	6.8	1.1	1.6	3.6
FBAQ	01/10/2005	01/01/2007	-0.5	2.2	-5.4	4.1	2.2	8.1	0.9	1.7	2.8
PICA	01/10/2005	27/05/2007	-3.0	1.8	-5.8	2.2	1.3	5.2	1.1	1.3	2.6
UAIQ	01/10/2005	27/02/2010	-0.1	0.4	-4.5	0.6	1.0	1.2	1.2	1.7	3.1

Table B.1: Tarapaca 2005 postseismic velocity values for each component (north (n), east (e) and vertical (v)) obtained from GPS time series from figure 3.9. The error (ΔV) of the trend and the standard deviation (σ) of the data for each calculation period are added as supplementary information. Velocities and their errors are given in mm/y and standard deviation in mm.

Coseismic displacements			
Stations	East (mm)	North (mm)	Vertical (mm)
AEDA	-44.9	-20.0	29.9
FBAQ	-12.1	0.5	3.9
IQQE	-45.7	-11.3	42.1
PICA	-5.3	31.9	-51.5
UAPE	-45.3	-12.1	36.3
UTAR	-7.1	3.5	6.2
QUIL	-2.0	2.0	1.0
COLL	-21.0	36.0	-28.0

Table B.2: Tarapaca 2005 observed coseismic displacements.

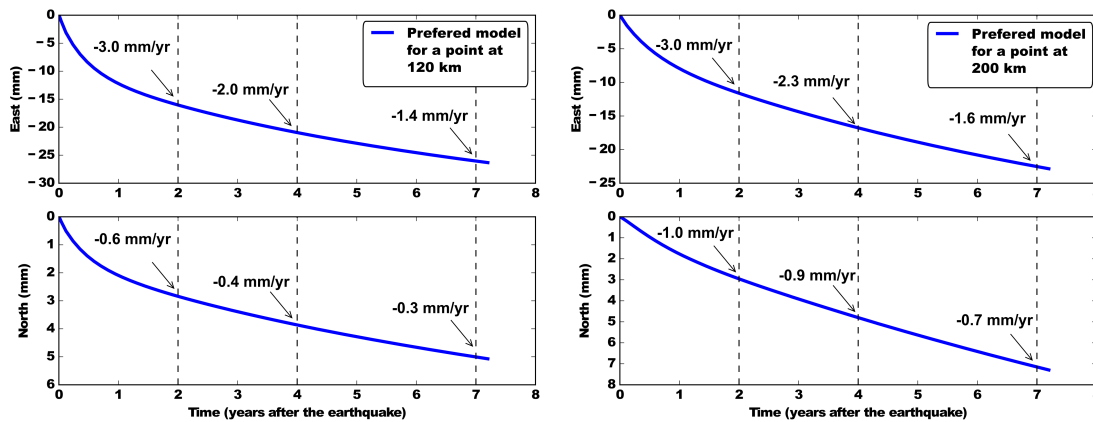


Figure B.2: Horizontal deformation predicted by our preferred model at 2 points located at 120 and 200 km from the trench. Deformation rates after 2, 4 and 7 (dashed vertical lines) years after the earthquake are indicated in the figure.

Résumé

Les zones de subduction impliquent le recyclage de la lithosphère océanique dans le manteau convectif pour former une croûte continentale par migration ascendante de la partie fondue du slab. Ce processus à long terme, où la plaque supérieure accumule des contraintes qui sont instantanément libérées sous la forme de séismes, se répète sur un processus cyclique: le cycle sismique de subduction (SEC). Néanmoins, le glissement rapide sur les failles n'est pas le seul processus contribuant à la déformation pendant le SEC. Des processus de glissement aisé sont observés sous la forme de creeping constant et de glissement lent transitoire. Exemple du dernier est le phénomène d'afterslip et les slow slip events (SSE) dont la durée est beaucoup plus longue que les séismes "normaux". De la même importance est l'effet du stress induit par un séisme dans le manteau. Parce qu'il se comporte comme un corps viscoélastique, le manteau détend ce stress au cours d'un processus de déformation lent de longue durée et à grande échelle. Tous ces phénomènes ont un impact sur la déformation de la plaque supérieure et doivent être pris en compte dans l'analyse du budget de glissement sur le SEC afin d'obtenir l'estimation réelle du risque sismique d'une région. En partant de cette prémisse, la principale motivation de ce travail est de contribuer à la détermination de l'état actuel de couplage de l'interface sismique de la zone nord de la subduction chilienne.

La majeure partie de cette étude a été menée dans deux directions: l'analyse et l'interprétation des déformations transitoires à court terme (jours, semaines) et à long terme (années) détectées par les stations GPS permanentes déployées au nord du Chili. Premièrement, en recherchant de façon exhaustive les signaux transitoires à court terme dans des séries géodésiques, nous cherchons à contribuer au débat actuel sur la question de savoir si des glissements lents se produisent dans la zone de subduction chilienne ou non. Jusqu'à présent, un seul cas de glissement lent associé à la phase de nucléation d'Iquique 2014 a été rapporté. Nos résultats, obtenus après filtrage et analyse approfondie des séries temporelles consacrées à la réduction de leur bruit inhérent, indiquent l'existence de seulement 3 événements susceptibles de correspondre à de petits épisodes de glissement sismique. Ils se produisent entre 2009 et 2011, avec des durées de quelques semaines et des amplitudes qui ne dépassent pas 4 mm. De plus, l'occurrence de l'épisode de glissement sismique plus important simultané à l'activité du séisme d'Iquique 2014 est confirmée, et l'analyse est poussée plus loin à l'aide d'enregistrements par inclinomètres à longue base. Grâce à cette analyse affinée et à la sensibilité de cet instrument, 4 événements de glissement lent distincts peuvent être identifiés dans la plus grande région de glissement lent révélée par les données GPS, survenant au cours des 3 mois précédant le choc principal avec des magnitudes comprises entre Mw 5,8 et 6,2. Enfin, une analyse à long terme a été effectuée afin d'identifier les changements mineurs mais significatifs des tendances sur de longues périodes. Les données disponibles indiquent une diminution à long terme de la déformation de la plaque supérieure après le séisme de profondeur moyenne de Tarapaca 2005 (Mw 7.7). Nous testons l'effet viscoélastique de l'asthénosphère sur la déformation de surface déclenchée par une rupture profonde (~ 100 km). Pour cela, nous construisons un modèle 3D viscoélastique réaliste d'éléments finis viscoélastiques et avons essayé les rhéologies viscoélastiques de Maxwell et Burgers. Nous trouvons une très bonne correspondance entre le signal post-sismique observé associé à cet événement et la déformation post-sismique modélisée en utilisant une rhéologie de Burgers avec une viscosité long terme de 1.9×10^{18} Pa s, contestant l'hypothèse d'une diminution du couplage interséismique conduisant finalement à le méga-thrust d'Iquique.

Mots Clés

GPS, inclinomètre, subduction, couplage, relaxation viscoélastique, Tarapaca 2005

Abstract

Subduction zones involve the recycling of oceanic lithosphere in the convective mantle to form continental crust by upward migration of the melted part of the slab. In this long-term process, the upper plate accumulates stresses that are instantaneously released in the form of earthquakes, repeating over a cyclic process: the subduction earthquake cycle (SEC). Nevertheless, fast slip on faults is not the only process contributing to the deformation during the SEC. For instance, the low frequency process of aseismic slip is observed in the form of steady fault creeping and transient slow slip. Examples of the latest are the phenomenon of afterslip, and slow slip earthquakes (SSEs) with much longer durations than "normal" earthquakes. Of the same importance is the effect of stress induced by an earthquake in the mantle. Because it behaves like a viscoelastic body, the mantle will relax this stress during a slow, long-lasting (up to decades) and large-scale (up to thousands of km) deformation process. All these phenomena impact the upper plate deformation and have to be considered in slip budget analysis over the SEC in order to obtain the real estimation of the seismic hazard of a region. Following this premise, the principal motivation of this work is to contribute to the determination of the actual locking state of the north seismic gap of the Chilean subduction zone.

The main part of this study was conducted along two directions: analyzing and interpreting both short-term (days, weeks) and long-term (several years) transient deformations detected by permanent GPS stations deployed in north Chile. First, with an exhaustive search for short-term transient signals in 15-years long geodetic time series, we aim at contributing to the current debate of whether slow slip events do occur in the Chilean subduction zone or not. Up to now, only a single and debated case of slow slip associated to the nucleation phase of Iquique 2014 has been reported. Our results, obtained after thorough filtering and analysis of the time series devoted to reduce their inherent noise, indicate the existence of only 3 events that are likely to correspond to small episodes of aseismic slip. They occur between 2009 and 2011, with durations of few weeks and amplitudes that do not exceed 4 mm. Additionally, the occurrence of the larger aseismic slip episode simultaneous to the foreshock activity of Iquique 2014 earthquake is confirmed, and the analysis is pushed further with the help of long-base tiltmeter records. Thanks to this refined analysis and to the sensitivity of this instrument, 4 distinct slow slip events can be identified in the larger region of slow slip revealed by GPS data, occurring during the 3 months previous to the mainshock with magnitudes ranging between Mw 5.8 and 6.2. Finally, a long-term analysis of the same cGPS time series was conducted in order to identify small but significant changes of trends over long durations. Available data indicate a long-term decrease of the upper plate deformation after the intermediate depth earthquake of Tarapaca 2005 (Mw 7.7). We test the viscoelastic effect of the asthenosphere on surface deformation triggered by deep failure (~ 100 km depth). For this, we build a realistic 3D viscoelastic finite element model and tried Maxwell and Burgers viscoelastic rheologies. We find a very good correspondence between the observed postseismic signal associated to this event and the modeled postseismic deformation using a Burgers rheology with a long-term viscosity of 1.9×10^{18} Pa s, challenging the hypothesis of a decrease of interseismic coupling eventually leading to the megathrust failure of Iquique.

Keywords

GPS, tiltmeter, subduction, coupling, viscoelastic relaxation, Tarapaca 2005